SULFATE RADICAL BASED ADVANCED OXIDATION PROCESSES COUPLED WITH CERAMIC MEMBRANES FOR WATER PURIFICATION

BAO YUEPING

2019

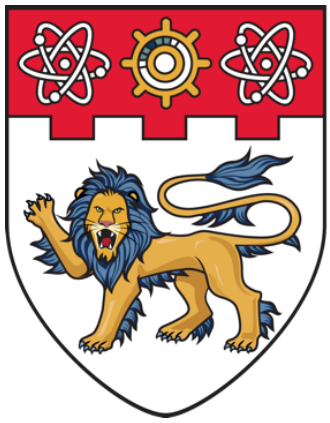

NANYANG TECHNOLOGICAL UNIVERSITY

SINGAPORE

SULFATE RADICAL BASED ADVANCED OXIDATION PROCESSES COUPLED WITH CERAMIC MEMBRANES FOR WATER PURIFICATION

BAO YUEPING
Interdisciplinary Graduate School
Nanyang Environment and Water Research Institute

2019

SULFATE RADICAL BASED ADVANCED OXIDATION PROCESSES COUPLED WITH CERAMIC MEMBRANES FOR WATER PURIFICATION

BAO YUEPING

Interdisciplinary Graduate School
Nanyang Environment and Water Research Institute

A thesis submitted to the Nanyang Technological University in partial fulfilment of the requirement for the degree of Doctor of Philosophy

2019

Statement of Originality

I hereby certify that the work embodied in this thesis is the result of original research, is free of plagiarised materials, and has not been submitted for a higher degree to any other University or Institution.

2019-07-03 BAO YUEPING 

. . . . . .
Date

. . . . . .
[Input Name Here]

Supervisor Declaration Statement

I have reviewed the content and presentation style of this thesis and declare it is free of plagiarism and of sufficient grammatical clarity to be examined. To the best of my knowledge, the research and writing are those of the candidate except as acknowledged in the Author Attribution Statement. I confirm that the investigations were conducted in accord with the ethics policies and integrity standards of Nanyang Technological University and that the research data are presented honestly and without prejudice.

2019-07-03	Prof. HU XIAO 
. . . . .	. . . . .
Date	[Input Supervisor Name Here]

Authorship Attribution Statement

This thesis contains material from 4 paper(s) published in the following peer-reviewed journal(s) where I was the first and/or corresponding author.

Chapter 3 is published as Bao, Y., Oh, W.-D., Lim, T.-T., Wang, R., Webster, R.D., Hu, X., 2018. Surface-nucleated heterogeneous growth of zeolitic imidazolate framework-A unique precursor towards catalytic ceramic membranes: synthesis, characterization and organics degradation. Chem. Eng. J. 353, 69–79.

Chapter 4 is published as Bao, Y., Lee, W J., Lim, T.-T., Wang, R., Hu, X., 2019. Pore-functionalized ceramic membrane with isotropically impregnated cobalt oxide for sulfamethoxazole degradation and membrane fouling elimination: Synergistic effect between catalytic oxidation and membrane separation. Appl Catal B: Environ. 254, 37–46.

Chapter 5 is published as Bao, Y., Lim, T.-T., Wang, R., Webster, R.D., Hu, X., 2018. Urea-assisted one-step synthesis of cobalt ferrite impregnated ceramic membrane for sulfamethoxazole degradation via peroxymonosulfate activation. Chem. Eng. J. 343, 737–747.

Chapter 6 is published as Bao, Y., Oh, W.-D., Lim, T.-T., Wang, R., Webster, R.D., Hu, X., 2019. Elucidation of stoichiometric efficiency, radical generation and transformation pathway during catalytic oxidation of sulfamethoxazole via peroxymonosulfate activation. Water Res. 151, 64–74.

The contributions of the co-authors are as follows:

- Prof. Hu and Prof. Wang provided the initial project direction and the funding support.
- I prepared the manuscript drafts as well as the data collection, which was revised by Mr. Lee W J, Dr. Oh W-D and Prof. Lim.
- Prof. Webster assisted in the collection of the EPR data.

2019-07-03	BAO YUEPING 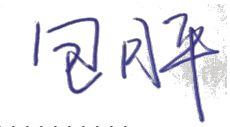
. . . . .	. . . . .
Date	[Input Name Here]

SUMMARY

The intensive use of antibiotics for human, veterinary and agricultural purposes results in their continuous release into the environment, which causes the concern in relation to the development of antibiotic resistance genes and bacteria. Sulfate radical based advanced oxidation processes (SR-AOPs) have been recognized as an effective alternative method to the destruction of recalcitrant organics in wastewater, in which highly-reactive sulfate radical was generated and utilized to oxidize organic contaminants to innocuous CO_2 and H_2O. However, most of the catalysts used in SR-AOPs are suspended in water during usage and therefore need a further separation process. On the other hand, membrane separation has been proved to be a promising technology for water purification in recent decades because of the high yield of production and low energy consumption. However, the membrane fouling caused by the accumulation of a broad range of foulants on top of membrane surface / inside the membrane pores results in a substantial decrease in their water permeability, which leads to a high permeability loss and energy consumption. Meanwhile, the separation principle for microfiltration (MF) is based on size exclusion, which means that it cannot remove many kinds of organic micro-pollutants during the physical separation process, resulting in the effluent discharge with potential hazard. The aim of this thesis work is to overcome these drawbacks by integrating MF with SR-AOPs in the water purification system to remove antibiotics, in which sulfamethoxazole (SMX) works as the target pollutant.

Firstly, a Co_3O_4 surface functionalized ceramic membrane (CoFCM) was synthesized via a novel ZIF-67 induced surface nucleated heterogeneous growth method (Chapter 3). The CoFCM showed an enhanced performance in SMX removal in a semi-batch experiment. In chapter 4, a Co_3O_4 impregnated ceramic membrane (CoCM) was developed via an in-situ self-scarified template method. With this method, Co_3O_4 was isotropically impregnated into the whole membrane while did not affect the pore size of the membranes. Due to the advantages

of mix-metal oxides on PMS activation, a cobalt ferrite ($CoFe_2O_4$) impregnated ceramic membrane was developed via a one-step urea combustion method (Chapter 5). Results showed that $CoFe_2O_4$ was impregnated into the membrane pores as well as the membrane surface. With increasing of repeating times, the catalyst loading amount increased while the pure water permeability decreased, which means the catalyst would form a dense catalytic layer on the membrane surface due to the aggregation during the combustion process. The membrane performance was evaluated in a home-made dead-end membrane filtration mode, and results showed the robust membrane can function well during a wide pH range as well as the existence of NOM and anions.

Finally, to have a better understanding on the SMX transformation via PMS in the presence of nano-bimetallic Co/Fe oxides, a systematic study was conducted in Chapter 6. The influencing factors (pH, NOM, catalyst loading and PMS dosage) were investigated and the radical generation as well as PMS activation mechanism were explored. The SMX transformation pathway including both non-radical and radical pathways was proposed.

ACKNOWLEDGEMENTS

During my PhD study, I have received lots of assistance and cooperation. Firstly, I would like to express my deepest gratitude and appreciation to my academic supervisor Prof. Hu Xiao for his wisdom, support, encouragement, suggestion and patience with his outstanding expertise in the thick of academic program and research work. His mentoring approach allows me to broaden my eyesight and I am honored to have the opportunity to be one of his students and learn from him.

I am also grateful to my academic supervisor Prof. Wang Rong for her encouragement and kind support. Her rich experience on membrane fabrication and process gives me lots of help and has motived me to continue my research. Meanwhile, her kind suggestions on paper writing also help me a lot.

Next I want to convey my appreciation to Prof. Lim Teik-Thye and Prof. Richard Webster for their kind help and patient guides. Meanwhile, I would like to thank all the research fellows in NEWRI for sharing their experience and knowledge without reservation.

I would like to thank all the officers and technical staffs in NEWRI, MSE and CEE for their cooperation and kind help. The research scholarship from Nanyang Technological University (NTU) is also gratefully acknowledged.

Finally, I would like to express my deepest appreciation to my family and friends for their understanding and support.

LIST OF PUBLICATIONS AND CONFERENCES

PUBLICATIONS

1. **Bao, Y.,** Lee WJ., Wang P., Xing J., Liang YN., Lim, T.-T., Hu X., A Novel Molybdenum-based Nanocrystal Decorated Ceramic Membrane for Organics Degradation via Catalytic Wet Air Oxidation (CWAO) at Ambient Conditions. Catalysis Today (Under Revision).
2. **Bao, Y.,** Tian, M., Lua, S.K., Lim, T.-T., Wang, R., Hu, X., 2019. Spatial confinement of cobalt crystals in carbon nanofibers with oxygen vacancies as a high-efficiency catalyst for organics degradation. Chemosphere 125407.
3. **Bao, Y.,** Tay, Y.-S., Lim, T.-T., Wang, R., Webster, R.D., Hu, X., Polyacrylonitrile (PAN)-induced carbon membrane with in-situ encapsulated cobalt crystal for hybrid peroxymonosulfate oxidation-filtration process: preparation, characterization and performance evaluation. Chem. Eng. J. 373, 425-436.
4. **Bao, Y.,** Lee WJ., Lim, T.-T., Wang, R., Hu, X., Pore-functionalized ceramic membrane with isotropically impregnated cobalt oxide for sulfamethoxazole degradation and membrane fouling elimination: Synergistic effect between catalytic oxidation and membrane separation. Appl Catal B: Environ. 254, 37–46.
5. **Bao, Y.,** Chen Y., Lim, T.-T., Wang, R., Hu, X., 2019. A novel MOF-mediated interfacial polymerization for facile and robust deposition of RO-like polyamide layer on ceramic substrates. Adv. Mater. Interfaces 6, 1900132.
6. **Bao, Y.,** Oh, W.-D., Lim, T.-T., Wang, R., Webster, R.D., Hu, X., 2019. Elucidation of stoichiometric efficiency, radical generation and transformation pathway during catalytic oxidation of sulfamethoxazole via peroxymonosulfate activation. Water Res. 151, 64–74.
7. **Bao, Y.,** Oh, W.-D., Lim, T.-T., Wang, R., Webster, R.D., Hu, X., 2018. Surface-

nucleated heterogeneous growth of zeolitic imidazolate framework-A unique precursor towards catalytic ceramic membranes: synthesis, characterization and organics degradation. Chem. Eng. J. 353, 69–79.

8. **Bao, Y.,** Lim, T.-T., Wang, R., Webster, R.D., Hu, X., 2018. Urea-assisted one-step synthesis of cobalt ferrite impregnated ceramic membrane for sulfamethoxazole degradation via peroxymonosulfate activation. Chem. Eng. J. 343, 737–747.
9. **Bao, Y.,** Lim, T.-T., Goei, R., Zhong, Z., Wang, R., Hu, X., 2018. One-step construction of heterostructured metal-organics@Bi_2O_3 with improved photoinduced charge transfer and enhanced activity in photocatalytic degradation of sulfamethoxazole under solar light irradiation. Chemosphere 205, 396–403.
10. **Bao, Y.,** Lim, T.-T., Zhong, Z., Wang, R., Hu, X., 2017. Acetic acid-assisted fabrication of hierarchical flower-like Bi_2O_3 for photocatalytic degradation of sulfamethoxazole and rhodamine B under solar irradiation. J. Colloid Interface Sci. 505, 489–499.
11. Lee, W.J., **Bao, Y.,** Hu, X., Lim, T.-T., 2019. Hybrid Catalytic Ozonation-Membrane Filtration Process with CeOx and MnOx Impregnated Catalytic Ceramic Membranes for Micropollutants Degradation. Chem. Eng. J. (Accepted)
12. Xing, J., Liang, H., Chuah, C.J., **Bao, Y.,** Luo, X., Wang, T., Wang, J., Li, G., Snyder, S.A., 2019. Insight into Fe (II)/UV/chlorine pretreatment for reducing ultrafiltration (UF) membrane fouling: Effects of different natural organic fractions and comparison with coagulation. Water Res. 167, 115112.
13. Oh, W.-D., Lee, M.G.-H., Udayanga, W.C., Veksha, A., **Bao, Y.,** Giannis, A., Lim, J.-W., Lisak, G., 2019. Insights into the single and binary adsorption of copper (II) and nickel (II) on hexagonal boron nitride: Performance and mechanistic studies. J. Environ. Chem. Eng. 7, 102872.

CONFERENCES

1. PPC-16 (16th Pacific Polymer Conference), 8-12 December, 2019, Suntec Singapore. Poster Presentation (Metal Organic Frameworks as the Intermediate Layer to Construct Inorganic/organic Composites).
2. ICCMR-14 (14th International Conference on Catalysis in Membrane Reactors), 8-11 July 2019, Eindhoven, The Netherlands. Oral Presentation (**Chair** and **Keynote Speaker** for Membrane Separation Section; Hybrid catalytic ceramic membranes for water reclamation).
3. ICMAT 2019 (10th International Conference on Materials for Advanced Technologies), 23-28 June 2019, Marina Bay Sands, Singapore. Symposium S) Innovations in Membrane Technology-Discovery, Process and Applications. Oral Presentation (Hybrid Membrane Process with Catalytic Micro-reactor).
4. IWA World Water Congress & Exhibition 2018. 16-21 September, 2018, Tokyo, Japan. Poster Presentation (Metal-organic Composites for Photocatalysis).
5. ICMAT 2017 (9th International Conference on Materials for Advanced Technologies), 18-23 June 2017, Suntec Singapore. Symposium CC) Poster Presentation (Thermally Modified Layer-by-Layer (TMLBL) Fabrication of MOF/Bi_2O_3 Composites for Photocatalysis).

TABLE OF CONTENTS

LIST OF TABLES

LIST OF FIGURES

LIST OF SYMBOLES AND ABBREVIATIONS

AOPs	Advanced oxidation processes
SR-AOPs	Sulfate radical based advanced oxidation processes
PMS/Oxone	Peroxymonosulfate
PS	Persulfate
SMX	Sulfamethoxazole
$SO_4^{\bullet-}$	Sulfate radical
$^{\bullet}OH$	Hydroxyl radical
ROS	Reactive oxygen species
E^0	Standard reduction potential
k	Rate constant
TBA	*tert*-butanol
MeOH	Methanol
ZIF	Zeolitic imidazolate framework
MOF	Metal organic framework
2-MIM	2-methylimidazole
HA	Humic acid
NOM	Natural organic matter
TMP	Trans-membrane pressure
ζ	Zeta potential
λ	Wavelength
MWCO	Molecular weight cut off
MF	Microfiltration
R_m	Intrinsic membrane resistance

DMPO	5,5-dimethyl-1-pyrrolidine N-oxide
BMPO	5-*tert*-Butoxycarbonyl-5-methyl-1-pyrroline-N-oxide
TEMP	2,2,6,6-tetramethylpiperidine
FESEM	Field emission scanning electron microscope
XRD	X-rays diffractometer
XPS	X-ray photoelectron spectroscopy
FTIR	Fourier transformed infra-red spectrometer
AFM	Atomic force microscopy
TGA	Thermogravimetric analysis
EPR	Electron paramagnetic resonance
HPLC	High performance liquid chromatography
ICP-OES	Inductively coupled plasma optical emission spectrometry
TOC	Total organic carbon
IC	Ion chromatography

CHAPTER 1 INTRODUCTION

1.1 Background

Because of climate changes, the surface water and ground water resources are diminishing globally. On the other hand, however, the demand for clean water keeps increasing. With decreasing fresh water availability and growing demand for clean water, alternative water sources like water desalination and water reuse have been used all over the world (Stefan, 2017). Meanwhile, the contamination of fresh water supplies poses a serious threat to mankind and the planet Earth. Based on the World Health Organization report, there are still 663 million people (1 in 10 people around the world) lack improved drinking water sources and every 90 seconds a child dies from a water-related disease (Organization et al., 2015). It is estimated that by 2025, half of the world's population will be living in water stressed areas. At the same time, the increasing water pollution with a variety of manmade chemicals makes it difficult to provide an efficient, cost-effective and environmentally friendly technology for water reclamation due to the existence of micropollutants in water.

In order to fully realize the function of water reclamation, the removal of different types of water-borne pollutants from wastewater needs to be considered. Among all the pollutants, antibiotics has emerged as one big focus of attention. The intensive use of antibiotics for medical, veterinary and agricultural purposes results in their continuous release into the environment (Brown et al., 2006; Hirsch et al., 1999). The major concern in relation to that is the development of antibiotic resistance genes and bacteria, which would reduce the therapeutic potential against human and animal pathogens (Rizzo et al., 2013). A novel and robust wastewater treatment is required to overcome the problems caused by different emerging contaminants, including antibiotics. Compared with conventional methods, the use of membrane separation for water purification has gained much interest in the last decades

because of lower energy consumption and higher efficiency (Li et al., 2011). As the first developed membrane, polymeric membrane has been the major kind used in industry because of the low cost and simple fabrication. However, polymeric membrane is susceptible to damage from the operation because of the low strength. Compared with polymeric membrane, ceramic membrane is more robust and hydrophilic which means they could be used in extreme environment with a less tend of fouling.

On the other hand, advanced oxidation processes (AOPs) have shown tremendous promise in water purification and treatment, including for the destruction of naturally occurring toxins, contaminants of emerging concern, pesticides and other deleterious contaminants (O'Shea and Dionysiou, 2012). AOPs have been widely investigated for the removal of organics in water. Generally, it is well accepted that the removal efficiency of antibiotics using AOPs is much higher than other technologies (Rodriguez-Narvaez et al., 2017). The commonly used AOPs include photocatalysis, Fenton oxidation and ozonation, in which hydroxyl radical ($^{\bullet}OH$) would be generated to attack the organics.

Different from the conventional hydroxyl radical ($^{\bullet}OH$) based AOPs, sulfate radical based advanced oxidation processes (SR-AOPs) have been developed and recognized as an effective alternative method to the destruction of recalcitrant organics in wastewater. In this process, the highly-reactive sulfate radical would be generated and utilized to oxidize organic contaminants to innocuous CO_2 and H_2O (Oh et al., 2016). Most commonly, sulfate radical could be generated via peroxymonosulfate (PMS) or persulfate (PS) activated with metal oxides (Anipsitakis and Dionysiou, 2004). The heterogeneous catalyst/PMS system is favorable in practical applications because it can minimize the adverse effect of metal ions on human healthy (P. R. Shukla et al., 2010). So far, various supporting materials including resin, zeolite , Al_2O_3 and mesoporous carbon have been designed and used for PMS activation (Chu et al., 2007; Kon'kova et al., 2015; P. Shukla et al., 2010; Zhuang et al., 2016). However, most of

them are suspended in water during use and therefore a further separation process is required.

The interest to couple AOPs and membrane separation has started with the introduction of photocatalytic oxidation treatment in tandem with a membrane separation treatment (Molinari et al., 2004, 2000) followed by the ozonation combined membrane technology. Even sulfate radical shows more advantages compared with hydroxyl radical, the study on SR-AOPs and membrane technology is rarely limited.

1.2 Motivation and knowledge gap

SR-AOPs and membrane technology have been developed as two important ways in water treatment process, especially in the antibiotics removal. Both technologies have some limitations in the real practice. For SR-AOPs, the limitation is the recovery of catalyst as well as the metal leaching issue. Since most of the catalysts are in power form, the recovery of the catalysts needs a further post treatment. For membrane technology, the limitations are membrane fouling and the post-treatment of concentrate. Meanwhile, only high pressure filtration (NF/RO) can remove the micro pollutants due to their small molecules, which generally indicates high energy consumption. To address these problems, SR-AOPs combined microfiltration ceramic membranes (SR-CMs), which combine catalysis and microfiltration separation, could been introduced as a sustainable solution to achieve multifunction like physical separation, chemical purification and improved antifouling property.

1.3 Research objectives

The general objective of this study was to fabricate a multifunctional low pressure microfiltration ceramic membrane for water purification, in which SR-AOPs and membrane technology were combined in one unit. Meanwhile, sulfamethoxazole (SMX) was chosen as the target antibiotic in this study due to the intensive usage and potential hazard in this study.

The specific scopes of work in each part of this study are outline below:

1. Fabrication of Co_3O_4 functionalized ceramic membrane (CoFCM) for organics removal, in which porous Co_3O_4 was coated on the ceramic membrane surface via a surface-nucleated heterogeneous growth method (Chapter 3).

a. To optimize the synthesis conditions for preparing Co_3O_4 functionalized ceramic membrane (CoFCM), including the concentrations of precursors and the calcination temperatures;

b. To evaluate the performance of CoFCM for SMX removal via PMS activation;

c. To investigate the effects of PMS dosage on SMX removal as well as the stability of CoFCM;

d. To propose the SMX removal mechanism in CoFCM/PMS/membrane system.

2. Fabrication of Co_3O_4 impregnated ceramic membrane (CoCM) and evaluation of its performance in SMX removal and fouling elimination in CoCM/PMS system (Chapter 4).

a. To prepare the CoCM via an in-situ self-scarified template method;

b. To evaluate the performance of CoCM in SMX removal in a dead-end filtration mode;

c. To evaluate the antifouling property of CoCM in humic acid removal;

d. To propose the organics (HA and SMX) removal mechanism in CoCM/PMS/membrane system.

3. Fabrication of a novel bi-metallic oxides $CoFe_2O_4$ impregnated ceramic membrane for SMX removal (Chapter 5).

a. To prepare the $CoFe_2O_4$ impregnated ceramic membrane via a one-step urea combustion method;

b. To optimize the synthesis conditions for $CoFe_2O_4$ impregnated ceramic membrane (calcination temperature and catalyst loading cycles);

c. To investigate the performance of $CoFe_2O_4$ impregnated ceramic membrane in SMX

removal, and the effects of PMS dosage, contact time, pH, NOM, anions were examined;

d. To propose the PMS activation mechanism in $CoFe_2O_4$ impregnated ceramic membrane.

4. Investigation the transformation pathway of SMX and PMS activation mechanism in the presence of nano-bimetallic Co/Fe oxides (Chapter 6).

a. To prepare a series of nano-bimetallic Co/Fe oxides with different stoichiometric ratios via a one-step combustion method;

b. To investigate the effects of experimental parameters (pH, catalyst loading, PMS dosage) on SMX removal;

c. To propose the SMX transformation pathway via both non-radical and radical pathway;

d. To propose the PMS activation mechanism and the different functions of Fe and Co.

The main tasks and whole scope for this research are shown in **Fig 1.1**.

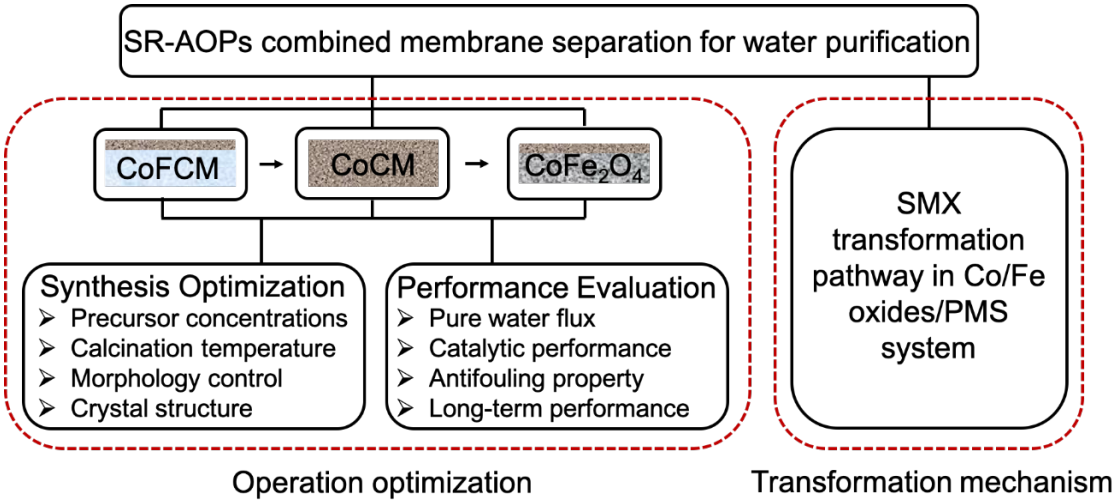

Fig 1.1. The flow-chart of the present study.

1.4 Scope of thesis

The thesis consists of seven chapters. This chapter presents a brief background of study, current knowledge gap and research motivation, objectives, scopes of the study and the organization of this thesis. Chapter 2 provides an up-to-date literature review of the SR-AOP and the combined technologies with membrane separation in water treatment. In Chapter 3, the

Co_3O_4 surface functionalized ceramic membrane (CoFCM) via a surface-nucleated heterogeneous growth method was developed and the performance of CoFCM in a semi-batch filtration system was investigated. Chapter 4 describes the synthesis of pore-functionalized ceramic membrane with isotropically impregnated Co_3O_4 (CoCM) as well as the performance evaluation in a home-made dead-end membrane filtration system. In Chapter 5, the synthesis of mixed metal oxides $CoFe_2O_4$ impregnated ceramic membrane was achieved via a one-step urea combustion method. The performance of $CoFe_2O_4$ impregnated ceramic membrane for SMX removal in water via PMS activation was presented. Chapter 6 investigates the SMX transformation pathway and PMS activation mechanism in the presence of bi-metallic Co/Fe oxides in a batch system. Finally, in Chapter 7, a summary of all the major findings in this thesis and several recommendations for future work are provided.

CHAPTER 2 LITERATURE REVIEW

2.1 Sulfate radical based AOPs (SR-AOPs)

Compared with hydroxyl radical ($^{\bullet}OH$)-based processes, the history of sulfate radical-based AOPs (SR-AOPs) is more recent and covers about half a century of research, with an increasing interest into sulfate radical ($SO_4^{\bullet-}$) driven oxidation for destruction of recalcitrant organics in water. The SR-AOPs utilize highly reactive sulfate radical (E^0 = 2.60 V) to oxidize organic contaminants to innocuous CO_2 and H_2O. **Table 2.1** lists the comparison between $^{\bullet}OH$ and $SO_4^{\bullet-}$. The $SO_4^{\bullet-}$ has a comparable standard redox potential with $^{\bullet}OH$, but the lifetime is much longer compared with $^{\bullet}OH$, which allows excellent mass transfer and contact between $SO_4^{\bullet-}$ with the target pollutants. The reactivity of $SO_4^{\bullet-}$ is pH independent while that of $^{\bullet}OH$ is pH dependent. Therefore, the $SO_4^{\bullet-}$ exhibits an even higher standard redox potential than the $^{\bullet}OH$ at neutral pH, which makes the $SO_4^{\bullet-}$ superior in mineralizing numerous organic compounds (Anipsitakis and Dionysiou, 2004). In aqueous solution, the $SO_4^{\bullet-}$ can also participate in pH-dependent reactions to produce $^{\bullet}OH$, especially in alkaline solutions (**Eq. 2.1**). Therefore, the dominate radical species changes depending on the solution pH. At pH<9, $SO_4^{\bullet-}$ is the dominant reactive radical while at pH>9, $^{\bullet}OH$ becomes the dominant reactive radical.

$$SO_4^{\bullet-} + OH^- \rightarrow SO_4^{2-} + {}^{\bullet}OH \qquad k = (6.5\pm1.0) \times 10^7\ M^{-1}\ s^{-1} \qquad (\mathbf{2.1})$$

Both $SO_4^{\bullet-}$ and $^{\bullet}OH$ react with organic compounds of various classes following three basic processes: hydrogen atom abstraction, one-electron transfer and addition to unsaturated bonds. However, $SO_4^{\bullet-}$ is more selective than the $^{\bullet}OH$ in the reactions with organic compounds, since it reacts more readily by electron transfer but slower by H-abstraction and addition (Stefan, 2017). Because of the slower reactions of H-abstraction, the $SO_4^{\bullet-}$ is less influenced by the

natural organic matter (NOM) compared to $^{\bullet}OH$, and thus $SO_4^{\bullet-}$ can selectively attacks the target pollutants in the presence of NOM. Furthermore, the $SO_4^{\bullet-}$ exhibits high oxidation efficiencies in both carbonate and phosphate buffer solutions (Anipsitakis and Dionysiou, 2003).

Table 2.1. Comparison of properties of hydroxyl radical and sulfate radical.

	$^{\bullet}OH$	$SO_4^{\bullet-}$	Ref.
E^0 (V)	1.80-2.70	2.50-3.10	(Eberson, 1982a; Lim et al., 2011)
Life time (μs)	=< 1	30-40	(Matta et al., 2011; Olmez-Hanci and Arslan-Alaton, 2013)
pH dependence	>9	1-9	(Fang et al., 2012)
Major reaction mechanism	H-abstraction	Electron transfer	(Oh et al., 2016; Stefan, 2017)
$k_{organics}$ ($M^{-1}s^{-1}$)	10^6-10^{11}	10^5-10^9	(Neta et al., 1977; Tsitonaki et al., 2010)
k_{NOM} (mg $C^{-1}s^{-1}$)	(2.2-6.7) × 10^4	6.8 × 10^3	(Lutze et al., 2015; Westerhoff et al., 1999)

Note*:* E^0-Standard reduction potential; *k-Second*-order rate constant

The most common $SO_4^{\bullet-}$ generation methods are based on the peroxymonosulfate (PMS, HSO_5^-) or persulfate (PS, $S_2O_8^{2-}$) activation via energy (heat, ultraviolet, ultrasound, radiolysis, etc) and catalyzer activation. PMS is commercially available by the trade name of Oxone. The structure of the PMS anion is HSO_5^- with the bond lengths of the three terminal S-O and one internal S-O bonds similar to those in PS ($S_2O_8^{2-}$) and the O-O distance similar to that in H_2O_2 (Zhang and Lin, 2010). Both PMS (E^0 = 1.82 V) and PS (E^0 = 2.01 V) are thermodynamically strong oxidants in acidic solutions, but direct reactions of PS or PMS with most pollutants are slow (Zhang et al., 2015). When appropriately activated, they can decompose to form sulfate radical, which is a strong one-electron oxidant that rapidly and effectively oxidizes many organic compounds.

Even though PMS or PS can be effectively activated by different energy activators, transition metal-based activation is the most viable for field application owing to avoiding the high requirement of energy and decreasing the complexity and the costs of the process. Meanwhile, due to the differences in their molecular structures (i.e. PMS is asymmetrical while PS is symmetrical) and bond dissociation energies, PMS is relatively easier to be activated with metal-based catalysts (Oh et al., 2016) with a relatively longer lifespan as they can potentially be regenerated through a redox cycle with PMS (M^{n+} - $M^{(n+1)+}$ - M^{n+}). As the commercial name of PMS, Oxone is a versatile and environmental friendly oxidant and has been widely utilized for bleaching, cleaning and disinfection (Ermer and Röbke, 2003; Sun et al., 2009). Therefore, in this thesis, we focus on the PMS activation via transition metal-based catalyst. The transition metal ions could activate PMS to form sulfate and other radicals through the following reactions (**Eqs.2.2-2.4**).

$$HSO_5^- + M^{n+} \rightarrow SO_4^{\bullet-} + OH^- + M^{(n+1)+} \quad (\mathbf{2.2})$$

$$HSO_5^- + M^{n+} \rightarrow SO_4^{2-} + {}^{\bullet}OH + M^{(n+1)+} \quad (\mathbf{2.3})$$

$$HSO_5^- + M^{(n+1)+} \rightarrow SO_5^{\bullet-} + H^+ + M^{n+} \quad (\mathbf{2.4})$$

The metal activation of PMS can be achieved in the homogeneous and heterogeneous systems. In the literatures, Co(II)/PMS was proved to be the most efficient catalysis system for the generation of sulfate radical, the adverse effect of dissolved Co ions on human health is always a concern. Therefore, it would be beneficial to activate PMS in a heterogeneous system, which may avoid the problem caused by dissolved or leached metal ions present in the treated water (Zhang et al., 2015). Solid catalysts have also attracted a great deal of attention due to high stability and durability, cost-effectiveness and ability to be easily separated (Davis and Davis, 2012).

2.2 Development of cobalt-based catalyst for PMS activation

Since cobalt was found to be the best catalyst activator of PMS, most of the heterogeneous catalysts for PMS activation are based on cobalt compounds. **Table 2.2** shows the synthesis methods and performances of Co-based catalyst as PMS activator. The group of Dionysiou first conducted the research about heterogeneous activation for sulfate radical generation to degrade contaminants. They used the commercial cobalt oxides, CoO and Co_3O_4, to activate PMS for oxidation of 2,4-DCP. Results showed that Co_3O_4-activated PMS heterogeneously exhibits higher 2,4-DCP removal efficiencies and lower Co leaching at neutral pH compared with CoO (Anipsitakis et al., 2005). However, undesirable Co leaching was still observed especially under acidic condition (Chen et al., 2008; Guo et al., 2013). To address the Co leaching problem, Co_3O_4 has been decorated on various supports including metal oxides (Yang et al., 2008, 2007), carbon materials (Lin et al., 2015b; Shi et al., 2012b; P. R. Shukla et al., 2010), industrial wastes (Muhammad et al., 2012a, 2012b; Saputra et al., 2012), and adsorbents (Shukla et al., 2011a) via different methods (**Table 2.2**). The main activation mechanism in Co_3O_4/PMS system shows in **Eqs.2.1, 2.5-2.9 (Fig 2.2)** (Kim and Edwards, 1995).

$$Co^{2+} + H_2O \leftrightarrow CoOH^+ + H^+ \quad (\mathbf{2.5})$$

$$CoOH^+ + HSO_5^- \rightarrow CoO^+ + H_2O + SO_4^{\bullet-} \quad (\mathbf{2.6})$$

$$CoO^+ + 2H^+ \rightarrow Co^{3+} + H_2O \quad (\mathbf{2.7})$$

$$Co^{2+} + SO_4^{\bullet-} \rightarrow Co^{3+} + SO_4^{2-} \quad (\mathbf{2.8})$$

$$Co^{3+} + HSO_5^- \rightarrow Co^{2+} + SO_5^{\bullet-} + H^+ \quad (\mathbf{2.9})$$

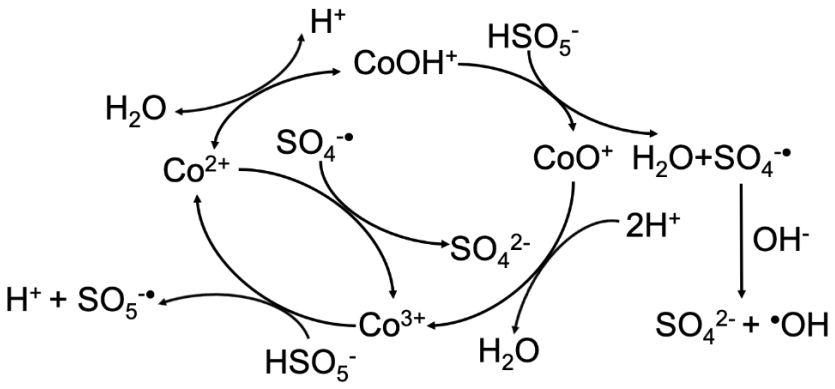

Fig 2.1. Mechanism on radical chain reactions in Co/PMS system.

Another alternative way to suppress the cobalt leaching is to prepare the cobalt based mixed metal oxide. One important example is cobalt ferrite ($CoFe_2O_4$), which show superior properties in PMS activation compared with Co_3O_4, including 1) the cobalt in $CoFe_2O_4$ is divalent, while Co (III) in Co_3O_4 shows some detrimental effects on PMS activation(Yang et al., 2009); 2) $CoFe_2O_4$ can markedly suppress cobalt leaching due to strong Fe-Co interactions (Kim et al., 2000) ; 3) $CoFe_2O_4$ is easier to be separated from reaction system by an external magnetic field due to its unique ferromagnetic properties (Sadri et al., 2014), 4) Fe can also activate PMS because of the multivalent states of Fe (**Eqs.2.2-2.4**); 5) the presence of Fe is found to be beneficial for enriching hydroxyl groups and $CoOH^+$ on the surface of Fe-Co catalyst, which is curial to active PMS (**Eqs. 2.10-2.11**). 6) The presence of Fe would promote the regeneration of Co^{2+} due to the standard reduction potentials difference (**Eq. 2.12**) (Su et al., 2013).

$$Fe^{3+} + H_2O \leftrightarrow FeOH^{2+} + H^+ \quad (\mathbf{2.10})$$

$$Co^{2+} + FeOH^{2+} \rightarrow CoOH^+ + Fe^{3+} \quad (\mathbf{2.11})$$

$$Fe^{2+} + Co^{3+} \rightarrow Fe^{3+} + Co^{2+} \ (E^0 = 1.04\ V) \quad (\mathbf{2.12})$$

2.3 Development of membrane technology for antibiotics removal

Due to the limitation of pore size distribution, only nanofiltration (NF) and reverse

osmosis (RO) can remove the small molecular of antibiotics accompanied with a high-energy consumption. Right now, the membrane based technology has been used to remove antibiotics in combination with other processes including adsorption and oxidation. Generally, the ceramic membrane was used to separate the suspended catalysts/adsorbents (Li et al., 2019; Sharma et al., 2017). The slurry system provides a higher mass transfer rate while the catalysts/adsorbents might also be a membrane fouling factor. In the slurry system, membrane filtration can be used as a single step for the complete recovery of catalysts/adsorbents from liquids. It is a physical separation process, which does not involve a phase change or interphase mass transfer, thus, the membrane flux would decline due to the particle fouling. Therefore, the immobilized catalysts system was developed to address this problem. The membrane works as a separation layer of suspended solid, a support of catalyst as well as a selective barrier for the contaminants. The most developed ceramic membrane based technology for antibiotics removal is photocatalytic membrane reactors. Generally, the catalyst (TiO_2) was coated on the membrane surface via dip-coating (Kermanpur et al., 2008; Syafei et al., 2008), spin coating (Wang et al., 2012), vacuum filtration (Bai et al., 2012) and gas deposition (Romanos et al., 2013, 2012). The limitations for photocatalytic membrane reactors in the real applications are the development of new photoatalysts with high quantum efficiency values as well as the light source.

2.4 Development of SR-AOPs combined with membrane technology

Even SR-AOPs have shown a great potential in organics removal in water treatment, most of the catalysts are in power form, which needs a further post-treatment before the water discharge. Membrane technology has been emerged as a potential method for the particle separation and recycle. **Table 2.3** lists the work on SR-AOPs combined with membrane technologies. The combined technology started with Cheng's work, in which Fe(II)/PMS was

chosen as a pre-treatment for ceramic ultrafiltration process. Results showed that the SR-AOPs pre-treatment can effectively reduce the membrane fouling during the ultrafiltration and it enhanced the removal of many kinds of micro pollutants (Cheng et al., 2018, 2017a, 2017b). Later, researchers focused on the preparation of catalytic membranes, in which catalyst was immobilized onto/into the membrane, thus the catalysis and separation would function simultaneously in one unit (Yao et al., 2017; Zhu et al., 2018).

2.5 Conclusions

Compared with polymeric membrane, ceramic membrane shows a high resistance to extreme environment, which makes it suitable to combine with advanced oxidation processes. As a physical separation process, membrane filtration can only transfer the contaminants from one phase to another, the post-treatment of the concentrate is required. Meanwhile, a high-pressure filtration system is needed to remove the artificial chemicals with small molecules. Another concern for membrane filtration is membrane fouling which would decrease the flux and increase the operation cost. On the other hand, advanced oxidation processes (AOPs) can decompose the organics into harmless products. Generally, the AOPs occur in the presence of catalysts, which are suspended in liquid. One major concern is the recovery of the catalysts, especially for drinking water system.

To fully utilize the advantages of ceramic membrane separation and advanced oxidation, a combine system could be applied. The first generation of AOPs combined membrane system is photocataytic membrane reactor followed by the ozonation combined membrane system. Generally, the catalytic membrane reactors have two configurations, which are suspended system and immobilized system. Due to the fact that fixation determines mass transfer limitations of pollutants to the surface of the catalyst and also a loss of photocatalytic activity, suspended system excel the immobilized ones with respect to catalytic degradation efficiency.

However, since membrane filtration is designed to be used as a single step for the complete recovery of catalysts, which would also be the fouling source for membrane, the fouling issue cannot be addressed. The immobilized system resolve the catalyst recovery issue even the mass transfer resistance limited its degradation efficiency. One possible solution is to load the catalyst inside the membrane pores to prepare a micro-reactor, in which forced transport of reactants by convection inside the pores would increase the reaction rate. As we discussion in the previous section, SR-AOPs show a greater potential in the organics decomposition. Therefore, in this thesis, we focus on the immobilized system in which the catalyst was loaded onto/into ceramic membrane for oxidation process.

Table 2.2. Summary on the Co-based catalysts for organics removal via PMS activation.

Cobalt Based-Catalysts	Synthesis method	Experimental Conditions	Performance	Ref.
Co_3O_4	Commercial	[2,4-DCP] = 20 mg L^{-1}; [catalyst] = 0.157 g L^{-1}; [Oxone] = 2.67 mM; [pH] = neutral	Removal > 99% (15 min), Co leaching < 0.07 mg L^{-1}	(Anipsitakis et al., 2005)
Co_3O_4	Commercial	[Amoxicillin] = 0.12 mM; [catalyst] = 0.060 g L^{-1}; [Oxone] = 10 mM; [pH] = 6.0; [T] = 60°C	Removal > 95% (60min) COD removal > 91% (45 min)	(Guo et al., 2013)
Co_3O_4	Precipitation	[AO7] = 0.2 mM; [catalyst] = 0.5 g L^{-1}; [PMS] = 2 mM; [pH] = neutral	Removal > 99% (30 min), Co leaching < 0.05 mg L^{-1} (120 min)	(Chen et al., 2008)
MCG (Magnetic cobalt-graphene nanocomposite)	Carbonization of ZIF-67 and GO	[AY] = 100 mg L^{-1}; [catalyst] = 0.5 g L^{-1}; [PMS] = 90 mg L^{-1}; [pH] = 3.8; [T] = 25°C	Removal > 75% (120 min), Regeneration efficiency ~ 97.6% over 50 cycles	(Lin et al., 2015b)
Co_3O_4/GO	Solvothermal method	[Orange II] = 0.2 mM L^{-1}; [catalyst] = 0.1 g L^{-1}; [PMS] = 2 mM; [pH] = neutral; [T]	Orange II removal ~100% (6min), Low cobalt leaching and high stability of	(Shi et al., 2012b)

		= 25°C	catalyst	
Co_3O_4/GO	Reflux and vacuum drying	[Orange II] = 0.2 mM L^{-1}; [catalyst] = 0.1 g L^{-1}; [PMS] = 2 mM; [pH] = 7.0	Orange II removal ~100% (6min) and Co leaching was 0.5 mg L-1	(Shi et al., 2012a)
Co/TiO_2	Wetness impregnation-calcination	[2,4-DCP] = 0.307 mM L^{-1}; [catalyst] = 0.1 g L^{-1}; [PMS/2,4-DCP molar ratio] = 3:1; [pH] = 7.0	2,4-DCP removal ~90% and Co leaching was ~80 μg L^{-1} (60 min)	(Yang et al., 2008)
Co/RM	Wetness impregnation-calcination	[phenol] = 25 mg L^{-1}; [catalyst] = 0.4 g L^{-1}; [Oxone] = 2 g L^{-1}; [T] = 25°C	Phenol removal ~100% and Co leaching was 1.48-1.60 mg L^{-1} (100 min)	(Muhammad et al., 2012a)
Co/FA	Wetness impregnation-calcination	[phenol] = 30 mg L^{-1}; [catalyst] = 0.4 g L^{-1}; [Oxone] = 2 g L^{-1}; [T] = 25°C	Phenol removal ~40% (100 min)	(Saputra et al., 2012)
Co/FA	Wetness impregnation-calcination	[phenol] = 30 mg L^{-1}; [catalyst] = 0.4 g L^{-1}; [Oxone] = 2 g L^{-1}; [T] = 25°C	Phenol removal ~70% (90 min)	(Muhammad et al., 2012b)
Co/MCS	impregnation-heat treatment	[phenol] = 20 mg L^{-1}; [catalyst] = 0.2 g L^{-1}; [Oxone] = 4 g L^{-1}; [T] = 25°C	Phenol removal ~100% (45min)	(Wang et al., 2014)

Co-SBA-15	Co-condensation	[phenol] = 30 mg L^{-1}; [catalyst] = 0.2 g L^{-1}; [Oxone] = 2 g L^{-1}; [T] = 25°C	Phenol removal ~100% and the Co leaching was 18.26% (180min)	(Shukla et al., 2011a)
Co/AC	Wet impregnation-reduction-oxidation	[phenol] = 25 mg L^{-1}; [catalyst] = 0.2 g L^{-1}; [Oxone] = 2 g L^{-1}; [T] = 25°C	Phenol removal ~100% and TOC removal was 80% (60min) Co leaching is undetectable	(P. R. Shukla et al., 2010)
Co-ZSM-5	Ion-exchange method	[phenol] = 25 mg L^{-1}; [catalyst] = 0.4 g L^{-1}; [PMS] = 2 g L^{-1}; [T] = 25°C	Phenol removal ~100% and TOC removal was 40% (360 min)	(P. Shukla et al., 2010)
Co/TiO_2	Wetness impregnation	[2,4-DCP] = 0.307 mM L^{-1}; [catalyst] = 0.1 g L^{-1}; [PMS/2,4-DCP molar ratio] = 3:1; [pH] = 7.0	2,4-DCP removal ~75% and Co leaching was ~36 μg L^{-1} (120 min)	(Yang et al., 2007)
Co_3O_4/PTFE	Dip-coating	[Orange II] = 0.05 mM L^{-1}; [PMS] = 1 mM L^{-1}; [pH] = 7.0	Orange II removal ~100% (120 min) and Co leaching was 50 μg L^{-1} (8 min)	(Raja et al., 2007)
Co_3O_4/SiO_2	Wet impregnation	[phenol] = 30 mg L^{-1}; [catalyst] = 0.2 g L^{-1}; [PMS] = 2 g L^{-1}; [T] = 25°C	Phenol removal ~78% and Co leaching was 4% (300 min)	(Shukla et al., 2011b)
Co_3O_4/MnO_2	impregnation	[phenol] = 25 mg L^{-1}; [catalyst] = 0.5 g L^{-1}	Phenol removal ~100% (20 min)	(Liang et al., 2012a)

		^{1}; [PMS] = 2 g L^{-1}; [T] = 25°C		
Co_3O_4/zeolites	impregnation	[phenol] = 25 mg L^{-1}; [catalyst] = 0.4 g L^{-1}; [PMS] = 2 g L^{-1}; [T] = 25°C	Phenol removal ~100% (300min)	(Muhammad et al., 2013)
Co_3O_4/CA	Sol-gel method followed by carbonization	[phenol] = 50 mg L^{-1}; [catalyst] = 0.2 g L^{-1}; [PMS] = 2 g L^{-1}	Phenol removal ~100% and Co leaching was 0.8-1.2 mg L^{-1} (120 min)	(Hardjono et al., 2011)
Co_3O_4/CX	impregnation	[phenol] = 50 mg L^{-1}; [catalyst] = 0.2 g L^{-1}; [PMS] = 2 g L^{-1}; [T] = 25°C	Phenol removal ~100% (40 min)	(Sun et al., 2012)
Co_3O_4/TiO_2	Solution combustion	[phenol] = 25 mg L^{-1}; [catalyst] = 0.5 g L^{-1}; [PMS] = 2 g L^{-1}; [T] = 25°C	Phenol removal ~100% (50 min)	(Liang et al., 2012b)
Co_3O_4/Bi_2O_3	Co-precipitation	[MB] = 20 μmol L^{-1}; [catalyst] = 0.05 g L^{-1}; [PMS] = 0.5 mM	MB removal was 98% (10 min) and the Co leaching was 43 μg L^{-1}	(Ding et al., 2012)
Co-MCM41	Co-precipitation	[caffeine] = 0.05 mM; [catalyst] = 0.2 g L^{-1}; [PMS] = 0.2 mM	Caffeine removal was ~99% (15 min) and the Co leaching was 2.6-3.9%	(Qi et al., 2013)
Co_3O_4/MgO	Wetness impregnation	[MB] = 40 mg L^{-1}; [catalyst] = 0.5 g L^{-1}; [PMS] = 0.5 mM	MB removal was ~100% (7 min) and the Co leaching was ~0.1 mg L^{-1} (30 min)	(Zhang et al., 2010)

Co/SBA-15	Wetness impregnation	[phenol] = 50 mg L^{-1}; [catalyst] = 0.1 g L^{-1}; [PMS] = 0.5 g L^{-1}; [T] = 25°C; [pH] = 7.0	Phenol removal was ~100% (10 min) and the Co leaching was < 25 μg L^{-1}	(Hu et al., 2011)
Co-TiO_2	Citric acid assisted sol-gel method	[RhB] = 0.1 mM; [catalyst] = 1.0 g L^{-1}; [PMS] = 0.4 mM; [pH] = 6.9	RhB removal was ~60% (60 min)	(Chen et al., 2013)
Co-Resin	Ion exchange	[Monuron] = 0.2 mM; [catalyst] = 0.5 g L^{-1}; [PMS] = 1 mM	Monuron removal was ~89% (45 min)	(Chu et al., 2007)
CoAlMn	Hydrothermal-calcination	[BPA] = 10 mg L^{-1}; [catalyst] = 0.02 g L^{-1}; [Oxone] = 0.15g L^{-1}; [pH] = 3.6; [T] = 25°C	BPA Removal ~100% and the leaching amounts for Co and Mn were 0.19 and 0.014 mg L^{-1} (120 min)	(Li et al., 2015)
$Fe_{0.8}Co_{2.2}O_4$	Heating nanospheres of $Fe_yCo_{1-y}[Co(CN)_6]_{0.67}\bullet nH_2O$	[BPA] = 20 mg L^{-1}; [catalyst] = 0.1 g L^{-1}; [PMS] = 0.2g L^{-1}; [pH] = 6.0; [T] = 298 K	BPA Removal > 95% and the leaching amount for Co and Fe were 0.36 and 0.11mg L^{-1} (60 min)	(Li et al., 2016)
$CoFe_2O_4$	Sol-gel method	[DBP] = 2 μmol L^{-1}; [catalyst] = 0.1 g L^{-1}; [PMS] = 20 μmol L^{-1}; [pH] = 7.0; [T] =	DBP removal ~80% and the leaching amount for Co and Fe were 0.518 and 0.028 mg L^{-1} (30min)	(Ren et al., 2015)

		20°C		
$Co_{0.75}Fe_{2.25}O_4$	Hydrothermal method	[RhB] = 14 μmol L^{-1}; [catalyst] = 0.05 g L^{-1}; [Oxone] = 1 mmol L^{-1}; [pH] = 6.0	RhB removal > 99% and TOC removal ~54% (40 min)	
Fe-Co mixed oxides	Thermal oxidation	[2,4-DCP] = 0.307 mmol L^{-1}; [catalyst] = 0.1 g L^{-1}; [PMS/2,4-DCP molar ratio] = 3:1; [pH] = 7.0	2,4-DCP removal ~80% and Co leaching was ~33 μg L^{-1} (120 min)	(Yang et al., 2009)
$CoMn_2O_4$	Hydrothermal-calcination	[RhB] = 0.03 g L^{-1}; [catalyst] = 0.2 g L^{-1}; [PMS] = 0.2 g L^{-1}; [pH] = 6.29; [T] = 25°C	RhB removal ~100% and the leaching amounts for Co and Mn were < 0.1 mg L^{-1} (80min)	(Yao et al., 2015)
$CoFe_2O_4$	Sol-gel method	[DCF] = 33.77 μM; [catalyst] = 0.213 mM; [PMS] = 1 mM; [T] = 25 ± 1°C; [pH] = 7	DCF removal was ~100% (30min) and the leaching amounts of Co and Fe were < 30 and 10 μg L^{-1} (120 min)	(Deng et al., 2013a)
CoMg/SBA-15	Wetness impregnation	[RhB] = 5 mg L^{-1}; [catalyst] = 0.1 g L^{-1}; [PMS] = 50 mg L^{-1}; [T] = 25°C;	RhB removal was ~100% (5 min) and the Co leaching was 80 μg L^{-1}	(Hu et al., 2013)

$CoFe_2O_4$/TNTs (Titanate nanotubes)	Impregnation-calcination	[RhB] = 100 mg L^{-1}; [catalyst] = 0.2 g L^{-1}; [Oxone] = 4 g L^{-1}; [T] = 20°C	RhB Removal ~100% and TOC removal 39.3% (60 min); Co leaching ~ 0.39 mg L^{-1}	(Du et al., 2016)
10Co9.5Fe/SBA-15-700	Wetness impregnation	[RhB] = 5 mg L^{-1}; [catalyst] = 0.1 g L^{-1}; [PMS/RhB molar ratio] = 20:1; [T] = 25°C	RhB Removal ~98% and Co leaching ~ 0.03 mg L^{-1} (120 min)	(Hu et al., 2015)
Graphene based (G)-$CoFe_2O_4$	Precipitation-reduction	[DMP] = 0.05 mmol L^{-1}; [catalyst] = 0.5 g L^{-1}; [PMS] = 2 mmol L^{-1}	DMP removal > 99 % (20 min)	(Xu et al., 2015)
$CoFe_2O_4$-rGO	Deposition-reduction	[Phenol] = 20 mg L^{-1}; [catalyst] = 0.067 g L^{-1}; [PMS] = 2 g L^{-1}	Phenol removal >99% (40min)	(Yao et al., 2012)

Note: 2,4-DCP-2,4-dichlorophenol; AO7-Acid Orange 7; ZIF-zeolitic imidazole framework; GO-graphene oxide; AY-Acid Yellow; RhB-Rhodamine B; BPA-Bisphenol A; DBP-di-n-butyl phthalate; DMP-dimethyl phthalate; rGO-reduced graphene oxide; RM-red mud; FA-fly ash; MCS-magnetic carbon nanosphere; AC-activated carbon; CA-carbon aerogel; CX-carbon xerogel; MB-methylene blue; DCF-diclofenac.

Table 2.3. Summaries on SR-AOPs combined with membrane technologies.

Membrane	Synthesis	Experimental conditions	Major findings	Ref.
Fe(II)/PMS + Ceramic UF membrane	UF membrane-Commercial flat sheet; Filtration area = 13.8 cm^2 MWCO = 50 kDa; Support layer-TiO_2; Filtration layer-ZrO_2/TiO_2	Fe(II)/PMS pretreatment: [PMS] = 15 or 50 μM; [Fe(II)] = 15 or 50 μM; Mixing for 1 min at 200 r min^{-1}, followed by 20 min at 50 r min^{-1}. Membrane filtration experiments: Dead-end filtration mode; [Volume] = 120 mL; [TMP] = 50 kPa	Fe(II)/PMS pretreatment effectively mitigated membrane fouling caused by HA, SA and HA-SA-BSA mixture, and the performance improved with the increase of Fe(II) or PMS dose. The fouling mitigation was mainly attributed to the effective reduction of organic loadings by coagulation with *in-situ* formed Fe(III);Fe(II)/PMS oxidation showed high performance in reducing DOC and UV_{254}, fluorescence intensities of fluorescent components and UV-absorbing compounds than single coagulation; Fe(II)/PMS pretreatment was efficient in ATZ degradation due to the generation of sulfate and hydroxyl radicals.	(Cheng et al., 2017a)
Fe(II)/PMS + Ceramic UF	Commercial flat sheet; Filtration	Fe(II)/PMS pretreatment: Fe(II)/PMS = 1:1 molar ratio;	Fe(II)/PMS-UF system exhibited high performance for dissolved organic carbon removal; Fe(II)/PMS pretreatment	(Cheng et al.,

membrane	area = 13.8 cm^2; MWCO = 50 kDa; Pure water flux = 143.5 ± 5.5 LMHB	Membrane filtration experiments: Dead-end filtration mode; [Volume] = 120 mL; [TMP] = 100 kPa	significantly increased the removal efficiency of ATZ, p-CNB and SMZ by 12-76% and 50-94%, respectively, whereas coagulation exerted a minor influence; Fe(II)/PMS pretreatment showed high performance for the reduction of both reversible and irreversible membrane fouling.	2017b)
Fe(II) PMS + Ceramic UF membrane	Commercial flat sheet(ZrO_2/TiO_2); Filtration area = 13.8 cm^2; MWCO = 150 kDa; Pure water flux 285.2 ± 4.5 LMHB;	Fe(II)/PMS pretreatment: [PMS] = 0.1 or 0.2 mM [Fe(II)] = 0.05 or 0.1 mM; Mixing for 30 or 60 min Membrane filtration experiments: Dead-end filtration mode; [Volume] = 125 mL; [TMP] = 100 kPa	Fe(II)/PMS pretreatment was very effective for decomposing high molecular biopolymers (>20,000 Da) into low molecular humic substances (1000–20,000 Da); Fe(II)/PMS pretreatment reduced reversible and irreversible fouling by oxidation and coagulation; Fe(II)/PMS pretreatment was also very effective to improve the removal of micro pollutants.	(Cheng et al., 2018)
NSC (N,S co-doped carbon)-Fe@PVDF	NSC-Fe: pyrolysis NSC-Fe@PVDF	Batch experiment: [Orange II] = 20 mg L^{-1}; [T] = 25 °C; [PMS] = 0.60 g L^{-1},	The NSC-Fe@PVDF membrane effectively decolorized orange II at a wide pH range (2.05-10.85); Membrane's porous structure and high internal surface area minimize the	(Yao et al., 2017)

membrane	membrane: Phase inversion	without pH adjustment.	nanoparticles agglomeration and allow the facile transport of catalytic reactants to the active surface of metal catalysts.	
α-Fe_2O_3 nanodisk/bacterial cellulose (BC) hybrid membranes	α-Fe_2O_3/BC nanocomposite: hydrothermal method; α-Fe_2O_3/BC membrane-vacuumed filtration	[Membrane] = ~7.5 mg; [Area] = 3.8 × 1.6 cm^2; [RhB] = 20 mg L^{-1}; [PMS] = 0.8 g L^{-1}; [Flow rate] = 3, 6 or 9 mL h^{-1} Light irradiation (Xe lamp)	The BC not only benefits stable membrane formation to avoid the separation and recycling problems but also helps disperse and accommodate α-Fe_2O_3 nanodisks, while the well-dispersed and tightly anchored α-Fe_2O_3 nanodisks benefit the enhancement of visible light-absorption efficiency, endowing the hybrid membrane with excellent PMS-based visible light degradation performances toward dyes.	(Zhu et al., 2018)
Co-Al_2O_3 nanofibrous membrane	Electrospinning	[Membrane] = 10 mg; [BPA] = 20 mg L^{-1}, buffered with 3 mM bicarbonate; [Volume] = 10 mL; [Oxone] = 0.5-4.0 mM; Semi-batch	The divalent cobalt ions distribute uniformly in the fibers by forming Al–O–Co bonds. 100% BPA could be removed within 40 min using the 11% Co-Al_2O_3-600 °C membrane with PMS addition. sulfate radicals and hydroxyl radicals were generated in the process and sulfate radical was the dominant active species.	(Wang et al., 2018)

Co_3O_4 functionalized ceramic membrane (CoFCM)	Al_2O_3 disc (D = 22 mm, thickness = 2 mm); Surface nucleated growth	Dead end-recycling filtration, [SMX] = 10 mg L^{-1}; [Oxone] = 0.10 g L^{-1}; [Flow rate] = 1 mL min^{-1}; [TMP] = 0.07 bar	Pure Co_3O_4 spinel phase formed a honeycomb structure on membrane surface via the ZIF-induced surface nucleated growth method; SMX removal efficiency was remarkably enhanced in CoFCM/PMS system; Mechanically robust CoFCM showed a self-cleaning potential.	(Bao et al., 2018b) This work
Co_3O_4 impregnated ceramic membrane (CoCM)	Al_2O_3 disc (D = 22 mm, thickness = 2 mm); Self-scarified template method	Dead end filtration mode; [SMX] = 0.04 mM; [PMS] = 0.4 mM; [HA] = 10 mg L^{-1}; [Flow rate] = 1 mL min^{-1}	The nanocatalytic Co_3O_4 was distributed uniformly throughout the whole membrane; The CoCM could be used to remove organics in water with antifouling property; The Co-O-Al bonding decreased the cobalt leaching in the filtration; The organics removal included a chemical degradation and physical separation.	This work
$CoFe_2O_4$ impregnated ceramic membrane $CoFe_2O_4/Al_2O_3$	Commercial Al_2O_3 disc (D = 22 mm, thickness = 2 mm);	Dead end filtration mode; [SMX] = 10 mg L^{-1}; [Oxone] = 0-0.10 g L^{-1}; [Flow rate] = 0.2-2 mL min^{-1}	The pure water permeability flux can maintain at ~3000 LMHB with the catalyst loading amount of 0.015 g/g Al_2O_3. The removal rate of SMX can achieve to ~98%, 70% and 40% with the residence time of 90, 36 and 18 s. The catalytic membrane shows a great tolerance at wide pH range (3–11),	(Bao et al., 2018a) This work

	Urea assisted solution combustion		the existence of HA and anions. Meanwhile, the membrane showed self-cleaning property by retaining > 90% of initial flux after 3 treatment cycles.	
α-MnO_2@CuO membrane	Vacuum drying followed by nanoseed mediated growth	Effective membrane area 9.07 cm^2 Constant flow rate [PMS] = 1 mM; [MB] = 0.1 mM	More than 99% of MB was degraded within 0.23 s using dead-end filtration cell. Moreover, the mechanism study indicated that hydroxyl radical and sulfate radical from the interaction between PMS and Mn/Cu species with different oxidation states mainly accounted for the dyes degradation.	(Luo et al., 2018)
Ag-LCF ($La_{0.8}Ca_{0.2}Fe_{0.94}O_{3-\delta}$) hollow fiber	Phase inversion-sintering	Recycling mode; Lumen side [MB] = 10 mg L^{-1}; [PMS] = 0.6 mM; [Volume] = 20 mL; [Membrane length] = 30 cm; [Flow rate] = 26 mL min^{-1};	The MB removal efficiency was up to 90% in 75 min; Sulfate and hydroxyl radicals play important roles on MB decolouration; Backwashing by acid solution was used to accomplish 94% membrane catalytic efficiency regeneration.	(Ma et al., 2019)
CuO-ceramic hollow fiber	Phase inversion-liquid phase sintering	Cross flow - recycling filtration, [RhB] = 20 mg L^{-1}; [Volume] = 500 mL; [CuO content] = ~0.1 g;	RhB removal was 81.5% in 60 min and the RhB degradation efficiency was decreased by less than 6% after five cycles of repeated use; Sulfate radical and hydroxyl radicals were	(Wang et al., 2019)

	[Flux] = 500 LMH; [PMS] = 2 mM; [pH] = 7	generated in this system; The membrane showed high performance for other organic compounds removal (BPA, SMX, phenol and chlorophenol)

Note: HA-humic acid; SA-sodium alginate; BSA-bovine serum albumin; ATZ-atrazine; pCNB - *p*-chloronitrobenzene; SMZ-sulfamethazine; MB-methylene blue; RhB-Rhodamine B; BPA-bisphenol A; SMX-sulfamethoxazole; EOM-extracellular organic matter; MWCO-molecular weight cut off; LMHB-Lm^{-2} h^{-1} bar^{-1}; TMP-trans-membrane pressure.

CHAPTER 3 PREPARATION OF SURFACE FUNCTIONALIZED CERAMIC MEMBRANE WITH COBALT OXIDES (CoFCM)

3.1 Introduction

As discussed in Chapter 2, lots of work have been done to prepare high performance Co-based nanomaterials for PMS activation (Lin et al., 2015b, 2015a; Lin and Chen, 2016; C. Wang et al., 2017). However, nanoparticles tend to aggregate, leading to loss of catalytic activity (Liu et al., 2015). Furthermore, surfaces of the nanocatalysts could be covered by deposited solute species including pollutants and their degradation products, leading to deactivation of active sites on their surface (Dong et al., 2015). To address these limitations, one possible way is to load nanocatalysts onto membrane surface to increase the surface area as well as decrease the aggregation.

To prepare a catalyst functionalized membrane, dip-coating and hydrothermal methods have been investigated (Li et al., 2014; Yu Wang et al., 2017). However, these methods need multiple steps and the morphologies are very difficult to control. Herein, we present a facile and scalable method to synthesize a magnetic hollow cobalt oxide functionalized ceramic membrane (CoFCM) for sulfamethoxazole (SMX) degradation. SMX is one kind of widely used antibiotics and has been detected in various systems (Godfrey et al., 2007; Lindberg et al., 2004; Nikolaou et al., 2007; Segura et al., 2009). Meanwhile, it is hard to be removed by the traditional methods because of its resistance to natural biodegradation (Alexy et al., 2004; Ryan et al., 2011). To address this problem, one potential strategy is the advanced oxidation processes owing to their non-selectivity to a wide variety of organic pollutants via generation of strong reactive species.

In this chapter, a Co-based zeolitic imidazolate framework, ZIF-67, was formed on the ceramic membrane surface via surface-nucleated growth. The hollow CoFCM structure could

be achieved easily through direct calcination of ZIF-67 by taking advantages of its thermal behavior and chemical reactivity (Li and Xu, 2013; Lin et al., 2015a). To our knowledge, this is the first report on synthesis of CoFCM via ZIF-67 template method and use it for PMS activation. The performance of the resulting CoFCM was examined in a home-made dead-end membrane filtration system. Also, the plausible PMS activation mechanism in CoFCM/Oxone system was evaluated via the radical trapping and electron paramagnetic resonance (EPR) experiments.

3.2 Experimental Section

3.2.1 Chemicals and materials

All chemicals were of reagent grade or higher and were used without further purification. Sulfamethoxazole (SMX), Sodium hydroxide (NaOH), methanol (CH_4O), *tert*-butanol ($C_4H_{10}O$), powder Al_2O_3 (100 mesh, 99%), cobalt(II) nitrate hexahydrate ($Co(NO_3)_2{\cdot}6H_2O$) and 2-methylimidazole (2-MIM) were purchased from Sigma-Aldrich, Singapore. Oxone (PMS, $2KHSO_5{\cdot}KHSO_4{\cdot}K_2SO_4$) was supplied by Alfa Aesar, Singapore. 5,5-dimethyl-1-pyrrolidine N-oxide (DMPO) was provided by Aladdin, China.

The commercial porous Al_2O_3 ceramic membrane was purchased from Nanjing Shuyihui Scientific Instruments CO., LTD (Nanjing, China). The as received membranes were disc shaped with a diameter of 22 mm and a thickness of 2 mm. Prior to use, the ceramic membranes were immersed into NaOH (0.5 M) and DI water for 30 min each followed by washing and drying at 120°C overnight.

3.2.2 Preparation of Co_3O_4 functionalized ceramic membrane (CoFCM)

Before the CoFCM preparation, the synthesis of zeolitic imidazolate framework (ZIF-67) was optimized via changing the precursor concentrations (33 mM to 330 mM based on Co concentration). To prepare CoFCM, the ceramic membranes were firstly washed with 1 M

NaOH to remove the impurities followed by washing with DI water to neutral pH and drying at 100 °C for 24 h for later use. Surface-nucleated heterogeneous growth method was used for the synthesis of porous hybrid CoFCM and the schematic illustration is shown in **Fig 3.1**. First, the ceramic disc was immersed in the 2-MIM (2-methylimidazole) solution (Solution A, 0.66 g of 2-MIM in 15 mL methanol) for 30 min, after washing several times with methanol to remove the redundant solution, the disc was placed into the metal precursor solution (Solution B, 0.291 g of $Co(NO_3)_2 \bullet 6H_2O$ in 15 mL methanol) for another 30 min. After washing with methanol, the disc was positioned into the mixture of two solutions (Solution A and Solution B) which was settled at room temperature in the quiescent solution. After aging for 24 h, the purple disc was washed with methanol to remove the reductant solution followed by washing with DI water and dried overnight at 105°C. The remaining purple ZIF-67 powders were collected from the mother solution and washed with methanol and DI water several times with the assistance of centrifuge for later test. To confirm the formation of covalent bonds between ceramic disc and ZIF-67, a control experiment in which the disc was replaced by Al_2O_3 powder was conducted in the same condition. In the surface-nucleated heterogeneous growth process, Al could be linked with 2-MIM via Al-N bond followed by the formation of ZIF-67 on the membrane surface, which would minimize the infiltration of ZIF-67 particles into the internal pores. The infiltration of ZIF-67 particles into the internal pores will result in undesirable pore plugging and decreased water permeability.

The CoFCM was then prepared through a one-step calcination of ZIF-67 functionalized membrane in a furnace with the temperature raising from room temperature to the desired temperature at a ramping rate of 5°C min^{-1}, and then stabilized for 3 h. The resulted CoFCM was denoted as M-temp while the pristine membrane without Co_3O_4 was referred as M0. In addition, Co_3O_4 powder was also prepared under the same condition using ZIF-67 as the precursor and was denoted as ZIF-67@temp in the following sections. After the calcination

process, all membranes were washed with DI water followed by drying in an oven at 60°C overnight for later use.

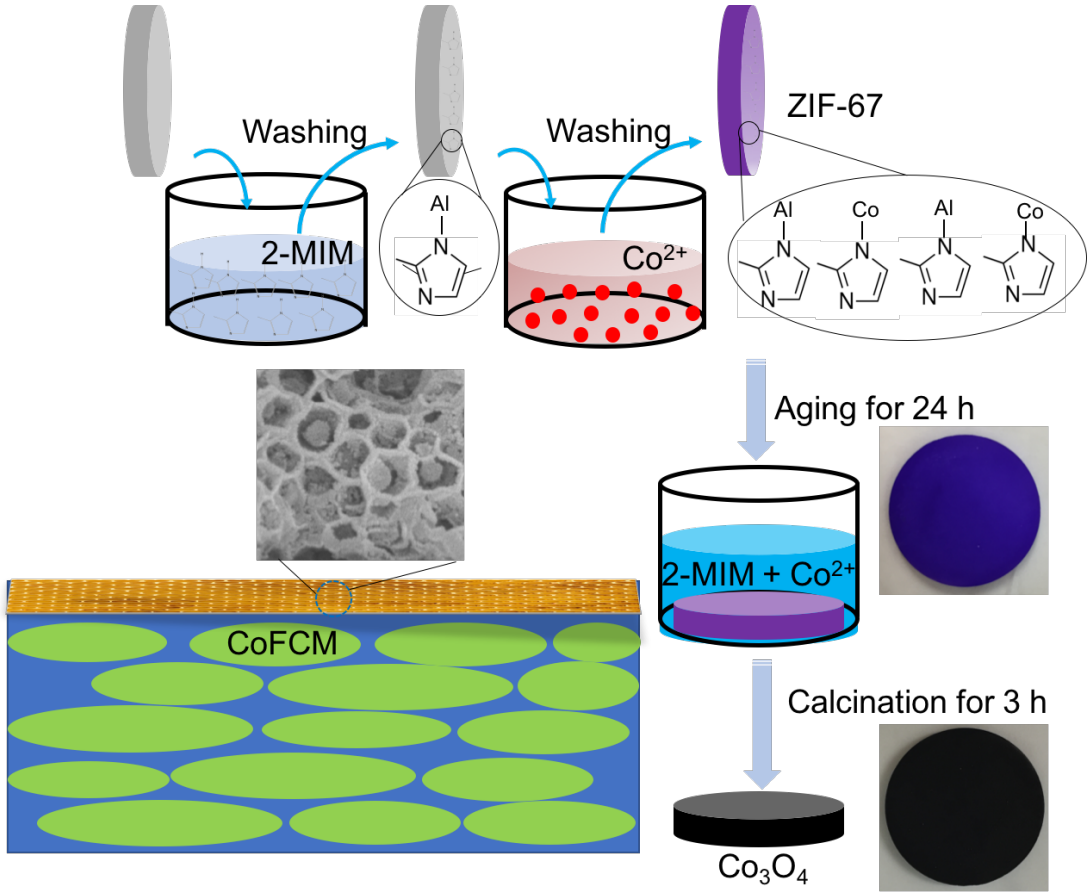

Fig 3.1. Schematic illustration of the fabrication of CoFCM via a surface-nucleated ZIF-67 growth method (Solution A, 0.66 g of 2-MIM in 15 mL methanol; Solution B, 0.291 g of $Co(NO_3)_2 \cdot 6H_2O$ in 15 mL methanol).

3.2.3 Characterization techniques

The thermo-transformation of ZIF-67 was investigated by thermogravimetric analysis (TGA) (SDT-Q600, TA instrument, USA) in the temperature range of 100-900°C under air atmosphere (heating rate of 10°C min^{-1} and air flow of 100 mL min^{-1}). Nitrogen adsorption-desorption analyses were conducted on a Quantachrome Autosorb-1 Analyzer at liquid N_2 temperature of 77 K. The resulting specific surface areas as well as porosities were calculated from N_2 adsorption data by the multipoint Brunauer-Emmett-Teller (BET) and DFT methods.

The surface morphologies as well as elements distribution were acquired by a field emission scanning electron microscope (FESEM, JSM-7600F, JEOL). Meanwhile, atomic force microscopy (AFM, Cypher S, Asylum Research) was employed to characterize the membrane surface roughness. X-rays diffractometer (XRD, Bruker D8 Advance) was used to analyze the crystal structures of the material. The 2θ range was scanned from 5-75° at a step size of 0.02 and the crystallite sizes of as-synthesized particles were calculated using Scherrer's equation:

$$D = \mathrm{R}\,\lambda / \beta \cos\theta \qquad (\mathbf{3.1})$$

where D is the estimated diameter of the particles (nm), R is 0.89 (Scherrer's constant), λ means the incident wavelength, which is 0.154 nm in this study, β (rad) is the peak width at half height and θ (°) is the diffraction angle.

The vibrational absorbance of as-synthesized particles was investigated by Fourier transformed infra-red spectrometer (FTIR, Perkin Elmer) and Raman spectrometer (HORIBA Scientific). Meanwhile, X-ray photoelectron spectroscopy (XPS) analysis (Kratos Axis Supra, Shimadzu) was conducted on to detect the elements' chemical states in ZIF-67 and Co_3O_4.

Electron paramagnetic resonance (EPR) experiments were employed on a Biospin ELEXSYS II E500 EPR spectrometer (Bruker) using DMPO as spin trapping agent to probe the free reactive oxygen species (ROS) and the information was analyzed by Xeon software (Bruker). Furthermore, chemical quenching experiments were conducted by adding methanol and *tert*-butanol as the scavengers due to their different reaction rates to hydroxyl radical and sulfate radical.

3.2.4 SMX degradation experiments with CoFCM

SMX degradation with CoFCM was evaluated in a dead-end filtration mode, which was operated under a constant flux **(Fig A3.1**). The initial pH of feed solution (50 mL) is 5 with a SMX concentration of 10 mg L^{-1}. A high-pressure metering pump (5979 Optos Pump 2HM,

Eldex) was used to feed the solution into the membrane cell module (SS316 stainless steel), in which the membrane was secured tightly. The constant flow mode (flow rate was set at 1 mL min^{-1}) was used and trans-membrane pressure (TMP) was recorded as 0.07 bar in a dead-end system and the permeate was then re-circulated back to the feed tank. A control experiment with the pristine Al_2O_3 membrane (M0) was also performed to quantify the performance of membrane. The membranes (M0 and CoFCMs) were compacted to a steady state for 5 min before filtration experiment.

3.2.5 Analytical methods

The SMX concentration was quantified using LC-2030C-3D liquid chromatography system (Shimadzu) with a reversed phase column (Inertsil ODS-3, 5 μm, 4.6 × 150 mm). The detection wavelength was set at 264 nm and the mobile phases are 60% methanol and 40% water (0.1% acetic acid). The flow rate was 0.8 mL min^{-1} and the injection volume was 10 μL. The intermediates were analyzed using an Agilent 1290 Infinity HPLC coupled to an Agilent 6460 Triple quadruple mass spectrometry, which was equipped with an Electrospray ionization (ESI) source using Agilent Jet Stream Technology (Agilent, USA). The mobile phases consisted of water with 0.1% formic acid (A) and acetonitrile with 0.1% formic acid (B). Separations were performed using a 75 mm × 2 mm Luna 3μ C18 column with a flow rate of 0.2 mL min^{-1}. A gradient elution method with two mobile phases was employed as follows: 90% A for 0-0.5 min; 90% A decreased to 10% A lineally for 0.5-5.5 min and kept for 5.5-8.0 min; 10% A increased to 90% A lineally for 8.0-9.5 min and kept for 9.5-10.0 min.

For Oxone quantification, 1 mL of the samples was initially mixed with 0.02 g of KI for the oxidation of I^- by HSO_5^- (**Eqs.3.2-3.3**)

$$2I^- + HSO_5^- + 2H^+ \rightarrow HSO_4^- + I_2 + H_2O \quad (\mathbf{3.2})$$

$$I_2 + I^- \rightarrow I_3^- \quad (\mathbf{3.3})$$

The concentration of I_3^- was then determined by a UV-1800 spectrophotometer (Shimadzu,

Japan) at λ_{max} = 352 nm (**Fig A3.2**). Inductively coupled plasma optical emission spectrometry (ICP-OES, Optima 8000, Perkin Elmer) was conducted to measure the mass of cobalt leached from membranes.

3.3 Results and discussion

3.3.1 Study of the ZIF-67-template method

In this study, the effect of different precursor concentrations on ZIF-67 synthesis was investigated and the results are shown in **Fig 3.2.** The optimum mole ratio of Co^{2+} to 2-MIM, which is 1:8, is important for the successful synthesis of ZIF-67 (Shao et al., 2014). The concentrations of precursors would affect both morphology and yield of ZIF-67. With increasing precursor concentration, the well-defined ZIF-67 particle size increased with a higher yield and subsequently became more irregular due to the presence of excessive precursors in solution. In this work, the $Co(NO_3)_2{\cdot}6H_2O$ concentration of 33 mM was chosen because it shows the most uniform particle distribution (**Fig 3.2 b**).

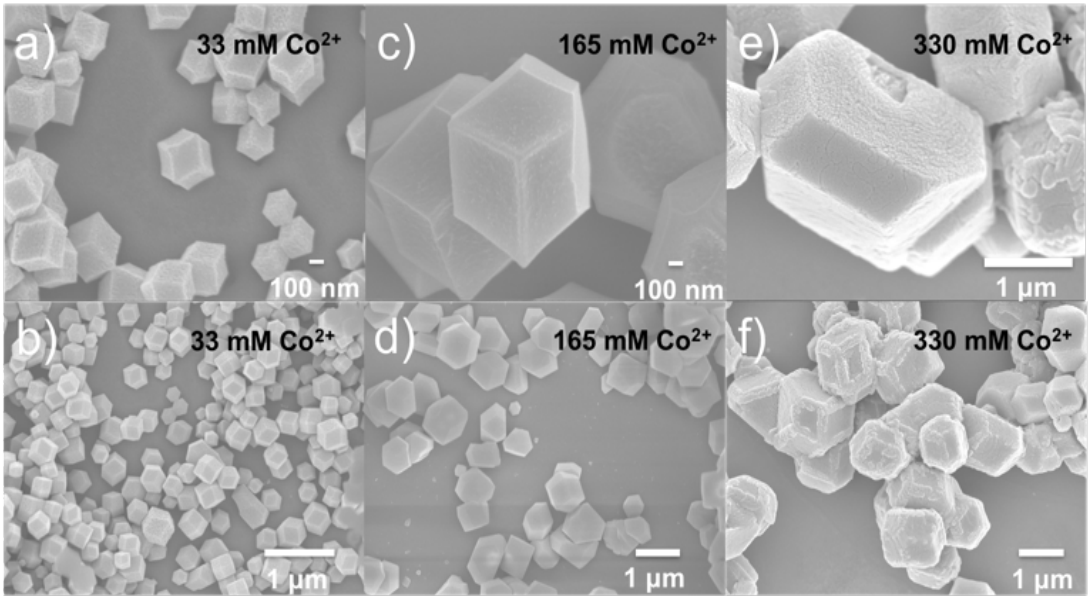

Fig 3.2. SEM images of ZIF-67 prepared with different $Co(NO_3)_2{\cdot}6H_2O$ concentrations (mole ratio of $Co(NO_3)_2{\cdot}6H_2O$ / 2-MIM was fixed at 1/8).

To examine the calcination temperature effect on the formation of Co_3O_4, different temperatures (350, 450 and 550°C) were used in the calcination process. The sizes and morphologies of as-synthesized ZIF-67 and Co_3O_4 calcined at different temperatures were observed by FESEM (**Fig 3.3**). The results show that all particles perform good uniformity in this study (**Figs 3.3 a-c**). However, when the temperature increased to 550°C, the ZIF-67 crystals aggregated and the structural backbone of the metal-organic framework disappeared (**Fig 3.3 d**). A magnified FESEM image in **Fig 3.3 a** depicts the very smooth surface over the whole particle, indicating the single-crystal-like feature of the ZIF-67. It displays a uniform rhombic dodecahedra structure due to the combination of Co ions and 2-methylimidazole through coordination bonds and shows a uniform particle size of approximately 200 nm with sodalite topology. After calcination at 350°C for 3 h, the pristine polyhedral morphology is retained well, but the size of polyhedral crystals shrinks slightly (**Fig 3.3 b**). When the calcination temperature increased to 450°C, part of the pristine polyhedral morphology is still retained and the size of polyhedral shrinks a bit more (**Fig 3.3 c**). Meanwhile, the surface of ZIF-67@450 becomes rougher after calcination, indicating the formation of inter-particle pores during the calcination process, leading to the increase in average pore radius (**Table 3.1**) (Wu et al., 2014). Once ZIF-67 was calcined to form Co_3O_4, its original sodalite structure deformed through concaving and shrinking due to the heat treatment. However, some edges of ZIF-67, even though skewed, can still be discerned. The morphology changes during calcination should be caused by the different rates of crystallization and specific plane growth under different calcination temperatures (**Fig A3.3 a**). The particle sizes observed in FESEM were slightly larger than that of those estimated from Scherrer's equation (**Table 3.1**).

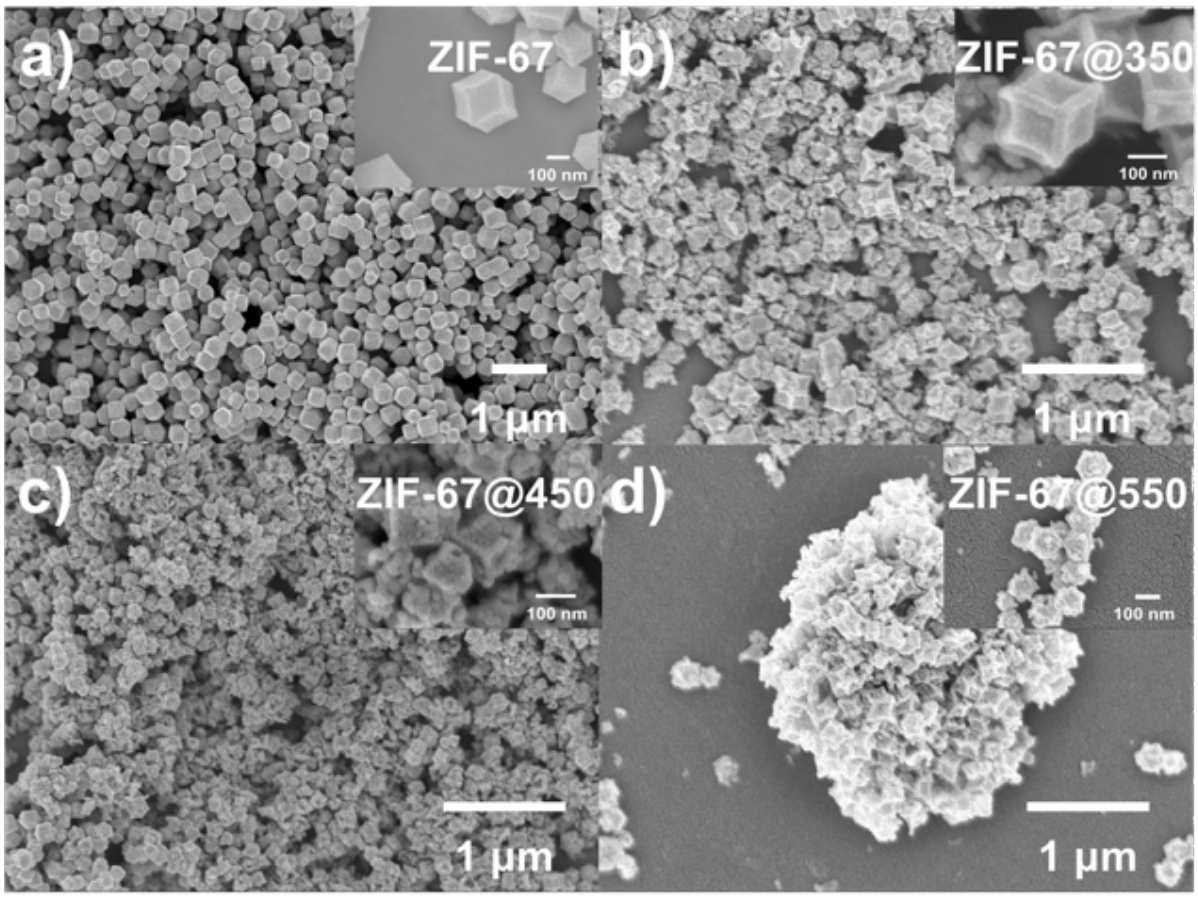

Fig 3.3. FESEM images of ZIF-67 (a) and Co_3O_4 calcined at different temperatures (b-350, c-450 and d-550).

Fig 3.4 shows ZIF-67 exhibits a gradual weight loss step of 4.5% up to 350°C, corresponding to the removal of guest molecule from the cavities and some unreacted reagents. A drastic weight loss of 65.7% is located in the temperature range of 350-400°C, indicating the decomposition of organic ligands in ZIF-67. Meanwhile, the sample calcined at 350°C still contains some carbon (**Fig A3.3 b**), showing the incomplete transformation. The presence of carbon in the sample is undesirable as it can compete with the pollutant for reaction with ROS during catalytic oxidation process. As the temperature further increased, a long plateau was obtained at the temperature range of 400-900°C with a residual weight of 34.3%, due to the formation of Co_3O_4. The results are consistent with the calculated weight loss from $Co(C_4H_5N_2)_2$ (molecular weight of 220) to $CoO_{4/3}$ (molecular weight of 80). To ensure

complete transformation form ZIF-67 to Co_3O_4 as well as to conserve the pristine polyhedral morphology, 450°C was chosen as the calcination temperature for the following studies and the Co_3O_4 prepared at this condition was denoted as ZIF-67@450.

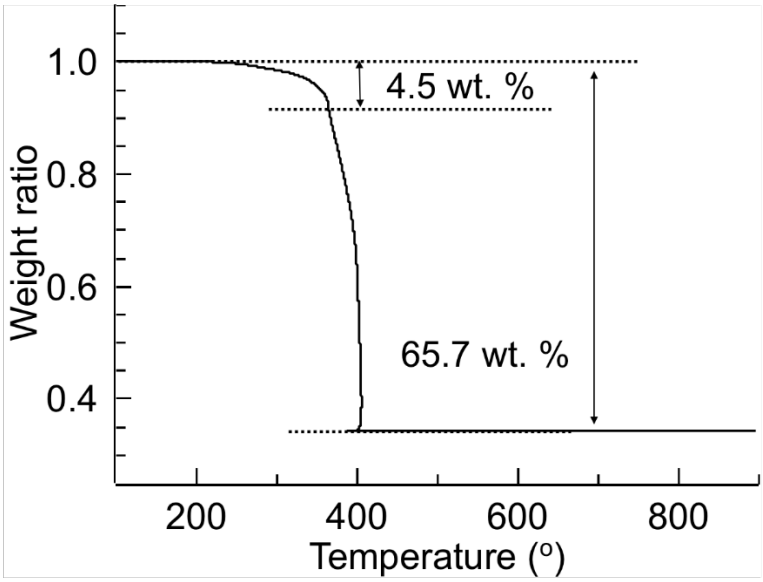

Fig 3.4. TGA curve of ZIF-67 showing weight change at heating under air atmosphere.

3.3.2 Characterization of ZIF-67 and ZIF-67@450.

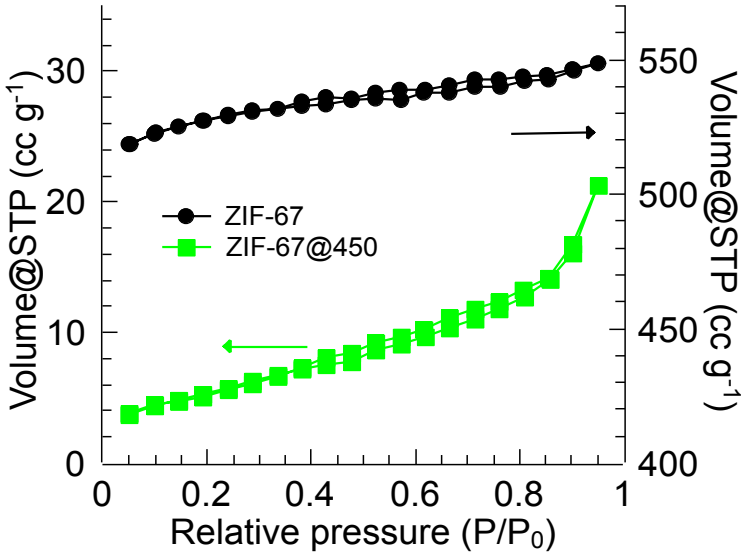

Fig 3.5. N_2 adsorption-desorption isotherms of ZIF-67 and ZIF-67@450.

To explore the textural property of ZIF-67@450, N_2 adsorption-desorption isotherms of

the ZIF-67 crystal and ZIF-67@450 particles were recorded at 77 K (**Fig 3.5**). The specific surface areas and total pore volumes were calculated and summarized in **Table 3.1**. The original ZIF-67 crystals showed typical microporous characters with a high surface area and large total pore volume. After calcination at 450°C for 3 h, notable reduction of the BET specific surface areas from 1463.0 to 20.4 m^2 g^{-1} and total pore volumes from 0.64 to 0.02 cm^3 g^{-1} were observed in the ZIF-67@450 because of the folding of ZIF-67 structure (**Table 3.1**).

Table 3.1. The physical properties of ZIF-67 and ZIF-67@450.

Parameters	ZIF-67	ZIF-67@450
BET specific surface area [a] (m^2 g^{-1})	1463.0	20.4
DFT cumulative surface area [b] (m^2 g^{-1})	2131.0	13.6
Pore volume [b] (cc g^{-1})	0.64	0.02
Pore radius [b] (nm)	0.92	1.39
DFT cumulative porosity [c] (%)	60.0	12.1
XRD crystallite size [d] (nm)	55.8	52.8

Note: [a] Calculated from multi-point BET method; [b] Calculated from DFT method; [c] Determined by assuming uniform densities of ZIF-67 and Co_3O_4 as 0.89 and 6.057 g cm^{-3} and [d] Calculated using Scherrer's equation.

Fig 3.6 a presents the X-ray diffraction (XRD) pattern of ZIF-67 and ZIF-67@450. All the diffraction peaks of ZIF-67 agree well with the simulated patterns (Torad et al., 2014). The XRD pattern of the product after the one-step calcination of ZIF-67 confirms that a pure Co_3O_4 spinel phase with a face-centered cubic lattice (04-016-4508) is obtained. The peaks at 19.0, 31.3, 36.9, 44.8, 59.4 and 65.2 can be indexed to the (111), (220), (311), (400), (511) and (440) planes of Co_3O_4 (04-016-4508) (**Fig A3.4**). The XRD patterns shown in **Fig 3.6 a** indicate that ZIF-67 had been completely converted to Co_3O_4 with the disappearance of original pattern of ZIF-67. While the broad diffraction peaks could be caused by the nano-sized effects of Co_3O_4.

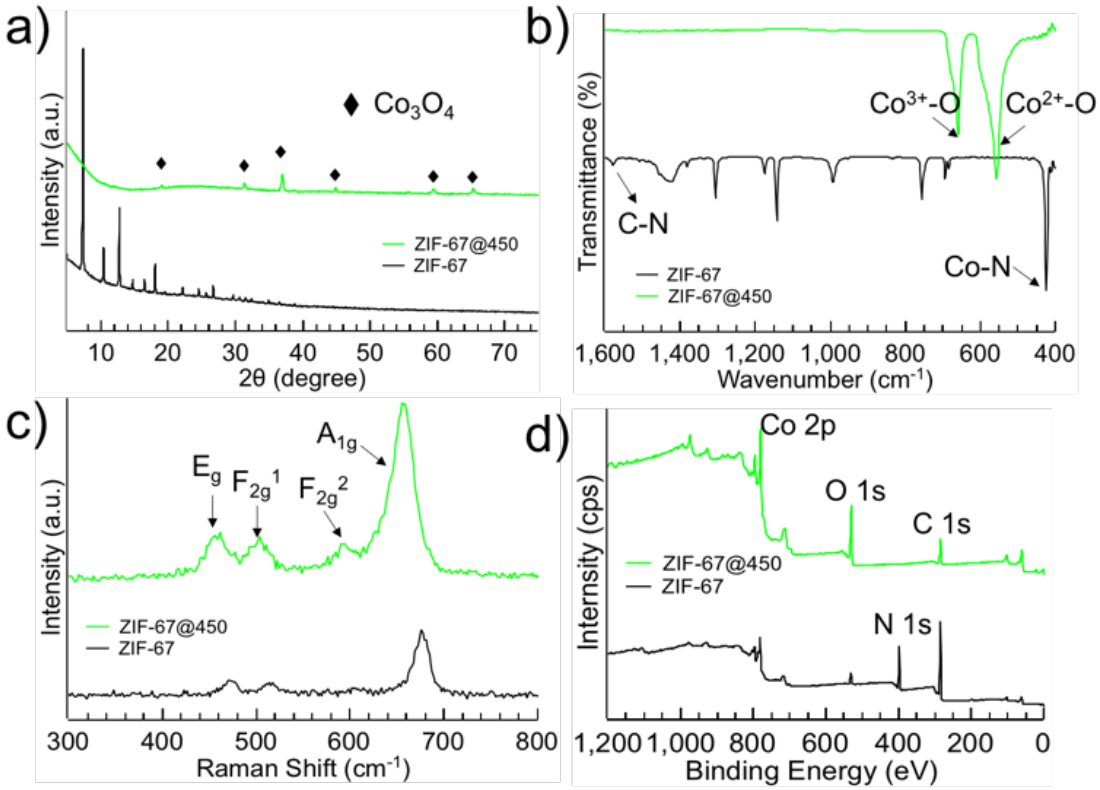

Fig 3.6. The chemical characterization of ZIF-67 and ZIF-67@450 (a-XRD, b-FTIR, c-Raman spectra and d-XPS).

The existence of Co_3O_4 was also verified by spectroscopic analyses. As reported previously, the Co_3O_4 with Co^{2+} ($3d^7$) and Co^{3+} ($3d^6$) located at tetrahedral and octahedral sites respectively (L. Zhang et al., 2013). The active modes for spinal crystallizes can be predicted via the space group theory:

$$\Gamma=A_{1g}(R)+E_g(R)+F_{1g}(IN)+3F_{2g}(R)+2A_{2u}(IN)+2E_u(IN)+4F_{1u}(IR)+2F_{2u}(IN) \quad (\mathbf{3.4})$$

where (R) is Raman active vibrations, (IR) means infrared-active vibrations and (IN) represents inactive modes.

Fig 3.6 c shows the Raman spectra of the ZIF-67 and ZIF-67@450. Four active Raman modes with the location at ~470, 510, 608 and 680 cm^{-1} could be distinguished, corresponding to E_g, F_{2g}^1, F_{2g}^2 and A_{1g} modes of Co_3O_4. All peaks are in agreement with the values of pure Co_3O_4 spinel structure yet with an average shift of $\Delta V < 5$ cm^{-1}, which could be caused by the

size effects and surface stress/strain. After calcination, the peak positions shift to low wavenumbers which is attributed to the optical phonon confinement effect in nanostructures that can cause uncertainty in the phonon wave vectors and then a downshift of Raman peaks (Ai and Jiang, 2009).

In addition, the FTIR spectrum (**Fig 3.6 b**) shows two main relatively sharp absorptions centered at ~580 and 660 cm^{-1} in ZIF-67@450, which originate from the fingerprint stretching vibrations of the Co-O bond of the Co_3O_4 spinel oxides. More precisely, the observed 580 cm^{-1} band is characteristic of Co-O with Co denoting the Co^{3+} in the octahedral site while the 660 cm^{-1} band is attributable to the Co^{2+} in the tetrahedral site vibration in the spinel lattice (Herrero et al., 2007). Meanwhile, the FTIR spectrum shows no residual organic compounds after calcination process. In the original ZIF-67 sample, the absorption bands at 425 and 1580 cm^{-1} are assigned to the stretching vibration of Co-N and C-N, respectively. The bands at 1380-1450 cm^{-1} are associated with the entire imidazole ring stretching and the bands in the region of 800-1350 cm^{-1} are for the in-plane bending of the ring while those below 800 cm^{-1} are related to the out-of-plane bending (Dou et al., 2017).

XPS investigations were carried out to characterize the elemental composition of the surface of the particles as well as the chemical environment of the cobalt and oxygen atoms. It is reasonably surmised that N atoms would disappear along with the calcination process with oxygen (**Fig 3.6 d**). In original ZIF-67, the N1s region spectra are deconvoluted into two components N1 (pyridinic-N, 398.2 eV) and N2 (Co-N, 399.1 eV) while the Co 2p core-level spectra are deconvoluted to display peaks of Co-Nx at 780.5 eV (**Fig A3.5**). In this structure, appropriately arranged N1 (pyridinic N) moieties with electron-donating properties are able to trap plentiful transitional metals to serve as outstanding metal-coordination (Co-N_X) active sites. Furthermore, free N1 atoms have excellent electronic storage ability to activate molecular oxygen under mild conditions (Liu and Zhang, 2013). After calcination, N1s peak disappears

due to 2-methylimidazole ligands ring opening and conversion of ZIF-67 to Co_3O_4 (**Figs 3.6 d and Fig A3.5**). The Co2p peaks show a slight broadening and shifting to lower binding energy, which could be deconvoluted to peaks related to the formed cobalt oxides (**Fig 3.7 a**).

In the Co2p core-level spectrum of ZIF-67@450, two major peaks with binding energies of 780 and 795 eV are observed, corresponding to Co $2p_{3/2}$ and Co $2p_{1/2}$ respectively (**Fig 3.7 a**). The 15 eV energy difference between the Co 2p peaks is indicative of spinel Co_3O_4 (Xu and Zeng, 2004). It is well known that both Co^{2+} and Co^{3+} exhibit similar binding energy peaks, however, the energy splitting (ΔE) between the two levels due to spin-orbit coupling should be different for the Co^{2+} and Co^{3+} configurations with ΔE = 15.0 eV for Co^{3+} and ΔE = 15.7 eV for Co^{2+} (Petitto et al., 2008). The XPS data (**Fig 3.7 a**) for the spinel Co_3O_4, which contains both Co^{2+} and Co^{3+} ions distributed on the A and the B sites as $[Co^{2+}]A[2Co^{3+}]BO_4$, clearly show the presence of doublet at D1 = 779.2 eV and D2 = 780.8 eV for the $Co2p_{3/2}$ level and a doublet for the $Co2p_{1/2}$ level centered at D3 = 794.1 eV and D4 = 796.5 eV. The separations between the doublet peaks are ΔE_{D3-D1} = 14.9 eV and ΔE_{D4-D2} = 15.7 eV, which are close to the above-mentioned values for Co^{3+} and Co^{2+}, respectively, thus confirming the presence of Co^{3+} and Co^{2+} in Co_3O_4. The peaks at 789.3 and 804.9 eV are considered shake-up satellite peaks, which further confirms the well-defined Co_3O_4 structure (Kang et al., 2003). Other small peaks at 783 and 795 eV may result from a chemical shift of the main spin-orbit components because of the chemical interaction between cobalt and hydroxide (Zhang et al., 2010).

Similar to that of Co 2p, the O 1s of ZIF-67@450 exhibits broadening and shifting to lower binding energy due to the formation of typical metal-oxygen bond (529.6 eV) (**Fig 3.7 b**). The peak at 531.4 eV could be assigned to hydroxyl group because of the possible water on or between the Co_3O_4 nanocrystals (Salunkhe et al., 2015) and a multiplicity of defect sites (Petitto et al., 2008). These results confirm that Co=N coordination bonds in ZIF-67 were broken and the Co species were oxidized to form Co_3O_4 by calcination in the air atmosphere.

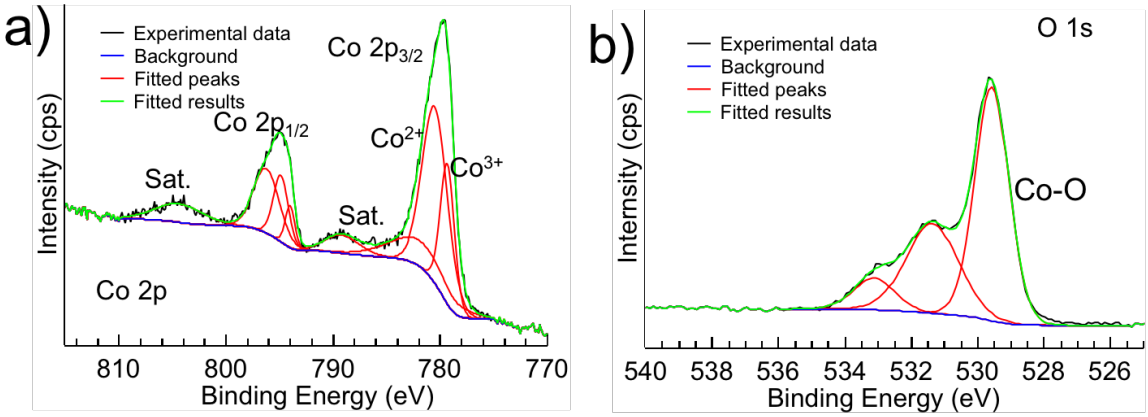

Fig 3.7. High resolution of Co2p (a) and O1s (b) XPS spectra of ZIF-67@450.

3.3.3 Characterization of CoFCMs

The effect of calcination temperature on the morphologies of CoFCMs is shown in **Fig A3.6**. Results indicate that M350 and M450 can form a porous network structure while M550 shows the aggregation of Co_3O_4, which is in accordance with the powder characterization (**Fig 3.3**). **Figs 3.8 a** and **b** show the morphologies of pristine ceramic membrane (M0) and CoFCM (M450), respectively. The membrane surface changes significantly and becomes rougher after ZIF-67-derived Co_3O_4 modification. It exhibits that Co_3O_4 particles are deposited on the surface of membrane, forming a porous network of connected polygons **(Fig 3.8 b).** The CoFCM increases the complexity of pore structure which would result in a great enhancement in pollutants retention ability. EDX microanalysis was performed on the surface of M450 (**Fig 3.8 c**). The element mapping images shows the Co_3O_4 has been deposited on Al_2O_3 (**Fig A3.7**). **Fig 3.8 d** shows a two-layer structure image of Co_3O_4 particle immobilized on the Al_2O_3 ceramic membrane. The top layer is the Co_3O_4 particle with an estimated thickness of 1.5-2 µm. AFM was used to characterize topography of M0 and M450. The two-dimensional amplitude retraces surface images (**Figs 3.8 e** and **f**) show that M450 (R_m = 86.9 nm) was slightly rougher compared with M0 (R_m = 79.5 nm), which could be caused by the formation of Co_3O_4 on membrane surface.

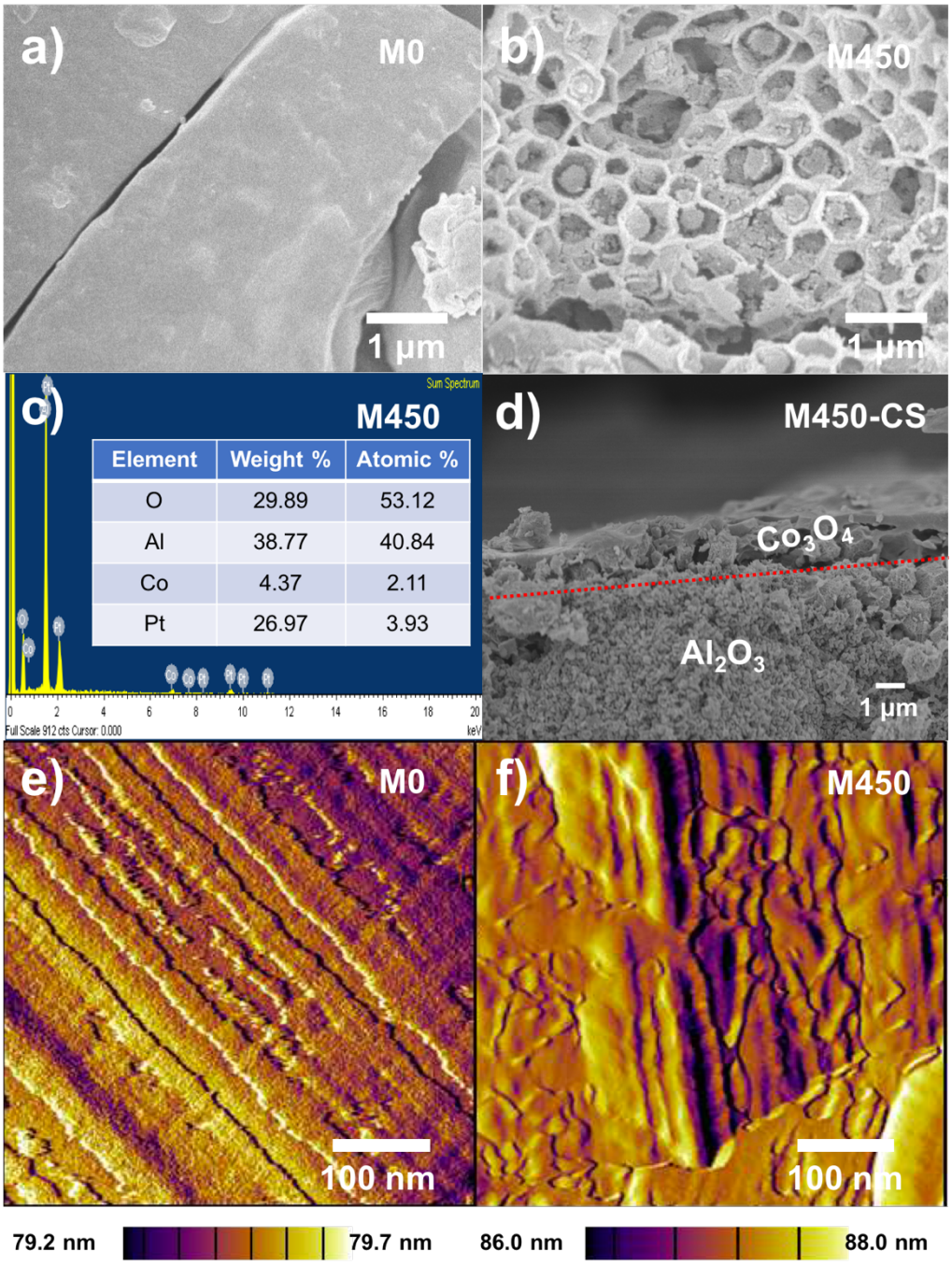

Fig 3.8. Physical properties of M0 (control) and M450 (a-FESEM of M0 surface, b-FESEM of M450 surface, c-EDX analysis of M450 surface, d-FESEM of M450 cross section, e-AFM of M0 surface, f-AFM of M450 surface).

To analyze the bonding mechanism of CoFCM, XPS tests were carried out by investigating the various elemental chemical oxidation states and the spectra are presented in **Fig 3.9**. According to the high resolution of Al 2p peak for Al_2O_3, (**Fig 3.9 a**), only Al-O

bonding for Al_2O_3 is present. However, in ZIF-67@450/Al_2O_3 (**Fig 3.9 b**), both Al-O for Al_2O_3 and Al-O-Co bonding are detected, showing the chemical interaction between powder Al_2O_3 and ZIF-67@450. On the other hand, the characteristic peak of O 1s in **Fig 3.9 d** was found to consists of both Al-O and Co-O. The N1s spectra in ZIF-67/Al_2O_3 shows the existence of Al-N bonding (**Fig A3.8**), which further confirmed the chemical interaction between Al_2O_3 and ZIF-67. The chemical bonding between catalyst and membrane surface can avoid catalyst aggregation as well as detachment effectively, improving the stability of CoFCM for catalytic oxidation reactions.

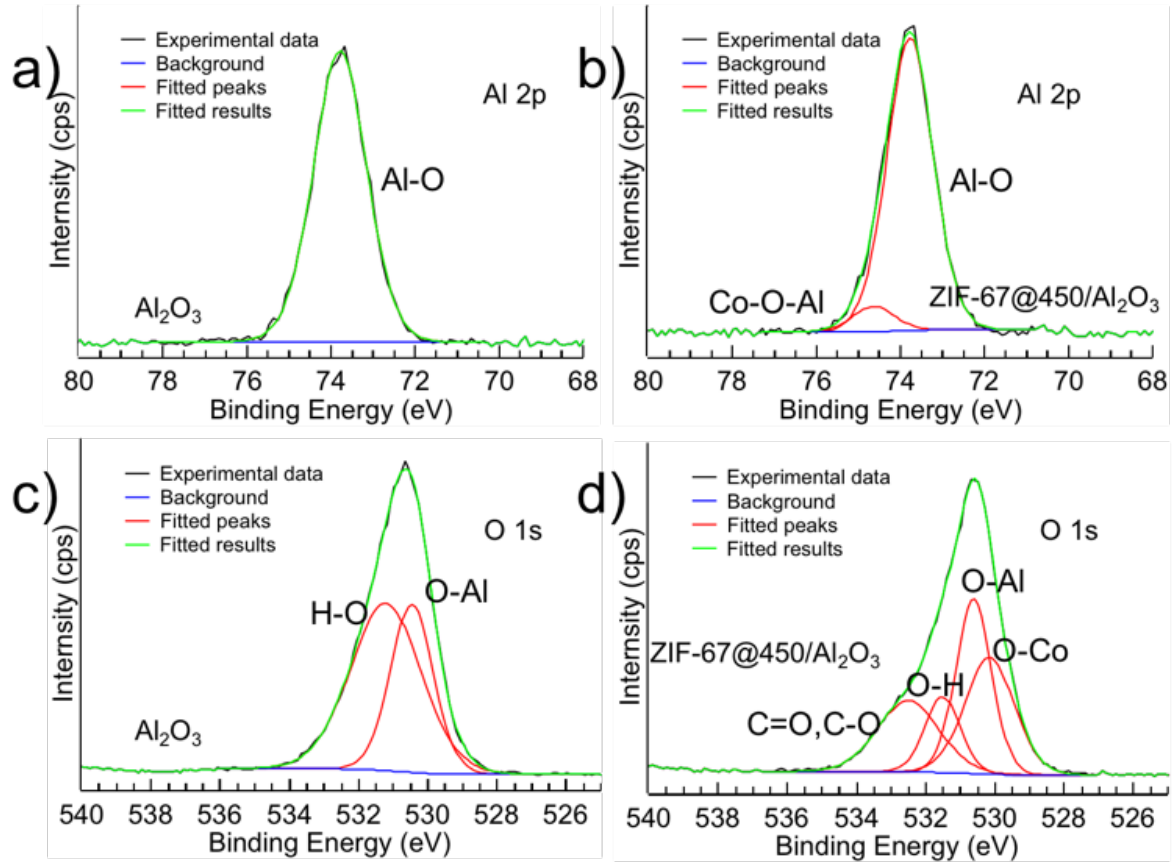

Fig 3.9. High resolution of Al 2p (a,b) and O1s (c,d) XPS spectra of Al_2O_3 and ZIF-67@450/Al_2O_3.

Table 3.2 shows the membrane properties of M0 and CoFCMs, the weight change could be ignored because of the low amount of Co_3O_4. The pure water permeability of M450 (3024 LMHB) was slightly lower (<10% difference) than that of M0 (3323 LMHB). This shows that

Co_3O_4 particle formed a very thin porous layer which only induced a minimal effect on the membrane filtration resistance (**Fig 3.8 d**). Meanwhile, M450 shows a more hydrophobic surface which might be caused by the honeycomb structure on the membrane surface (**Table 3.2**). For M550, due to the highly hydrophility of Co_3O_4, the contact angle of M550 decreased, resulting a higher pure water flux (**Table 3.2**). The effect of the Co_3O_4 on the pure water permeability can be evaluated by the intrinsic membrane resistance (Goei et al., 2013), R_m (m^{-1}), which are defined as:

$$R_m = (\Delta P)\, A\, t / \mu\, V \qquad (3.5)$$

where ΔP is the trans-membrane pressure (Pa), A is the effective surface area of the membrane (m^2), t is the filtration time (s), μ is the kinematic viscosity of water (1×10^{-3} Pa•s) and V is the volume of water flowing through the membrane. Before the modification, the R_m for M0 is calculated as 1.08×10^{11} m^{-1}, while the R_m for M450 is 1.19×10^{11} m^{-1}.

Table 3.2. Membrane properties of M0 and CoFCMs.

Parameters	M0	M350	M450	M550
Weight (g)	1.97±0.05	1.97±0.04	1.97±0.03	1.97±0.07
LMHB [a]	3323	3121	3024	3420
R_m (m^{-1})	1.08×10^{11}	1.14×10^{11}	1.19×10^{11}	1.11×10^{11}
V [b] (cm^3)	0.2874	0.2859	0.2835	0.2839
P [c] (%)	56.5	56.2	55.7	55.8
Contact Angle [d] (°)	68.5	70.5	80.8	67.8

Note: [a] Pure water permeability (L m^{-2} h^{-1} bar^{-1}); [b] Pore volume (cm^3); [c] Porosity (%); [d] Tested at 0.3 s

3.3.4 Catalytic performance of CoFCMs

Figs 3.10 a and **b** show the effect of Oxone dosage on removal of SMX over M0 and

M450 in the membrane filtration system. During the filtration and catalytic oxidation processes, SMX can be retained on the membrane surface, which consists of high density of Co_3O_4 particle. When Oxone is introduced into the system, the Co_3O_4 particle acts as active sites for Oxone activation, generating ROS for SMX degradation. Once degraded, the smaller SMX intermediates can be constantly removed from the reaction zone on the membrane surface. This promotes more efficient SMX degradation. For the pristine membrane (M0), due to inactivity of Al_2O_3, even when Oxone dosage was increased to 0.1 g L^{-1}, the SMX removal in 90 min is insignificant (less than 15%, **Fig 3.10 a**), which confirmed the negligible effect of Oxone oxidation in this process. However, with the M450 membrane, it shows significantly increased removal efficiency with increase of Oxone dosage (**Fig 3.10 b**) because of the presence of Co_3O_4 on the membrane, which works as the catalyst to activate Oxone for radicals' generation. The enhancement of SMX degradation with increasing Oxone dosage means the active sites on membrane surface were not totally occupied by Oxone. When Oxone dosage was set as 0.01 g L^{-1}, the removal efficiency reached a plateau after 40 min, indicating that Oxone is exhausted in this system. When the Oxone dosage was increased to 0.05 g L^{-1}, the SMX removal follows a first order removal kinetics (**Fig A3.9**) and Oxone is consumed at 90 min, since no redundant Oxone was detected in the solution (**Fig 3.10 c**). The increase of reaction rate could be caused by the higher density of catalytic sites as well as the higher reactant concentrations. If Oxone dosage was further increased to 0.1 g L^{-1}, there is no significant change in the rate constant, indicating that active sites on membrane surface became the rate limited factor when Oxone dosage is in excess (i.e. more than 0.05 g L^{-1}) and the flow rate is fixed (1 mL min^{-1}). Under a certain catalyst active sites for membranes, limited Oxone-surface contact was achieved. After reaction, the residual Oxone was detected and the maximum consumption rate was calculated as 0.56 mg L^{-1} min^{-1} in this system. Other CoFCMs (M350 and M550) shows the similar kinetics of SMX degradation (**Fig A3.10**). However, the M350 is not stable considering the

TGA result indicates incomplete conversion of precursor to Co_3O_4.

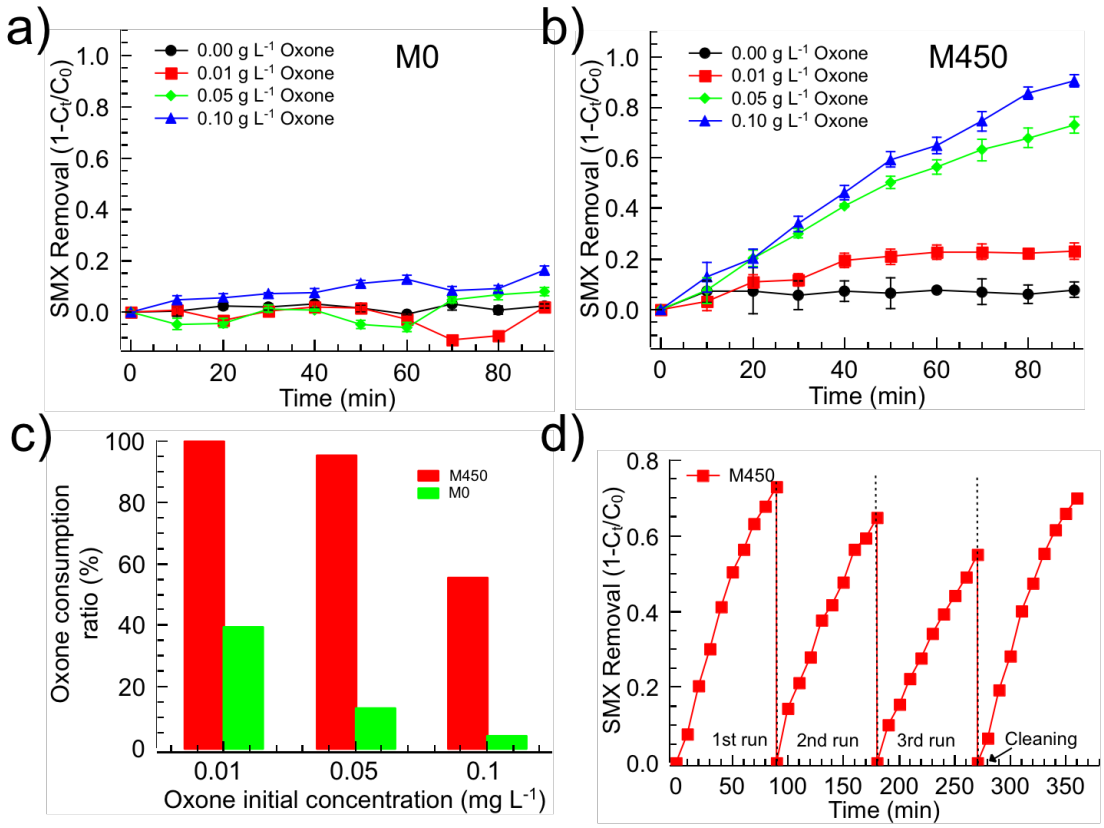

Fig 3.10. Catalytic performance of M0 and M450 (a,b-Effect of Oxone dosage; c-Oxone consumption ratios, d-durability of M450. Flow rate: [1 mL min^{-1}], TMP: [0.07 bar], SMX initial concentration: [10 mg L^{-1}]).

To evaluate the membrane durability, it was used for 3 operational cycles (the initial concentration of SMX was 10 mg L^{-1} and the Oxone dosage was 0.05 g L^{-1} based on the Oxone consumption result (**Fig 3.10 c**). **Fig 3.10 d** shows a slight decrease (< 10%) in the SMX removal rate with increasing operational cycles, which could be caused by the accumulative adsorption of SMX and its degradation products onto the surface of the membrane that reduced the density of active reaction sites. The detected leached cobalt ion was 0.084 mg L^{-1} after the 3rd run, which would not cause the acute toxic effects to aquatic life (Nagpal, 2004). After cleaning with Oxone solution (0.1 g L^{-1}) without adding SMX, more than 95% of the SMX removal efficiency could be reclaimed in the subsequent experimental run. This indicates the

durability could be achieved via Oxone assisted cleaning. Meanwhile, during the filtration test, TMP was monitored at 0.07 bar with a constant flow rate of 1 mL min^{-1}, which shows the insignificant fouling property of the membrane.

Three ROS including $^{\bullet}OH$, $SO_4^{\bullet-}$ and $SO_5^{\bullet-}$, and thus have been reported in a Co-Oxone catalytic system (Anipsitakis and Dionysiou, 2003). To verify the ROS in the CoFCM, EPR experiments were performed using DMPO as the spin trapping agent. As shown in **Fig 3.11 a**, when only Oxone solution was tested with the addition of DMPO, no peaks were detected, suggesting that no significant ROS was formed. However, in the presence of ZIF-67@450, the characteristic signals of 5,5-dimethyl-2-pyrrolidone-N-oxyl (DMPOX) with heptet were detected, which was formed from the oxidation of DMPO with strong ROS ($^{\bullet}OH$ and $SO_4^{\bullet-}$) (X. Chen et al., 2018; Zalibera et al., 2009).

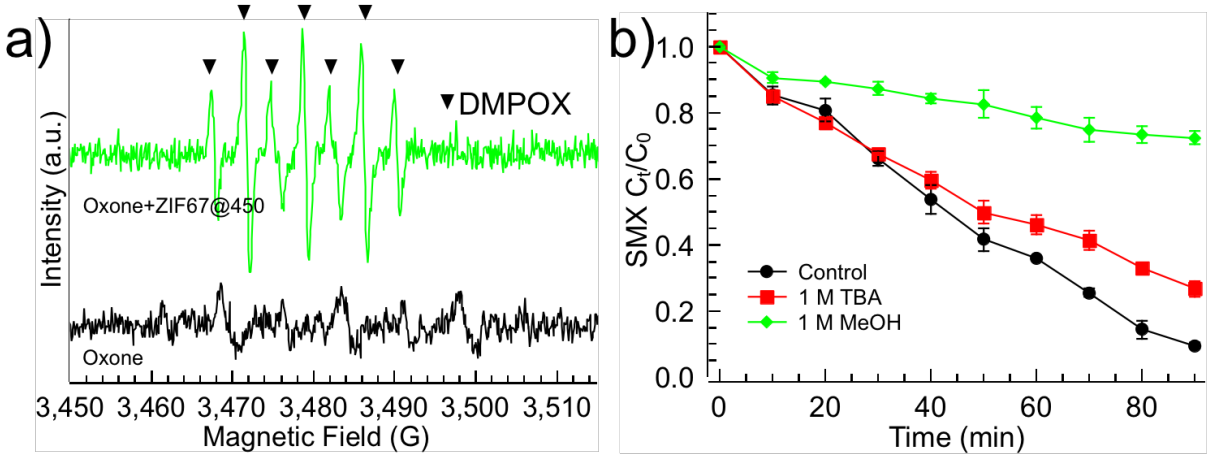

Fig 3.11. a) EPR spectra with DMPO as the spinning agent (Reaction condition: [Oxone] = 0.10 g L^{-1}, [SMX] =10 mg L^{-1}, [catalyst] = 0 or 2 g L^{-1} and [DMPO] = 100 mM) and b) The effect of scavengers towards the SMX degradation.

To further validate the primary ROS in the system, quenching experiments were conducted by adding methanol and *tert*-butanol (TBA) as the scavengers. It is widely accepted that methanol with an α-hydrogen ensures the quenching of both $SO_4^{\bullet-}$ (2.5×10^7 M^{-1} s^{-1}) and $^{\bullet}OH$ (9.7×10^8 M^{-1} s^{-1}) (Buxton et al., 1988; Neta et al., 1988), while TBA without α-hydrogen

reacts more easily with $^{\bullet}OH$ (3.8 - 7.6 × 10^8 M^{-1} s^{-1}), but in a slower reaction rate with $SO_4^{\bullet-}$ (4.0 - 9.1 × 10^5 M^{-1} s^{-1}) (Anipsitakis and Dionysiou, 2004). Meanwhile, $SO_5^{\bullet-}$ is relatively inert to both methanol and TBA due to its low rate constant with alcohols (≤ 10^3 M^{-1} s^{-1}) (Feng et al., 2016). **Fig 3.11 b** depicts the inhibition effects of different scavengers on the SMX degradation in the CoFCM/Oxone system. The degradation of SMX was inhibited entirely by addition of 1 M methanol, which indicated that the ROS generated in the system were mostly quenched. The results also confirmed the insignificant contribution of $SO_5^{\bullet-}$ on the SMX decomposition. Meanwhile, 1 M of TBA has little influence on the degradation of SMX in this system, implying that $^{\bullet}OH$ plays a smaller role in the SMX decomposition compared with $SO_4^{\bullet-}$. In the SMX degradation process, several intermediate products were detected via LC-MS-MS. The detailed detected products are listed in **Table A3.1**. The main degradation pathway is accompanied with the cleavage of sulfonamide bond as well as the formation of nitro-SMX molecule via the electron transfer reaction, which is in accordance with the previous study (Bao et al., 2018a).

Based on the above observation, the proposed reaction mechanism in CoFCM is illustrated in **Fig 3.12**. In this system, $SO_4^{\bullet-}$ is the dominant ROS responsible for the SMX decomposition and the major reactions include **Eqs. 2.1-2.4**.

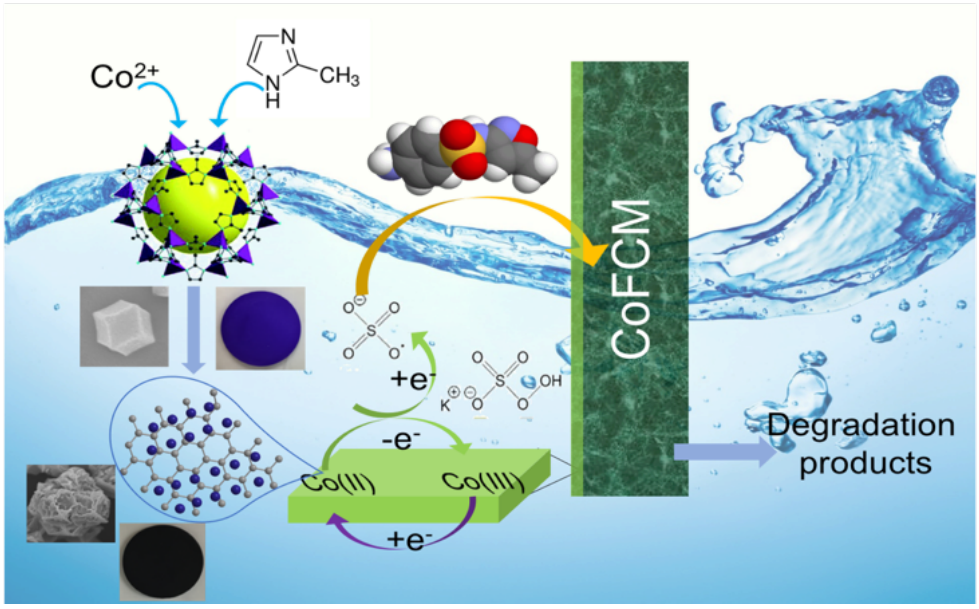

Fig 3.12. Illustration of the proposed reaction mechanism on SMX degradation in CoFCM.

3.4 Conclusions

A novel cobalt oxide functionalized ceramic membrane (CoFCM) was successfully prepared by a facile surface-nucleated zeolitic imidazolate framework (ZIF-67) growth method to activate Oxone for SMX degradation in a dead-end membrane filtration mode. The method to synthesize ZIF-67 as well as Co_3O_4 was optimized. The porous Co_3O_4 hollow structure was produced after one-step calcination of ZIF-67 precursor at 450°C and was distributed as a honeycomb structure on the membrane surface. The CoFCM shows a high performance on the removal of SMX as well as a high durability via Oxone-assisted cleaning. Overall, the CoFCM shows a new prospect for plentiful catalytic applications. Meanwhile, the MOF-directed surface-nucleated growth followed by one-step calcination is a promising method for fabrication of nanocatalysts functionalized ceramic membranes.

CHAPTER 4 PREPARATION OF PORE-FUNCTIONALIZED CERAMIC MEMBRANE WITH COBALT OXIDES (CoCM)

4.1 Introduction

An integrated system with membrane filtration and SR-AOPs could be employed to enhance the membrane performance as well as to avoid the catalyst recycling. In Chapter 3, a surface functionalized ceramic membrane with cobalt oxides (CoFCM) was developed for organics degradation in a membrane filtration system (Bao et al., 2018b). The surface modification changed the morphology as well as chemical properties of the ceramic membrane, and the catalytic performance test confirmed the radical generation process. However, the active sites on the membrane surface were limited by surface modification since the intermediate products can still pass through the membrane without further degradation. Meanwhile, there is rare study on the mechanism of catalytic membrane for PMS activation, especially the synergistic effect between catalyst and membrane.

Therefore, in this chapter, we developed a novel pore-functionalized ceramic membrane with isotropically impregnated Co_3O_4 (CoCM) via an in-situ self-scarified template method. It is the first report on the pore-functionalized ceramic membrane with Co_3O_4 for PMS activation. Meanwhile, the performance of CoCM was investigated via sulfamethoxazole (SMX) degradation and humic acid (HA) removal in the membrane filtration system. Finally, the PMS activation as well as organics removal mechanism via synergistic effect between Co_3O_4 and ceramic membrane in the CoCM were proposed and the sulfate radical generated in the process was quantified.

4.2 Experimental Section

4.2.1 Chemicals and materials

The same chemicals and materials used was listed in **Section 3.2.1**. Cobalt (II) nitrate hexahydrate ($Co(NO_3)_2{\cdot}6H_2O$), manganese (II) nitrate tetrahydrate ($Mn(NO_3)_2{\cdot}4H_2O$), nickel (II) nitrate hexahydrate ($Ni(NO_3)_2{\cdot}6H_2O$), humic acid (HA), glacial acetic acid ($C_2H_4O_2$), methanol (MeOH, CH_4O), *tert*-butanol (TBA, $C_4H_{10}O$), ceric sulfate tetrahydrate ($CeH_8O_{12}S_2$) and cerium(III) sulfate octahydrate ($Ce_2(SO_4)_3{\cdot}8H_2O$) were purchased from Sigma-Aldrich. Urea (CH_4N_2O) was supplied by VWR.

4.2.2 Preparation of Co_3O_4 impregnated ceramic membrane (CoCM)

A pore-functionalized ceramic membrane with isotropically impregnated Co_3O_4 was developed via an in-situ self-scarified template method (**Fig 4.1**). Urea has been served well as a precipitant, because it decomposes very slowly at 90°C in aqueous media according to the following reaction (**Eq.4.1**) (Richardson, 2013). Consequently, hydroxyl groups are formed slowly and uniformly throughout the membrane pores, followed by the metal hydroxides precipitation taking place homogeneously.

$$CO(NH_2)_2 + 3H_2O \rightarrow 2OH^- + 2NH_4^+ + CO_2\ (90\ °C) \qquad (\mathbf{4.1})$$

As demonstrated in **Fig 4.1**, the ceramic membrane was first immersed into the precursor solution (containing a certain amount of cobalt nitrate and urea) for 30 min. After the excess solution was drained off, the wet membrane was put into an oven at 90°C for 12 h, resulting in precipitation of metal hydroxide via the slow hydrolysis of urea in the membrane pores. After the reaction, the membrane was washed with DI water followed by drying at 90°C overnight. To decompose the precipitated metal hydroxide to metal oxides, the membrane was heated at 5°C min^{-1} till 450 °C and calcined for 3 h in an air atmosphere. The resulted membrane was named as CoCM.

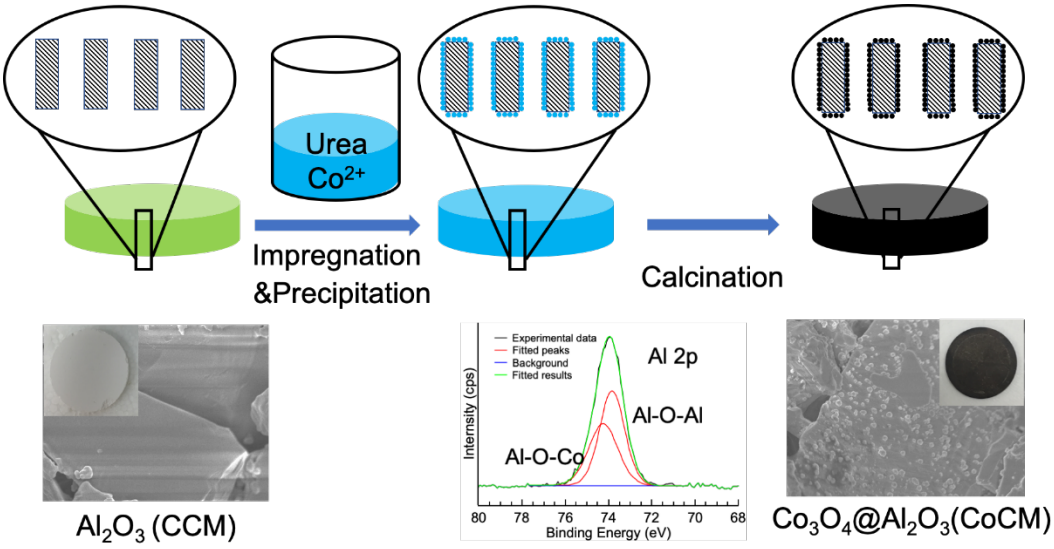

Fig 4.1. The preparation of Co_3O_4 impregnated ceramic membrane (CoCM).

4.2.3 Characterization techniques

The physical and chemical characterization techniques was listed as **Section 3.2.3**. The overall porosity ε (%) of membrane, which is defined as the volume of the pores divided by the total volume of the membrane was calculated by a dry-wet weight method through the following equation (**Eq. 4.2**).

$$\varepsilon = \frac{\frac{W_{wet}-W_{dry}}{\rho_{H_2O}}}{\frac{W_{wet}-W_{dry}}{\rho_{H_2O}}+\frac{W_{dry}}{\rho_{CM}}} \quad (4.2)$$

where W_{wet} and W_{dry} represent the weights of wet and dry membranes, ρ_{H_2O} and ρ_{CM} are the density of DI water and Al_2O_3 membrane.

4.2.4 Performance evaluation

The water permeability, catalytic performance and antifouling properties of the membranes were evaluated through a home-made dead-end filtration system (**Fig A4.1**). The pure water permeate flux was measured by varying the transmembrane pressure (TMP) in the range of 0.1-0.5 bar. The mass of permeate was measured and converted to permeate flux according to the **Eq. 4.3** and the intrinsic membrane resistance R_m (m^{-1}) is defined by **Eq. 3.5**.

$$J = V / \mathrm{A}\, t \quad (\mathbf{4.3})$$

where J represents permeate flux (LMH), V is volume of permeate (L), A is effective membrane surface area (m^2), t represents the filtration time (h).

The catalytic performance was evaluated by degradation of SMX ($C_{10}H_{11}N_3O_3S$, MW = 254 g mol^{-1}), which is found ubiquitous in the aquatic system and responsible for the development of antibiotic resistance (Rizzo et al., 2013). The rejection and antifouling tests were performed with an aqueous solution of humic acid (HA). All the filtration processes were carried out at room temperature under a constant flow of 236 LMH and the trans-membrane pressure (TMP) was recorded. In a typical filtration experiment, the feed (SMX/HA) and oxidant (PMS) were mixed before the membrane cell and the concentration of SMX/HA in the permeate side was analyzed. The effects of contact time as well as PMS dosage were investigated by changing the flow rate and PMS concentration.

4.2.5 Determination of chemicals and degradation products

The determination of SMX and its degradation products was described in **Section 3.2.5**. The total organic carbon (TOC) was analyzed before and immediately after the filtration using a TOC analyzer (Shimadzu TOC-L analyzer). The concentrations of dissolved metals were measured using the inductively coupled plasma optical emission spectrometry (ICP-OES, Perkin Elmer, Optima 8000). PMS and HA were quantified by UV-1800 spectrophotometer (Shimadzu, Japan) at UV_{352} and UV_{300} (Bao et al., 2018b).

A spectrophotometric determination method was used to quantify the sulfate radical concentration in aqueous solutions. Cerium (III) could be oxidized by sulfate radical to form Ce(IV) (**Eq. 4.4**) and the generated Ce (IV) was then quantitated by UV-1800 spectrophotometer (Shimadzu, Japan) at UV_{320} (W. Chen et al., 2018). The calibration curves for PMS, HA and Ce (IV) are shown in **Figs A3.2** and **A4.2**.

$$SO_4^{\bullet -} + \mathrm{Ce\ (III)} \rightarrow SO_4^{2-} + \mathrm{Ce\ (IV)},\ k = 1.43 \pm 0.3 \times 10^8\ M^{-1}s^{-1} \quad (\mathbf{4.4})$$

4.3 Results and discussion

4.3.1 Chemical and physical characterizations

FESEM characterizations of both surface and cross section (internal pores) of CCM and CoCM are displayed in **Fig 4.2**. The CCM showed a smooth surface as well as internal pores, while it changed significantly after the Co_3O_4 impregnation. As shown in **Figs 4.2 d** and **e**, after the impregnation, the Co_3O_4 could be distributed evenly on the membrane surface as well as internal pores. No obvious catalytic separation layer was observed in the images, meaning there was no Co_3O_4 compact skin layer on the membrane surface. The AFM images show that there was no obvious different after the impregnation of Co_3O_4 (**Figs 4.2 c** and **f**).

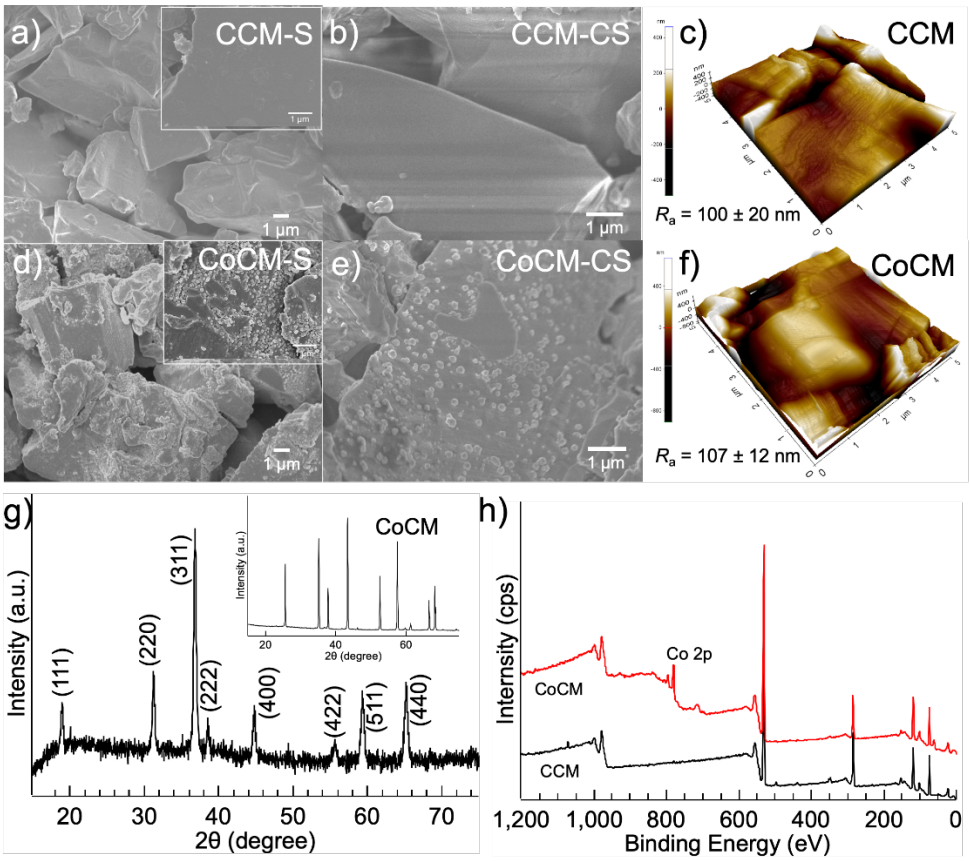

Fig 4.2. Chemical and physical characterizations (a-FESEM of CCM surface; b-FESEM of CCM cross-section; c-AFM of CCM surface; d-FESEM of CoCM surface; e-FESEM of CoCM cross-section; f-AFM of CoCM surface; g-XRD of both Co_3O_4 particle and CoCM (Inset); h-XPS wide scan for both CCM and CoCM).

XRD was used to characterize the structural and crystallographic properties of the as-prepared Co_3O_4 (**Fig 4.2 g**). The diffraction pattern for the Co_3O_4 has eight broad peaks at 18.9°, 31.5°, 37.0°, 38.5°, 44.8°, 55.6°, 59.8° and 65.7°, corresponding to (111), (220), (311), (222), (400), (422), (511) and (440) of cubic Co_3O_4 (Entry No. 04-006-9495), respectively. The CoCM was also characterized (**Inset of Fig 4.2 g**). Results show that only Al_2O_3 phase was identified, which should be caused by the less impregnated amount of Co_3O_4 as well as extremely high signal of Al_2O_3.

To further analyze the bonding mechanism of CoCM, XPS analysis was carried out by investigating the various elemental chemical oxidation states in both CCM and CoCM. As shown in **Fig 4.2 h**, Co 2p was observed in the XPS survey spectrum in CoCM, demonstrating the successful impregnation of Co_3O_4. The spectrum of Al 2p shown in **Fig 4.3 a** could be readily assigned to Al-O, indicating the CCM surface is mainly covered by the Al_2O_3. However, the Al 2p spectrum (**Fig 4.3 c**) in CoCM could be fitted into two peaks which are corresponded to Al-O-Al and Co-O-Al, respectively. The existence of Co-O-Al bond could avoid Co_3O_4 aggregation as well as decrease the leaching of Co during the filtration test, improving the stability of CoCM. For both CCM and CoCM, two O 1s sub-peaks can be resolved with their binging energies at around 532 and 531 eV, which could be assigned to hydroxyl species (O_B) and lattice oxygen species (O_A), respectively (Biesinger et al., 2011). On the surface of CoCM, the ratio of O_A/O_B is significantly increased to 3.46 (**Fig 4.3 d**) from 1.06 for CCM (**Fig 4.3 b**) due to the contribution of oxide from the Co_3O_4. Meanwhile, the presence of the surface hydroxyl groups can lead to the formation of Co-OH complex, which is crucial for the sulfate radical generation (Anipsitakis et al., 2005). High resolution XPS of Co 2p further revealed the successful synthesis of Co_3O_4, in which the peaks appear at around 781 and 796 eV are ascribed to $Co2p_{3/2}$ and $Co2p_{1/2}$ (**Fig 4.3 e**).

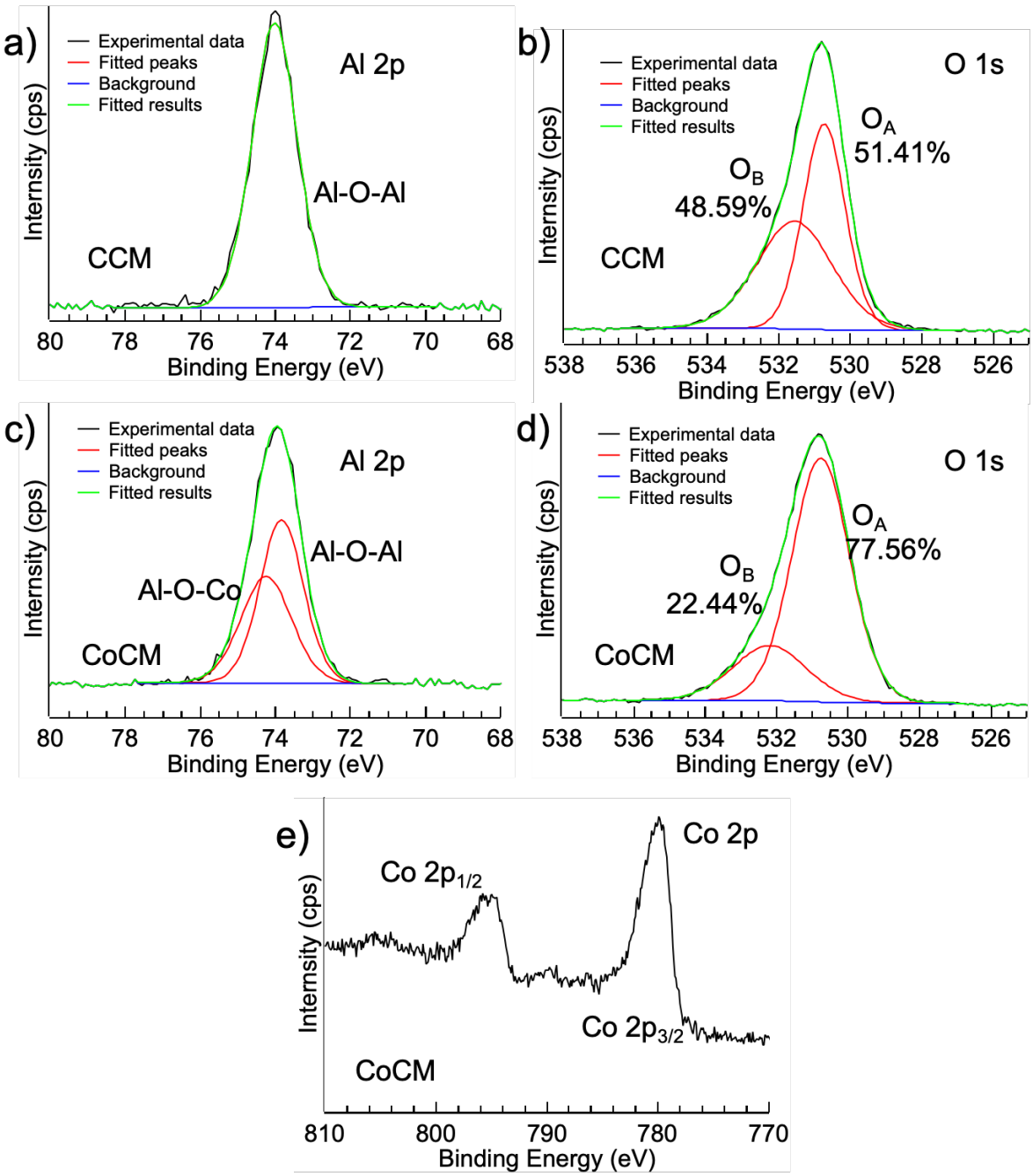

Fig 4.3. High resolution of Al 2p, O 1s and Co 2p in CCM and CoCM.

4.3.2 Characterization of membrane properties

The summary on the membrane properties of CCM and CoCM is shown in **Table 4.1**. The porosity of CoCM was calculated as 41.9 ± 0.4 % (**Eq. 4.2**), which was similar to that of the original membrane (CCM). The unchanged porosity revealed that Co_3O_4 was formed conformally on the surface of Al_2O_3 grains, without blocking the pores of the membranes,

which could also be evidenced by FESEM images (**Fig 4.2**).

Table 4.1. Summary on the membrane properties of CCM and CoCM.

Membranes	Porosity (%)	Surface Roughness (nm)	Contact Angle (°)	Permeability (LMHB)	Intrinsic membrane resistance (m^{-1})
CCM	41.8 ± 0.5	100 ± 20	73.5 ± 3.4	3960 ± 330	9.16×10^{10}
CoCM	41.9 ± 0.4	107 ± 12	52.4 ± 5.3	7902 ± 527	4.58×10^{10}

The roughness and hydrophilicity of membrane surface are significant factors influencing the permeability and antifouling properties of membranes. The surface roughness for CCM and CoCM was estimated via AFM (**Figs 4.2 c** and **f**) as 100 ± 20 nm and 107 ± 12 nm. The hydrophilicity of membrane surface was estimated through water contact angle between the air-water interface and the membrane surface, which reflects the wettability of the membrane surface (F. Chen et al., 2018). As compared with the CCM which had a contact angle of 73.5 ± 3.4°, the contact angle of CoCM decreased to 52.4 ± 5.3°.

The pure water permeability of membranes was investigated in the home-made dead-end filtration system (**Fig A4.2**). Results showed that with imprganation of Co_3O_4, the pure water permeability increased from 3960 ± 330 to 7902 ± 527 LMHB while the intrinsic membrane resistance decreased from 9.16 to 4.58×10^{10} m^{-1}, corresponding to the changes of membrane surface hydrophilicity (**Table 4.1**). These observations confirmed that hydrophilicity and wettability of the ceramic membranes can be improved by the impregnation of Co_3O_4 via the as described in-situ self-sacrified template method.

4.3.3. Membrane performance in SMX removal

Fig 4.4 illustrates the removal of SMX in membrane filtration system. When SMX was fed into the system, the removal efficiency was around 25% for CCM while it increased to 59%

when CoCM was employed (**Fig 4.4 a**). Meanwhile, there was no significant change in TMP throughout the filtration test (100 min), indicating a negligible fouling of the membrane surface due to the low molecular size of SMX (**Fig 4.4 b**). Therefore, the removal of SMX should be attributed to its catalytic degradation while the membrane separation had no significant contribution. The metal leaching test showed Co_3O_4 was quite stable in CoCM with a low detected concentration of Co (0.045 ± 0.004 mg L^{-1}) in the permeate (**Fig 4.4 b**).

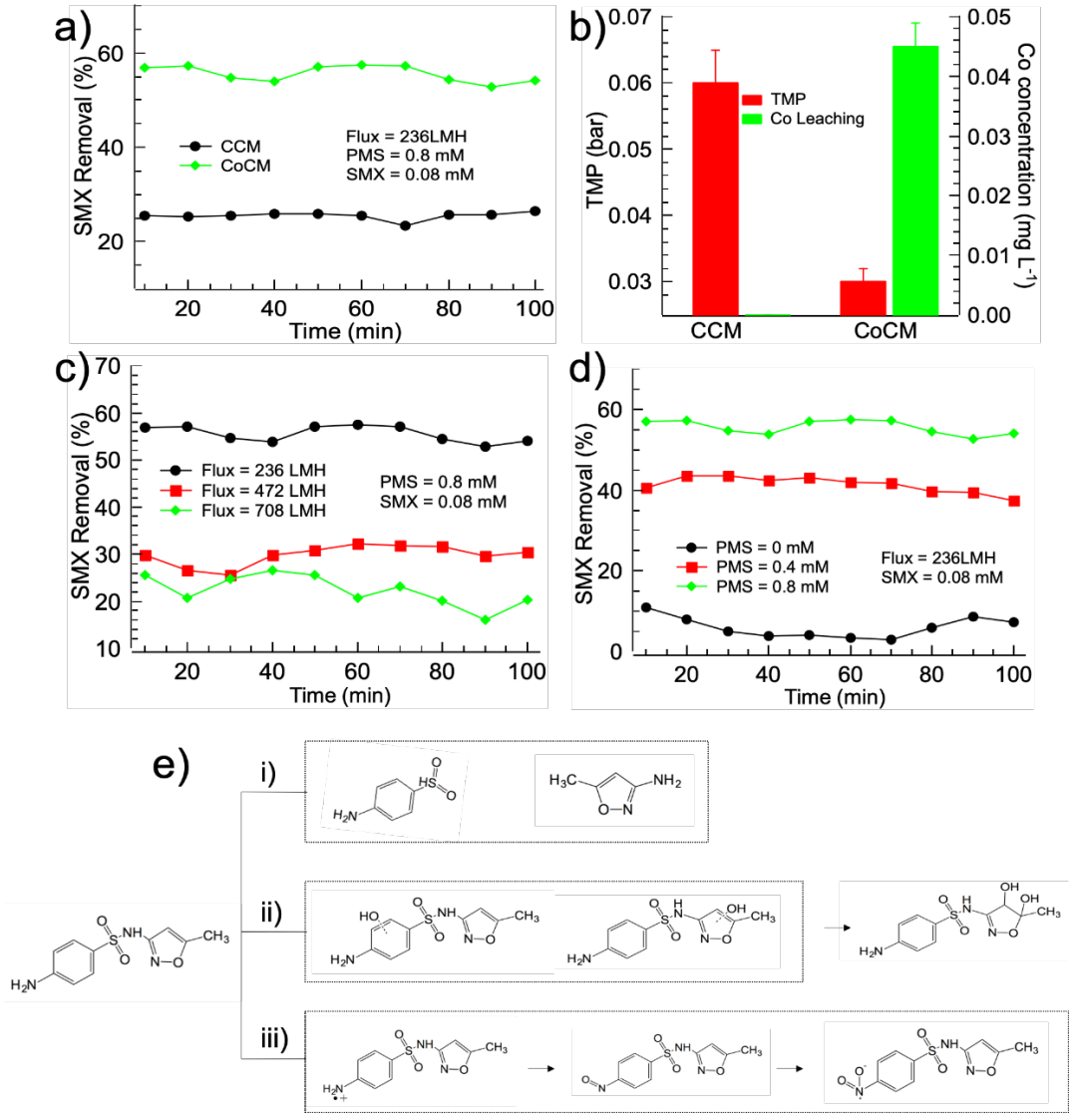

Fig 4.4. SMX removal in membrane filtration system (a, effect of membranes; b, records for TMP and Co leaching in 100 min filtration; c, effect of retention time; d, effect of PMS dosage; e, proposed SMX degradation pathway in PMS/CoCM system).

The effects of contact time and PMS dosage on SMX removal over CoCM in the membrane filtration system were further investigated. The results showed that with increase of flux from 236 to 708 LMH, the retention time was decreased from 16.8 to 5.6 s, resulting in the decrease of SMX removal from 59% to 20% (**Fig 4.4 c**). Meanwhile, being the source of free radicals, increasing PMS dosage caused more PMS to occupy the active sites, improving the probability of PMS and CoCM interaction, resulting in a higher SMX removal efficiency (**Fig 4.4 d**).

Even at 60% SMX removal efficiency for CoCM when the flux was set at 236 LMH and the PMS dosage was 0.8 mM, the TOC removal was only 15.3% (**Fig A4.3**). The results showed that the SMX was mostly degraded into smaller molecules but not mineralized to CO_2 and H_2O. The intermediate products were analyzed by LC-MS-MS and the proposed degradation pathway involved i) the cleavage of sulfonamide bond, ii) OH addition and iii) electron transfer reaction (**Fig 4.4 e**). The cleavage of sulfonamide bond (i) was most likely caused by the PMS direct oxidation via a non-radical pathway. PMS can work as an inorganic oxidizer to react with SMX through nucleophilic reactions, in which the S atom of the sulfanilamide group could be selectively attacked. In the radical-pathway, two major radicals ($SO_4^{\bullet-}$ and $^{\bullet}OH$) were involved in the process, $SO_4^{\bullet-}$ has a highly-selective electrophile mainly acting by electron-transfer from N to $SO_4^{\bullet-}$ yielding to a N-centered radical as a first intermediate (iii), while $^{\bullet}OH$ exhibits high reactivity with olefinic double bonds and anilines (Buxton et al., 1988), therefore, the radical addition on the benzene ring was observed (ii).

4.3.4. Membrane performance in HA removal

HA is the most ubiquitous natural organic matter (NOM) in the natural aquatic system and it is also present in the effluent of wastewater treatment plant due to its biorecalcitrance. In the membrane filtration system, when the feed was changed to HA solution, the HA removal efficiency increased from 60% (CCM) to ~100% for CoCM (**Fig 4.5 a**). Noticeably, the

removal of HA was 46% for CCM at the beginning (< 60 min), and then gradually increased to ~60% with continuous filtration to 100 min. Meanwhile, the recorded TMP increased from around 0.06 bar to 0.12 bar (**Fig 4.5 b**), corresponding to the evolution of membrane fouling by HA cake layer formation, which simultaneously increased the HA removal efficiency. However, for CoCM, the TMP change was much slower than that of CCM and the removal of HA was maintained at > 95% throughout the filtration test, showing the antifouling property of the CoCM. Apparently, the generated radicals in CoCM could attack HA molecule into smaller ones, reducing the membrane pore blocking.

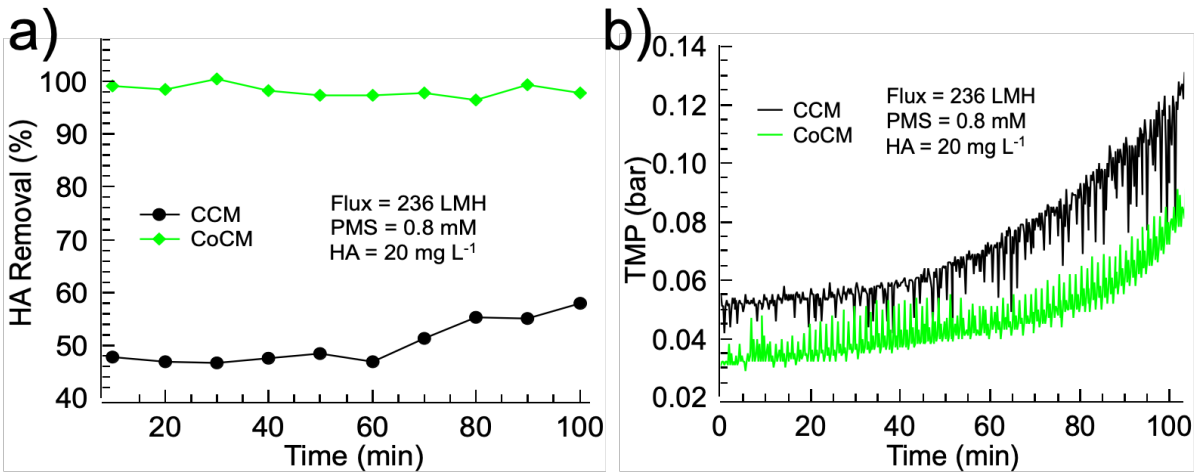

Fig 4.5. HA removal (a) and TMP changes (b) in membrane filtration system.

4.3.5. Membrane performance in SMX-HA removal

In this experiment, the membrane performance was tested when SMX and HA were co-existed in the feed. The SMX removal decreased from ~60% (10 min) to 46% (100 min) for CoCM (**Fig 4.6 a**) while the increase of HA removal after 60 min filtration was observed, indicating the existence of membrane fouling (**Fig 4.6 b**). Compared with the single species system (SMX or HA), both SMX and HA removal efficiency decreased in the SMX-HA co-existence system. The decrease in SMX removal is believed to be due to the scavenging of sulfate radical by HA (Bao et al., 2018a), while the decrease in HA removal could be caused by the decrease of active sites on the membrane surface. The results showed that the catalytic

performance of CoCM would be partially suppressed in the natural water which consists of recalcitrant bulk organic matters (e.g., humic acid). The AFM images of membranes after filtration test are shown in **Fig 4.6**. The surface roughness was slightly decreased for both CCM and CoCM, which could be caused by the partially deposition of HA on the membrane surface.

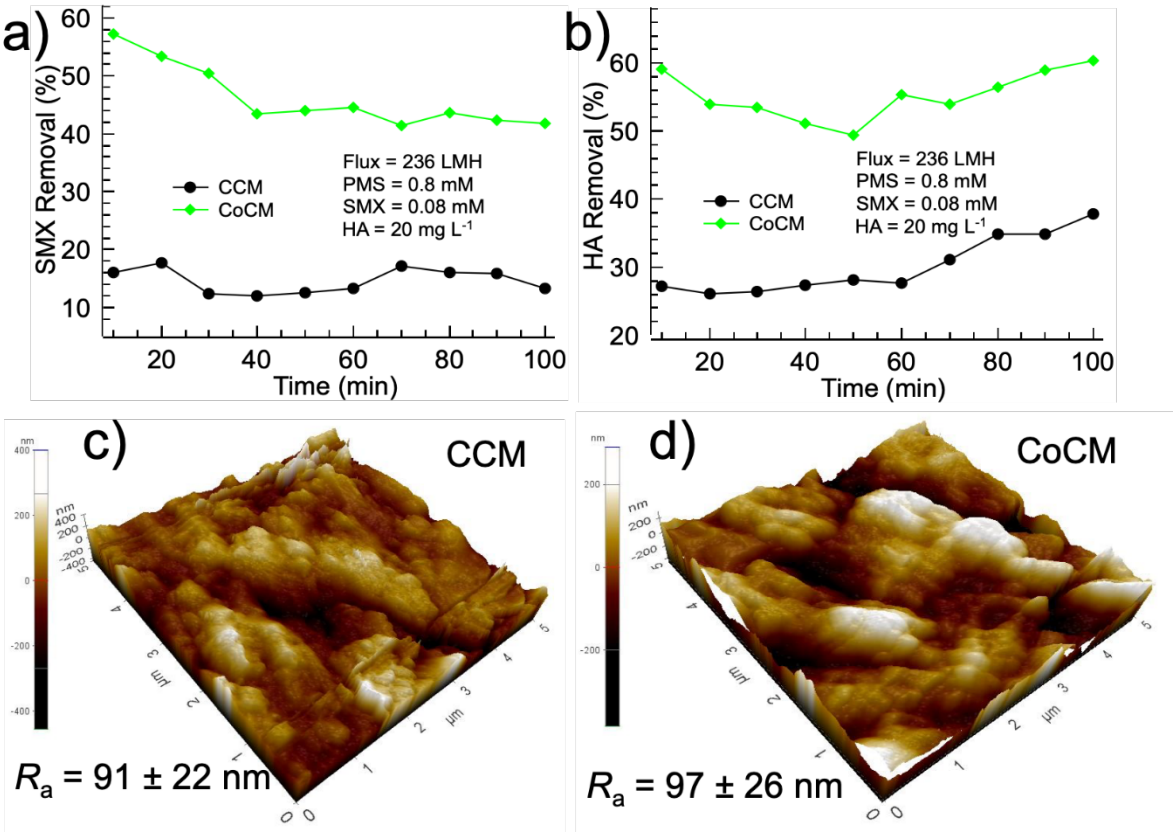

Fig 4.6. SMX and HA removal in the SMX-HA system (a and b) and the AFM images of used membranes (c and d).

4.3.6. Membrane fouling elimination in SMX-HA system

Analysis of the time-dependent pressure variations in the membrane filtration system could provide membrane fouling evolution in the process. Three treatment cycles in SMX-HA system over CCM and CoCM were conducted at a constant flux operational mode. For each treatment cycle, the operation time was 100 min followed by the washing with PMS solution for 60 min. As depicted in **Fig 4.7 a**, with the prolong of filtration time, TMP increased noticeably for CCM because of the deposition of HA molecules on the membrane surface as

well as in the internal pores. As compared with CCM, the TMP increase in CoCM was much slower due to the decomposition of HA via radicals. After 100 min filtration, the PMS washing had no significant effect on the flux recovery for both CCM and CoCM, indicating the active sites on CoCM might have been enveloped by HA, resulting in the deactivation of catalyst. To decompose the HA accumulated on the surface of active sites, both CCM and CoCM were regenerated via a heat-treatment method at 450°C for 1 h. Results showed that fully recovery of initial flux could be achieved by this method while the membrane fouling rate increased in the following treatment.

Fig 4.7 b shows that in the treatment cycles of 1-3, the removal of HA for CoCM slightly increased while the removal of SMX decreased. The increase in HA removal was attributed to the partly membrane fouling, in which rejection of HA by size-exclusion mechanism could take effect. For SMX, once the active sites on catalyst were fouled by HA, the degradation efficiency decreased. For CCM, during three treatment cycles, the HA removal increased while the SMX removal maintained at 15 ± 5% (**Fig 4.7 b**). The removal of HA should be mainly caused by the membrane rejection from the cake layer on the surface (**Fig 4.7 c**) while the removal of SMX should be caused by the catalytic oxidation by PMS. In comparison with CCM, CoCM did not show the formation of cake layer (**Fig 4.7 c**), further confirmed its antifouling property.

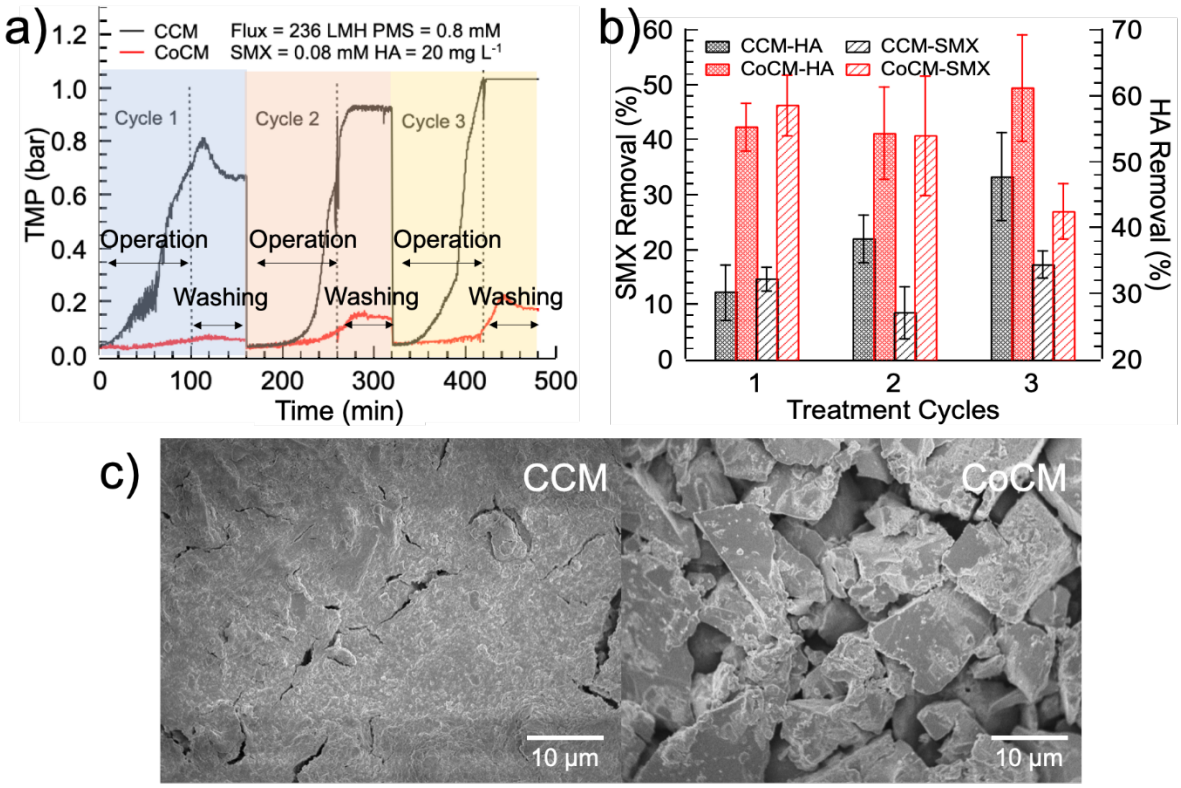

Fig 4.7. a) TMP changes and b) SMX and HA removal in different treatment cycles for CCM and CoCM; c) FESEM images of CCM and CoCM after 3 treatment cycles.

4.3.7. PMS activation and organics removal mechanism in CoCM

In the PMS/CoCM system, $SO_4^{\bullet-}$ and $^{\bullet}OH$ could be formed (Anipsitakis and Dionysiou, 2003). Literature reported that methanol can react with $^{\bullet}OH$ and $SO_4^{\bullet-}$ at high and comparable rates with reaction rate constants of $k_{[^{\bullet}OH]} = 1.2 - 2.8 \times 10^9\ M^{-1}\ s^{-1}$ and $k_{[SO4^{\bullet-}]} = 1.6 - 7.7 \times 10^7\ M^{-1}\ s^{-1}$ (Buxton et al., 1988; Hayon et al., 1972), while $SO_5^{\bullet-}$ is quite inert toward alcohols because of the low reaction rate which is less than $10^3\ M^{-1}\ s^{-1}$ (Hayon et al., 1972). Meanwhile, alcohols with no α-hydrogen such as *tert*-butanol (TBA) are more effective in quenching $^{\bullet}OH$ ($3.8 - 7.6 \times 10^8\ M^{-1}\ s^{-1}$) compared with that of $SO_4^{\bullet-}$ ($4.0 - 9.1 \times 10^5\ M^{-1}\ s^{-1}$) (Feng et al., 2016).

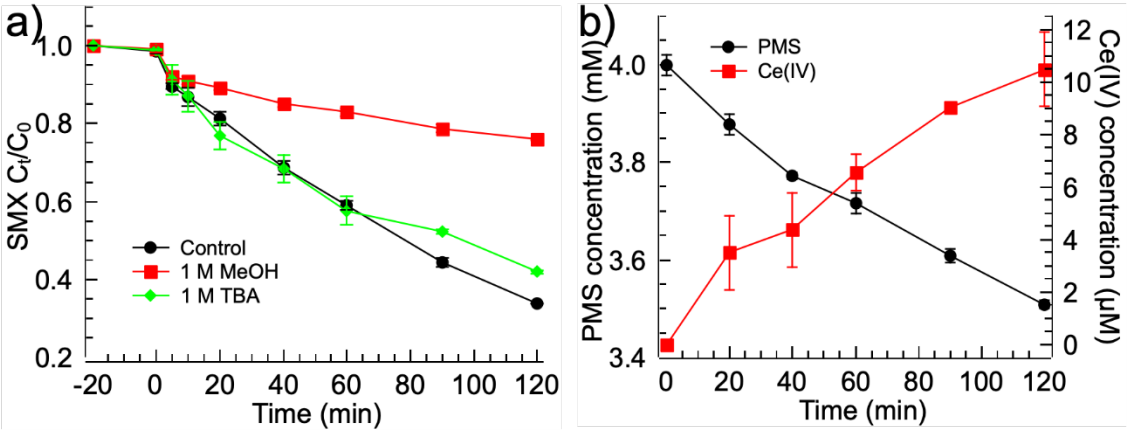

Fig 4.8. a) Effect of different scavengers on SMX degradation in PMS/CoCM system. (Conditions: [PMS] = 0.4 mM, [SMX] = 0.04 mM); and b) PMS decomposition and the $SO_4^{\bullet-}$ generation in PMS/CoCM system (Conditions: [PMS] = 4 mM, [Ce (III)] = 10 mM).

To identify the major reactive oxygen species that were responsible for PMS/CoCM system in the degradation of SMX in natural pH, TBA and methanol were used as quenching agents in a batch system (Xu and Wang, 2011). **Fig 4.8 a** shows the effect of different scavengers on the degradation of SMX. In the control experiment, the SMX removal could be achieved to 66% in 120 min, while the removal decreased to 24% and 58% when 1 M MeOH and 1 M TBA were added, respectively. The results showed that $SO_4^{\bullet-}$ should be the major contribution in the SMX degradation under the experimental conditions (**Eqs. 2.1-2.4**). To further determine the $SO_4^{\bullet-}$generation process, a PMS self-decomposition experiment without SMX was conducted and the results are shown in **Fig 4.8 b**. The calculation of $SO_4^{\bullet-}$ was conducted based on a spectrophotometric method via the oxidation of Ce (III) to Ce (IV), which has an adsorption at wavelength of 320 nm (W. Chen et al., 2018). At the initial concentration of 4 mM, PMS consumption rate was calculated as 12.3% (0.49 mM), while the generated $SO_4^{\bullet-}$ was calculated as 10.5 μM (Eq.6) in 120 min.

Fig 4.9 presents the XPS of Co2p of the Co_3O_4 before and after oxidation reaction. The ratio of Co^{2+}/Co^{3+} slightly decreased from 2.09 to 1.63 after reaction, showing Co^{2+} underwent

a partial transfer to Co^{3+} in the oxidation process. The ratio of O_A in the O1s spectrum decreased to 76.7% after the reaction (**Fig A4.4**), evidencing the electronic transformation process via Co^{2+} to Co^{3+}. The oxidizing reaction occurs on the surface and Co^{2+} would provide the electrons. In order to keep the balance of charge on the catalyst surface, Co^{3+} will accept the electrons from the system. It manifests the involvement of Co^{2+}-Co^{3+}-Co^{2+} redox processes during the reaction. The slight decrease of the ratio of Co^{2+}/Co^{3+} showed that the Co^{3+} could not be fully reduced in the system after a prolonged use of CoCM.

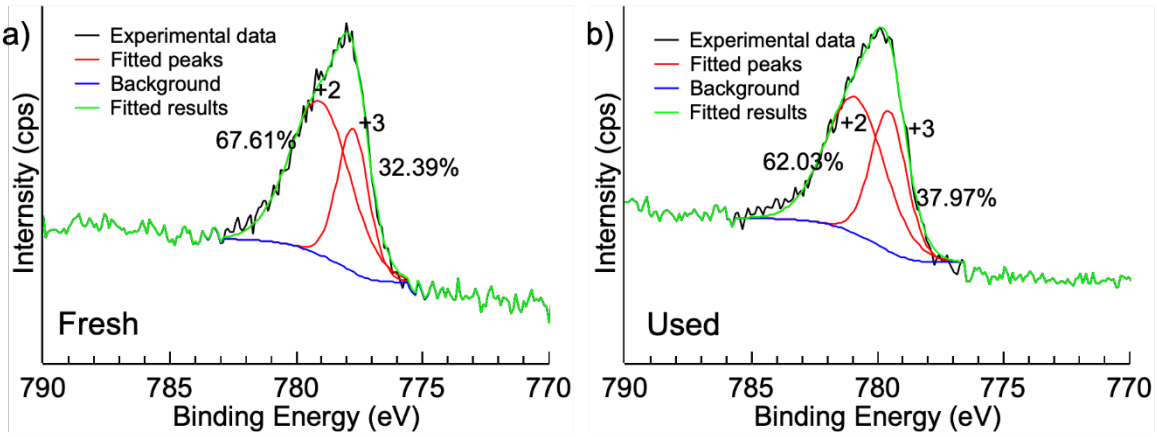

Fig 4.9. The high resolution of Co2p in fresh and used CoCM.

Herein, the radical generation and organics removal in CoCM is proposed as shown in **Fig 4.10**. As analyzed before, Co_3O_4 distributed uniformly on the surface of the Al_2O_3 in the form of Co-O-Al (**Fig 4.2** SEM analysis and **Fig 4.3** XPS analysis), forming a conformal coating across both the membrane surface as well as the internal pores. Apparently, the nanocatalytic Co_3O_4 in CoCM functioned as a stable cobalt source to accelerate the generation of radicals from PMS. Generally, sulfate radical would be generated by the reduction of HSO_5^- via accepting electrons from Co^{2+}, and at the same time, it could be regenerated by reducing from Co^{3+}, in which HSO_5^- was transformed into $SO_5^{\bullet-}$ and H^+ (Anipsitakis and Dionysiou, 2004). $SO_4^{\bullet-}$ can further transform into $^{\bullet}OH$ by reacting with H_2O (Hu and Long, 2016). In the heterogeneous cobalt-catalyzed system, it is believed that the redox cycle of cobalt species

occurring in Co_3O_4 facilitates the radical generation. As shown in this work, the leaching of cobalt ions into solutions was minimal since the two different oxides of cobalt were bounded and could interact autogenously (Anipsitakis et al., 2005; Zhang et al., 2010). For the organics removal in CoCM, part of organics could be rejected by membrane separation via size exclusion mechanism. At the same time, radicals produced could degrade the organics into smaller molecular, some of which might pass through the membrane.

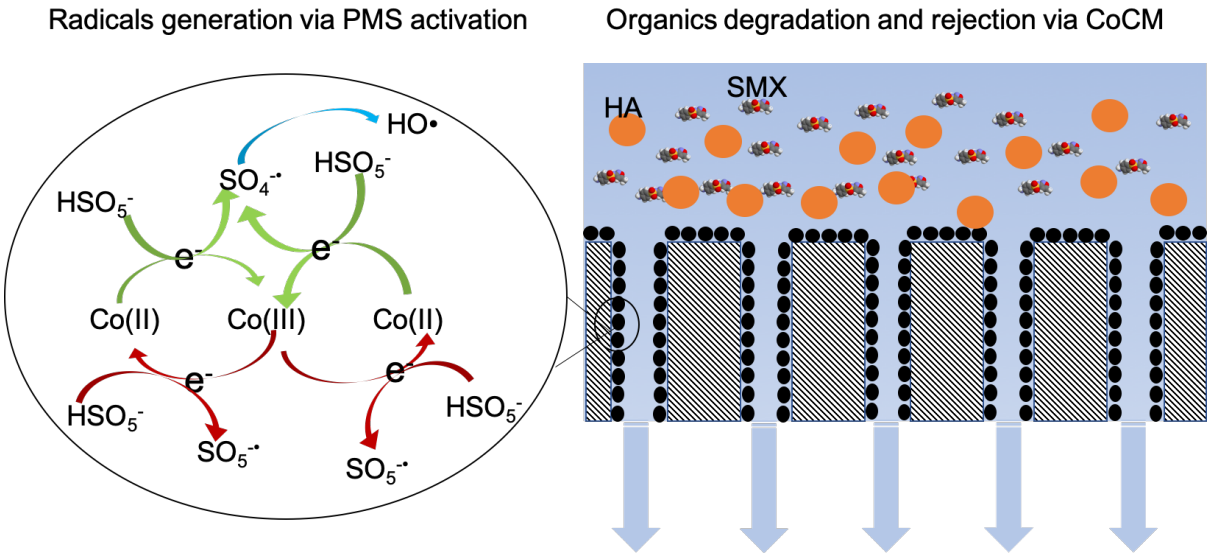

Fig 4.10. Schematic illustration of the proposed radical generation and organics removal in CoCM.

4.3.8. Versatility of in-situ self-scarified template method

One primary benefit of the in-situ self-scarified template method reported herein is its versatality for different metal oxides. Theorectically, any metal oxides could be formed via this process and disturbuted uniformally across the whole membrane substrate. Therefore, to investigate the versatality of this method, Mn oxides and Ni oxides impregnated ceramic membranes were prepared via the same method, in which cobalt nitrate was replaced by manganese nitrate and nickel nitrate (**Figs A4.5-4.7** and **Text A4.1**). Results showed that Mn oxides and Ni oxides could also be impregnated successfully and uniformly throughout the membrane pores, and both catalytic ceramic membranes showed an enhanced performance in

SMX degrdation and HA removal. Thus, the in-situ self-scarified template method should be universally applicable for the fabrication of metal oxides impregnated ceramic membranes for water treatment.

4.4. Conclusions

A novel pore-functionalized ceramic membrane with isotropically impregnated cobalt oxide (CoCM) was prepared via in-situ self-scarified template method and used for organics removal in membrane filtration system. Based on the results presented, the following conclusions are drawn:

1) The nanocatalytic Co_3O_4 was distributed evenly and uniformly throughout the whole membrane via an in-situ self-scarified template method without significantly changing the membrane surface roughness.
2) The CoCM showed high pure water permeability and catalytic performance in SMX-HA system. The SMX removal efficiency could be affected by both contact time and PMS dosage.
3) The formation of Co-O-Al bonding made CoCM more robust and stable with a low cobalt leaching.
4) The CoCM showed an antifouling property and could be regenerated via a heat treatment.
5) The Co^{2+}/Co^{3+} ratio change after reaction evidenced the PMS activation and the quantitative calculation of $SO_4\bullet^-$ further confirmed the radical generation in the oxidation process.
6) The organics removal in CoCM included catalytic degradation via radical generation and membrane separation via size-exclusion.

CHAPTER 5 PREPARATION OF COBALT FERRITE IMPREGNATED CERAMIC MEMBRANE

5.1 Introduction

As described in Chapter 2, cobalt ion and its composites have been reported to be more efficient as PMS activators in degradation of most organic pollutants (Chen et al., 2017; Hu and Long, 2016). Meanwhile, iron has been widely applied in water treatment because of its low cost, abundant supply, low toxicity and environmental friendliness. The addition of iron into cobalt compound can not only enhance PMS activation through enriching hydroxyl groups on the catalyst surface, but also endow the catalyst with easier separation and recovery properties due to its magnetism and suppress cobalt leaching owing to the strong Co-Fe interactions (Yang et al., 2009).

Herein, a simple urea-assisted one-step combustion method was used to prepare $CoFe_2O_4$ impregnated Al_2O_3 ceramic membrane in this Chapter. The performance of catalytic ceramic membrane impregnated with $CoFe_2O_4$ was evaluated in a membrane filtration system. Meanwhile, a comprehensive performance evaluation of $CoFe_2O_4$ catalyst as PMS activator for SMX degradation was investigated and the SMX degradation pathway was proposed via the determination of dominant radicals and the SMX degradation products in the $CoFe_2O_4$/membrane/PMS system.

5.2 Experimental Section

5.2.1 Chemicals and materials

The same chemicals and materials used was listed in **Section 3.2.1** and **Section 4.2.1**. Iron(III) nitrate nonahydrate ($Fe(NO_3)_3{\cdot}9H_2O$) was received from Acros organics. Sodium chloride (NaCl), sodium sulfate (Na_2SO_4), sodium nitrite ($NaNO_3$) and sodium carbonate

(Na_2CO_3) were from Merck. 5,5-dimethyl-1-pyrrolidine N-oxide (DMPO) was purchased from Aladdin and 5-*tert*-Butoxycarbonyl-5-methyl-1-pyrroline-N-oxide (BMPO) was from Cayman Chemical.

5.2.2 Preparation and characterization of $CoFe_2O_4$ impregnated membrane

Impregnation of $CoFe_2O_4$ in Al_2O_3-based ceramic membrane pores via a urea-assisted one-step combustion method is shown in **Fig 5.1**. Briefly, the membranes were firstly washed with DI water and dried in oven at 100 °C for 24 h. Before the impregnation process, the disc was weighed as W_0. Subsequently, 1-3 pieces of discs were immersed into 10 mL of the impregnation solution, which is a mixture of urea, $Co(NO_3)_2{\cdot}6H_2O$ and $Fe(NO_3)_3{\cdot}9H_2O$. After 30 min immersion, an additional force was applied on the solution to penetrate the pores, after the excess solution was drained off, the discs were put in a furnace with settled temperature. To get the $CoFe_2O_4$ impregnated Al_2O_3 ceramic membrane, the discs were calcined for 30 min in an air atmosphere. After the calcination, the $CoFe_2O_4$ impregnated Al_2O_3 ceramic membrane was weighed as W_1. The final catalyst loading amount was calculated by the weight difference $W = W_1-W_0$. Meanwhile, the residual impregnation solution was put into the furnace at the same condition to get the $CoFe_2O_4$ powders. For the multiple impregnation experiments, all previous steps (immersion and calcination) were repeated.

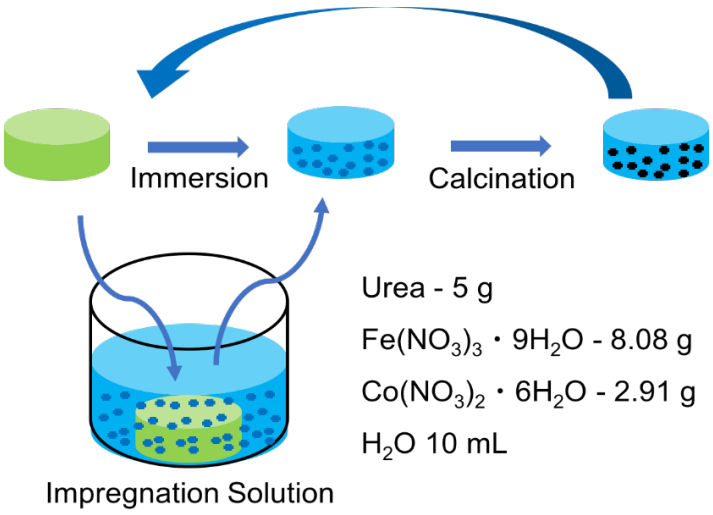

Fig 5.1. Urea-assisted one-step synthesis of $CoFe_2O_4$ impregnated membrane.

5.2.3 Characterization techniques

The physical and chemical characterization techniques was listed as **Section 3.2.3** and **Section 4.2.3**. Zeta potential (ζ) of $CoFe_2O_4$ in water solution was measured by a zetasizer (Malvern, UK).

5.2.4 Catalytic degradation of SMX in $CoFe_2O_4$/membrane/PMS system

For batch experiment, unless otherwise specified, all degradation experiments were carried out in 100 mL glass beakers at room temperature with magnetic stirring at 500 rpm. Before the reaction, SMX with a certain concentration was prepared in the beakers followed by the addition of Oxone. Later, the catalysts or catalytic membranes were loaded into the solution to activate the reaction. Samples were withdrawn at specified time intervals followed by the addition of methanol to quench the reaction. The samples were then filtered with 0.45 μm polytetrafluoroethylene (PTFE) syringe filters and transferred into auto-sampler vials for further analysis.

The catalytic activity of the $CoFe_2O_4$ impregnated membrane was investigated in the homemade filtration setup as shown in **Fig A5.1** (modified from **Fig A4.1**). In this system, the membrane (with/without $CoFe_2O_4$) was fitted into a circular membrane cell. In the dead-end filtration mode, the feed (SMX) and oxidant (Oxone) solutions were pumped separately and mixed before entering the membrane cell. The effects of flow rate (0.2 - 2 mL min^{-1}), Oxone dosage (0 - 0.1 g L^{-1}) and pH were investigated. The permeate was collected and its volume was recorded by measuring its weight, which is controlled by a computer (**Fig A5.1**). Before the determination of SMX, a certain amount of methanol was added to quench the reaction.

5.2.5. Determination of chemicals and degradation products

The determination of SMX and its degradation products was described in **Section 3.2.5** and **Section 4.2.5**. The nitrate in solution was detected by ion chromatography (Dionex, ICS-1100) using the mixture of Na_2CO_3 and $NaHCO_3$ as the effluent.

5.3. Results and discussion

5.3.1. Study of the urea-assisted one-step combustion method

The effect of calcination temperature on the morphology, crystal structure and catalytic performance of as-prepared $CoFe_2O_4$ particle was investigated (**Fig A5.2**). The SEM images of all catalysts prepared under different calcination temperatures (300 - 800°C) show the similar surface morphology composing of closely packed particles with a particle size of 50 - 100 nm. The intensity of the diffraction peaks increased with the increase of calcination temperature from 300 to 600 °C, indicating the higher crystallinity and larger particle size. Interestingly, when the calcination temperature increased to 800 °C, the characteristic peak of (311) for $CoFe_2O_4$ deceased with the appearance of new peaks, meaning the crystal structure changed under high calcination temperature (**Fig A5.2 e**). The catalytic performance of catalysts prepared with different calcination temperatures was investigated in a SMX/Oxone batch system. As shown in **Fig A5.2 f**, the degradation efficiency of SMX decreased with increasing of calcination temperature. When the calcination temperature was increased from 300 to 800°C, the SMX removal in 60 min in this system decreased from 92.4% to 24.5%. That could be caused by the lower crystallinity of the catalyst prepared at 300°C, indicating the presence of more defects which is in favor of electron transfer. Meanwhile, the leached metal ions due to the low crystallinity should be also considered (**Table A5.1**). Another reason is the particle aggregation increased with the increase of calcination temperature, resulting a larger particle size (**Figs A5.2 a-d**).

Fig 5.2 displays the N_2 adsorption-desorption isotherm and corresponding pore size distribution (inset) of $CoFe_2O_4$ particle. The sharp distribution of pore diameter around 1.8 nm suggests that the NPs have high monodispersity. The isotherm with hysteresis loop at relatively high pressure of 0.4 - 1.0 indicates the existence of meso-pores to micro-pores generated due

to the accumulation of nanoparticles. The BET specific surface area of the sample was calculated from N_2 isotherms at 77 K, and was found to be as much as about 57.5 m^2 g^{-1}. The single-point total volume of pores was calculated as 0.10 cm^3 g^{-1}. The high BET surface area and low total pore volume strongly supported the fact that the NPs have a nonporous structure with small particles (Li et al., 2010; Senapati et al., 2011), which is in good accordance with the SEM results (**Fig A5.2 a**).

The crystalline structure of $CoFe_2O_4$ was determined by XRD (**Fig 5.2 b**), the diffraction peaks at 35.5°, 53.5° and 62.6° of as-prepared catalyst can be attributed to $CoFe_2O_4$ spinel ferrite (04-007-8945 in the database of PDF-4+2015 RDB), corresponding to (311), (422) and (440).

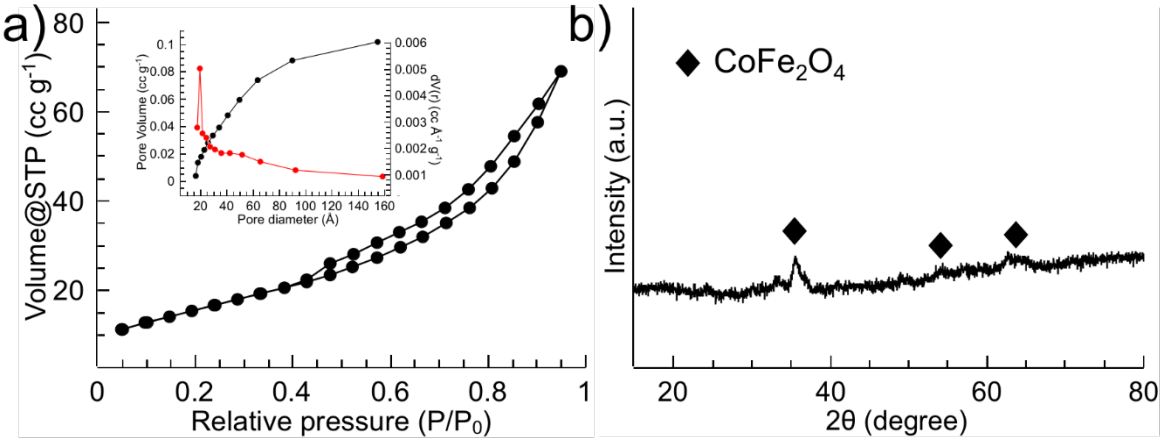

Fig 5.2. N_2 adsorption-desorption isotherms (a) and pore size distribution (inset of a), and XRD patterns of $CoFe_2O_4$ catalyst (calcination temperature of 300°C).

The chemical composition and metal oxidation states of $CoFe_2O_4$ were further investigated using X-ray photoelectron spectroscopy (XPS). The survey spectrum (**Fig 5.3 a**) confirmed the presence of Fe, Co and O. The C in the spectra should come from the carbon tape used for sample preparation. The high-resolution XPS spectra of the Co, Fe and O in $CoFe_2O_4$ are shown in **Figs 5.3 b-d**. The peaks centered at 779.3 eV and 794.8 eV correspond to Co 2p3/2 and Co 2p1/2 (**Fig 5.3 b**), respectively, which reveals that the oxidation state of

cobalt in $CoFe_2O_4$ is +2 (WP et al., 2012). The peaks at 710.1 and 723.7 eV can be ascribed as Fe 2p3/2 and Fe 2p1/2 spin-orbits of $CoFe_2O_4$ (**Fig 5.3 c**), which shows the main oxidation states of Fe is +3 in the $CoFe_2O_4$ lattice. Additionally, one satellite peak appeared at 715.5 eV further verified the existence of Fe^{3+} (Zhu et al., 2017). The peak at 528.3 eV can be assigned to oxygen atoms from $CoFe_2O_4$, while the peak at higher energy (530.5 eV) can be ascribed to chemisorbed or dissociated oxygen, or OH species on the surface of $CoFe_2O_4$ (Xia et al., 2013, p. 3).

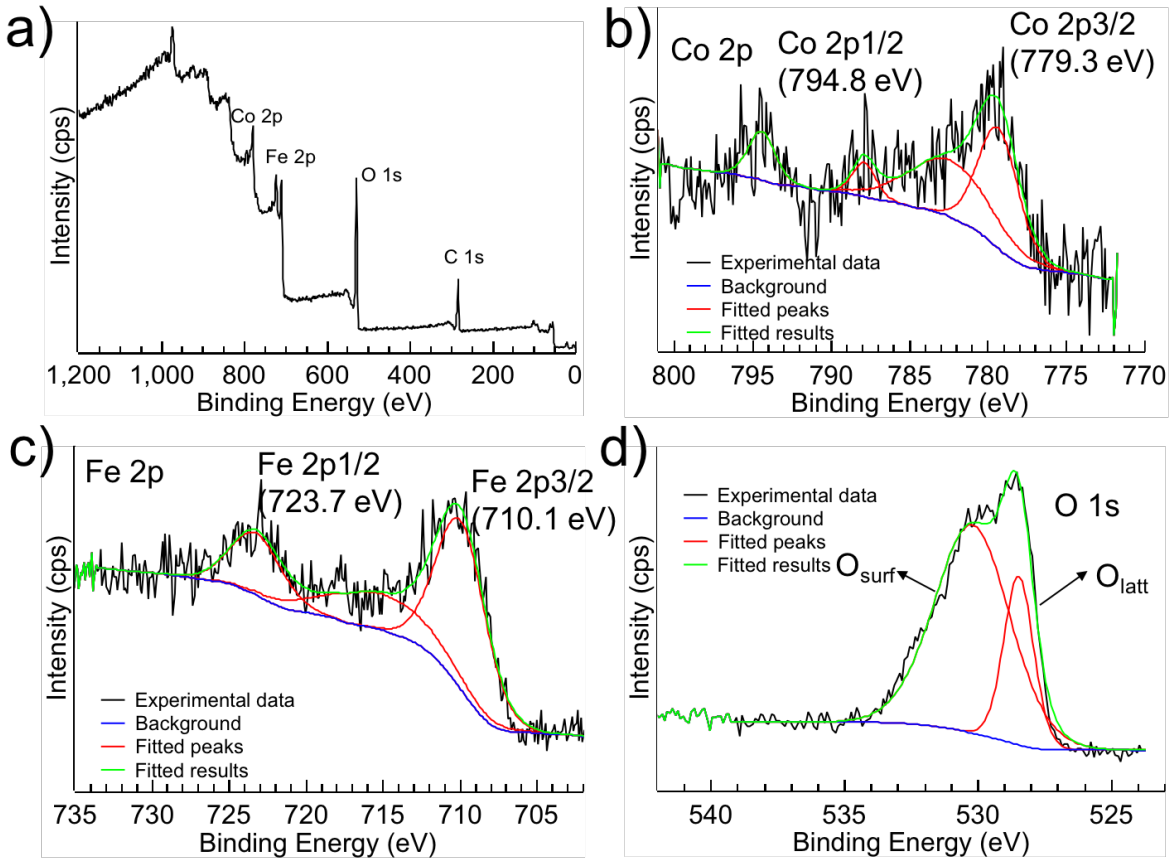

Fig 5.3. The XPS survey spectrum of $CoFe_2O_4$ a) and high-resolution XPS spectra of b) Co 2p, c) Fe 2p and d) O1s.

5.3.2. Characterization of $CoFe_2O_4$ impregnated membrane

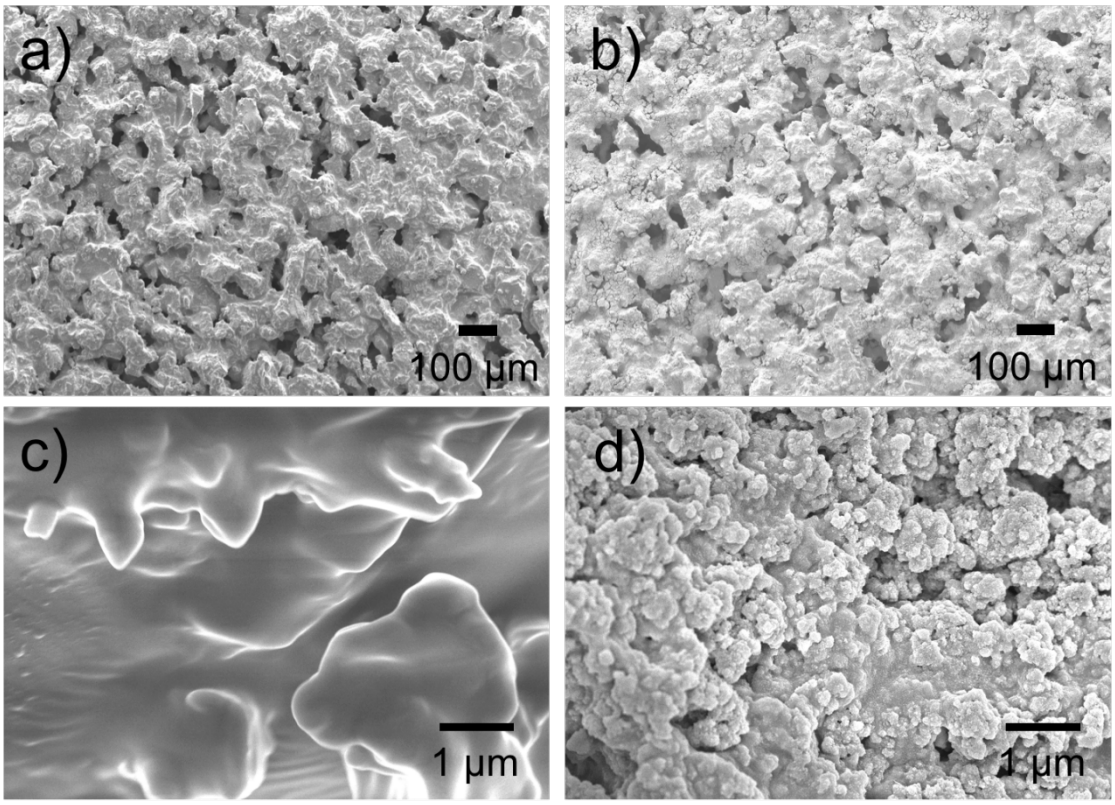

Fig 5.4. Morphologies of membranes: FESEM images of the top surface (a, b) and cross-section (c, d) of various membranes: pristine (a, c) and $CoFe_2O_4$ impregnated (b, d) membrane.

Fig 5.4 shows the top surface and cross-section FESEM images of pristine membrane and $CoFe_2O_4$ impregnated membrane. Compared with pristine membrane, the $CoFe_2O_4$ impregnated membrane shows a much rougher surface (including the top surface and inter pores surface) because of the attachment of $CoFe_2O_4$ (**Fig 5.4**). The results evidence the successfully impregnation of $CoFe_2O_4$ into the whole membrane substrate. To further prove that $CoFe_2O_4$ was impregnated into the Al_2O_3 membrane internal pores, EDX elemental mapping of Co and Fe was conducted for the whole membrane cross section (**Figs 5.5** and **A5.3**). The results indicate that both Fe and Co are distributed homogeneously across the whole $CoFe_2O_4$ impregnated Al_2O_3 membrane. This indicates that the urea-assisted one-step combustion method could be used to prepare the nanocatalyst-functionalized ceramic

membrane in a simple way.

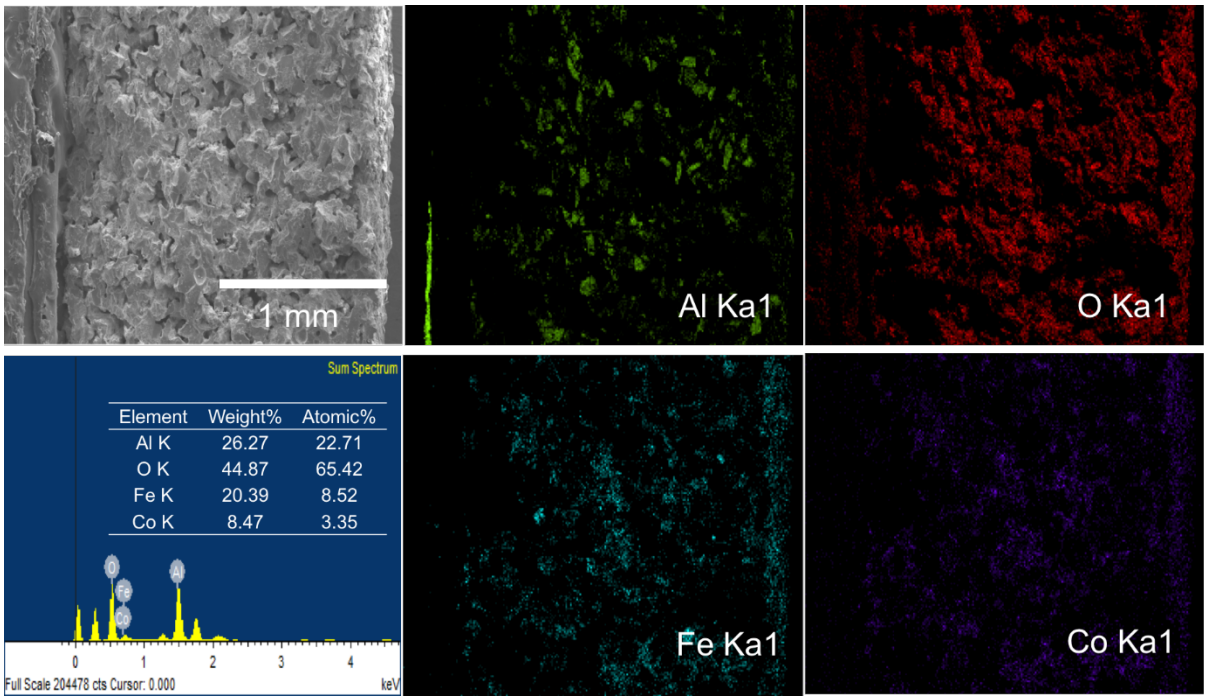

Fig 5.5. SEM-EDX mappings of cross section for the $CoFe_2O_4$ impregnated membrane.

Meanwhile, with the increase of repeated impregnation process from 1 to 5 cycles, catalyst loading amount increased from 0.015 to 0.08 g/g Al_2O_3, accompanying with the decreasing of water permeability from 3402 to 47 LMHB (**Table 5.1**). The decrease of membrane water permeability means that the nanocatalysts attaches on the membrane surface, resulting a much denser skin layer. Meanwhile, with the increase of catalyst loading amount, the characteristic peaks of $CoFe_2O_4$ peak can be identified in the XRD patterns (**Fig A5.4**).

Table 5.1. The catalyst loading amount based on different coating cycles.

Membrane code	Catalyst loading (%)	LMHB	Weight (g)
Pristine	0.0	3402	2.00
#1	1.5	2667	2.03
#3	3.5	226	2.07
#5	8.0	47	2.16

Note: LMHB-pure water flux (L m^{-2} h^{-1} bar^{-1})

5.3.3 Performance evaluation of $CoFe_2O_4$ impregnated membrane

In a batch experiment, the catalytic performance of the $CoFe_2O_4$ impregnated membrane was investigated. Typically, the $CoFe_2O_4$ impregnated membranes with different coating cycles were fully submerged in 50 mL solution of 10 mg L^{-1} SMX. Oxone was then added into the solution to activate the reaction. Solution samples were withdrawn at specified time intervals followed by the addition of methanol to quench the reaction before the further analysis.

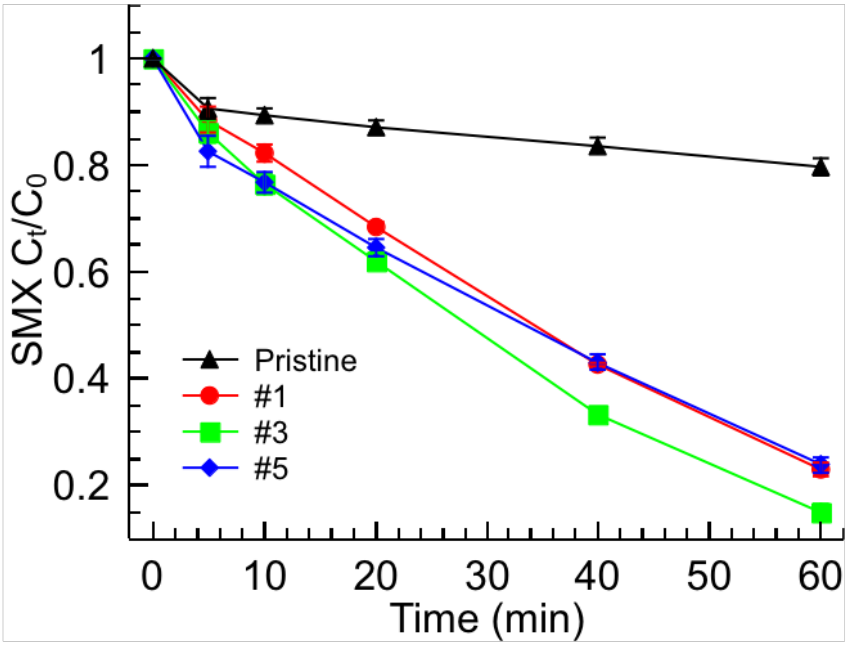

Fig 5.6. The effects of impregnation cycles for $CoFe_2O_4$ impregnated membrane on SMX degradation in the $CoFe_2O_4$/membrane/PMS system. Batch experiment conditions: initial pH = 5, [SMX] = 10 mg L^{-1} and [Oxone] = 0.10 g L^{-1}.

Fig 5.6 shows the contribution of SMX removal by pristine membrane is much slighter compared with that of $CoFe_2O_4$ impregnated membranes. In this study, the catalyst loading amounts are 0.015, 0.035 and 0.08 g/g Al_2O_3 for #1, #3 and #5, respectively, which could be ignored compared with the pristine Al_2O_3 substrate (~ 2 g). Therefore, the surface area difference caused by the catalyst loading was not considered in the study. With increase of $CoFe_2O_4$ loading amount, a higher density of redox active catalytic sites for $SO_4^{\cdot -}$ generation

from PMS activation could be achieved. However, the SMX degradation did not show significant difference with increasing $CoFe_2O_4$ amount, meaning that compared with radical generation process, mass transfer is the rate-determining step in this system.

In the hybrid membrane filtration system, #1 was chosen to investigate the effects of flow rate, PMS dosage and pH on SMX removal efficiency. As shown in **Fig 5.7a**, when the flow rate is set at 0.2 mL min^{-1} with a calculated contact time of 90 s, nearly 100% removal of SMX could be achieved with the Oxone dosage of 0.1 g L^{-1}. While, when the flow rate is increased to 1 mL min^{-1} to shorten the catalytic reaction time to 18 s, the removal efficiency decreases to around 40%. Meanwhile, the removal of SMX by direct membrane filtration (no Oxone) is negligible. A higher PMS dosage increases the probability of PMS and $CoFe_2O_4$ interaction, resulting in a higher SMX degradation rate.

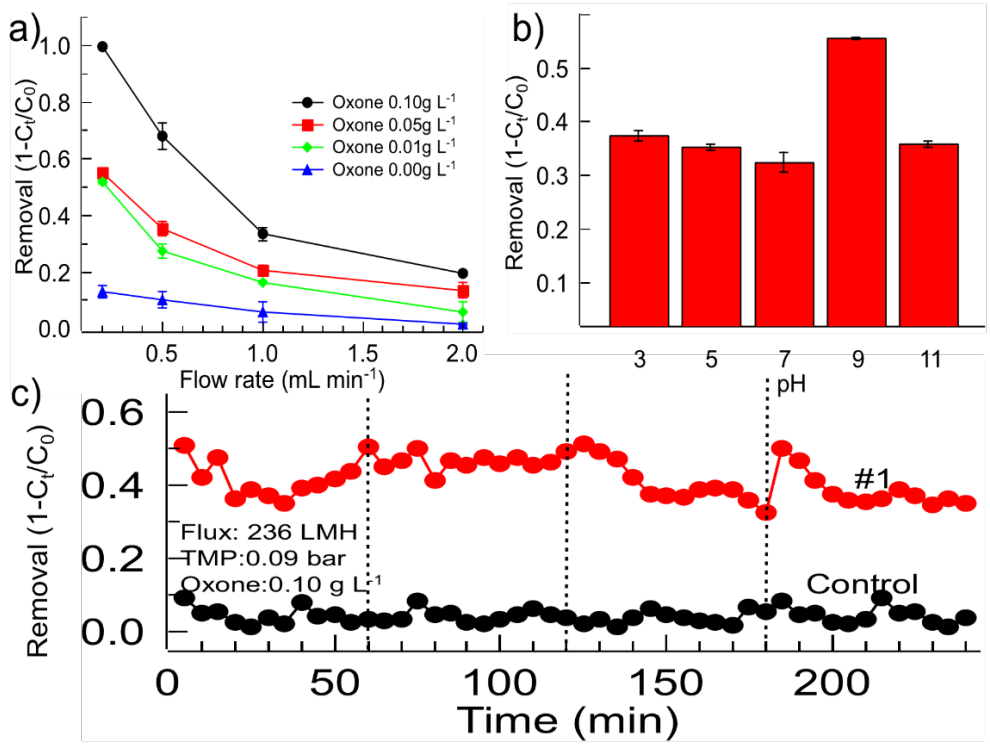

Fig 5.7. The effects of a) flux and Oxone dosage, b) pH and c) durability of $CoFe_2O_4$ impregnated membrane on SMX degradation in the filtration system. Conditions: [SMX] = 10 mg L^{-1}, initial pH = 5 (for a and c) and flow rate = 1 mL min^{-1}, [Oxone] = 0.10 g L^{-1} (for b and c).

Fig 5.7 b shows the effect of initial pH on the SMX removal in the $CoFe_2O_4$/membrane/PMS system. Under acidic condition (pH 3-7), the Oxone stabilization effect promotes the adherence of H^+ to the electronegative peroxide bond (-O-O-) (T. Zhang et al., 2013). Similarly, the surface of the catalyst which consists of abundant hydroxyl groups (-OH) is also protonated ($-OH_2^+$) leading to the positive charged surface (**Fig A5.5 a**) (Ding et al., 2013; Ma et al., 2005). The -OH group has a critical role in Oxone activation process while $-OH_2^+$ has deleterious effect on the overall catalytic activity (Zhang et al., 2010). These factors could lead to the inherent negative effect on the catalytic activity in acidic condition.

Interestingly, when pH value was increased from 9 to 11, the catalytic degradation of SMX in $CoFe_2O_4$/PMS system is inhibited (**Fig 5.7 b**). The increase of pH can raise the amount of negative surface charge of the catalyst as well as SMX molecular (**Fig. A5.5 b**), resulting in the electrostatic repulsion (Bao and Niu, 2015; Zhang et al., 2014) . Meanwhile, since the pK_a of HSO_5^- > 9.4 (Guan et al., 2011), higher pH can also increase the proportion of less oxidative SO_5^{2-} by the deprotonation of PMS (Rani et al., 2009). Another effect of pH is that it can affect the reactive species. When $SO_4^{\bullet-}$ are generated, $^{\bullet}OH$, which can also attack SMX, could be introduced into the system particularly under moderate alkaline condition. However, oxidation potential of $^{\bullet}OH$ decreases linearly with pH and the generated $^{\bullet}OH$ (pK_a = 11.9) becomes unstable and tends to decompose under high pH value.

Durability of membrane could significantly lower the operation cost of water and wastewater treatment plants. A representative #1 membrane was used for 3 treatment cycles of 10 mg L^{-1} SMX solution with the flux of 236 LMH, and the results are shown in **Fig 5.7 c**. A stable SMX removal efficiency could be maintained on $CoFe_2O_4$ impregnated membrane over multiple cycles of 60 min each. In this system, average cobalt ion leaching was recorded as 0.04 mg L^{-1} in the effluent during each treatment cycle. The decrease of SMX removal in each cycle could be explained by the accumulative adsorption of SMX onto/into the membrane,

reducing the density of active catalytic sites. However, upon each cleaning cycle with Oxone for 5 min, more than 95% of the SMX removal efficiency could be recovered, indicating the reusability potential of $CoFe_2O_4$ impregnated membrane via Oxone-assisted self-cleaning. During multiple-cycle experimental run, the permeability flux was maintained at > 98% of the initial flux.

Natural organic matter (NOM) is one type of substances existing in water and plays a number of important roles including controlling the pH balances, governing the mobility of contaminants through adsorption, aggregation and sedimentation, and chelating metals (Bao and Niu, 2015; Kim and Corapcioglu, 2002). HA as one typical model was chosen to investigate the effect of NOM on the degradation of SMX in $CoFe_2O_4$/membrane/PMS system.

As shown in **Fig 5.8 a**, at low concentration of HA (5 ppm), there is a slightly enhancement on the SMX degradation. This could be caused by the sensitizer function of HA to produce various reactive species (Canonica et al., 1995). While with the increasing of HA concentration, the inhibiting effect became more obvious. The inhibition is caused by the attachment of HA on the active sites of catalyst as well as the radical quenching effects to hinder the catalytic process. The results showed that the catalytic performance of $CoFe_2O_4$ might be suppressed in natural water which consists of NOM.

On the other hand, since anions are omnipresent in natural waters, the effects of four common anions in water namely Cl^-, NO_3^-, SO_4^{2-} and CO_3^{2-} on SMX removal in $CoFe_2O_4$/membrane/PMS system were also investigated (**Fig 5.8 b**). The results indicated that SMX degradation rates were almost unchanged (within 5%) with addition of 100 mM Cl^- and NO_3^-, while SO_4^{2-} and CO_3^{2-} showed inhibitive effects (14% and 30%) on the catalytic process.

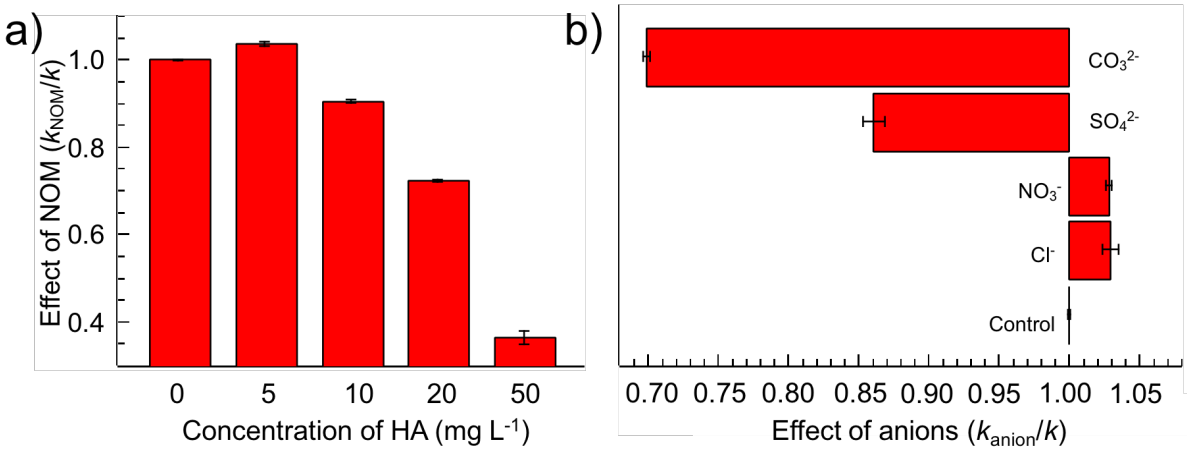

Fig 5.8. Normalized effects of (a) NOM and (b) anions on SMX degradation in the $CoFe_2O_4$/membrane/PMS system. Conditions: initial pH = 5, [SMX] = 10 mg L^{-1}, [Oxone] = 0.10 g L^{-1} and [anions] = 100 Mm.

The slightly higher removal efficiency in presence of Cl^- is caused by the generation of active chlorine species like Cl·, Cl_2·, HOCl and Cl_2 (**Eqs. 5.1-5.5**) (Dodd and Huang, 2004). In previous study, the reaction between PMS and Cl^- to produce OCl^- has been verified (Lente et al., 2009). Also, the degradation of SMX by HOCl/Cl_2 was investigated (Sichel et al., 2011). In this work, HOCl and Cl_2 were produced by the addition of Cl^- into the $CoFe_2O_4$/membrane/PMS system, which enhanced the SMX degradation (Deng et al., 2013b).

$$SO_4^{\bullet-} + Cl^- \rightarrow SO_4^{2-} + Cl^{\bullet} \qquad k = 2.7 \times 10^8\ M^{-1}s^{-1} \qquad \textbf{(5.1)}$$

$$Cl^{\bullet} + Cl^- \rightarrow Cl_2^{\bullet-} \qquad k = 8 \times 10^9\ M^{-1}s^{-1} \qquad \textbf{(5.2)}$$

$$Cl^{\bullet} + OH^- \rightarrow {}^{\bullet}OH + Cl^- \qquad k = 1.8 \times 10^{10}\ M^{-1}s^{-1} \qquad \textbf{(5.3)}$$

$$Cl_2^{\bullet-} + OH^- \rightarrow HOCl^{\bullet-} + Cl^- \qquad k = 4.5 \times 10^7\ M^{-1}s^{-1} \qquad \textbf{(5.4)}$$

$$Cl_2^{\bullet-} + Cl_2^{\bullet-} \rightarrow Cl_2 + 2Cl^- \qquad k = 2.1 \times 10^9\ M^{-1}s^{-1} \qquad \textbf{(5.5)}$$

$$SO_4^{\bullet-} + NO_3^- \rightarrow SO_4^{2-} + NO_3^{\bullet} \qquad k = 2.1 \times 10^6\ M^{-1}s^{-1} \qquad \textbf{(5.6)}$$

$$SO_4^{\bullet-} + SO_4^{2-} \rightarrow S_2O_8^{2-} + e^- \qquad k = 4.4 \times 10^8\ M^{-1}s^{-1} \qquad \textbf{(5.7)}$$

$$SO_4^{\bullet-} + HCO_3^- \rightarrow H^+ + CO_3^{\bullet-} + SO_4^{2-} \qquad k = 9.1 \times 10^6\ M^{-1}s^{-1} \qquad \textbf{(5.8)}$$

$$^{\bullet}OH + HCO_3^- \rightarrow CO_3^{\bullet-} + H_2O \qquad k = 1.0 \times 10^7\ M^{-1}s^{-1} \qquad (\mathbf{5.9})$$

The competitive adsorption of anions and SMX on the surface of catalyst can result in the blockage of the active sites on the catalyst surface. Meanwhile, $SO_4^{\bullet-}$ generated in $CoFe_2O_4$/membrane/PMS system could be scavenged by NO_3^- through electron transfer reaction (**Eq. 5.6**). However, in this work, NO_3^- shows a slight promotional effect on the removal of SMX, indicating that NO_3· can better oxidize SMX in $CoFe_2O_4$/membrane/PMS system because of the selectivity to SMX (Venkatachalapathy and Ramamurthy, 1996).

The inhibition effects of SO_4^{2-} in this system was observed which is caused by its scavenger effect for $SO_4^{\bullet-}$ (**Eq. 5.7**) (Shah et al., 2013). We need to mention that when CO_3^{2-} is added to the solution, it would proceed to react due to the hydrolysis of CO_3^{2-} with H_2O to achieve the CO_3^{2-} - HCO_3^- system. Both CO_3^{2-} and HCO_3^- are scavengers of hydroxyl and sulfate radicals. They remarkably react with the sulfate and hydroxyl radicals to generate much less reactive radicals such as $CO_3^{\bullet-}$ and $HCO_3^{\bullet}$ (**Eqs. 5.8-5.9**) (Tan et al., 2013). In addition, the pH value increased with increasing CO_3^{2-} concentration and the radicals start to decompose under higher pH values, resulting in the decrease of SMX removal efficiency (**Fig 5.7 b**).

5.3.4. Proposed SMX degradation mechanism

Since the contributions of SMX degradation by direct Oxone oxidation and catalyst adsorption are negligible (**Fig A5.6**), the radical-based oxidation process was deduced as the mechanism of SMX degradation. Previous investigations have pointed out that in the $CoFe_2O_4$/PMS system, $SO_4^{\bullet-}$ and $^{\bullet}OH$ can always be identified as the main reactive species (Du et al., 2016). Therefore, an attempt with EPR experiments was made to verify the presence of $SO_4^{\bullet-}$ and $^{\bullet}OH$ in $CoFe_2O_4$/PMS system. As shown in **Fig 5.9 a**, there were no obvious characteristic signals present in the EPR spectra of experiments conducted with DMPO + Oxone + SMX system. However, in the presence of $CoFe_2O_4$, the characteristic signals of 5,5-dimethyl-2-pyrrolidone-N-oxyl (DMPOX) with heptet were detected, which was formed by

the oxidation of DMPO via $^{\bullet}OH$ (X. Chen et al., 2018; Zalibera et al., 2009). When BMPO was used as the spin trapping agent (**Fig 5.9 b**), seven-line spectrum can be observed, which can be assigned to 5-tert-butoxycarbonyl-5-methyl-2-oxo-pyrroline-1-oxyl (BMPOX), a reaction product of BMPO with $SO_4^{\bullet-}$ (Yanbin Wang et al., 2017).

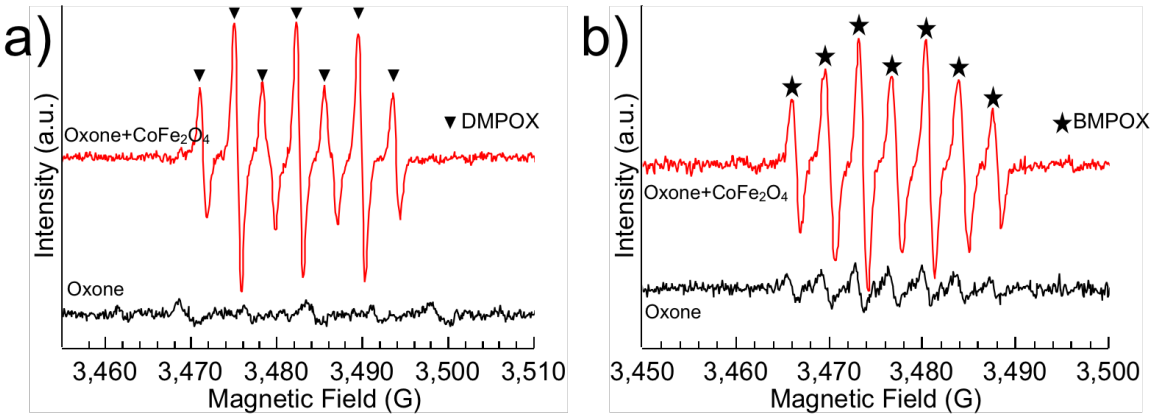

Fig 5.9. EPR spectra obtained from Oxone oxidative process and $CoFe_2O_4$ activated Oxone oxidation process in the presence of (a) DMPO and (b) BMPO. (Reaction conditions: [Oxone] = 0.10 g L^{-1}, [SMX] =10 mg L^{-1}, [$CoFe_2O_4$] = 0 or 2 g L^{-1}, [DMPO] = 100 mM, [BMPO] = 25 mM, reaction time = 3 min).

Furthermore, it is widely accepted that alcohols with an α-hydrogen readily react with both $SO_4^{\bullet-}$ and $^{\bullet}OH$ (1.6 - 7.7 × 10^7 M^{-1} s^{-1} and 1.2 - 2.8 × 10^9 M^{-1} s^{-1}, respectively), while those without α-hydrogen react more easily with $^{\bullet}OH$ (3.8 - 7.6 × 10^8 M^{-1} s^{-1}), but in a much more slower reaction rate with $SO_4^{\bullet-}$ (4.0 - 9.1 × 10^5 M^{-1} s^{-1}) (Feng et al., 2016). To identify the major reactive oxygen species that were responsible for catalytic degradation of SMX in natural pH, *tert*-butanol without α-hydrogen was chosen as the scavenger for $^{\bullet}OH$ while methanol (MeOH) with α-hydrogen was used as a quenching agent for both $^{\bullet}OH$ and $SO_4^{\bullet-}$ (Xu and Wang, 2011) in a batch system.

As shown in **Fig A5.7 a**, the inhibition of MeOH on SMX degradation is dependent on their initial concentrations. The inhibition is not significant at low MeOH concentrations

because the hydroxyl methyl radical ($^{\bullet}CH_2OH$) produced by the reaction of methanol with $SO_4^{\bullet-}$/$^{\bullet}OH$ could stimulate the decomposition of Oxone towards radicals and alleviate the inhibition of MeOH (Guan et al., 2011). Further increasing the concentration of MeOH to 100 mM, the removal of SMX decreased to 74.9%, with the rate constant decreasing from 4.7×10^{-2} to 1.8×10^{-2} min^{-1}. Compared with MeOH, *tert*-butanol plays a much less aggressive role in inhibiting SMX degradation (**Fig A5.7 b**), which shows that $^{\bullet}OH$ played a much less important role compared with that of $SO_4^{\bullet-}$ under this condition (**Fig 5.10 a**).

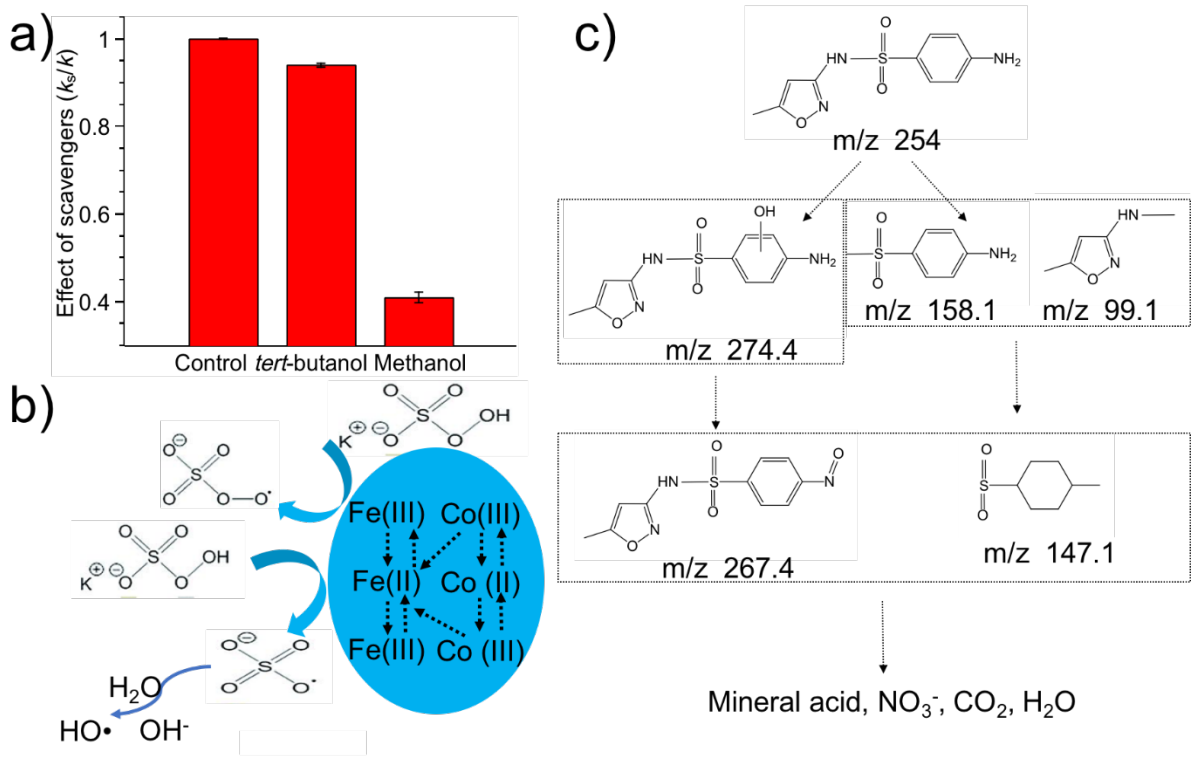

Fig 5.10. The effects of scavengers on SMX degradation (a, *tert*-butanol 100 mM, Methanol 100 mM); the radical generation process (b) and the proposed degradation pathway of SMX (c, initial pH = 5, [SMX] = 10 mg L^{-1}, [Oxone] = 0.10 g L^{-1}, [$CoFe_2O_4$] = 0.2 g L^{-1} and reaction time = 60 min.

The radical generation process ($^{\bullet}OH$ and $SO_4^{\bullet-}$) is shown in **Fig 5.10 b**. The redox cycles of Co (II)/Co (III) and Fe (II)/Fe (III) are responsible for evolution of sulfate radicals based on

the **Eqs. 2.2-2.4**. Further the sulfate radicals can generate hydroxyl radical by reacting with H_2O or OH^- (**Eq. 2.1**). Besides, the interconversion among Fe^{2+}/Fe^{3+} and Co^{3+}/Co^{2+} (**Eq. 2.12**) makes the catalyst more effective compared to respective single metal oxides.

Based on the metal ions leaching results (**Table A5.1**), it shows the surface active Co^{2+} should play a critical role in the decomposition of O-O bond in Oxone to generate sulfate radicals. Meanwhile, the active Co^{2+} can react with hydroxyl group to form Co-OH complexes, which would further react with HSO_5^- to generate sulfate radicals (**Eqs. 2.5-2.6**) (Shi et al., 2014). The transformation from Co^{2+} to Co^{3+} could be well demonstrated by the difference of XPS Co2p spectra before and after reaction. As shown in Fig 5.3b, the Co 2p3/2 peak (centered at 779.3 eV) of fresh $CoFe_2O_4$ was attributed to the Co^{2+}. However, a new component (785.3 eV) occurred after the oxidation reaction, which was ascribed to the Co^{3+} in octahedral sites (Fig A5.8) (L. Chen et al., 2018a; Zhou et al., 2008).

The TOC detection result showed that the TOC reduction was approximately 20% after 60 min reaction, which was much less than the SMX removal efficiency (92.4%). This result indicated that SMX mineralization occurred during the catalytic degradation, whereas most of SMX molecules were probably transformed into other intermediates rather than being completely oxidized to CO_2 and H_2O. Meanwhile, the concentration of NO_3^- detected in the reaction solution after 60 min achieved to 1.3 mg L^{-1}, around 4 times higher than the initial one of 0.3 mg L^{-1}, evidencing the generation of NO_3^- in the catalytic process.

To explore the intermediate products and degradation pathway of SMX, LC/MS/MS was utilized via the ES (+) mode (**Fig A5.9**). Peaks at m/z 99.1, 147.1, 158.1, 267.4 and 274.4 were detected. As shown in **Fig 5.10 c**, the degradation happens with the cleavage of sulfonamide bond (m/z 99.1 and 158.1) as well as the formation of mono-hydroxylated derivative (m/z 274.4). Subsequently, the electron transfer reaction between $SO_4^{\bullet-}$ and the amine group can form nitro-SMX molecule (m/z 267.4) (Ji et al., 2015). The radicals can attack the C=C to form

C-C (m/z 147.1) followed by the formation of inorganic ions (NO_3^-) and mineral acid via ring opening reactions.

5.4. Conclusions

This study investigated the activation of PMS by $CoFe_2O_4$ impregnated Al_2O_3 ceramic membrane to degrade SMX in a membrane filtration system. It is the first report on the one-step combustion synthesis of $CoFe_2O_4$ impregnated membrane and the utilization of SMX degradation in an integrated continuous system. Based on the results presented, the following conclusions are drawn:

1) A robust and uniform $CoFe_2O_4$ impregnated membrane could be successfully prepared via a urea-assisted one-step combustion method.
2) The pure water permeability flux can maintain at ~ 3000 L m^{-2} h^{-1} bar^{-1} (LMHB) with the catalyst loading amount of 0.015 g/g Al_2O_3.
3) The $CoFe_2O_4$ impregnated membrane could be applied in an integrated continuous filtration system and the SMX removal could achieve at nearly 100% at the contact time of 90 s.
4) The $CoFe_2O_4$ impregnated membrane shows a great durability potential via Oxone-assisted self-cleaning as well as great tolerance at a wide pH range (3-11), existence of NOM and different anions.
5) The degradation of SMX started from the cleavage of sulfonamide bond and the formation of mono-hydroxylated derivative, in which the major reactive radical is sulfate radical in natural pH condition.

Overall, the novel $CoFe_2O_4$ impregnated membrane exhibits a promising prospect for numerous catalytic application. Meanwhile, the urea-assisted one-step combustion is a promising method for impregnation of nanocatalysts into ceramic membrane pores.

CHAPTER 6 ELUCIDATION OF STOICHIOMETRIC EFFICIENCY, RADICAL GENERATION AND TRANSFORMATION PATHWAY DURING CATALYTICALLY OXIDATION OF SULFAMETHOXAZOLE VIA PEROXYMONOSULFATE ACTIVATION

6.1 Introduction

As described in the previous chapters, sulfamethoxazole (4-amino-N-(5-methyl-3-isoxazolyl)-benzene sulfonamide, SMX) is one kind of widely used antibiotics due to its low cost and broad-spectrum antimicrobial ability (Jansomboon et al., 2016). The uncontrolled usage of SMX can have an undesired chronic effect on ecological system by inducing the appearance of antibiotic-resistant bacteria and genes (Rizzo et al., 2013). To date, SMX has been detected in various municipal sewage treatment plants, hospital effluents, surface water and even drinking water system (Godfrey et al., 2007; Lindberg et al., 2004; Nikolaou et al., 2007; Segura et al., 2009). Thus, it is necessary to conduct a comprehensive study for its transformation fate in the environment.

Generally, SMX would be treated by various advanced oxidation processes because it cannot be removed effectively by the conventional treatment processes/technologies due to their biorecalcitrance (Alexy et al., 2004; Ryan et al., 2011). In recent years, sulfate radical-based advanced oxidation process (SR-AOP) has emerged as a potential solution for removing persistent organic pollutants in water (Zhang et al., 2015) due to its high redox potential of 2.60, wide pH flexibility (pH 1-9) (Fang et al., 2012) and high selective oxidation ability via electron transfer (Eberson, 1982b; Hayon et al., 1972; Oh et al., 2016). It has been proven that the $SO_4^{\bullet-}$ radicals can be generated from peroxymonosulfate (PMS) via various activation methods (e.g., thermal, ultraviolet irradiation, ultra-sonication and catalytic activation) (Ghanbari and Moradi, 2017; Oh et al., 2017).

Due to the advantages of mix metal oxides (Refer to Chapter 5), they have been synthesized and used for PMS activation. In a recent study, the Co/Fe bimetallic oxides with different stoichiometric ratios were synthesized for the activation of PMS to degrade norfloxacin, in which surface hydroxyl groups were proposed as the reason for higher efficiency and the sulfate radical dominated the degradation process (L. Chen et al., 2018b). Yu et al. reported the synergism between Mn and Fe in a bimetallic oxide ($Mn_{1.8}Fe_{1.2}O_4$) for PMS activation for Bisphenol A (BPA) degradation, in which Fe works as the main adsorption site while Mn is the active site to generate radicals (Huang et al., 2017). Meanwhile, bimetallic oxides have also been used in PMS activation for SMX degradation (Bao et al., 2018a; Oh et al., 2017). However, the transformation mechanism of SMX especially the non-radical transformation pathway involved in this system is still unclear. Furthermore, the stoichiometric efficiencies of catalysts have rarely been calculated and reported.

Herein, in this chapter, a comprehensive transformation of SMX in PMS system in the presence of Co/Fe bimetallic oxides was explored. The SMX transformation pathways (i.e., non-radical pathway and radical pathway) as well as PMS activation mechanism were investigated. Meanwhile, the stoichiometric efficiencies of the as-prepared catalysts were calculated for the first time. Furthermore, the radical generation and electron transfer mechanism in the catalytic oxidation system were proposed.

6.2 Experimental Section

6.2.1 Chemicals and materials

The same chemicals and materials used was listed in **Section 3.2.1, Section 4.2.1** and **Section 5.2.1**. Nitrobenzene (NB, $C_6H_5NO_2$), benzoquinone (BQ, $C_6H_4O_2$), phenol (C_6H_6O) and sodium azide (NaN_3) were purchased from Sigma-Aldrich. 2,2,6,6-tetramethylpiperidine (TEMP) was provided by Merck.

6.2.2 Nano-bimetallic Co/Fe oxides preparation and characterization

The nano-bimetallic Co/Fe oxides were synthesized via a novel one-step solution combustion method. In brief, a predetermined amount of $Co(NO_3)_2 \bullet 6H_2O$ and $Fe(NO_3)_3 \bullet 9H_2O$ were first dissolved in water followed by the addition of urea as the reductant. The detailed sample preparation is shown in **Table A6.1**. The as-prepared solutions were treated in a furnace at 400°C for 1 h to get the catalysts. The resulting catalysts are named as φ = x:y, where x:y is the molar ratio of Co and Fe.

The morphological and textural properties of the as-prepared catalysts were examined with a field emission scanning electron microscope (FESEM, JSM-7600F, JEOL, Japan) and X-rays diffractometer (XRD, Bruker D8 Advance) with a monochromated high intensity Cu-K_α (λ =1.54 Å) radiation. The specific surface areas of the catalysts were measured using the Brunauer-Emmett-Teller (BET) N_2 adsorption-desorption method with Quantachrome Autosorb -1 Analyzer. The valence states of the constituent elements were determined using X-ray photoelectron spectroscopy (XPS) (Kratos Axis Supra, Shimadzu) and the surface bonding properties of the catalysts and PMS were characterized using Fourier transform infrared spectroscopy (FTIR, Perkin Elmer).

6.2.3 Decomposition experiments

The SMX decomposition experiments were conducted in a batch system at room temperature unless otherwise stated. A certain amount of the as-prepared catalysts (10 mg) was dispersed into the SMX solution (40 μM, 50 mL). After that, a desired volume of PMS stock solution (40 mM) was added into the mixture to initiate the degradation process. At pre-determined sampling intervals, the mixture was collected and filtered through a 0.45 μm PTFE filter immediately. To quench the residual radicals, an equal volume of methanol was injected into the filtered samples before the detection (Oh et al., 2014; Yun et al., 2018). The initial pH of SMX solution was 5 and was adjusted with 0.1 M NaOH solution if necessary. Meanwhile,

the quenching experiments were carried out by adding different scavengers prior to the PMS (**Table A6.2**). The PMS self-decomposition experiments were conducted in the same condition while without SMX.

6.2.4. Determination of chemicals and degradation products

The determination of SMX and its degradation products was described in **Section 3.2.5** and **Section 4.2.5**.

6.3 Results and discussion

6.3.1 Characterization of nano-bimetallic Co/Fe oxides

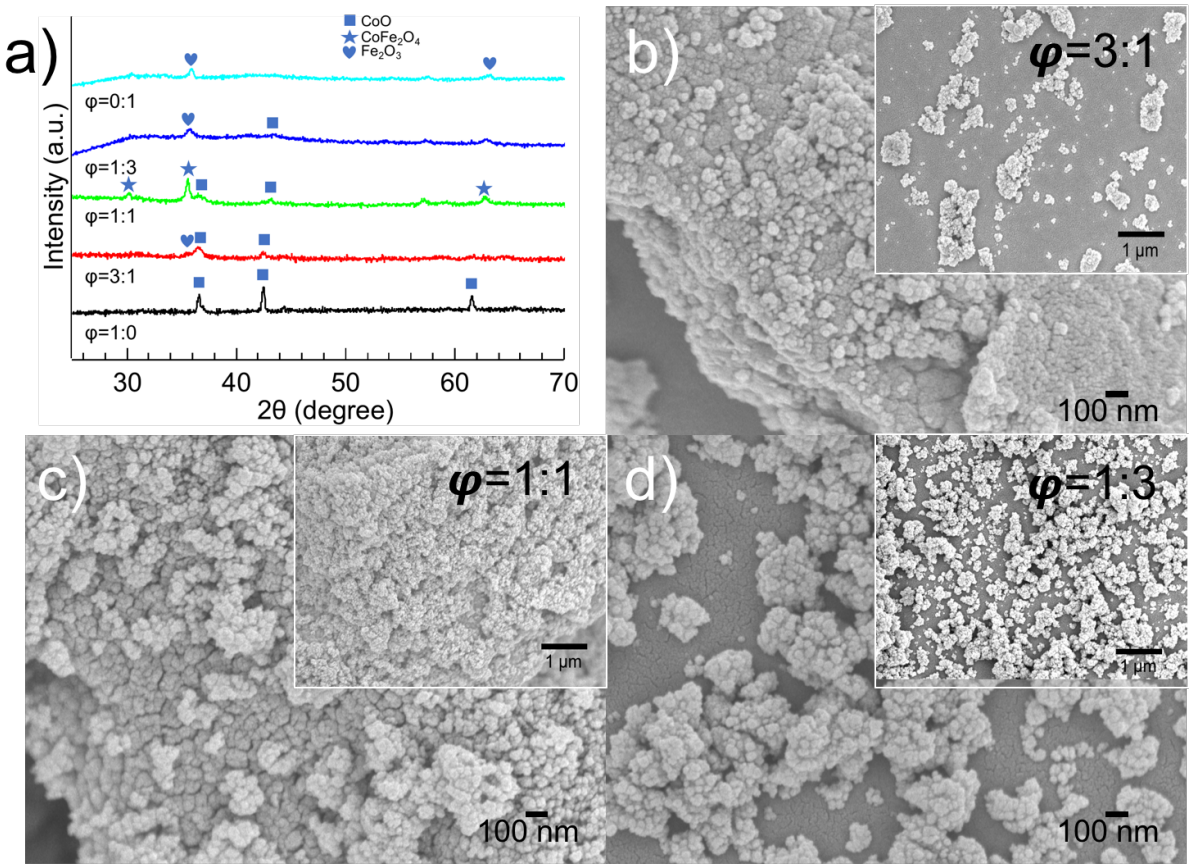

Fig 6.1. XRD patterns and FESEM images of nano-bimetallic Co/Fe oxides.

In the present study, three bimetallic oxides with different Co/Fe stoichiometric ratios (φ) were prepared (**Fig 6.1**). Meanwhile, the pure cobalt oxide and iron oxide were also prepared with a similar method for comparison (**Fig A6.1**). **Fig 6.1 a** shows the XRD patterns of the as-

prepared samples. The single metal oxides were identified as CoO (PDF. No. 96-154-1663) and Fe_2O_3 (PDF. NO. 96-901-2693), respectively. In all the bimetallic oxides, cobalt and iron would share the octahedral sites in the structure, resulting a mixed composites (Costa et al., 2006). Meanwhile, all particles consisted of irregular spherical nanoparticles with an average diameter of 50-200 nm (**Figs 6.1 b-d**). The nano-sized structures could cause the broad peaks in XRD patterns (**Fig 6.1 a**). Pure cobalt oxide shows a wire-like morphology while iron oxide shows a diamond shape with larger diameter (**Fig A6.1**). For bimetallic oxides, with the increasing of Co amount, the morphology changed from nanoparticles to rhombic nanosheets, which indicated that the stoichiometric ratio of Co/Fe affects the morphology of the products. Meanwhile, the bimetallic oxides show more porous and finer particles with increasing of Fe amount. The corresponding EDX spectra clearly demonstrated the presence of Fe, Co and O in the catalysts and the atomic ratios were close to the theoretical Co/Fe ratios, which were calculated as 3.09, 1.23 and 0.35 for φ=3:1, φ=1:1 and φ=1:3, respectively (**Fig A6.2**).

6.3.2 Catalytic decomposition of PMS in the presence of nano-bimetallic Co/Fe oxides

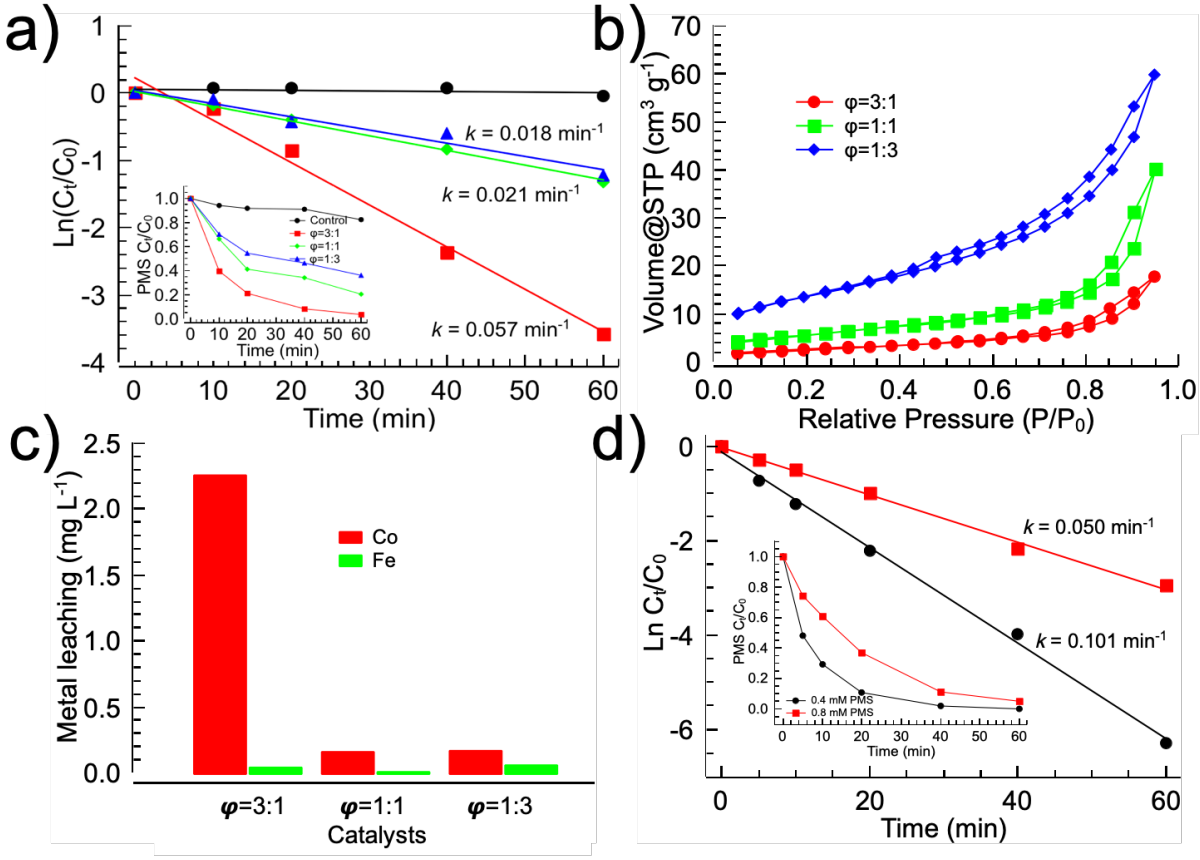

Fig 6.2. a) Catalytic decomposition of PMS in the presence of different nano-bimetallic Co/Fe oxides; b) the surface areas of as-prepared nano-bimetallic Co/Fe oxides; c) metal leaching test for different nano-bimetallic Co/Fe oxides and d) the PMS decomposition in homogeneous system in the presence of Co^{2+} [Experimental Conditions: Catalyst = 0.2 g L^{-1} and PMS = 0.4 mM for a, Co^{2+} = 2 mg L^{-1} for d].

As shown in **Fig 6.2 a**, the PMS self-decomposition rate without catalyst was negligible (< 5%). In contrast, the heterogeneous system with nano-bimetallic Co/Fe oxides exhibited a significantly accelerated PMS decomposition rate, with the $k_{obs\text{-}PMS}$ of 0.057, 0.021, 0.018 min^{-1} for φ = 3:1, 1:1 and 1:3, respectively. To further examine the effect of different φ on the PMS decomposition rate, the results were fitted with the following kinetics:

$$d\,[PMS] / d\,t = - k_{obs\text{-}PMS}\,[PMS] = - k_{SA\text{-}PMS}\,C_S\,[PMS] = - k_{SA\text{-}PMS}\,(S_S\,C)\,[PMS] \qquad \textbf{(6.1)}$$

where $k_{obs\text{-}PMS}$ represents the observed pseudo-first-order rate constant (min^{-1}) in PMS decomposition, $k_{SA\text{-}PMS}$ is the PMS decomposition rate constant normalized with the specific surface area ($L\ m^{-2}\ min^{-1}$), Cs is the surface area of catalyst in solution ($m^2\ L^{-1}$), S_S is the specific surface area of catalyst ($m^2\ g^{-1}$), and C is the catalyst loading amount ($g\ L^{-1}$). The calculated results are shown in **Table 6.1**. The $k_{SA\text{-}PMS}$ of the catalysts followed the order φ = 3:1 > φ = 1:1 > φ = 1:3. The nano-bimetallic Co/Fe oxides with φ = 3:1 has the highest PMS decomposition rate, but it also shows the highest Co leaching (**Table 6.1**). Therefore, the higher PMS decomposition rate for φ = 3:1 could be resulted from the contribution of leached Co^{2+} in the solution instead of that of the catalyst. To verify this assumption, a homogeneous control experiment with addition of Co^{2+} was conducted, which shows that Co^{2+} in the homogeneous system possesses high activity in PMS decomposition (**Fig 6.2 d**). For nano-bimetallic Co/Fe oxides with φ = 1:1 and φ = 1:3, the metal leaching was much lower, which might be caused by the formation of stronger interaction between Co and Fe (**Table 6.1**). In the present study, the nano-bimetallic Co/Fe oxides with φ = 1:1 was selected for use in the following section. Based on the EDX results, the chemical formula for φ = 1:1 is $CoFeO_{2.5}$, which could be a composite of $CoFe_2O_4$ and CoO (**Fig A6.2**).

Table 6.1. Summary on the kinetic studies and metals leaching in PMS decomposition in presence of different nano-bimetallic Co/Fe oxides [PMS = 0.4 mM, reaction time = 60 min].

Catalysts	$k_{obs\text{-}PMS}$ (min^{-1})	$k_{SA\text{-}PMS}$ ($L\ m^{-2}\ min^{-1}$)	Cs ($m^2\ L^{-1}$)	BET S_S ($m^2\ g^{-1}$)	C ($g\ L^{-1}$)	Co ($mg\ L^{-1}$)	Fe ($mg\ L^{-1}$)
φ=1:0	0.138	--	--	< 2	0.2	15.9	--
φ=3:1	0.057	3.0×10^{-2}	1.9	9.5	0.2	2.26	0.04
φ=1:1	0.021	5.2×10^{-3}	4.1	20.3	0.2	0.16	0.01
φ=1:3	0.018	1.8×10^{-3}	9.8	49.2	0.2	0.17	0.06

φ=0:1	0.002	2.9×10^{-3}	0.7	3.5	0.2	--	0.01

6.3.3 Catalytic performance of $CoFeO_{2.5}$ in PMS activation for SMX degradation

Previously, it was reported that in the presence of organic contaminants, the radical chain decomposition of persulfate increased (Liu et al., 2014). However, in the present study, it was found that with the presence of SMX, the PMS decomposition rate decreased (**Fig 6.3 a**). As shown in **Fig 6.3 b**, with the increase of SMX concentration from 0-40 μM, the rate constant *k* for PMS decomposition decreased from 0.021 to 0.007 min^{-1}, which could be explained by the multiple reactions including radical and non-radical oxidation in this system (**Fig 6.3 e**). Because of the chemical structure of SMX, the 8N atom on the benzene ring and 7S atom of the sulfonamide group could be attacked by PMS via the electrophilic and nucleophilic reactions (Boreen et al., 2004; Yin et al., 2018). The decrease of PMS decomposition rate in the presence of SMX indicated that the radical generation was inhibited (reaction to the right side of **Fig 6.3 e**), which verified the existence of non-radical oxidation pathway. As shown in Fig 3e, when PMS was consumed by SMX directly, the reaction for radical generation would be inhibited, resulting a lower PMS decomposition rate (**Fig 6.3 b**).

Based on these observations, other organics might also affect the PMS decomposition. To investigate the effect of natural organic matters (NOMs) on the PMS decomposition and SMX degradation, humic acid (HA) with different concentrations (0-20 mg L^{-1}) was added in the system as a surrogate of NOM. Results showed that with addition of HA, the degradation of SMX decreased which could be attributed to radical scavenging by HA (**Fig A6.3 a**). However, the addition of HA also increased PMS consumption (**Fig A6.3 b**). These results indicated that SMX degradation efficiency would be suppressed in the natural environment, especially in the presence of NOM.

The degradation efficiency of SMX with initial concentration range of 10-40 μM is shown in **Fig A6.4**. Before addition of PMS, the removal of SMX is negligible (±2% in 60 min). This

indicates that adsorption of SMX by the catalyst is negligible. Therefore, the removal of SMX in the PMS/$CoFeO_{2.5}$ system was caused by its degradation instead of adsorption. Results in **Fig A6.4** show that the degradation rate decreases with increased SMX initial concentration. To gain a better understanding on SMX transformation pathway in PMS/$CoFeO_{2.5}$ system, a higher initial concentration of 40 µM was chosen for the following experiments.

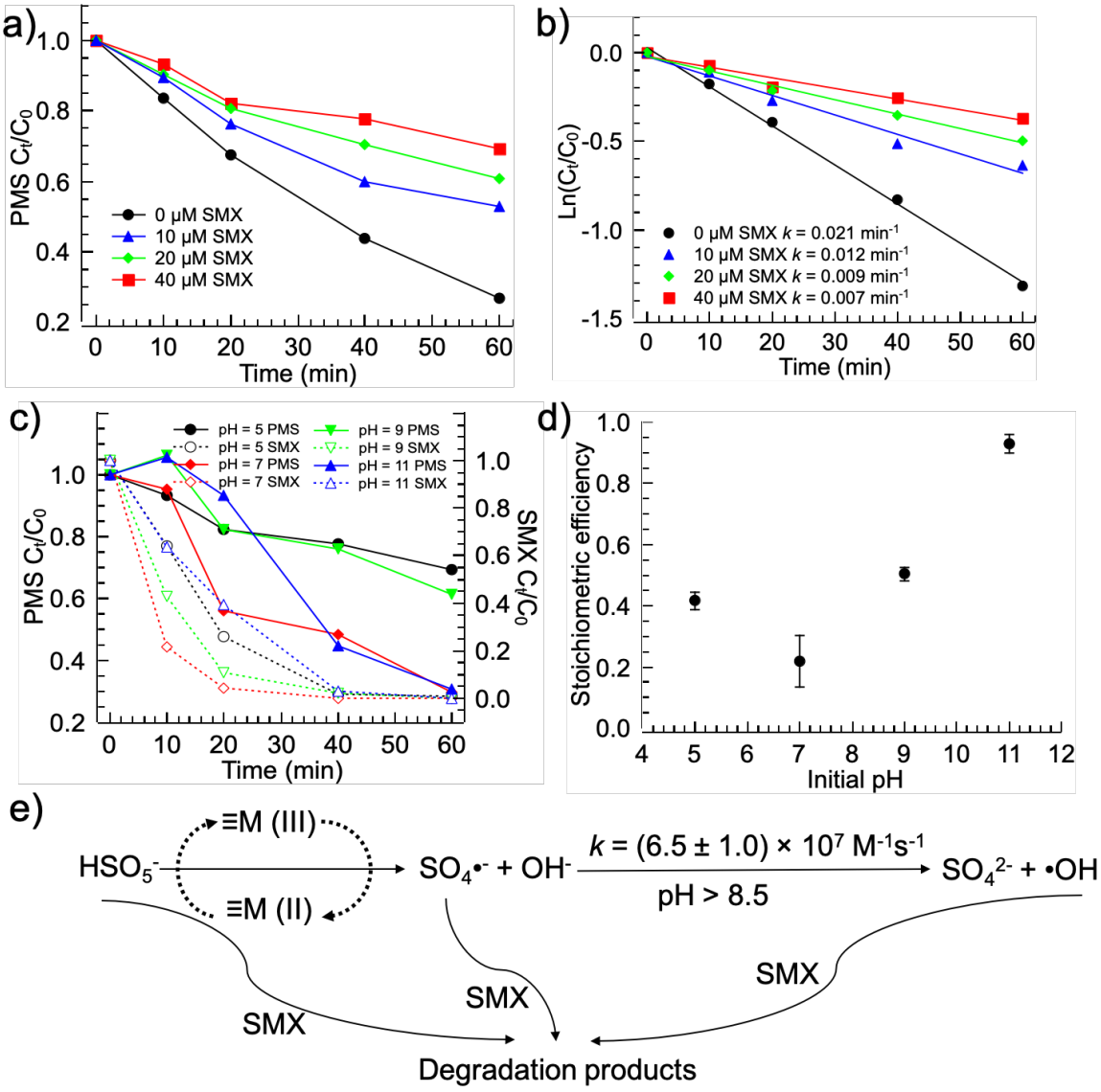

Fig 6.3. a-b) PMS decomposition with/without SMX in the presence of $CoFeO_{2.5}$; c-d) effect of pH on PMS and SMX degradation as well as the calculated stoichiometric efficiencies and e) the possible reactions in PMS/$CoFeO_{2.5}$/SMX system [Experimental Conditions: $CoFeO_{2.5}$ = 0.2 g L^{-1}; PMS = 0.4 mM; pH = 5 for a and b; SMX = 40 µM for c].

The stoichiometric efficiency, which is defined as the number of moles of SMX oxidized for every mole of PMS activated in the presence of $CoFeO_{2.5}$ is calculated for different pH values.

$$\eta = \Delta [SMX] / \Delta [PMS] \quad (\mathbf{6.2})$$

Fig 6.3 d shows that the stoichiometric efficiency (calculated at the reaction time of 20 min with the initial SMX concentration of 40 μM) increased with increasing initial pH value except pH 5. At pH 7, SMX degradation shows the highest reaction rate (**Fig 6.3 c**), while the stoichiometric efficiency is lower than that of pH 9 and 11 due to the high consumption of PMS at pH 7 (**Eq. 6.2**). As shown in **Fig 6.3 e**, SMX could be oxidized by PMS via non-radical pathway ($^1O_2$ oxidation/direct PMS oxidation) (Yin et al., 2018), the consumption of PMS would inhibit the radical generation process due to the limiting PMS concentration (Oh et al., 2016). Meanwhile, SMX can also react with radicals produced by PMS decomposition, which would accelerate the radical generation (**Fig 6.3 e**). Furthermore, sulfate radical generated via PMS decomposition would be transformed to hydroxyl radical at high pH values, which would further increase the decomposition of PMS.

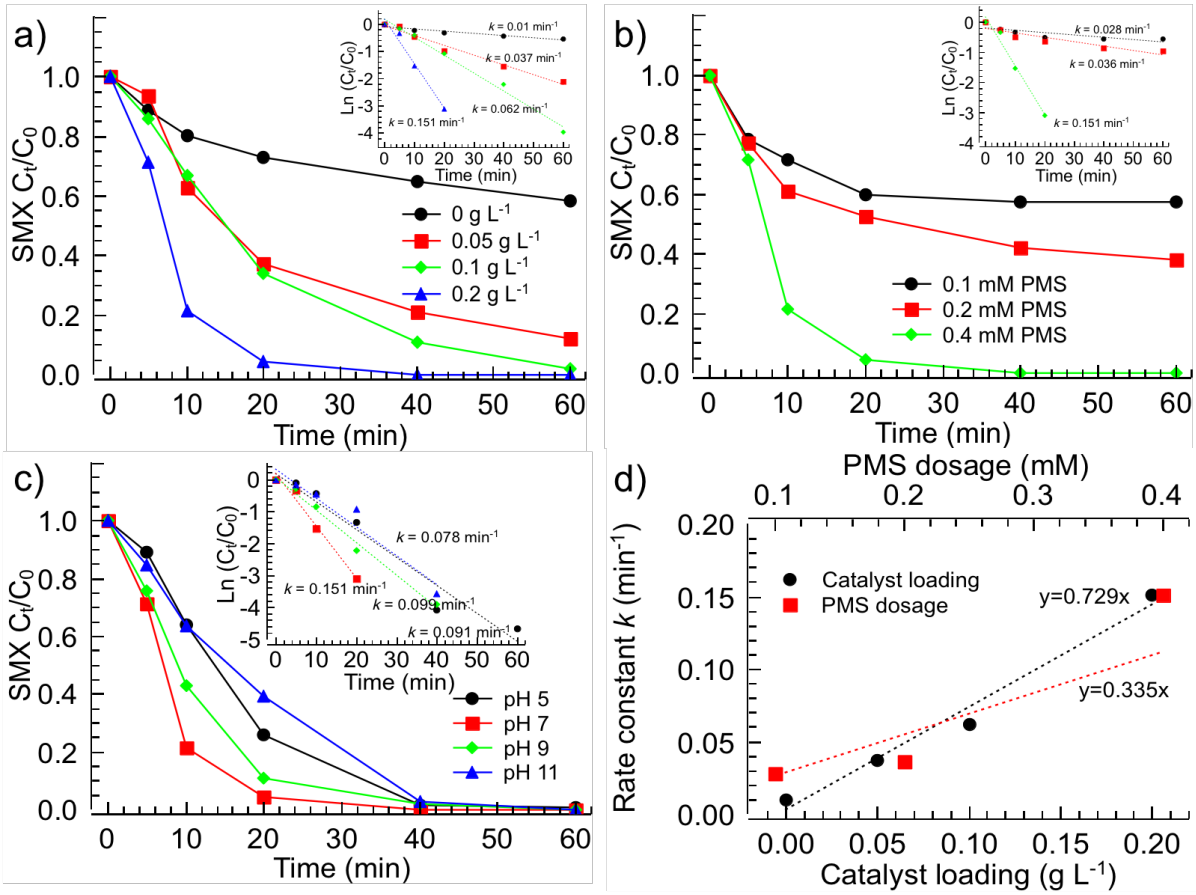

Fig 6.4. Effects of catalyst loading amount (a), PMS dosage (b) and pH (c) on the degradation of SMX and (d) effects of catalyst loading and PMS dosage on SMX degradation kinetic rate constants [Experimental Conditions: a - SMX = 40 μM, PMS = 0.4 mM, pH = 7; b - SMX = 40 μM, $CoFeO_{2.5}$ = 0.2 g L^{-1}, pH = 7; c - SMX = 40 μM, PMS = 0.4 mM, $CoFeO_{2.5}$ = 0.2 g L^{-1}].

As shown in **Fig 6.4**, the SMX degradation data were fitted using the pseudo first-order kinetics (Eq.3) and the apparent rate constants are calculated and summarized in **Table 6.2**.

$$d\,[SMX] / d\,t = - k_{obs\text{-}SMX}\,[SMX] = - k_{SA\text{-}SMX}\,(C_S)\,[SMX] \quad (6.3)$$

where $k_{obs\text{-}SMX}$ represents the observed pseudo-first-order rate constant (min^{-1}) for SMX degradation, $k_{SA\text{-}SMX}$ is the SMX degradation rate constant normalized with the specific surface area (L m^{-2} min^{-1}) and Cs is the surface area of catalyst in solution (m^2 L^{-1}). Results show that SMX degradation is enhanced with the increase of catalyst loading amount which is in

accordance of Cs (**Fig 6.4 a**). The degradation efficiency was around 40% for at 0.4 mM PMS without $CoFeO_{2.5}$, while the removal efficiency increased to 88%, 98% and 100% for $CoFeO_{2.5}$ dosage of 0.05, 0.1 and 0.2 g L^{-1}, respectively. Meanwhile, SMX degradation also showed a positive dependence on PMS dosage. The degradation efficiency remained at 40% at 0.1 mM PMS and increased to 60% and 100% for 0.2 and 0.4 mM PMS, which shows the active sites on $CoFeO_{2.5}$ surface was not totally occupied by PMS at concentrations of less than 0.4 mM. The observed rate constant shows a liner relationship with both catalyst loading as well as PMS dosage (**Fig 6.4 d**), in which the catalyst loading amount has a more significant effect. The effect of initial pH on SMX degradation was investigated by adding NaOH and the results show that the catalyst has a wide pH range tolerance (**Fig 6.4 c**). All degradation efficiencies can achieve to ~100% at 40 min in the pH range of 5-11 and the pH decreased slightly (<0.5) during the reaction. The optimized condition happens at pH 7 with an observed rate constant k of 0.151min^{-1}.

Table 6.2. Summary on the SMX degradation kinetics with different parameters.

Parameters	$k_{obs\text{-}SMX}$ (min^{-1})	$k_{SA\text{-}SMX}$ (L m^{-2} min^{-1})	Cs (m^2 L^{-1})
$CoFeO_{2.5}$			
0 g L^{-1}	0.010	N.A.	N.A.
0.05 g L^{-1}	0.037	0.078	0.475
0.1 g L^{-1}	0.062	0.065	0.950
0.2 g L^{-1}	0.151	0.079	1.900
PMS			
0.1 mM	0.028	0.015	1.900
0.2 mM	0.036	0.019	1.900
0.4 mM	0.151	0.079	1.900

pH			
5	0.091	0.045	1.900
7	0.151	0.079	1.900
9	0.099	0.052	1.900
11	0.078	0.041	1.900

6.3.4 Mechanism for the radical generation

PMS could be activated by heterogeneous or homogeneous reaction to generate $SO_4^{\bullet-}$, $^{\bullet}OH$ and $SO_5^{\bullet-}$. In literatures, TBA and MeOH have been widely used to indirectly indicate the presence of reactive radicals ($SO_4^{\bullet-}$ and $^{\bullet}OH$) in the PMS/catalyst system due to the low rate constant with $SO_5^{\bullet-}$ ($\leq 10^3$ M^{-1} s^{-1}) (Feng et al., 2016; Xu and Wang, 2011). Meanwhile, it has been proven that compared with $SO_4^{\bullet-}$ and $^{\bullet}OH$, $SO_5^{\bullet-}$ shows an insignificant contribution on the organic degradation (Bao et al., 2018b). However, except for the different abilities for scavenging radicals, alcohols also show the different adsorption properties onto the catalyst and subsequent in activation of the active sites (Guan et al., 2013). Hence, it is necessary to use other scavengers to identify the reactive species in heterogeneous metal oxides catalyzed oxidation. In the present study, different chemical scavengers including TBA, MeOH, nitrobenzene (NB), phenol, benzoquinone (BQ) and NaN_3 were used as an indirect technique to identify the presence of reactive radicals. The screening of scavengers (**Table A6.2**) was performed and the details are shown in **Fig A6.5** and **A6.6**. Results show that phenol and BQ have no significant selectivity on the radicals scavenging, while the alcohols might affect the chemical polarity of the system as well as the HPLC detection.

Based on the screening results of different scavengers, NB was selected as $^{\bullet}OH$ probe compound due to its low reactivity with $SO_4^{\bullet-}$, with the rate constants of $k_{NB+\bullet OH}$ of (3.0-3.9) $\times 10^9$ M^{-1} s^{-1} and $k_{NB+SO_4^{\bullet-}}$ of $<10^6$ M^{-1} s^{-1} (Liang and Su, 2009). NaN_3 was used to quench all reactions since it has been reported to be effective for quenching $^{\bullet}OH$ (1.2×10^{10} M^{-1} s^{-1}), $SO_4^{\bullet-}$

(2.51×10^9 M^{-1} s^{-1}) and non-radical oxidation process ($^1O_2$ and PMS direct oxidation) (Zhou et al., 2015). The degradation of NB verified the formation of $^{\bullet}OH$ in this system (**Fig 6.5 d**) and the kinetic expressions of NB and SMX degradation could be expressed as follows:

$$-dC_{NB}/dt = k_{NB+\bullet OH}\,[\bullet OH]\,C_{NB} = k_{obs\text{-}NB}\,C_{NB} \quad \textbf{(6.4)}$$

$$-dC_{SMX}/dt = k_{SMX+\bullet OH}\,[\bullet OH]\,C_{SMX} + k_{SMX+SO_4^{\bullet-}}\,[SO_4^{\bullet-}]\,C_{SMX} + k_{SMX+PMS}\,[PMS]\,C_{SMX}$$

$$= k_{obs\text{-}SMX},\,C_{SMX} \quad \textbf{(6.5)}$$

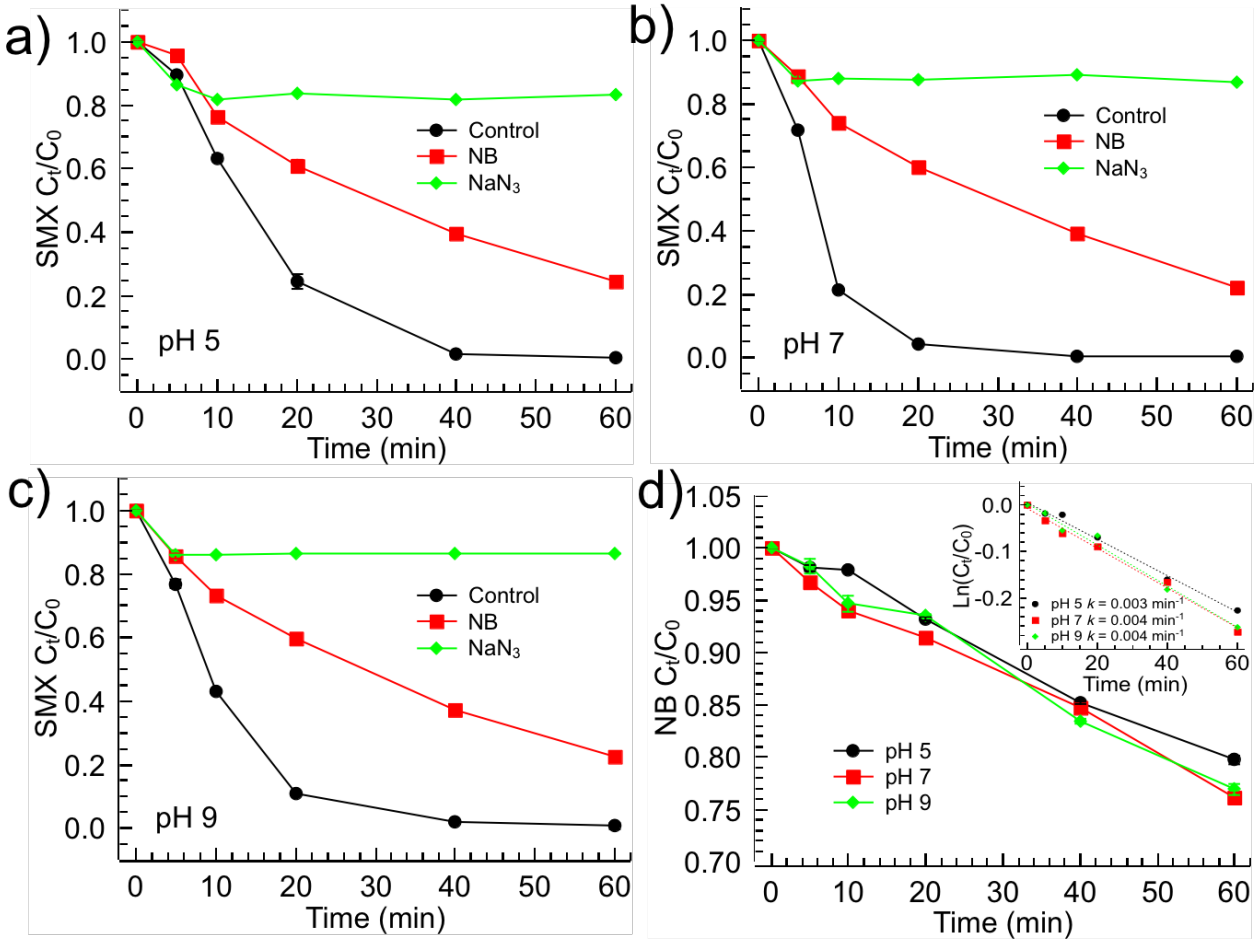

Fig 6.5. Effects of different scavengers on the degradation of SMX (Experimental Conditions: [SMX] = 40 µM; [PMS] = 0.4 mM; [$CoFeO_{2.5}$] = 0.2 g L^{-1}; [NB] = 10 mg L^{-1} and [NaN_3] = 5 mM).

The degradation of SMX without $CoFeO_{2.5}$ shows the non-radical pathway (e.g. PMS direct oxidation and $^1O_2$ oxidation) with a rate constant k of 0.01 min^{-1} (**Fig 6.4 a**). In this work,

due to the high reactivity of radicals, we assumed that $k_{SMX+PMS}$ is much less significant compared with those of $k_{SMX+\bullet OH}$ ((8.5±0.3) × 10^9 M^{-1} s^{-1}) and $k_{SMX+SO_4^{\bullet-}}$ (12.5× 10^9 M^{-1} s^{-1}). The inhibition on SMX degradation rate constants by NB verified the role of $^{\bullet}$OH in the degradation process. In the presence of NB, $^{\bullet}$OH can react with both SMX (1) and NB (2) at the calculated rate constants of k_1= $k_{SMX+\bullet OH}$ (8.5±0.3) × 10^9 M^{-1} s^{-1}) × C_{SMX} (0.04 mM) = 0.34 × 10^6 s^{-1}, k_2 = $k_{NB+\bullet OH}$ (3.0-3.9) × 10^9 M^{-1} s^{-1} × C_{NB} (10 mg L^{-1}) = 0.28 × 10^6 s^{-1}. Therefore, the possibility of hydroxyl radical to react with NB is assumed as P = 0.28 × 10^6/(0.28+0.34) × 10^6 = 45%. The calculated $^{\bullet}$OH generation increased from (1.03-1.33) × 10^{-10} M to (1.37-1.78) × 10^{-10} M when the initial pH increased from 5 to 9 (**Eq. 6.4**). Under higher pH, $SO_4^{\bullet-}$ would decompose to $^{\bullet}$OH (**Fig 6.3 e**), increasing the $^{\bullet}$OH concentration.

Table 6.3. The calculated observed reaction rate constants k_{obs} in SMX/NB system (a) and SMX system (b) (Experimental Conditions: [SMX] = 40 μM; [PMS] = 0.4 mM; [$CoFeO_{2.5}$] = 0.2 g L^{-1} and [NB] = 10 mg L^{-1}).

pH	$k_{obs\text{-}NB}$ (min^{-1})[a]	$k_{obs\text{-}SMX'}$ (min^{-1}) [a]	$k_{obs\text{-}SMX}$ (min^{-1}) [b]
5	0.003	0.023	0.091
7	0.004	0.025	0.151
9	0.004	0.025	0.099

Table 6.3 shows that NB exhibits the inhibition on the SMX degradation in all pH ranges (5-9), which verified the role of $^{\bullet}$OH on SMX degradation. If we assumed that $^{\bullet}$OH is the only functional radical, $k_{obs\text{-}SMX'}/k_{obs\text{-}NB}$ should be around 2-3 (**Eqs. 6.4-6.5**). However, the calculated value of $k_{obs\text{-}SMX'}/k_{obs\text{-}NB}$ is in the range of 6-8 (**Table 6.3**), indicating the other contributions (non-radical pathway as well as other radical pathway, i.e., $SO_4^{\bullet-}$) on SMX degradation.

To further identify the radicals generated in PMS/$CoFeO_{2.5}$/SMX system, an attempt with EPR experiments was conducted. There were no obvious characteristic signals present in the EPR spectra of experiments conducted without catalyst (**Fig A6.7**). However, spin trapping adducts DMPO-$^{\bullet}$OH and DMPO-$SO_4^{\bullet-}$ were identified when catalyst was introduced (**Fig 6.6 a**), suggesting that the as-prepared catalyst could effectively activate PMS to generate radicals (Wang et al., 2016). Meanwhile, $^{\bullet}$OOH was also detected in this system when BMPO was used as the spin trapping agent (**Fig 6.6 a**) and the detection of $^1O_2$ further confirmed the non-radical pathway of SMX degradation (**Fig 6.6 b**).

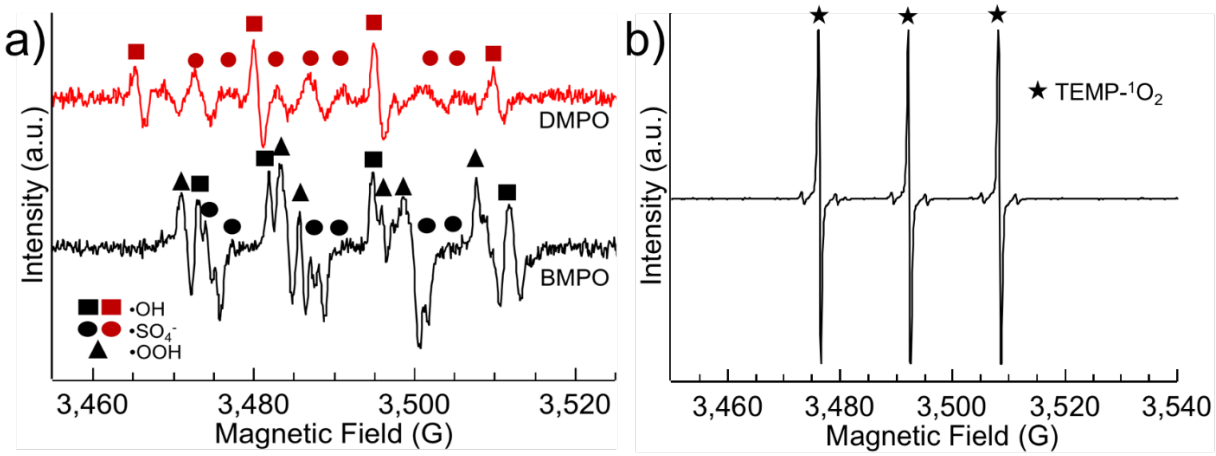

Fig 6.6. EPR spectra in activation of PMS with different spin trapping agents in the presence of the as-prepared catalyst.

6.3.5 Proposed SMX transformation pathways in PMS/$CoFeO_{2.5}$ system

Based on the radical scavenger experiments and EPR results, both non-radical pathway and radical pathway are involved in the SMX degradation processes. Through the identification of oxidation products, the possible transformation pathways for SMX oxidation in PMS/$CoFeO_{2.5}$ system is proposed in **Fig 6.7**. The main transformation products from SMX degradation are summarized in **Table A6.3** and **Fig A6.8**. In the transformation process, three major transformation pathways are proposed to occur simultaneously: 1) oxidation of the amine group on the benzene ring to yield the nitro-SMX derivative; 2) hydroxylation of the benzene

and isoxazole rings; and 3) cleavage of the sulfonamide bond.

In the non-radical oxidation pathway, PMS played a role as inorganic oxidizer that can react with SMX through both electrophilic and nucleophilic reactions. Meanwhile, $^1O_2$ which could be generated via PMS decomposition might also affect the SMX transformation. However, due to the limited amount of $^1O_2$, PMS direct oxidation on SMX transformation should be the dominant non-radical oxidant pathway (Yin et al., 2018). As reported, the density functional theory (DFT) calculation confirmed PMS non-radical oxidation, in which the N atom on the benzene ring and S atom of the sulfanilamide group could be selectively attacked by PMS direct oxidation. The results show that the 8N atom on the benzene ring is the most susceptible sites to be attacked by PMS to form nitroso- or nitro group adducted SMX in the electrophilic oxidation (Yin et al., 2018). During the transformation process, SMX exhibited a color changes from colorless to yellow and back to colorless over extended time periods. Considering the chromogenic properties of the dyes, the nitro group is an efficient functional group for light absorption. Thus, SMX could be degraded through the attack of 8N atom via non-radical pathway to generate the products P1 and P2. In the nucleophilic reaction, the DFT calculation shows that 7S atom of the sulfonamide group was the most vulnerable site which could be attacked by nucleophilic species to break down the functional groups (Boreen et al., 2004; Yin et al., 2017). The possible products formed by attacking the S atom of SMX were detected as P5 and P11. Meanwhile, the isomerization reaction of isoxazole ring on the SMX could also occur in the non-radical pathway, resulting in the rearrangement of isoxazole ring on the SMX (P3). This was also reported in permanganate oxidation and photodegradation of SMX (Gao et al., 2014; Trovó et al., 2009). It is suggested that P11 would further undergo a reaction from the addition of hydroxyl group on the benzene ring (P12) and the loss of the SO_2 group (P13) followed by the substitution of $–NH_2$ group (P14).

1

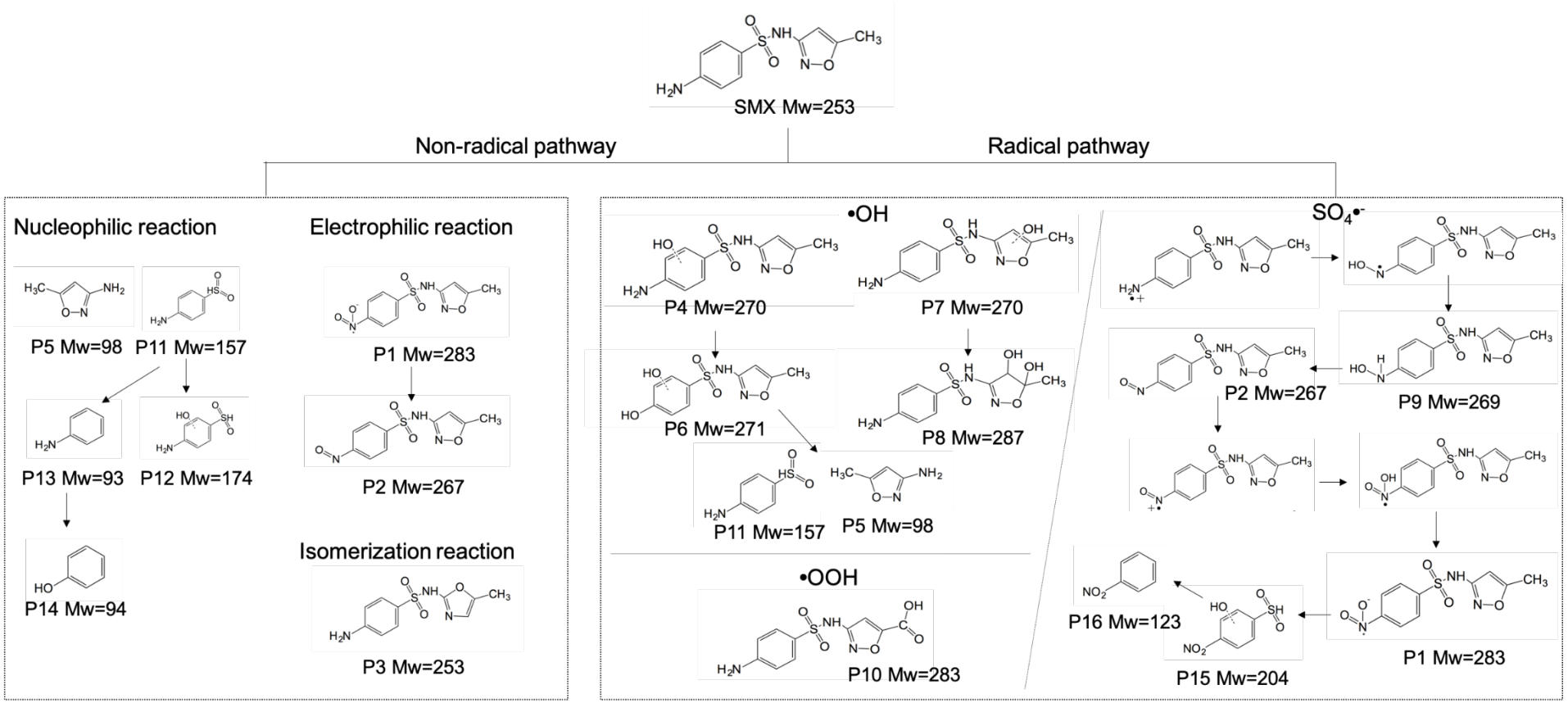

Fig 6.7. Proposed SMX transformation pathways in PMS system in the presence of $CoFeO_{2.5}$.

In the radical pathway, three radicals (i.e., $SO_4^{\bullet-}$, $^{\bullet}OH$ and $^{\bullet}OOH$) were detected and functionalized in this system. $SO_4^{\bullet-}$ has a highly-selective electrophile mainly acting by electron-transfer from N to $SO_4^{\bullet-}$ yielding to a N-centered radical as a first intermediate. This radical cation underwent a fast-reversible hydration to yield an aniline radical, which was further neutralized by molecular oxygen probably leading to hydroxylamine (P9) and nitroso derivatives (P2), which were readily hydrolyzed into nitro-SMX (P1) (Ahmed et al., 2012). The nitro-SMX could be furthered oxidized to become P15 and P16 via the broken of S-N functional bond. Thus, $SO_4^{\bullet-}$ would attack -NH_2 group more efficiently and favor the formation of nitrogen oxidized products. Different from the $SO_4^{\bullet-}$ pathway, $^{\bullet}OH$ exhibits high reactivity with olefinic double bonds and anilines (Buxton et al., 1988), therefore, the radical addition on the benzene and isoxazole rings was commonly observed as the first step to generate products (P4 and P7) in $^{\bullet}OH$ transformation pathway. The $^{\bullet}OH$ can further oxidize the double bond C=C on the isoxazole ring to yield a tertiary carbon-centered radical, with can react with oxygen to generate a peroxy radical. This peroxy radical can abstract a hydrogen from a donor and form the corresponding hydroperoxide, which can produce a hydroxyl radical and an alkoxy radical to form dihydroxylated SMX (P8) via hydrogen abstraction (Hu et al., 2007; Yang et al., 2017). P6 could be generated by the substitution of -NH_2 group with hydroxyl group. Meanwhile, the hydroxyl radicals can also attack the 7S atom to break down the S-N bond to generate the products of P5 and P11 (similar with the nucleophilic pathway). Furthermore, it is proposed that carboxylic acid group (P10) might be formed due to the oxidation at the methyl group on the isoxzaole ring via $^{\bullet}OOH$ radical, which can be exist as superoxide ion in higher pH (**Eq. 6.6**).

$$\bullet OOH + OH^- \leftrightarrow \bullet O_2^- + H_2O \qquad (pK_b = 9.12) \qquad (\mathbf{6.6})$$

6.3.6 Mechanism of PMS activation in the presence of $CoFeO_{2.5}$

The chemical bonding between $CoFeO_{2.5}$ and PMS was investigated by FTIR (**Fig A6.9**). The peaks at the region of 900-1340 cm^{-1} for PMS alone are generally assigned to the symmetric and asymmetric stretching of the S-O bonds (Gonzalez et al., 2010). However, a slightly blue-shift was observed when $CoFeO_{2.5}$ was added into PMS solution suggesting the change of S-O bond.

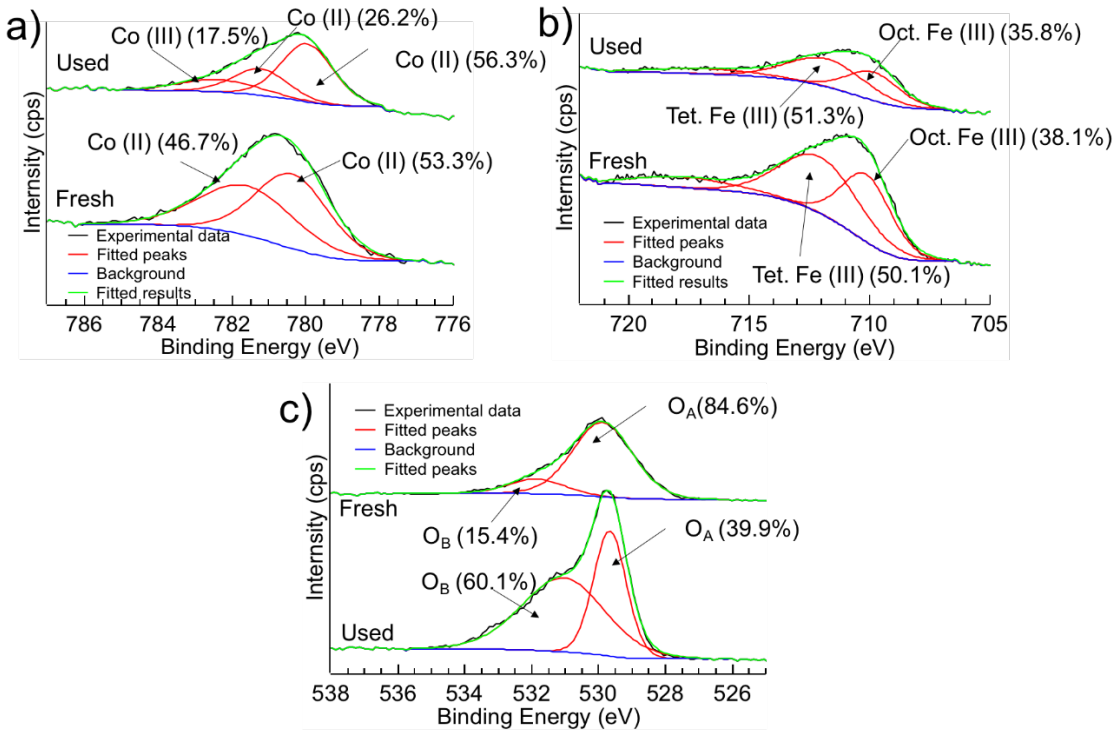

Fig 6.8. XPS spectra of $CoFeO_{2.5}$ before and after the reaction in PMS/$CoFeO_{2.5}$/SMX system.

To explore the PMS activation mechanism, the XPS spectra of the $CoFeO_{2.5}$ before and after the reaction were analyzed. The binding energies and relative intensities are summarized in **Fig 6.8**. The deconvoluted Fe 2p3/2 spectrum displayed three peaks with binding energies at 710.1, 712.1 and 717.6 eV, which could be assigned to octahedral Fe (III), tetrahedral Fe (III) and satellite Fe (III), respectively (**Fig 6.8 b**) (Petran et al., 2016). After the reaction, the ratio of different Fe states changed marginally (< 5%), indicating that no significant redox reaction

has occurred for iron. As shown in **Fig 6.8 a**, two peaks with binding energy appearing at 780.4 and 781.6 eV are ascribed to Co^{2+} ions in octahedral and tetrahedral sites with the relative contributions to the overall Co are 53.3% and 46.7%, respectively. However, the Co 2p3/2 peak is composed of three peaks at 780.0, 781.2 and 782.4 eV, with relative contributions to the overall Co intensity of 56.3% 26.2% and 17.5%, respectively, which is ascribed to Co^{2+} in octahedral sites, tetrahedral sites and Co^{3+} in octahedral sites (Zhou et al., 2008). The results show that the active site in this process is Co, which is mainly present in +2 valent state before reaction and undergoes a partial increase to +3 valent state after catalytic reaction. The oxidizing reaction occurs on the surface and Co^{2+} would provide the electrons in order to keep the balance of charge on the catalyst surface, meanwhile Co^{3+} will accept the electrons from the system, resulting the Co^{2+}-Co^{3+}-Co^{2+} redox process in the system (**Fig 6.9**). The high-resolution O1s spectra are deconvoluted into two peaks at 529 and 531 eV, which are assigned to the lattice oxygen (O_A) and surface hydroxyl species (O_B). After reaction, it is found out that the O_A decreased from 84.6 to 39.9%, which should be accompanied with the oxidation reaction from Co^{2+} to Co^{3+} (Ren et al., 2015). Meanwhile, the metal leaching results show that Fe shows a much less leaching compared with Co (**Table 6.1**). Therefore, in this system, it was proposed that Co works as the active site while Fe works as the adsorption site since the surface area of nano-bimetallic oxides increased with increasing of Fe amount (**Fig 6.2 b**), the similar results could be found in the previous study (Huang et al., 2017).

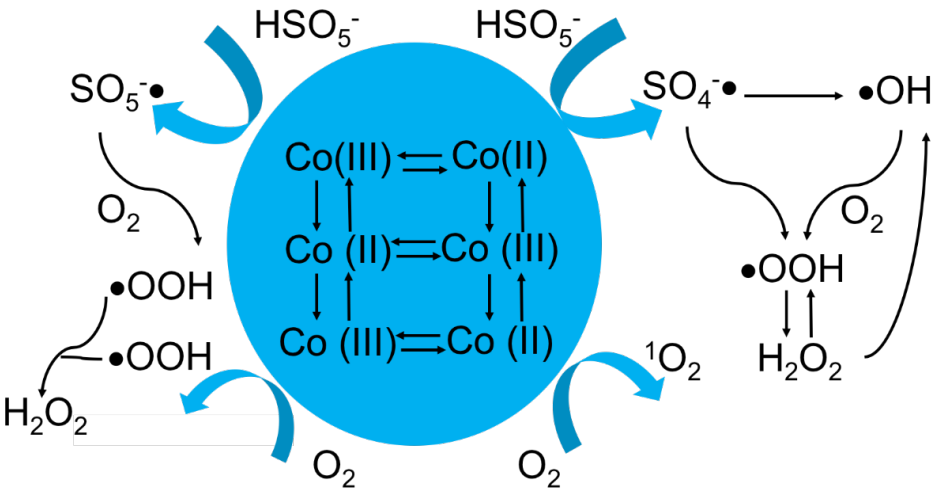

Fig 6.9. The radical generation mechanism via PMS activation in the presence of $CoFeO_{2.5}$.

Therefore, these results confirm that Co^{2+} donated electrons to PMS and initiated its decomposition (**Eq. 6.7**). Co^{3+} was then reduced by HSO_5^- to complete the redox cycles, resulting in the continuous reaction (Anipsitakis and Dionysiou, 2004; Oh et al., 2016). In this process, $^{\bullet}OH$ could be generated through the reaction between $SO_4^{\bullet-}$ and H_2O/OH^- and can react with HSO_5^- to produce $SO_5^{\bullet-}$ (Hayon et al., 1972; Norman et al., 1970) (Refer to the previous Chapters). Based on the EPR results, $^{\bullet}OOH$ was proposed to be formed via the reaction of $SO_4^{\bullet-}/^{\bullet}OH$ and H_2O/O_2 (**Fig 6.9**). $^{\bullet}OOH$ could react to produce H_2O_2, which can further generate radicals in the presence of catalyst (Sehested et al., 1968). Meanwhile, $^1O_2$ can be produced by O_2 in the presence of radicals (Daimon et al., 2008).

Furthermore, the stability test of $CoFeO_{2.5}$ to activate PMS for SMX degradation was investigated. The catalyst was recycled by magnetic assisted centrifugation and the reusability test showed the degradation efficiency could be maintained at > 95% after five cycles (**Fig A6.10**).

6.4 Conclusions

A series of nano-bimetallic Co/Fe oxides with different stoichiometric ratios were prepared and used for the heterogeneous activation of PMS for SMX degradation. Based on the results presented, the following conclusions can be drawn:

1) Nano-bimetallic Co/Fe oxides with different stoichiometric ratios could be prepared via a one-step combustion method.
2) The as-prepared catalyst of $CoFeO_{2.5}$ shows the highest stability and the stoichiometric efficiency in PMS/$CoFeO_{2.5}$/SMX system has a positive relationship with initial pH value.
3) The EPR results and chemical quenching experiments confirmed the generation of multiple radicals or reactive oxygen species (i.e., $SO_4\bullet^-$, •OH, •OOH and $^1O_2$).
4) The transformation of SMX in PMS/$CoFeO_{2.5}$ system includes both radical pathway and non-radical pathway, in which radical pathway ($SO_4\bullet^-$ and •OH) plays a major role.
5) The change of S-O bond showed the generation of radicals from PMS oxidation and the XPS spectra of $CoFeO_{2.5}$ before and after reaction demonstrated the electron transfer between PMS and $CoFeO_{2.5}$.
6) Based on the XPS and ICP results, it could be hypothesized that Fe functioned as the absorption site while Co functioned as the active site in the catalyst.

Overall, a comprehensive transformation of SMX in PMS/$CoFeO_{2.5}$ system was explored in this study. Meanwhile, the one-step combustion method could be used for the nano-bimetallic oxides preparation which could be applied for the water treatment.

CHAPTER 7 CONCLUSIONS AND RECOMMENDATIONS

7.1 Conclusions

In the first part of this thesis (Chapter 3), a Co_3O_4 functionalized ceramic membrane (CoFCM) was synthesized via a ZIF-67 induced surface nucleated heterogeneous growth method. The CoFCM showed an enhanced performance in SMX removal in a semi-batch experiment. But the surface coating limited the further degradation of organics when they pass through the membrane.

Therefore, a Co_3O_4 impregnated ceramic membrane (CoCM) was developed via an in-situ self-scarified template method (Chapter 4). With this method, Co_3O_4 was isotropically impregnated into the whole membrane while did not affect the pore size of the membranes. Due to the hydrophilicity of Co_3O_4, the pure water permeability of CoCM increased compared with the initial one. Furthermore, the membrane showed an antifouling property to humic acid due to the catalytic decomposition of HA on the membrane surface. A novel organics removal mechanism involving catalytic degradation as well as membrane filtration in CoCM was proposed.

Compared with the single metal oxide (Co_3O_4), lots of studies have shown that mix-metal oxides showed an enhanced performance in PMS activation. Therefore, a Co-Fe mix metal oxide, cobalt ferrite ($CoFe_2O_4$) impregnated ceramic membrane was developed (Chapter 5). The $CoFe_2O_4$ impregnated ceramic membrane was developed via a urea assisted one-step combustion method, in which urea works as fuel. Results showed that with this method, $CoFe_2O_4$ could be formed and impregnated into the membrane pores as well as the membrane surface. With increasing of repeating times, the catalyst loading amount increased while the pure water permeability decreased, which means the catalyst would form a dense catalytic layer on the membrane surface due to the aggregation during the combustion process. The membrane

performance was evaluated in a dead-end membrane filtration mode, and results showed the robust membrane can function well during a wide pH range as well as the existence of NOM and anions.

The last part of the thesis is the systematic study of SMX transformation pathway via PMS oxidation in the presence of nano-bimetallic Co/Fe oxides. The influencing factors (pH, NOM, catalyst loading and PMS dosage) were investigated. The radical generation and PMS activation mechanism were explored. Furthermore, a novel SMX transformation pathway including both non-radical and radical pathways was proposed.

In summary, the as-prepared catalytic ceramic membranes showed the improved performance for the organics removal in water treatment. On one hand, the catalysts were immobilized onto/into ceramic membrane, reducing the metal leaching and avoiding the catalyst aggregation. On the other hand, the catalytic ceramic membranes showed an enhanced antifouling property with a self-cleaning potential. The coupling technology with SR-AOPs and membrane separation shows a promising prospect in water reclamation.

7.2 Recommendations for the future work

7.2.1 Long term performance of the catalytic ceramic membrane

During the real application, the operation cost (chemical dosage, electricity and manual work) needs to be considered. Meanwhile, the stability of membrane in a long-term operation needs to be examined, including the catalyst leaching as well as the regeneration of membranes. Therefore, the calculation of PMS consumption as well as the PMS dosage frequency during the reaction needs to be addressed. To make sure the high performance, the configuration of multi-dosage should be considered (**Fig 7.1**) and the calculation needs to be done to make sure the optimization dosage.

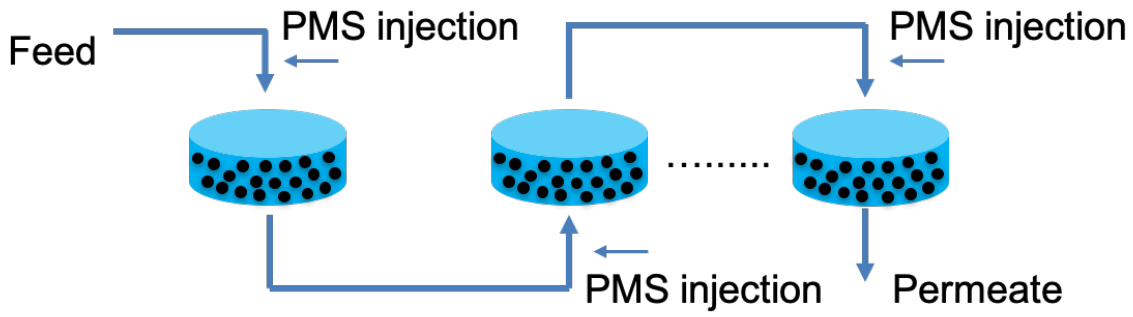

Fig 7.1. Multi-stage design for SR-AOPs combined with membrane separation.

Meanwhile, most study works on artificial system, in which one model compound is concerned, it is important to investigate real wastewater containing compounds of different chemical nature to elucidate the mutual effects of these compounds on their degradation rate.

7.2.2 The non-metal carbon-based catalyst development

Recently, non-mental carbon-based catalysts such as CNTs, GO and rGO have been employed as PMS activators (Duan et al., 2016, 2015a, 2015b). The carbon-based materials provided a potential solution to the metal leaching problem. However, the low durability for long term use due to cannibalistic oxidation limits its further application (Sun et al., 2013). Therefore, how to improve the durability of carbon-based catalysts needs to be addressed.

Meanwhile, the mechanisms of PMS activation involving carbon-based catalyst are not fully understood. Besides radical-based mechanism, it has been reported that a non-radical pathway emerged along with the formation of radicals (Duan et al., 2014; Zhou et al., 2015). The occurrence of radical and non-radical pathways depends on the type of carbon structure (Duan et al., 2016). Further investigation needs to be conducted to detect the reaction mechanism between generated radical and non-radical pathways.

In the first-try out, we used polyacrylonitrile (PAN) as the carbon precuror to prepare a nitrogen-doped carbon membrane for PMS activation. Results showed that the addition of metals in the precursors can tune the carbonization process of PAN, resulting different morphologies. Also the metal can work as active site for PMS activation (Paper published as

APPENDIX B). Furtherwork can focus on the metal-induced carbon membrane development for oxidation.

7.2.3 Multi-AOPs combined ceramic membranes

For single AOP/ceramic membrane system, the common AOP includes photocatalysis, ozonation and Fenton reaction. The final objective for photocatalysis is to utilize sunlight, therefore, it is important to develop the visible-light driven photocatalyst. In our work, we tried to synthesize bismuth based catalysts for photocatalysis (Papers published as **APPENDIX C** and **D**). The in-situ hydrothermal method was applied to prepare catalytic ceramic membrane, but the performance is unsatisfied. A more suitable method to load the as-prepared catalyst onto/into membrane is required. For ozonation and Fenton reaction, since the self-decomposition rate of ozone and hydroxyl peroxide is quite high, the surface modification is more important compared with the impregnation of catalysts into membrane pores. For SR-AOP, since PMS is quite stable, it is more meaningful for preparing a micro-reactor.

Recently, the combined AOPs have been employed in the catalytic degradation and results showed the multi-AOPs combined technologies improved the organics removal efficiency significantly, while the reaction mechanism is still unclear (Anandan et al., 2010; Beltrán et al., 2009; Guan et al., 2011; Yanbin Wang et al., 2017). Therefore, it is necessary to understand the fundamental reaction mechanism during the radicals' elucidation.

7.2.4 Multi-functional ceramic membrane preparation

As discussed in the thesis, a catalytic ceramic membrane could be prepared by loading catalyst onto/into membrane, the further challenge is the preparation of separation layer uniformly. We utilized metal-organic framework as the internal layer to connect the ceramic substrate and polyamide separation layer for nanofiltration (**APPENDIX E**). More work should focus on the catalytic ceramic membrane preparation with both catalytic separation layer and substrate.

APPENDIX A

Table A3.1. The main detected intermediate products in SMX degradation.

m/z	Structure	Detected mode
98	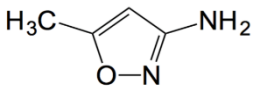	Negative/Positive
157	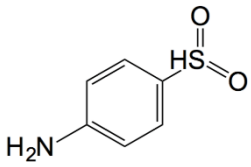	Negative/Positive
267	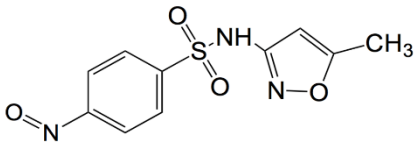	Positive
270	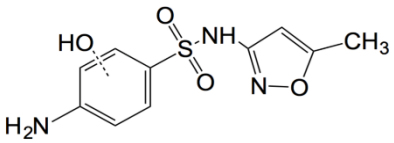	Positive
283	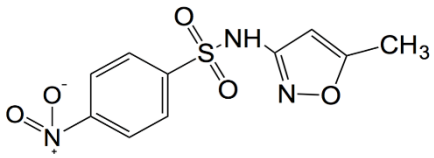	Negative

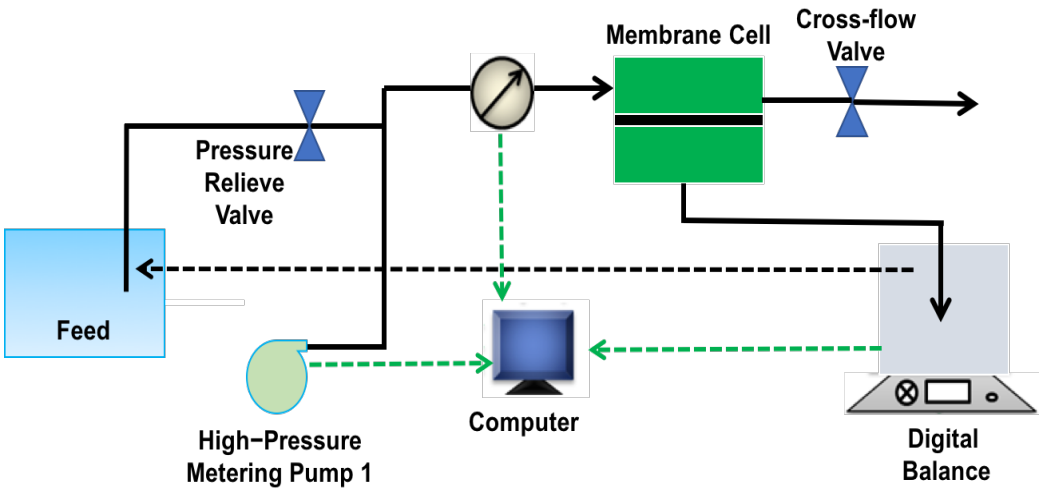

Fig A3.1. Process flow diagram of membrane filtration system.

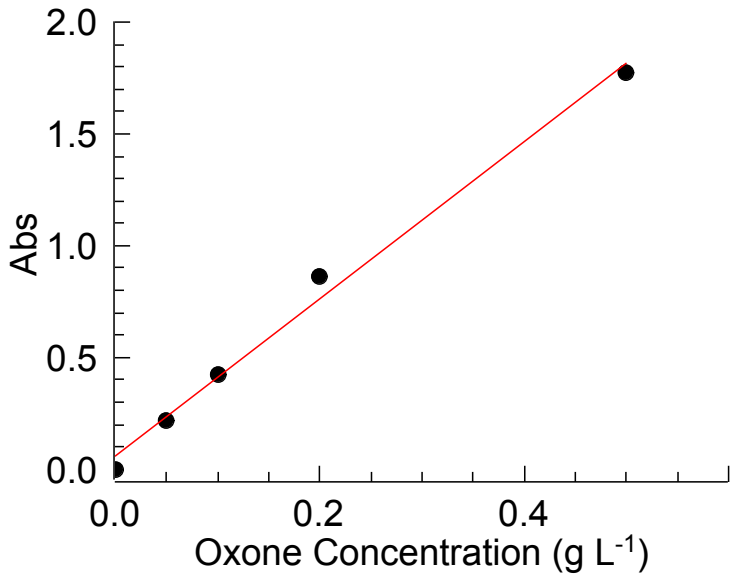

Fig A3.2. The calibration curve of Oxone concentration

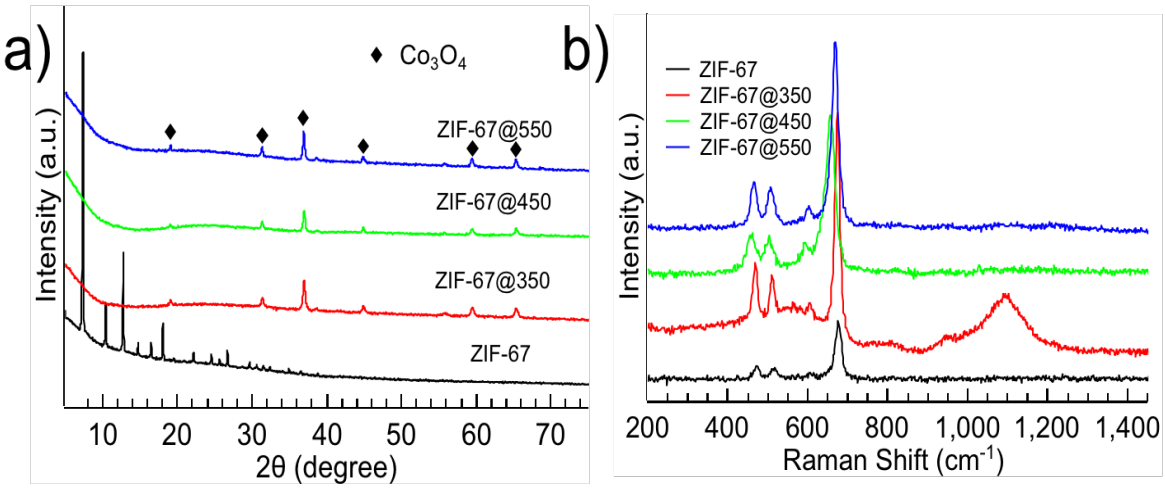

Fig A3.3. XRD pattern (a) and Raman spectra (b) of Co_3O_4 calcined at different temperatures.

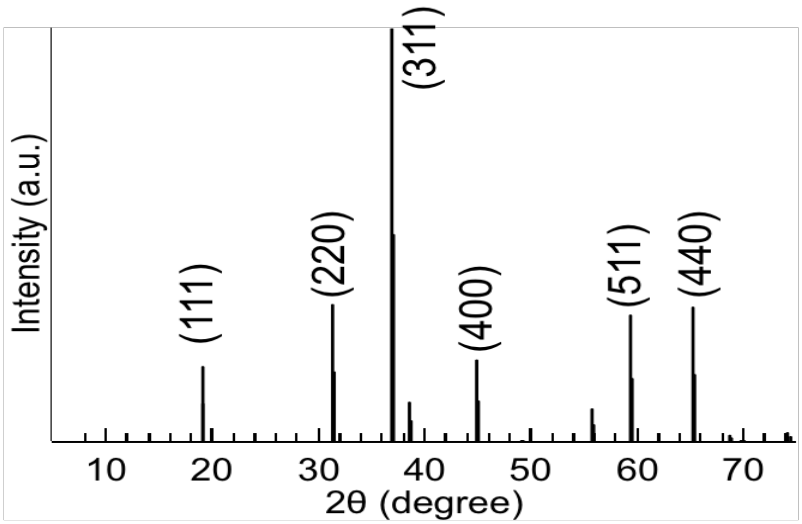

Fig A3.4. XRD pattern of Co_3O_4 (04-016-4508).

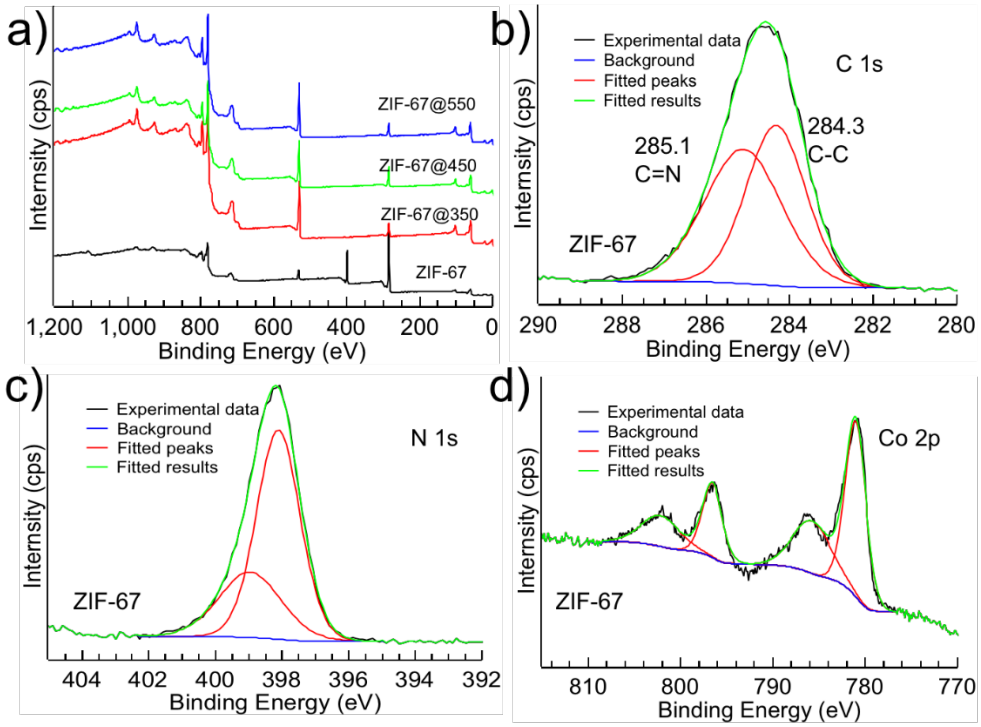

Fig A3.5. Wide scan of ZIF-67 and Co_3O_4 prepared under different temperatures (a) and high resolution of C1s (b), N1s (c) and Co2p (d) in ZIF-67.

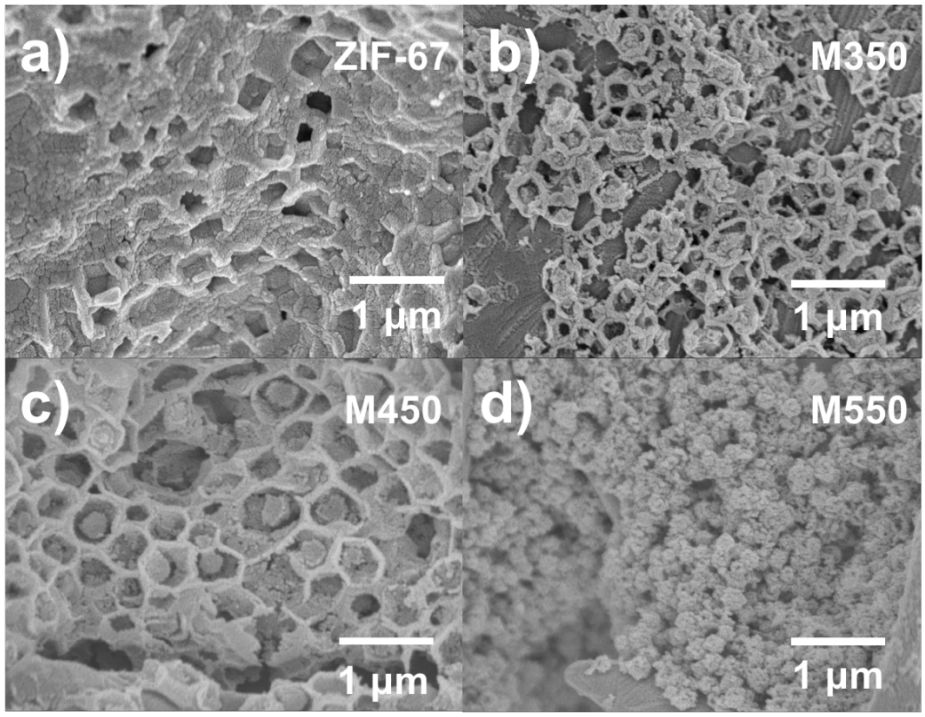

Fig A3.6. FESEM images of ZIF-67 membrane (a) and CoFCMs with different calcination temperatures (b-d).

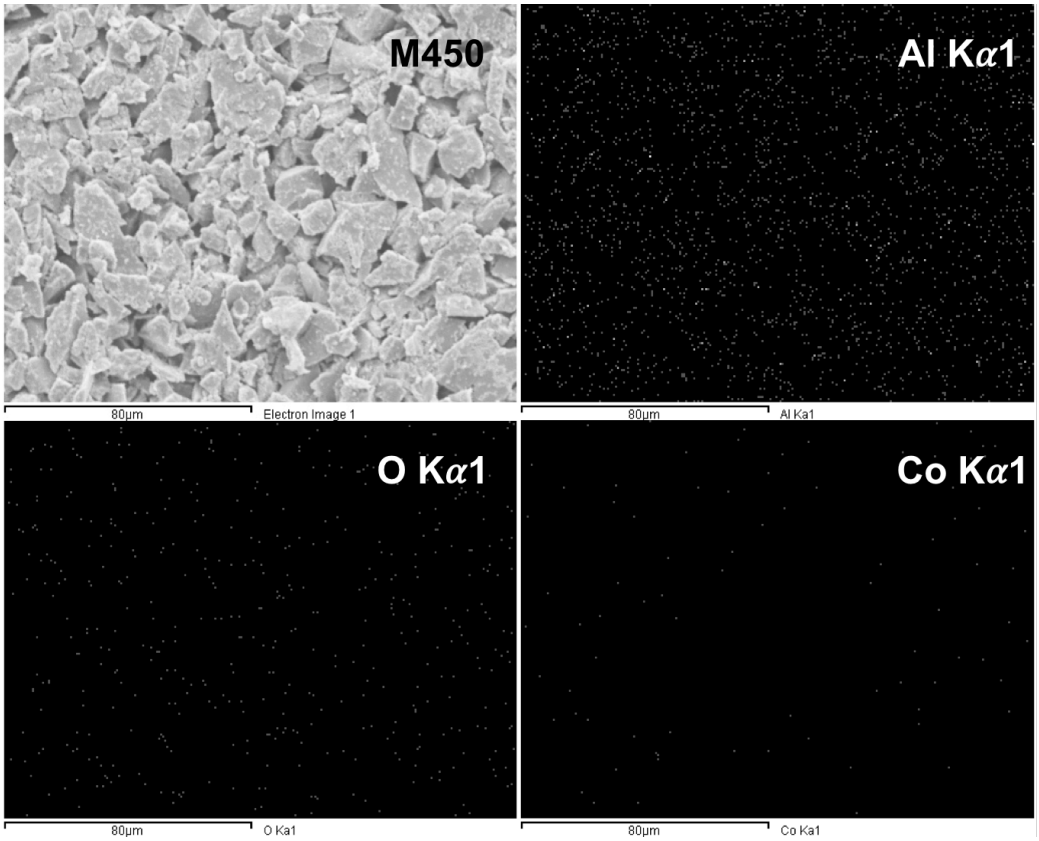

Fig A3.7. The element mapping images of M450.

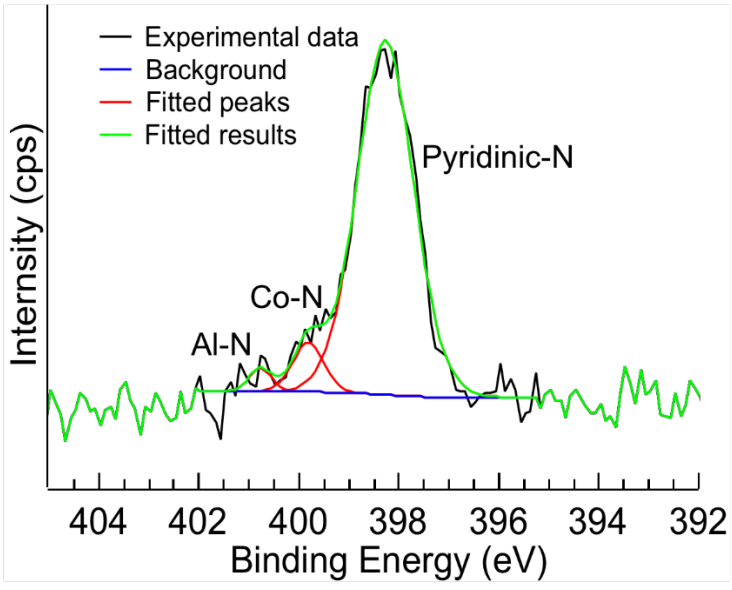

Fig A3.8. High resolution of N1s in ZIF-67/Al_2O_3.

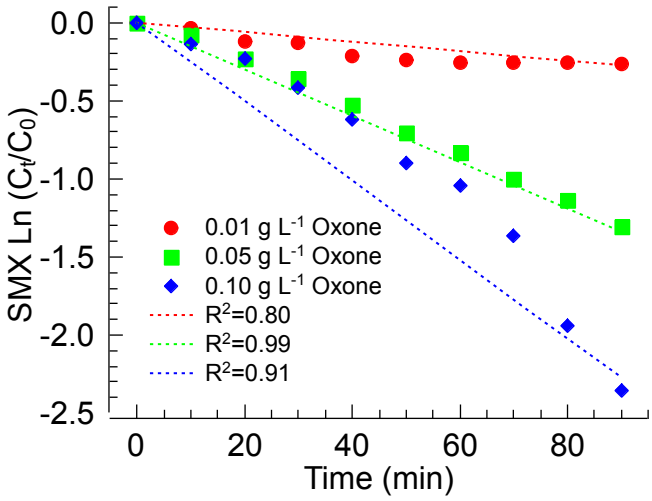

Fig A3.9. Effect of Oxone dosage on SMX degradation over M450.

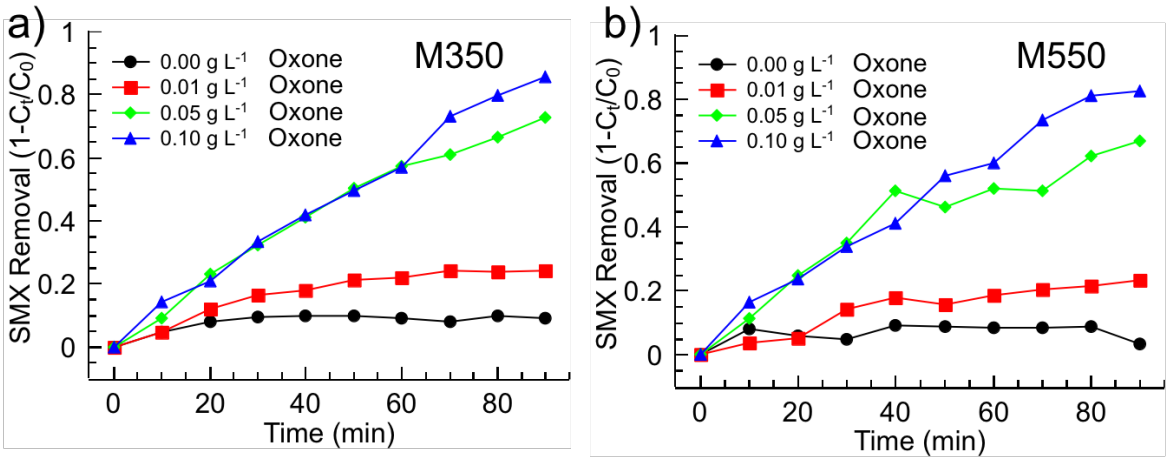

Fig A3.10. Effect of Oxone dosage on catalytic performance of M350 and M550.

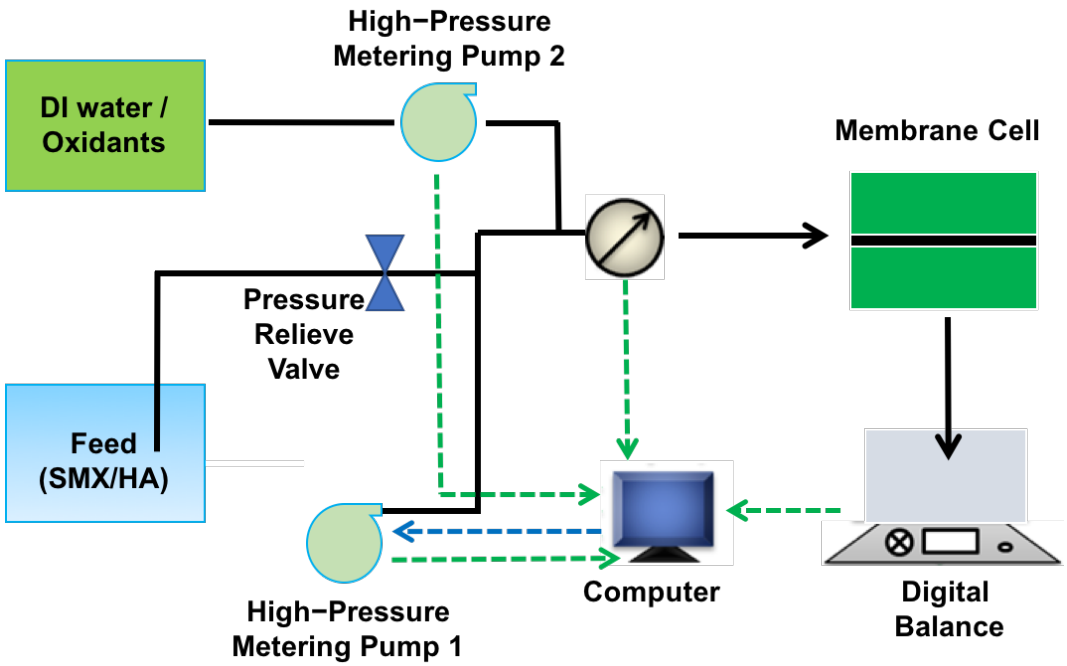

Fig A4.1. The schematic diagram of the experimental setup for membrane filtration.

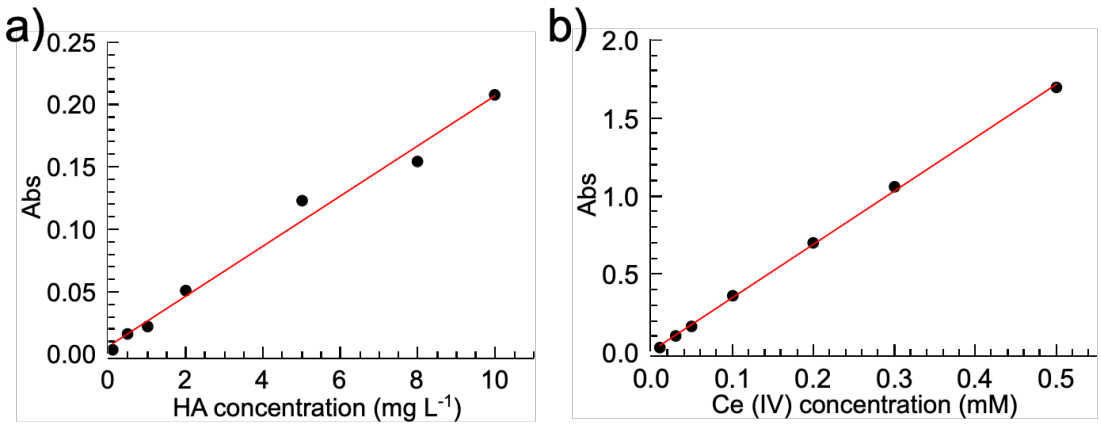

Fig A4.2. Calibration curves for HA and Ce (IV).

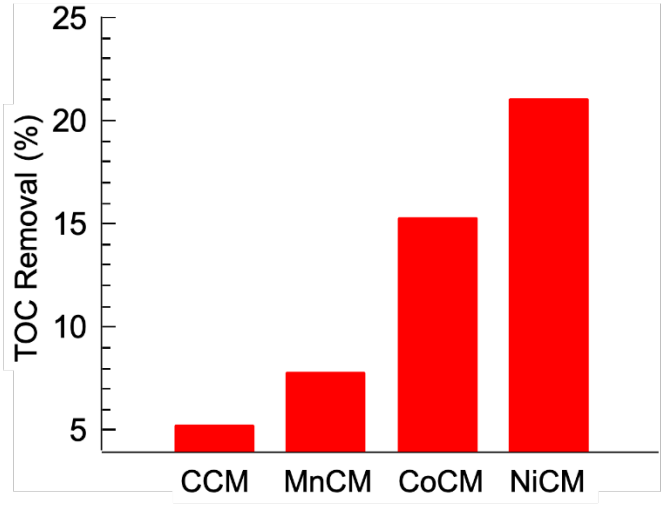

Fig A4.3. TOC removal for different membranes in membrane filtration system.

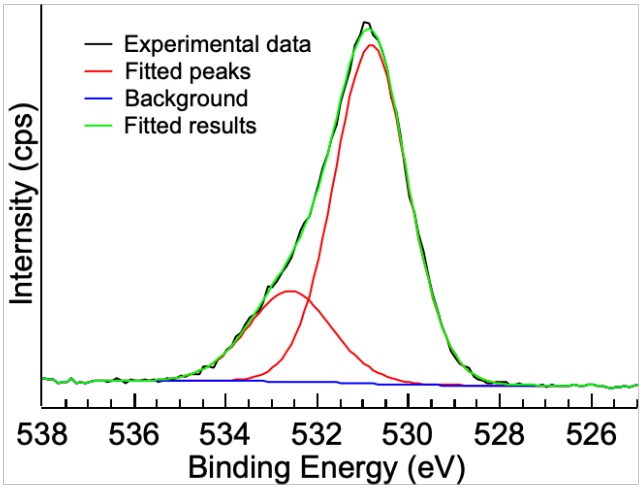

Fig A4.4. High resolution of O1s in used CoCM.

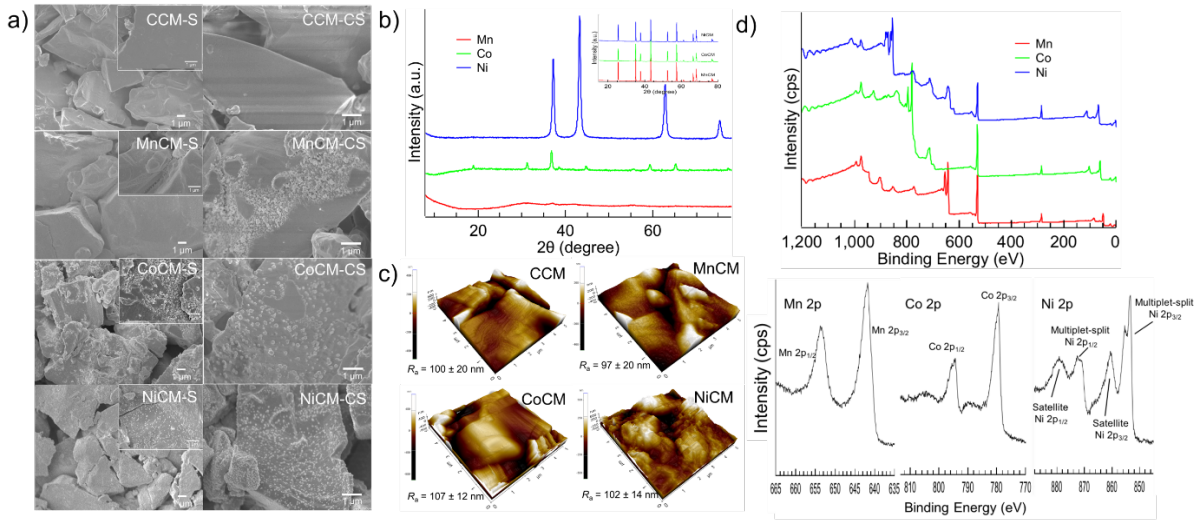

Fig A4.5. Chemical and physical properties of metal oxides impregnated CMs (a-FESEM, in which S means surface and CS means cross-section; b-XRD of both particles and membranes; c-AFM of membranes and d-XPS of particles).

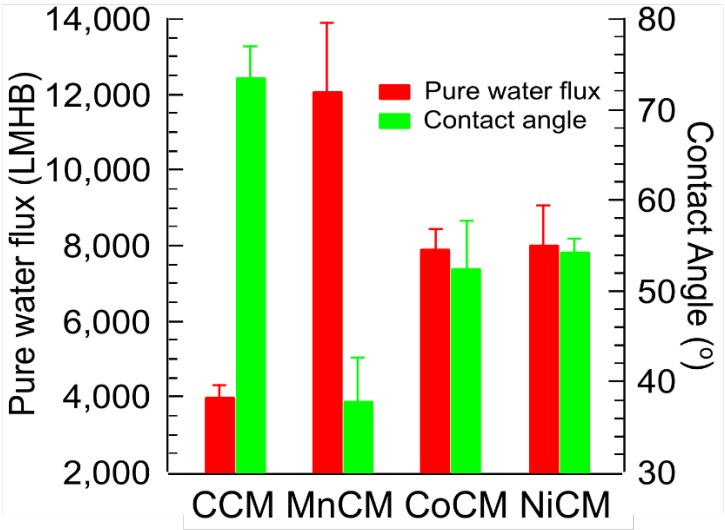

Fig A4.6. Pure water flux and surface water contact angles of membranes.

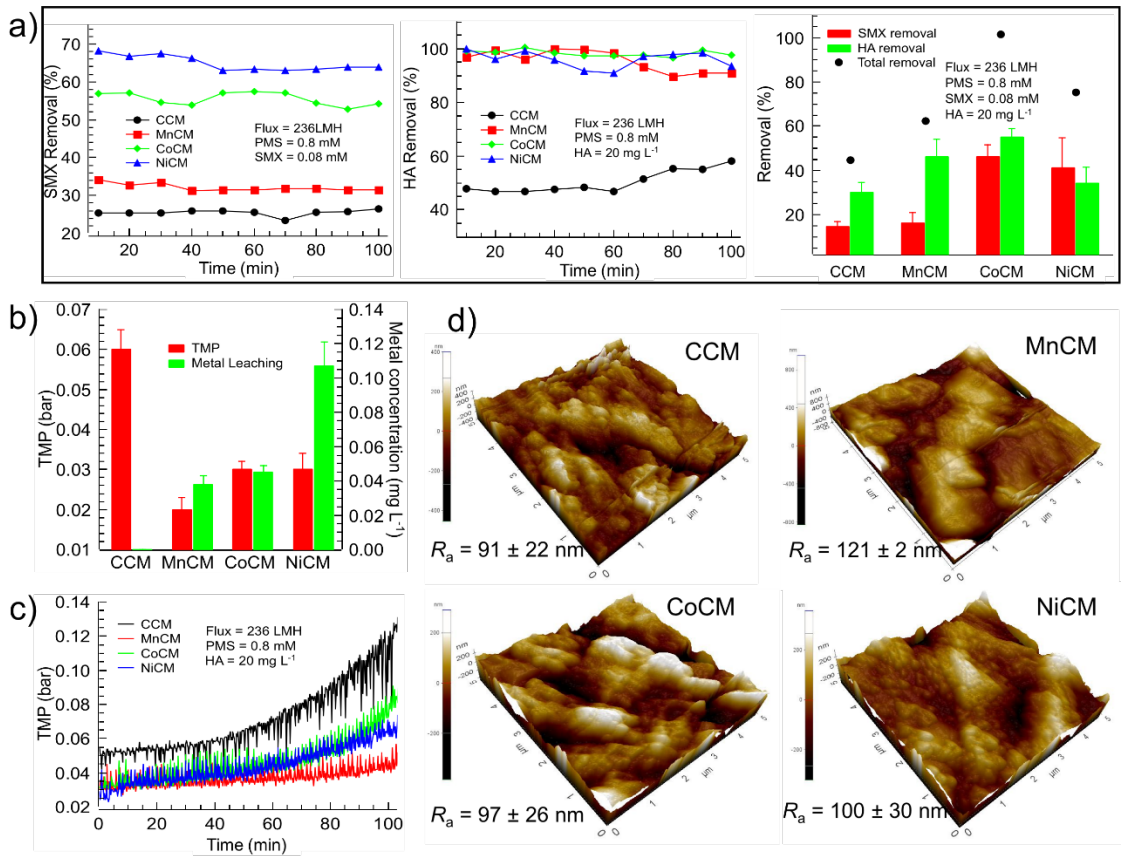

Fig A4.7. a) SMX and HA removal in membrane filtration system (from left to right: SMX only, HA only and SMX+HA); b) the recording TMP and metal leaching in SMX removal; c) the recording TMP in HA removal; and d) the AFM images of used membranes.

Text A4.1. The analysis of MnCM and NiCM.

FESEM characterizations of both surface and cross section (internal pores) of MnCM and NiCM are displayed in **Fig A4.5 a**. The CCM shows a smooth surface as well as internal pores, while it changes significantly after the metal oxides impregnation. Similar with CoCM, Mn oxides and Ni oxides could be impregnated successfully and distributed uniformly onto/into the membranes. The AFM images show that the average surface roughness of MnCM was slightly decreased (**Fig A4.5 c**), implying that the Mn oxides filled the pores and valleys on the membrane surface, which is consistent with FESEM images. The results in **Fig A4.5 b** show that Mn oxides prepared by this method has a lower crystallinity compared with Ni oxides, which are corresponded as NiO (Entry No.00-004-0835). High resolution XPS of Mn 2p and Ni 2p further reveals the existence of Mn and Ni in the as-prepared catalysts (**Fig A4.5 d**). The contact angles of MnCM and NiCM decreased to 37.7 ± 5.0° and 54.3 ± 1.4° compared with CCM and the pure water permeability increased from 3960 ± 330 LMHB to 12071 ± 1810 and 8009 ± 1067 LMHB (**Fig A4.6**). In SMX system, the SMX removal was around 30% and 64% for MnCM and NiCM and the concentrations of Mn and Ni in the permeate were 0.038 ± 0.005 and 0.107 ± 0.014 mg L^{-1}. When the feed was changed to HA solution, the removal of HA achieved > 90% for both MnCM and NiCM. In SMX-HA system, the HA removal decreased from > 90% to 46 % and 34 % while the SMX removal decreased to 16% and 41% for MnCM and NiCM, respectively (**Fig A4.7**).

Table A5.1. The concentrations of metal ions in the reaction solutions (Condition: [SMX] = 10 mg L^{-1}, [catalyst loading] = 0.2 g L^{-1}, [Oxone] = 0.10 g L^{-1}, pH = 5, reaction time = 60 min).

Ions concentration (µg L^{-1})	@300	@400	@600	@800
Co	275.5±1.33	312.2±4.49	158.0±0.20	116.2±0.37
Fe	13.37±0.53	51.0±0.62	36.2±0.13	31.1±0.39

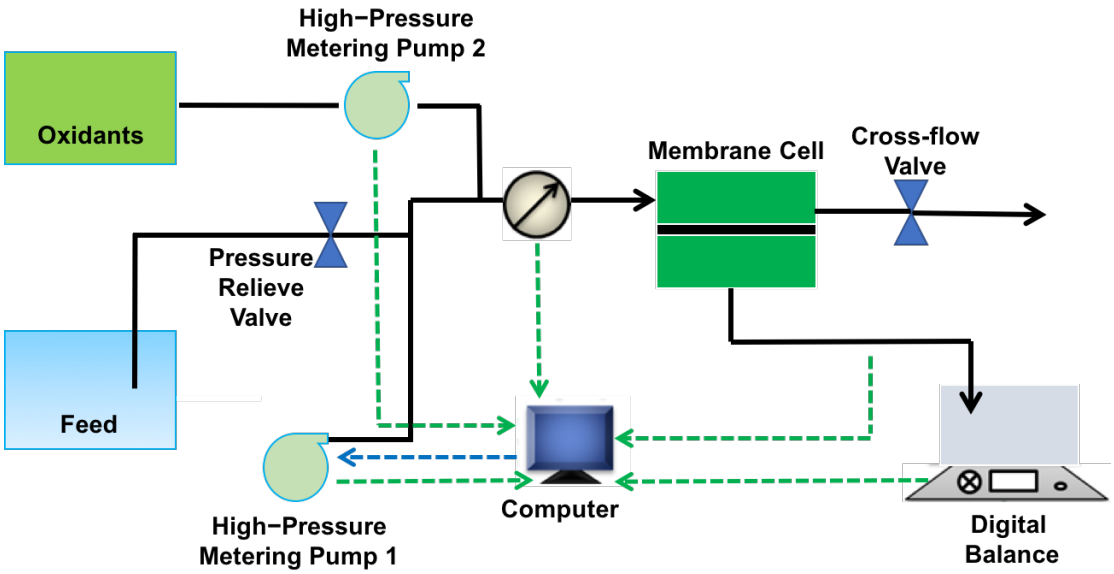

Fig A5.1. Process flow diagram of membrane filtration system (modified from **Fig A4.1**).

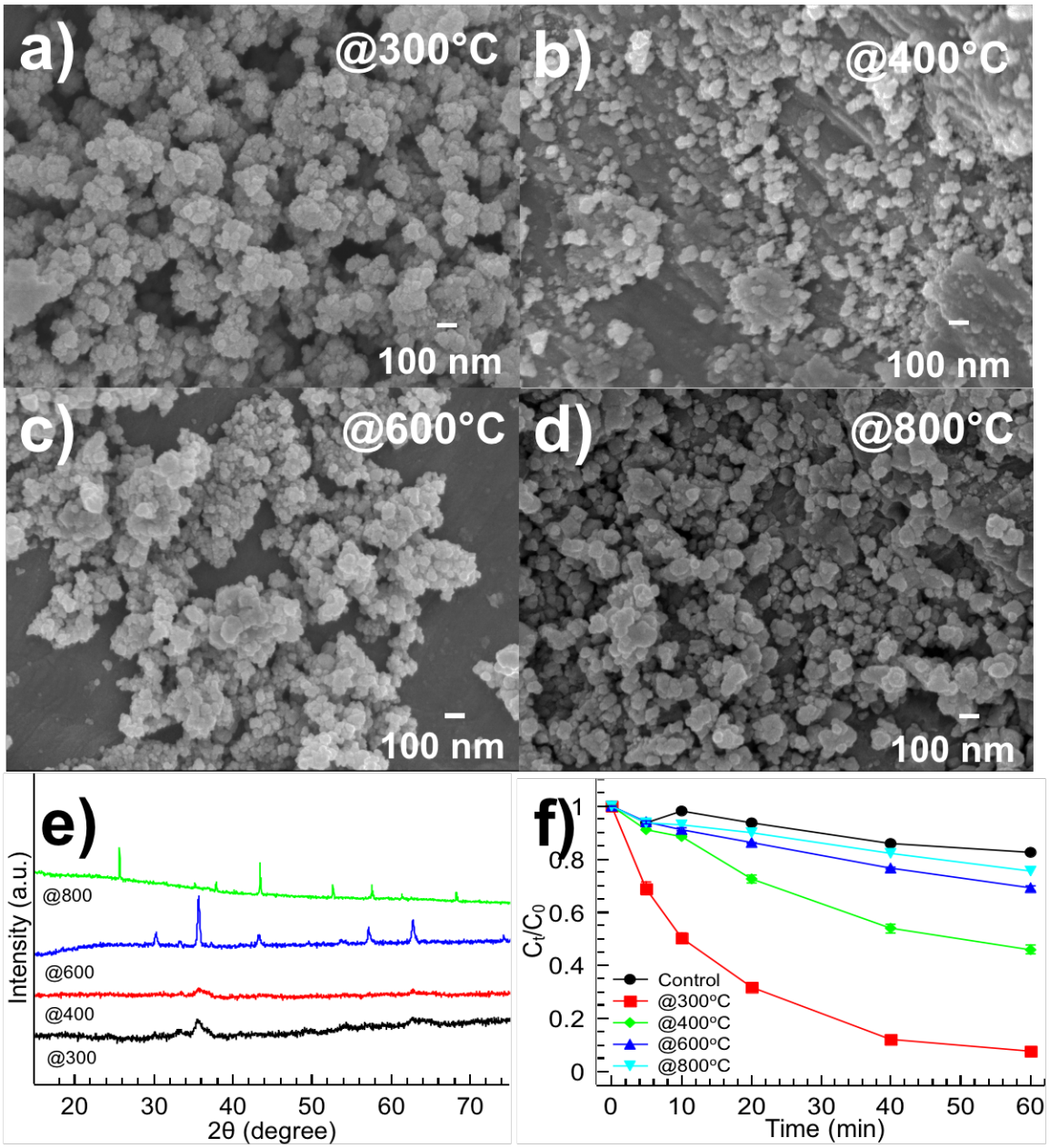

Fig A5.2. Effect of calcination temperature on the morphology (a-d), crystal structure (e) and catalytic performance (f) (Condition: [SMX] = 10 mg L^{-1}, [catalyst loading] = 0.2 g L^{-1}, [Oxone] = 0.10 g L^{-1}, pH = 5) of $CoFe_2O_4$.

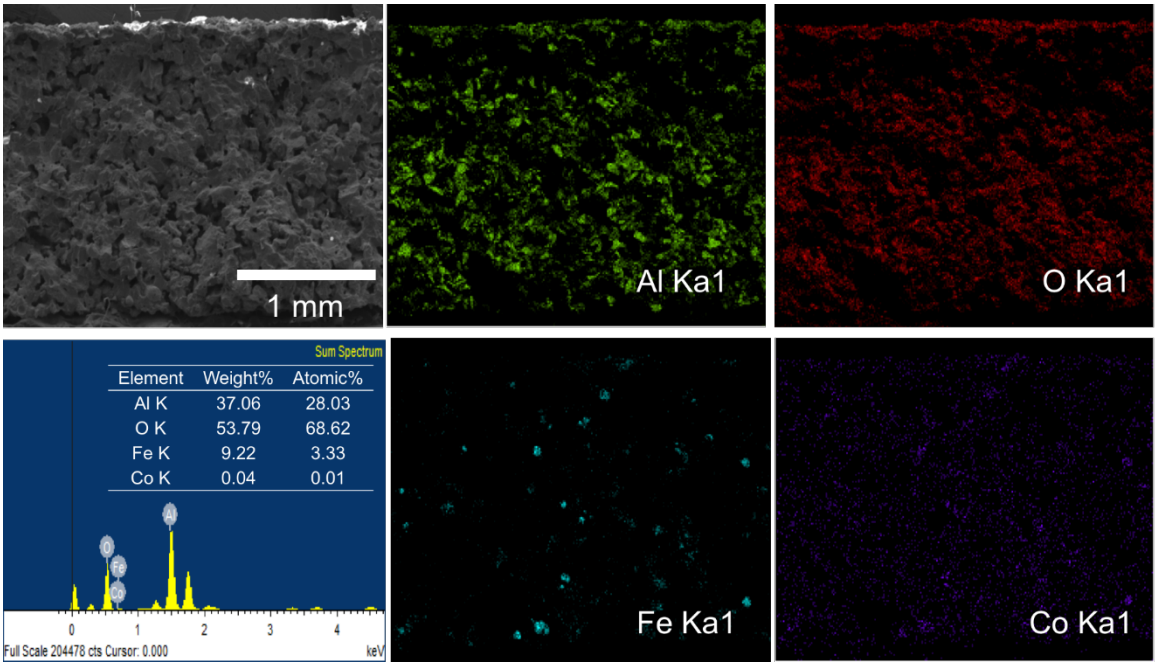

Fig A5.3. SEM-EDX mappings of cross section for the pristine membrane.

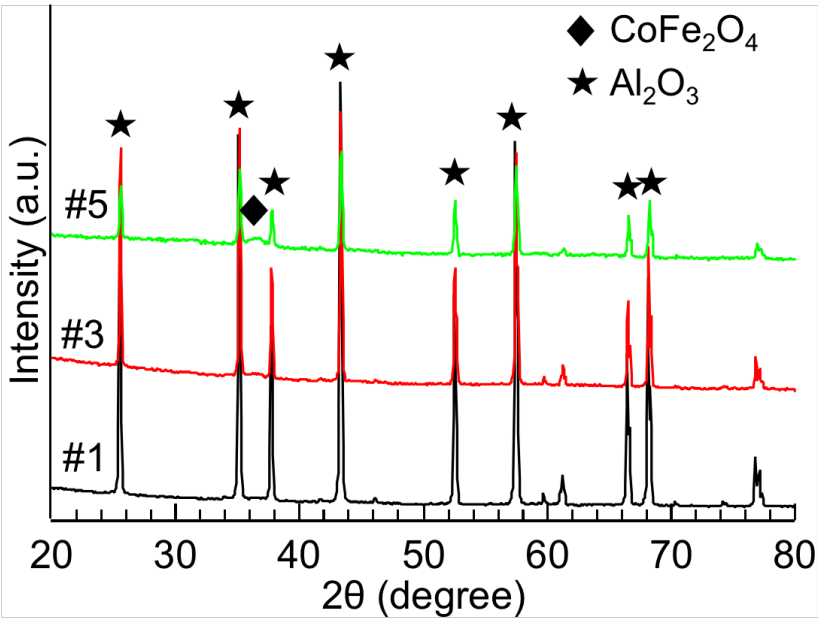

Fig A5.4. XRD patterns of $CoFe_2O_4$ impregnated membrane with different impregnation cycles.

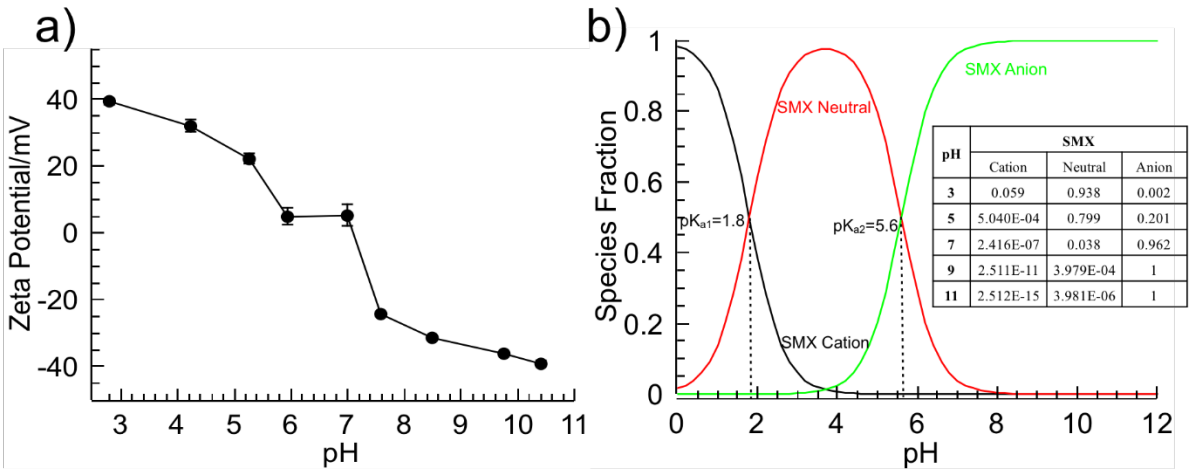

pH	SMX		
	Cation	Neutral	Anion
3	0.059	0.938	0.002
5	5.040E-04	0.799	0.201
7	2.416E-07	0.038	0.962
9	2.511E-11	3.979E-04	1
11	2.512E-15	3.981E-06	1

Fig A5.5. Zeta potential of $CoFe_2O_4$ particles in water (a) and distribution coefficient of SMX molecular (b) as a function of pH value.

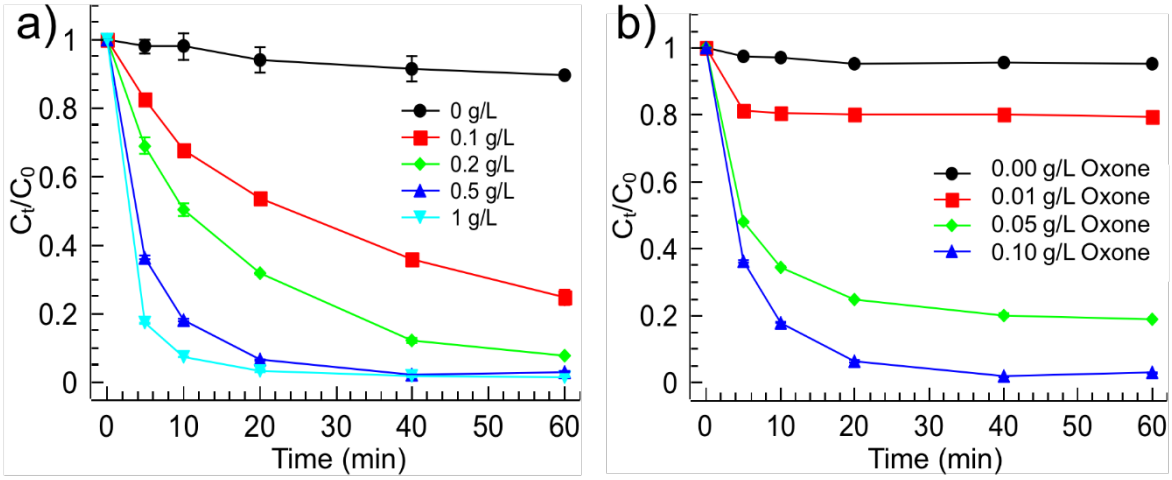

Fig A5.6. The effects of catalyst loading (a) and PMS dosage (b) on SMX degradation in $CoFe_2O_4$/Oxone system. Conditions: initial pH = 5, [SMX] = 10 mg L^{-1}, [Oxone] = 0.10 g L^{-1} (for a) and [$CoFe_2O_4$] = 0.5 g L^{-1} (for b).

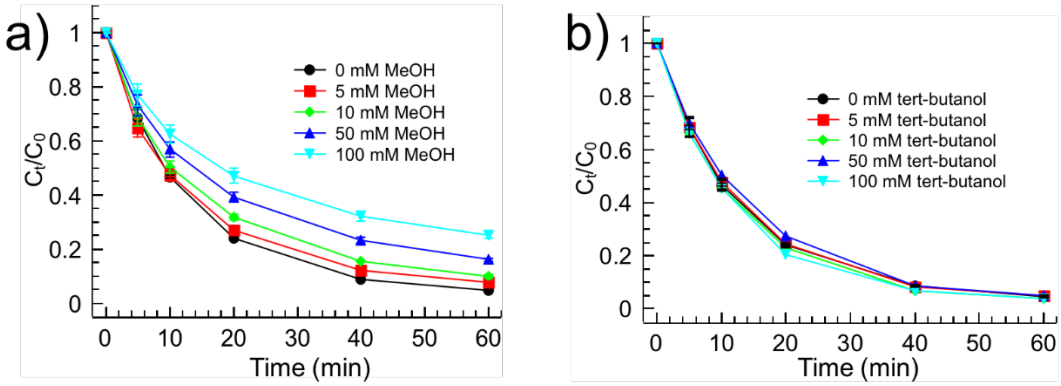

Fig A5.7. The effects of scavengers on SMX degradation in batch experiments.

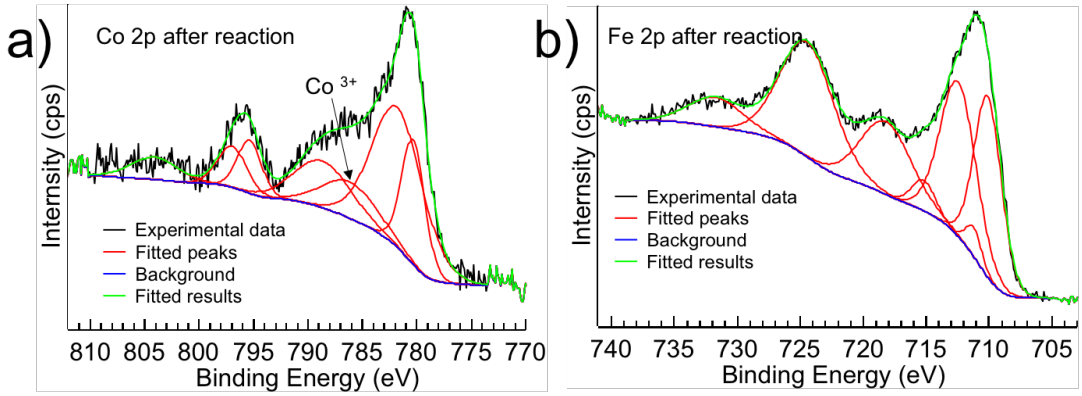

Fig A5.8. The high-resolution XPS spectra of a) Co 2p and b) Fe 2p in used $CoFe_2O_4$.

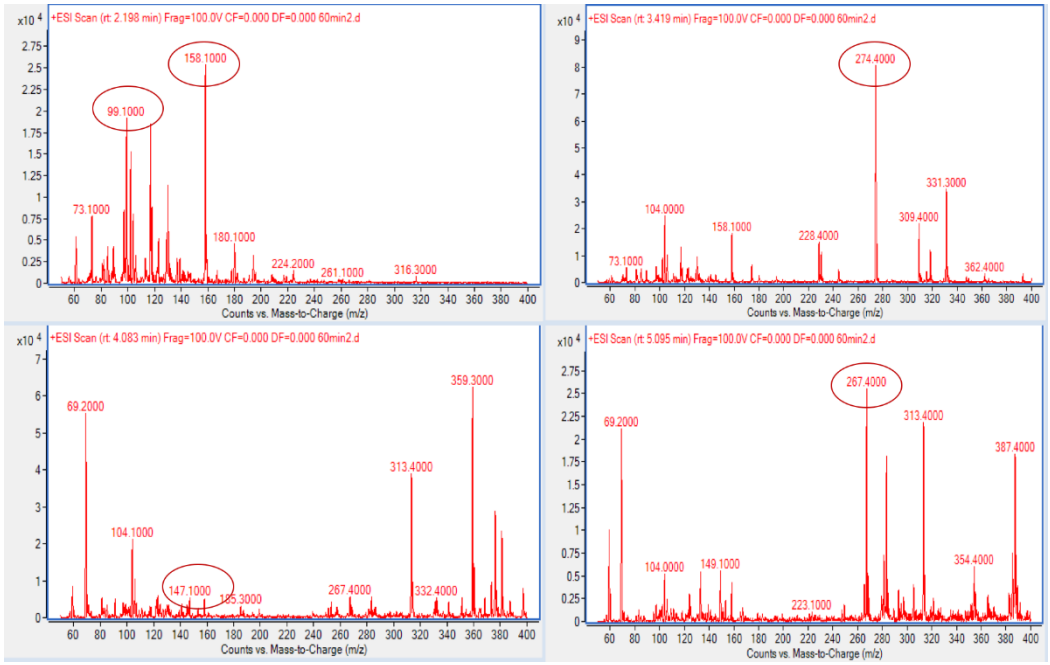

Fig A5.9. Mass spectra in the ES (+) mode for SMX after 60 min reaction.

Table A6.1. The preparation of nano-bimetallic oxides.

Catalysts	$Co(NO_3)_2 \cdot 6H_2O$ (g)	$Fe(NO_3)_3 \cdot 9H_2O$ (g)	Urea (g)	H_2O (mL)
φ=1:0	2.91	0	2	5
φ=3:1	2.18	1.01	2	5
φ=1:1	1.46	2.02	2	5
φ=1:3	0.73	3.03	2	5
φ=0:1	0	4.04	2	5

Table A6.2. Experimental details on the quenching agents.

Quenching agents	Concentration	$k_{\bullet OH}$ ($M^{-1}s^{-1}$)	$k_{SO_4^{\bullet-}}$ ($M^{-1}s^{-1}$)
TBA	0-200 mM	$3.8 - 7.6 \times 10^8$	$4.0 - 9.1 \times 10^5$
MeOH	0-200 mM	$1.2 - 2.8 \times 10^9$	$1.6 - 7.7 \times 10^7$
NB	10 mg L^{-1}	$(3.0\text{-}3.9) \times 10^9$	$<10^6$
BQ	10 mg L^{-1}	--	--
Phenol	10 mg L^{-1}	--	--
NaN_3	5 mM	1.2×10^{10}	2.51×10^9

Table A6.3. The main products detected in different conditions.

m/z	Structure	Detected mode	Relative Intensity (Abund)		
			pH 5	pH 7	pH 9
94	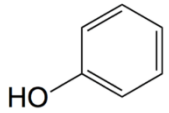	Negative	430.06	N.A.	266.1
98	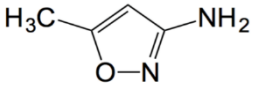	Negative/Positive	2167.28	33075.86	543.4
157	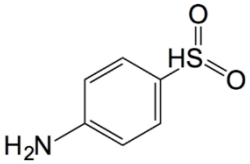	Negative/Positive	3844.64	2621.62	1958.7
174	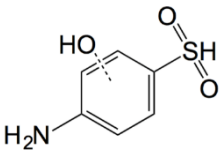	Negative	3531.6	2959.64	2010.8

204	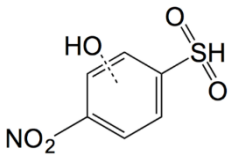	Negative	107137.33	78210.37	54182.14
267	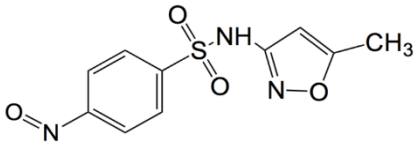	Positive	42569.16	28796.64	23629.8
270	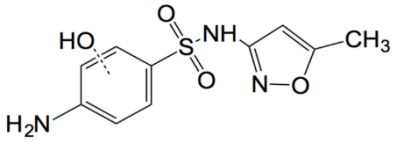	Positive	5043.88	3794.68	3539.94
271	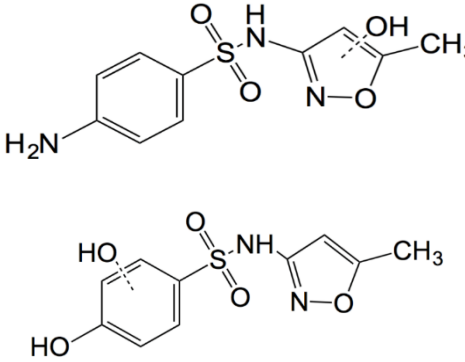	Positive	3647.76	2354.62	1803.68

283	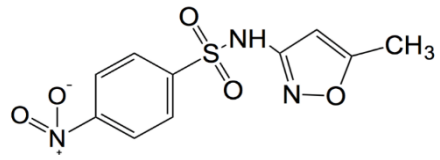	Negative	212366.22	226875.94	142973.39
287	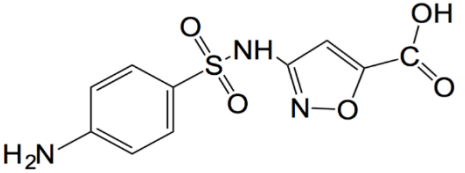	Positive	6818.72	N.A.	N.A.
253	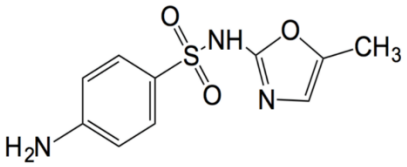	Negative/Positive	5801.34	3839.78	5088.4

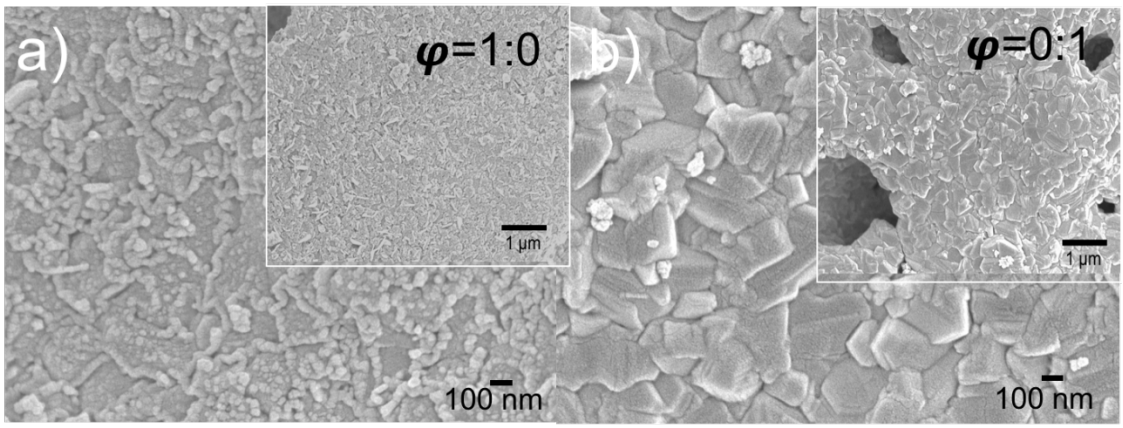

Fig A6.1. FESEM images of pure cobalt oxide (a) and iron oxide (b).

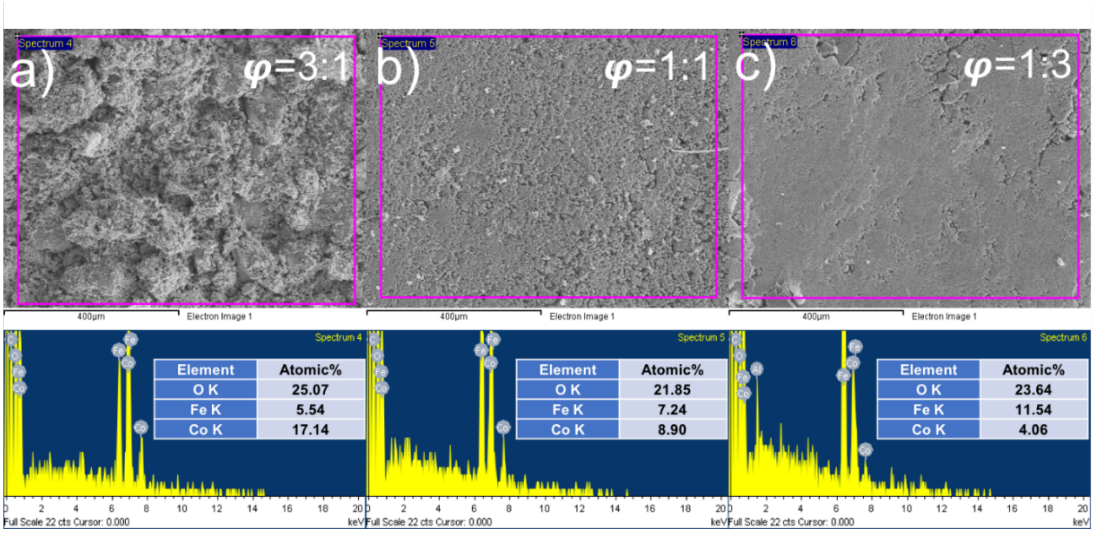

Fig A6.2. EDX analysis of as-prepared nano-bimetallic oxides.

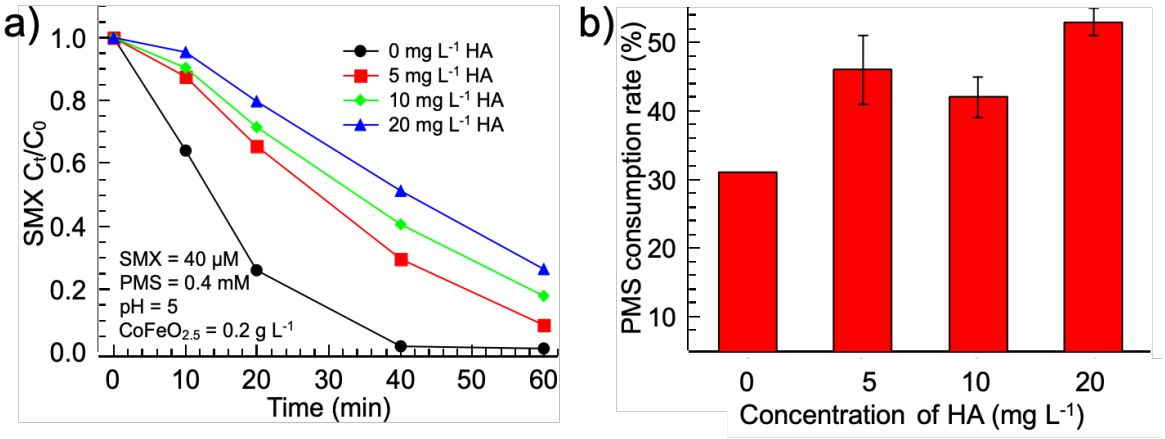

Fig A6.3. Effect of humic acid on the SMX degradation (a) and PMS consumption (b, reaction time = 60 min) in the PMS/$CoFeO_{2.5}$/SMX system.

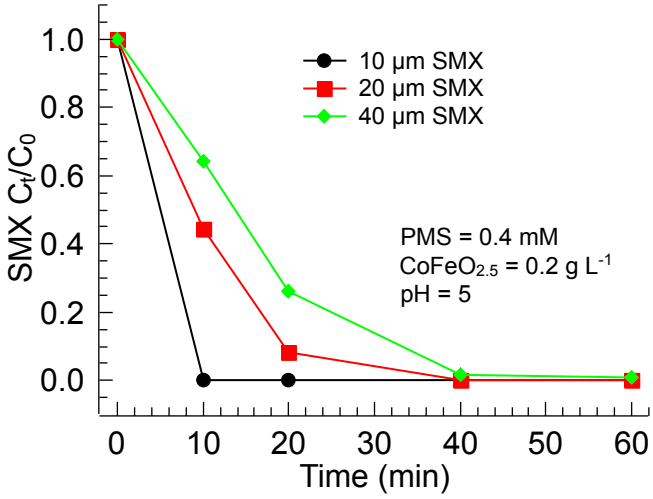

Fig A6.4. Effect of SMX initial concentration on the degradation of SMX in PMS/$CoFeO_{2.5}$/SMX system.

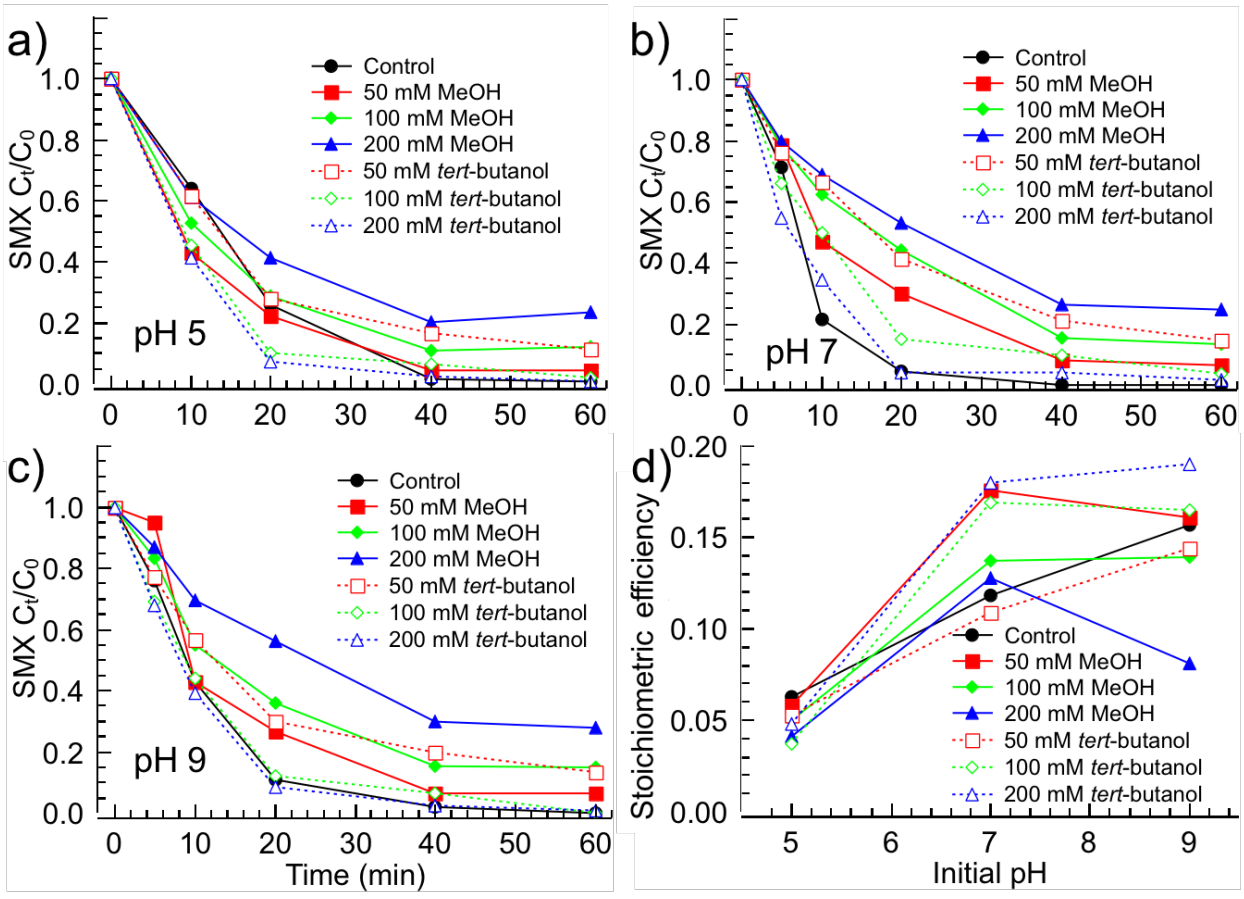

Fig A6.5. Effects of concentration of MeOH and TBA on the degradation of SMX and stoichiometric efficiency (Conditions: [SMX] = 0.04 mM; [PMS] = 0.4 mM; [$CoFeO_{2.5}$] = 0.2 g L^{-1}).

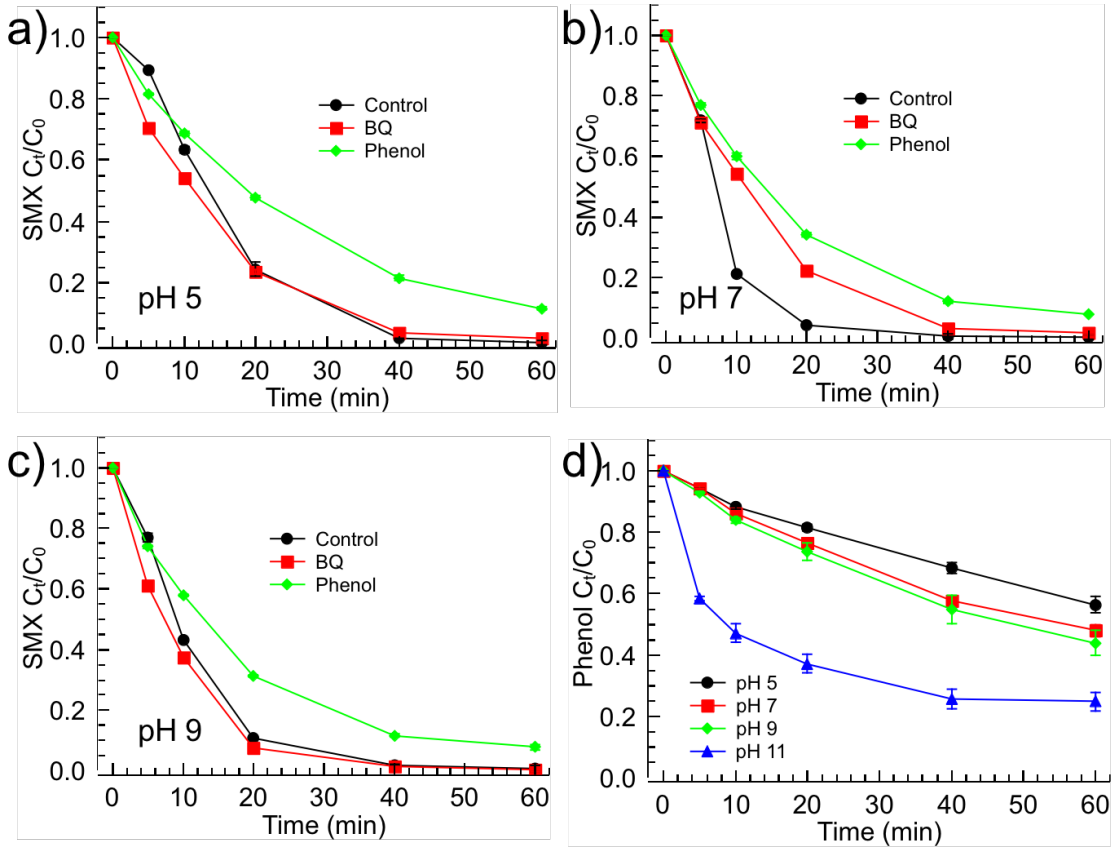

Fig A6.6. Effects of different scavengers on the degradation of SMX (Conditions: [SMX] = 0.04 mM; [PMS] = 0.4 mM; [$CoFeO_{2.5}$] = 0.2 g L^{-1}; [BQ] = 10 mg L^{-1}; [Phenol] = 10 mg L^{-1}).

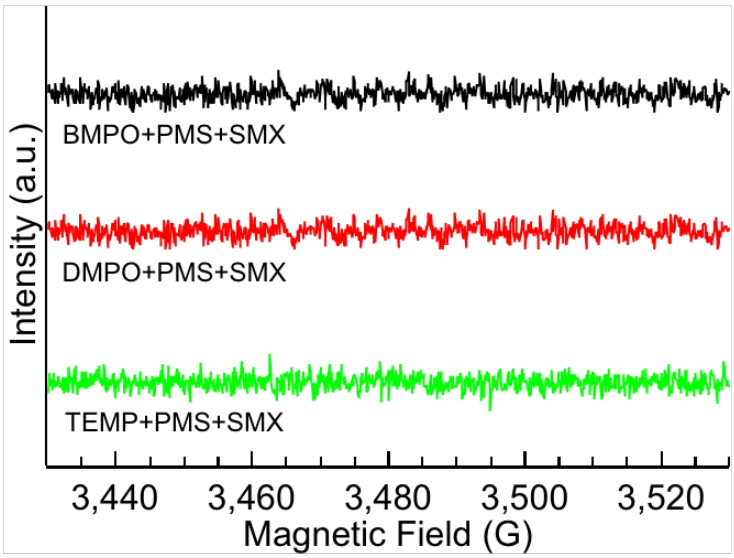

Fig A6.7. EPR spectra using different spin trapping agents in the absence of catalyst.

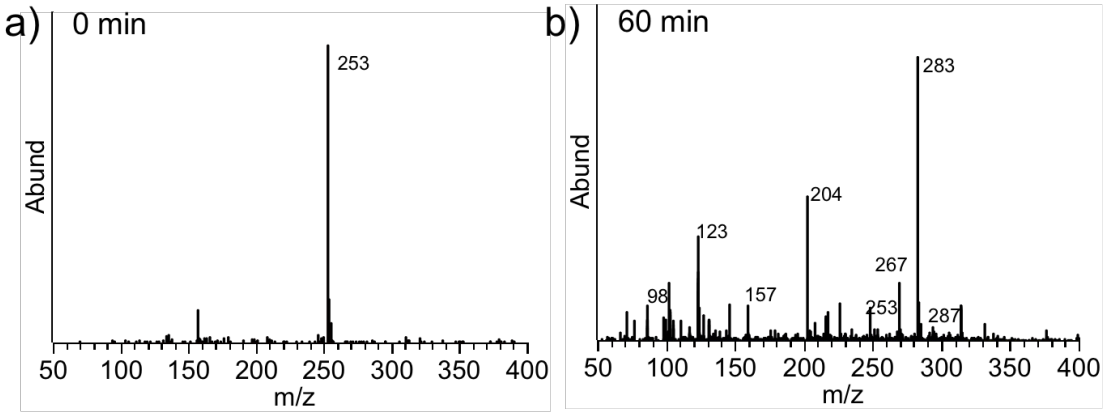

Fig A6.8. Mass spectra for initial SMX (a) and after 60 min reaction (b).

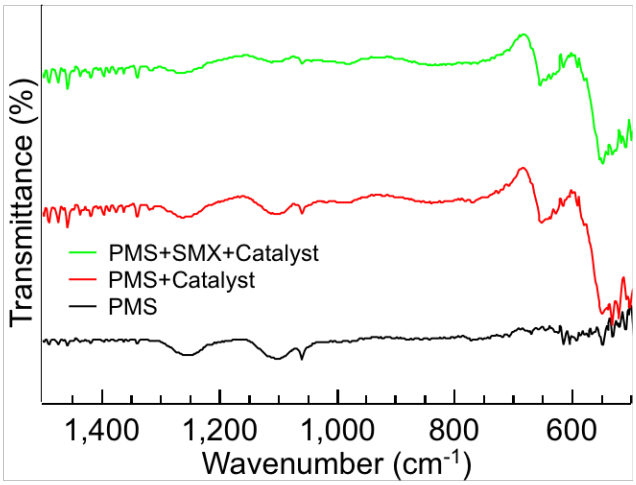

Fig A6.9. FTIR spectra of PMS in the presence and absence of catalyst.

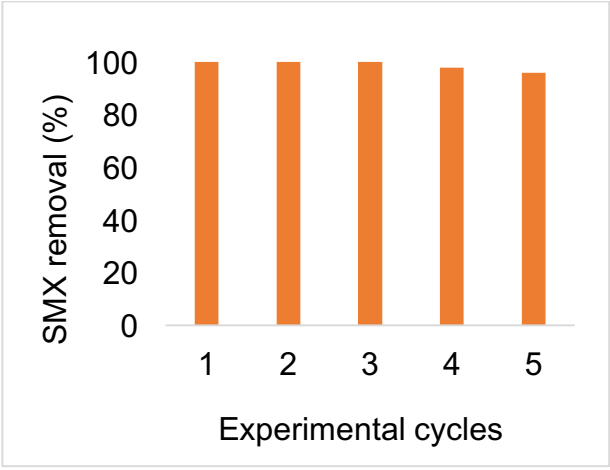

Fig A6.10. Reusability test of the as-prepared catalyst (Conditions: [SMX] = 0.04 mM; [PMS] = 0.4 mM; [$CoFeO_{2.5}$] = 0.2 g L^{-1}; [Reaction time] = 60 min).

APPENDIX B

Bao, Y., Tay, Y.-S., Lim, T.-T., Wang, R., Webster, R.D., Hu, X., Polyacrylonitrile (PAN)-induced carbon membrane with in-situ encapsulated cobalt crystal for hybrid peroxymonosulfate oxidation-filtration process: preparation, characterization and performance evaluation. Chem. Eng. J. 373, 425-436.

APPENDIX C

Bao, Y., Lim, T.-T., Zhong, Z., Wang, R., Hu, X., 2017. Acetic acid-assisted fabrication of hierarchical flower-like Bi_2O_3 for photocatalytic degradation of sulfamethoxazole and rhodamine B under solar irradiation. J. Colloid Interface Sci. 505, 489–499.

APPENDIX D

Bao, Y., Lim, T.-T., Goei, R., Zhong, Z., Wang, R., Hu, X., 2018. One-step construction of heterostructured metal-organics@Bi_2O_3 with improved photoinduced charge transfer and enhanced activity in photocatalytic degradation of sulfamethoxazole under solar light irradiation. Chemosphere 205, 396–403.

APPENDIX E

Bao, Y., Chen Y., Lim, T.-T., Wang, R., Hu, X., 2019. A novel MOF-mediated interfacial polymerization for facile and robust deposition of RO-like polyamide layer on ceramic substrates. Adv. Mater. Interfaces 6, 1900132.

REFERENCES

Ahmed, M.M., Barbati, S., Doumenq, P., Chiron, S., 2012. Sulfate radical anion oxidation of diclofenac and sulfamethoxazole for water decontamination. Chemical engineering journal 197, 440–447.

Ai, L.-H., Jiang, J., 2009. Rapid synthesis of nanocrystalline Co_3O_4 by a microwave-assisted combustion method. Powder Technology 195, 11–14.

Alexy, R., Kümpel, T., Kümmerer, K., 2004. Assessment of degradation of 18 antibiotics in the closed bottle test. Chemosphere 57, 505–512.

Anandan, S., Lee, G.-J., Chen, P.-K., Fan, C., Wu, J.J., 2010. Removal of orange II dye in water by visible light assisted photocatalytic ozonation using Bi_2O_3 and Au/Bi_2O_3 nanorods. Industrial & Engineering Chemistry Research 49, 9729–9737.

Anipsitakis, G.P., Dionysiou, D.D., 2004. Radical generation by the interaction of transition metals with common oxidants. Environmental science & technology 38, 3705–3712.

Anipsitakis, G.P., Dionysiou, D.D., 2003. Degradation of organic contaminants in water with sulfate radicals generated by the conjunction of peroxymonosulfate with cobalt. Environmental science & technology 37, 4790–4797.

Anipsitakis, G.P., Stathatos, E., Dionysiou, D.D., 2005. Heterogeneous activation of oxone using Co_3O_4. The Journal of Physical Chemistry B 109, 13052–13055.

Bai, H., Liu, Z., Sun, D.D., 2012. A hierarchically structured and multifunctional membrane for water treatment. Applied Catalysis B: Environmental 111, 571–577.

Bao, Y., Lim, T.-T., Wang, R., Webster, R.D., Hu, X., 2018a. Urea-assisted one-step synthesis of cobalt ferrite impregnated ceramic membrane for sulfamethoxazole degradation via peroxymonosulfate activation. Chemical Engineering Journal 343, 737–747.

Bao, Y., Niu, J., 2015. Photochemical transformation of tetrabromobisphenol A under simulated sunlight irradiation: Kinetics, mechanism and influencing factors. Chemosphere 134, 550–556.

Bao, Y., Oh, W.-D., Lim, T.-T., Wang, R., Webster, R.D., Hu, X., 2018b. Surface-nucleated heterogeneous growth of zeolitic imidazolate framework–A unique precursor towards catalytic ceramic membranes: Synthesis, characterization and organics degradation. Chemical Engineering Journal 353, 69–79.

Beltrán, F.J., Aguinaco, A., García-Araya, J.F., 2009. Mechanism and kinetics of sulfamethoxazole photocatalytic ozonation in water. Water research 43, 1359–1369.

Biesinger, M.C., Payne, B.P., Grosvenor, A.P., Lau, L.W., Gerson, A.R., Smart, R.S.C., 2011. Resolving surface chemical states in XPS analysis of first row transition metals, oxides and hydroxides: Cr, Mn, Fe, Co and Ni. Applied Surface Science 257, 2717–2730.

Boreen, A.L., Arnold, W.A., McNeill, K., 2004. Photochemical fate of sulfa drugs in the aquatic environment: sulfa drugs containing five-membered heterocyclic groups. Environmental Science & Technology 38, 3933–3940.

Brown, K.D., Kulis, J., Thomson, B., Chapman, T.H., Mawhinney, D.B., 2006. Occurrence of antibiotics in hospital, residential, and dairy effluent, municipal wastewater, and the Rio Grande in New Mexico. Science of the Total Environment 366, 772–783.

Buxton, G.V., Greenstock, C.L., Helman, W.P., Ross, A.B., 1988. Critical review of rate constants for reactions of hydrated electrons, hydrogen atoms and hydroxyl radicals ($\cdot$OH/$\cdot$O- in aqueous solution. Journal of physical and chemical reference data 17, 513–886.

Canonica, S., Jans, U.R.S., Stemmler, K., Hoigne, J., 1995. Transformation kinetics of phenols in water: photosensitization by dissolved natural organic material and aromatic ketones. Environmental science & technology 29, 1822–1831.

Chen, F., Shi, X., Chen, X., Chen, W., 2018. An iron (II) phthalocyanine/poly(vinylidene fluoride) composite membrane with antifouling property and catalytic self-cleaning function for high-efficiency oil/water separation. Journal of Membrane Science 552, 295–304.

Chen, L., Cai, T., Sun, W., Zuo, X., Ding, D., 2017. Mesoporous bouquet-like Co_3O_4 nanostructure for the effective heterogeneous activation of peroxymonosulfate. Journal of the Taiwan Institute of Chemical Engineers 80, 720–727.

Chen, L., Ding, D., Liu, C., Cai, H., Qu, Y., Yang, S., Gao, Y., Cai, T., 2018a. Degradation of norfloxacin by $CoFe_2O_4$-GO composite coupled with peroxymonosulfate: A comparative study and mechanistic consideration. Chemical Engineering Journal 334, 273–284.

Chen, L., Zuo, X., Zhou, L., Huang, Y., Yang, S., Cai, T., Ding, D., 2018b. Efficient heterogeneous activation of peroxymonosulfate by facilely prepared Co/Fe bimetallic oxides: Kinetics and mechanism. Chemical Engineering Journal 345, 364–374.

Chen, Q., Ji, F., Liu, T., Yan, P., Guan, W., Xu, X., 2013. Synergistic effect of bifunctional Co–TiO_2 catalyst on degradation of Rhodamine B: Fenton-photo hybrid process. Chemical engineering journal 229, 57–65.

Chen, W., Chen, R., Zhang, R., Zhang, N., 2018. Simple spectrophotometric determination of sulfate free radicals. Analytical Methods.

Chen, X., Chen, J., Qiao, X., Wang, D., Cai, X., 2008. Performance of nano-Co_3O_4/peroxymonosulfate system: kinetics and mechanism study using Acid Orange 7 as a model compound. Applied Catalysis B: Environmental 80, 116–121.

Chen, X., Oh, W.-D., Hu, Z.-T., Sun, Y.-M., Webster, R.D., Li, S.-Z., Lim, T.-T., 2018. Enhancing sulfacetamide degradation by peroxymonosulfate activation with N-doped graphene produced through delicately-controlled nitrogen functionalization via tweaking thermal annealing processes. Applied Catalysis B: Environmental 225, 243–257.

Cheng, X., Liang, H., Ding, A., Tang, X., Liu, B., Zhu, X., Gan, Z., Wu, D., Li, G., 2017a. Ferrous iron/peroxymonosulfate oxidation as a pretreatment for ceramic ultrafiltration membrane: Control of natural organic matter fouling and degradation of atrazine. Water Research 113, 32–41.

Cheng, X., Liang, H., Ding, A., Zhu, X., Tang, X., Gan, Z., Xing, J., Wu, D., Li, G., 2017b. Application of Fe (II)/peroxymonosulfate for improving ultrafiltration membrane performance in surface water treatment: Comparison with coagulation and ozonation. Water research 124, 298–307.

Cheng, X., Wu, D., Liang, H., Zhu, X., Tang, X., Gan, Z., Xing, J., Luo, X., Li, G., 2018. Effect of sulfate radical-based oxidation pretreatments for mitigating ceramic UF membrane fouling caused by algal extracellular organic matter. Water research 145, 39–49.

Chu, W., Choy, W.K., Kwan, C.Y., 2007. Selection of supported cobalt substrates in the presence of oxone for the oxidation of monuron. Journal of agricultural and food chemistry 55, 5708–5713.

Costa, R.C., Lelis, M.F.F., Oliveira, L.C.A., Fabris, J.D., Ardisson, J.D., Rios, R., Silva, C.N., Lago, R.M., 2006. Novel active heterogeneous Fenton system based on $Fe_{3-x}M_xO_4$ (Fe, Co, Mn, Ni): the role of M^{2+} species on the reactivity towards H_2O_2 reactions. Journal of Hazardous Materials 129, 171–178.

Daimon, T., Hirakawa, T., Kitazawa, M., Suetake, J., Nosaka, Y., 2008. Formation of singlet molecular oxygen associated with the formation of superoxide radicals in aqueous suspensions of TiO_2 photocatalysts. Applied Catalysis A: General 340, 169–175.

Davis, M.E., Davis, R.J., 2012. Fundamentals of chemical reaction engineering. Courier Corporation.

Deng, J., Shao, Y., Gao, N., Tan, C., Zhou, S., Hu, X., 2013a. $CoFe_2O_4$ magnetic nanoparticles as a highly active heterogeneous catalyst of oxone for the degradation of diclofenac in water. Journal of hazardous materials 262, 836–844.

Deng, J., Shao, Y., Gao, N., Xia, S., Tan, C., Zhou, S., Hu, X., 2013b. Degradation of the antiepileptic drug carbamazepine upon different UV-based advanced oxidation processes in water. Chemical engineering journal 222, 150–158.

Ding, S., Niu, J., Bao, Y., Hu, L., 2013. Evidence of superoxide radical contribution to demineralization of sulfamethoxazole by visible-light-driven $Bi_2O_3/Bi_2O_2CO_3/Sr_6Bi_2O_9$ photocatalyst. Journal of hazardous materials 262, 812–818.

Ding, Y., Zhu, L., Huang, A., Zhao, X., Zhang, X., Tang, H., 2012. A heterogeneous Co_3O_4–Bi_2O_3 composite catalyst for oxidative degradation of organic pollutants in the presence of peroxymonosulfate. Catalysis Science & Technology 2, 1977–1984.

Dodd, M.C., Huang, C.-H., 2004. Transformation of the antibacterial agent sulfamethoxazole in reactions with chlorine: kinetics, mechanisms, and pathways. Environmental science & technology 38, 5607–5615.

Dong, Z., Le, X., Dong, C., Zhang, W., Li, X., Ma, J., 2015. Ni@Pd core–shell nanoparticles modified fibrous silica nanospheres as highly efficient and recoverable catalyst for reduction of 4-nitrophenol and hydrodechlorination of 4-chlorophenol. Applied Catalysis B: Environmental 162, 372–380.

Dou, S., Dong, C.-L., Hu, Z., Huang, Y.-C., Chen, J., Tao, L., Yan, D., Chen, D., Shen, S., Chou, S., 2017. Atomic-Scale CoO_x Species in Metal–Organic Frameworks for Oxygen Evolution Reaction. Advanced Functional Materials 27.

Du, Y., Ma, W., Liu, P., Zou, B., Ma, J., 2016. Magnetic $CoFe_2O_4$ nanoparticles supported on titanate nanotubes ($CoFe_2O_4$/TNTs) as a novel heterogeneous catalyst for peroxymonosulfate activation and degradation of organic pollutants. Journal of hazardous materials 308, 58–66.

Duan, X., Ao, Z., Sun, H., Indrawirawan, S., Wang, Y., Kang, J., Liang, F., Zhu, Z.H., Wang, S., 2015a. Nitrogen-doped graphene for generation and evolution of reactive radicals by metal-free catalysis. ACS applied materials & interfaces 7, 4169–4178.

Duan, X., Ao, Z., Sun, H., Zhou, L., Wang, G., Wang, S., 2015b. Insights into N-doping in single-walled carbon nanotubes for enhanced activation of superoxides: a mechanistic study. Chemical Communications 51, 15249–15252.

Duan, X., Ao, Z., Zhou, L., Sun, H., Wang, G., Wang, S., 2016. Occurrence of radical and nonradical pathways from carbocatalysts for aqueous and nonaqueous catalytic oxidation. Applied Catalysis B: Environmental 188, 98–105.

Duan, X., Sun, H., Wang, Y., Kang, J., Wang, S., 2014. N-doping-induced nonradical reaction on single-walled carbon nanotubes for catalytic phenol oxidation. Acs Catalysis 5, 553–559.

Eberson, L., 1982a. Electron-transfer reactions in organic chemistry, in: Advances in Physical Organic Chemistry. Elsevier, pp. 79–185.

Eberson, L., 1982b. Electron-transfer reactions in organic chemistry. Advances in physical organic chemistry 18, 79–185.

Ermer, O., Röbke, C., 2003. Crystal structure and chemical stabilization of the triple salt $(KHSO_5)_2 \cdot KHSO_4 \cdot K_2SO_4$. Helvetica chimica acta 86, 2908–2913.

Fang, G.-D., Dionysiou, D.D., Wang, Y., Al-Abed, S.R., Zhou, D.-M., 2012. Sulfate radical-based degradation of polychlorinated biphenyls: effects of chloride ion and reaction kinetics. Journal of hazardous materials 227, 394–401.

Feng, Y., Wu, D., Deng, Y., Zhang, T., Shih, K., 2016. Sulfate radical-mediated degradation of sulfadiazine by $CuFeO_2$ rhombohedral crystal-catalyzed peroxymonosulfate: synergistic effects and mechanisms. Environmental science & technology 50, 3119–3127.

Gao, S., Zhao, Z., Xu, Y., Tian, J., Qi, H., Lin, W., Cui, F., 2014. Oxidation of sulfamethoxazole (SMX) by chlorine, ozone and permanganate—a comparative study. Journal of hazardous materials 274, 258–269.

Ghanbari, F., Moradi, M., 2017. Application of peroxymonosulfate and its activation methods for degradation of environmental organic pollutants. Chemical Engineering Journal 310, 41–62.

Godfrey, E., Woessner, W.W., Benotti, M.J., 2007. Pharmaceuticals in On-Site Sewage Effluent and Ground Water, Western Montana. Groundwater 45, 263–271.

Goei, R., Dong, Z., Lim, T.-T., 2013. High-permeability pluronic-based TiO_2 hybrid photocatalytic membrane with hierarchical porosity: fabrication, characterizations and performances. Chemical engineering journal 228, 1030–1039.

Gonzalez, J., Torrent-Sucarrat, M., Anglada, J.M., 2010. The reactions of SO_3 with HO_2 radical and $H_2O \cdot\cdot HO_2$ radical complex. Theoretical study on the atmospheric formation of HSO_5 and H_2SO_4. Physical Chemistry Chemical Physics 12, 2116–2125.

Guan, Y.-H., Ma, J., Li, X.-C., Fang, J.-Y., Chen, L.-W., 2011. Influence of pH on the formation of sulfate and hydroxyl radicals in the UV/peroxymonosulfate system. Environmental science & technology 45, 9308–9314.

Guan, Y.-H., Ma, J., Ren, Y.-M., Liu, Y.-L., Xiao, J.-Y., Lin, L., Zhang, C., 2013. Efficient degradation of atrazine by magnetic porous copper ferrite catalyzed peroxymonosulfate oxidation via the formation of hydroxyl and sulfate radicals. Water research 47, 5431–5438.

Guo, W., Su, S., Yi, C., Ma, Z., 2013. Degradation of antibiotics amoxicillin by Co_3O_4-catalyzed peroxymonosulfate system. Environmental Progress & Sustainable Energy 32, 193–197.

Hardjono, Y., Sun, H., Tian, H., Buckley, C.E., Wang, S., 2011. Synthesis of Co oxide doped carbon aerogel catalyst and catalytic performance in heterogeneous oxidation of phenol in water. Chemical engineering journal 174, 376–382.

Hayon, E., Treinin, A., Wilf, J., 1972. Electronic spectra, photochemistry, and autoxidation mechanism of the sulfite-bisulfite-pyrosulfite systems. SO_2-, SO_3-, SO_4-, and SO_5-radicals. Journal of the American Chemical Society 94, 47–57.

Herrero, M., Benito, P., Labajos, F., Rives, V., 2007. Nanosize cobalt oxide-containing catalysts obtained through microwave-assisted methods. Catalysis Today 128, 129–137.

Hirsch, R., Ternes, T., Haberer, K., Kratz, K.-L., 1999. Occurrence of antibiotics in the aquatic environment. Science of the Total Environment 225, 109–118.

Hu, L., Flanders, P.M., Miller, P.L., Strathmann, T.J., 2007. Oxidation of sulfamethoxazole and related antimicrobial agents by TiO_2 photocatalysis. Water Research 41, 2612–2626.

Hu, L., Yang, F., Lu, W., Hao, Y., Yuan, H., 2013. Heterogeneous activation of oxone with CoMg/SBA-15 for the degradation of dye Rhodamine B in aqueous solution. Applied Catalysis B: Environmental 134, 7–18.

Hu, L., Yang, F., Zou, L., Yuan, H., Hu, X., 2015. CoFe/SBA-15 catalyst coupled with peroxymonosulfate for heterogeneous catalytic degradation of rhodamine B in water. Chinese Journal of Catalysis 36, 1785–1797.

Hu, L., Yang, X., Dang, S., 2011. An easily recyclable Co/SBA-15 catalyst: Heterogeneous activation of peroxymonosulfate for the degradation of phenol in water. Applied Catalysis B: Environmental 102, 19–26.

Hu, P., Long, M., 2016. Cobalt-catalyzed sulfate radical-based advanced oxidation: a review on heterogeneous catalysts and applications. Applied Catalysis B: Environmental 181, 103–117.

Huang, G.-X., Wang, C.-Y., Yang, C.-W., Guo, P.-C., Yu, H.-Q., 2017. Degradation of bisphenol A by peroxymonosulfate catalytically activated with $Mn_{1.8}Fe_{1.2}O_4$ nanospheres: synergism between Mn and Fe. Environmental science & technology 51, 12611–12618.

Jansomboon, W., Boontanon, S.K., Boontanon, N., Polprasert, C., Da, C.T., 2016. Monitoring and determination of sulfonamide antibiotics (sulfamethoxydiazine, sulfamethazine, sulfamethoxazole and sulfadiazine) in imported Pangasius catfish products in Thailand using liquid chromatography coupled with tandem mass spectrometry. Food chemistry 212, 635–640.

Ji, Y., Fan, Y., Liu, K., Kong, D., Lu, J., 2015. Thermo activated persulfate oxidation of antibiotic sulfamethoxazole and structurally related compounds. Water research 87, 1–9.

Kang, M., Song, M.W., Lee, C.H., 2003. Catalytic carbon monoxide oxidation over CoO_x/CeO_2 composite catalysts. Applied Catalysis A: General 251, 143–156.

Kermanpur, A., Ghassemali, E., Salemizadeh, S., 2008. Synthesis and characterisation of microporous titania membranes by dip-coating of anodised alumina substrates using sol–gel method. Journal of Alloys and Compounds 461, 331–335.

Kim, J., Edwards, J.O., 1995. A study of cobalt catalysis and copper modification in the coupled decompositions of hydrogen peroxide and peroxomonosulfate ion. Inorganica chimica acta 235, 9–13.

Kim, S.-B., Corapcioglu, M.Y., 2002. Contaminant transport in riverbank filtration in the presence of dissolved organic matter and bacteria: a kinetic approach. Journal of Hydrology 266, 269–283.

Kim, S.J., Lee, S.W., An, S.Y., Kim, C.S., 2000. Mössbauer studies of superexchange interactions and atomic migration in $CoFe_2O_4$. Journal of magnetism and magnetic materials 215, 210–212.

Kon'kova, T.V., Prosvirin, I.P., Alekhina, M.B., Skornikova, S.A., 2015. Cobalt-containing catalysts based on Al_2O_3 for the oxidative destruction of organic dyes in the aqueous phase. Kinetics and Catalysis 56, 206–211.

Lente, G., Kalmár, J., Baranyai, Z., Kun, A., Kék, I., Bajusz, D., Takács, M., Veres, L., Fábián, I., 2009. One-versus two-electron oxidation with peroxomonosulfate ion: reactions

with iron (II), vanadium (IV), halide ions, and photoreaction with cerium (III). Inorganic chemistry 48, 1763–1773.

Li, L., Zhou, G., Shan, X.-Y., Pei, S., Li, F., Cheng, H.-M., 2014. Co_3O_4 mesoporous nanostructures@ graphene membrane as an integrated anode for long-life lithium-ion batteries. Journal of Power Sources 255, 52–58.

Li, N.N., Fane, A.G., Ho, W.W., Matsuura, T., 2011. Advanced membrane technology and applications. John Wiley & Sons.

Li, Q., Jia, R., Shao, J., He, Y., 2019. Photocatalytic degradation of amoxicillin via TiO_2 nanoparticle coupling with a novel submerged porous ceramic membrane reactor. Journal of Cleaner Production 209, 755–761.

Li, S.-L., Xu, Q., 2013. Metal–organic frameworks as platforms for clean energy. Energy & Environmental Science 6, 1656–1683.

Li, W., Wu, P., Zhu, Y., Huang, Z., Lu, Y., Li, Y., Dang, Z., Zhu, N., 2015. Catalytic degradation of bisphenol A by CoMnAl mixed metal oxides catalyzed peroxymonosulfate: performance and mechanism. Chemical Engineering Journal 279, 93–102.

Li, X., Wang, Z., Zhang, B., Rykov, A.I., Ahmed, M.A., Wang, J., 2016. $Fe_xCo_{3-x}O_4$ nanocages derived from nanoscale metal–organic frameworks for removal of bisphenol A by activation of peroxymonosulfate. Applied Catalysis B: Environmental 181, 788–799.

Li, Z.H., Zhao, T.P., Zhan, X.Y., Gao, D.S., Xiao, Q.Z., Lei, G.T., 2010. High capacity three-dimensional ordered macroporous $CoFe_2O_4$ as anode material for lithium ion batteries. Electrochimica Acta 55, 4594–4598.

Liang, C., Su, H.-W., 2009. Identification of sulfate and hydroxyl radicals in thermally activated persulfate. Industrial & Engineering Chemistry Research 48, 5558–5562.

Liang, H., Sun, H., Patel, A., Shukla, P., Zhu, Z.H., Wang, S., 2012a. Excellent performance of mesoporous Co_3O_4/MnO_2 nanoparticles in heterogeneous activation of peroxymonosulfate for phenol degradation in aqueous solutions. Applied Catalysis B: Environmental 127, 330–335.

Liang, H., Ting, Y.Y., Sun, H., Ang, H.M., Tadé, M.O., Wang, S., 2012b. Solution combustion synthesis of Co oxide-based catalysts for phenol degradation in aqueous solution. Journal of colloid and interface science 372, 58–62.

Lim, T.-T., Yap, P.-S., Srinivasan, M., Fane, A.G., 2011. TiO_2/AC composites for synergistic adsorption-photocatalysis processes: present challenges and further developments for

water treatment and reclamation. Critical reviews in environmental science and technology 41, 1173–1230.

Lin, K.-Y.A., Chang, H.-A., Chen, R.-C., 2015a. MOF-derived magnetic carbonaceous nanocomposite as a heterogeneous catalyst to activate oxone for decolorization of Rhodamine B in water. Chemosphere 130, 66–72.

Lin, K.-Y.A., Chen, B.-C., 2016. Efficient elimination of caffeine from water using Oxone activated by a magnetic and recyclable cobalt/carbon nanocomposite derived from ZIF-67. Dalton Transactions 45, 3541–3551.

Lin, K.-Y.A., Hsu, F.-K., Lee, W.-D., 2015b. Magnetic cobalt–graphene nanocomposite derived from self-assembly of MOFs with graphene oxide as an activator for peroxymonosulfate. Journal of Materials Chemistry A 3, 9480–9490.

Lindberg, R., Jarnheimer, P.-AAke, Olsen, B., Johansson, M., Tysklind, M., 2004. Determination of antibiotic substances in hospital sewage water using solid phase extraction and liquid chromatography/mass spectrometry and group analogue internal standards. Chemosphere 57, 1479–1488.

Liu, H., Bruton, T.A., Doyle, F.M., Sedlak, D.L., 2014. In situ chemical oxidation of contaminated groundwater by persulfate: decomposition by Fe (III)-and Mn (IV)-containing oxides and aquifer materials. Environmental science & technology 48, 10330–10336.

Liu, H., Feng, Y., Chen, D., Li, C., Cui, P., Yang, J., 2015. Noble metal-based composite nanomaterials fabricated via solution-based approaches. Journal of Materials Chemistry A 3, 3182–3223.

Liu, Q., Zhang, J., 2013. Graphene Supported Co-g-C_3N_4 as a Novel Metal–Macrocyclic Electrocatalyst for the Oxygen Reduction Reaction in Fuel Cells. Langmuir 29, 3821–3828.

Luo, X., Liang, H., Qu, F., Ding, A., Cheng, X., Tang, C.Y., Li, G., 2018. Free-standing hierarchical α-MnO_2@CuO membrane for catalytic filtration degradation of organic pollutants. Chemosphere 200, 237–247.

Lutze, H.V., Bircher, S., Rapp, I., Kerlin, N., Bakkour, R., Geisler, M., von Sonntag, C., Schmidt, T.C., 2015. Degradation of chlorotriazine pesticides by sulfate radicals and the influence of organic matter. Environmental science & technology 49, 1673–1680.

Ma, J., Sui, M., Zhang, T., Guan, C., 2005. Effect of pH on MnO_x/GAC catalyzed ozonation for degradation of nitrobenzene. Water Research 39, 779–786.

Ma, T., Liu, L., Meng, B., Gao, J., Wang, S., Liu, S., 2019. Heterogeneous activation of peroxymonosulfate via a Ag-$La_{0.8}Ca_{0.2}Fe_{0.94}O_{3-\delta}$ perovskite hollow fibre membrane reactor for dye degradation. Separation and Purification Technology 211, 298–302.

Matta, R., Tlili, S., Chiron, S., Barbati, S., 2011. Removal of carbamazepine from urban wastewater by sulfate radical oxidation. Environmental chemistry letters 9, 347–353.

Molinari, R., Mungari, M., Drioli, E., Di Paola, A., Loddo, V., Palmisano, L., Schiavello, M., 2000. Study on a photocatalytic membrane reactor for water purification. Catalysis Today 55, 71–78.

Molinari, R., Pirillo, F., Falco, M., Loddo, V., Palmisano, L., 2004. Photocatalytic degradation of dyes by using a membrane reactor. Chemical Engineering and Processing: Process Intensification 43, 1103–1114.

Muhammad, S., Saputra, E., Sun, H., Ang, H.-M., Tadé, M.O., Wang, S., 2013. Removal of phenol using sulphate radicals activated by natural zeolite-supported cobalt catalysts. Water, Air, & Soil Pollution 224, 1721.

Muhammad, S., Saputra, E., Sun, H., Ang, H.-M., Tadé, M.O., Wang, S., 2012a. Heterogeneous catalytic oxidation of aqueous phenol on red mud-supported cobalt catalysts. Industrial & Engineering Chemistry Research 51, 15351–15359.

Muhammad, S., Saputra, E., Sun, H., Izidoro, J. de C., Fungaro, D.A., Ang, H.M., Tadé, M.O., Wang, S., 2012b. Coal fly ash supported Co_3O_4 catalysts for phenol degradation using peroxymonosulfate. Rsc Advances 2, 5645–5650.

Nagpal, N.K., 2004. Technical Report, Water Quality Guidelines for Cobalt. Government of British Columbia.

Neta, P., Huie, R.E., Ross, A.B., 1988. Rate constants for reactions of inorganic radicals in aqueous solution. Journal of Physical and Chemical Reference Data 17, 1027–1284.

Neta, P., Madhavan, V., Zemel, H., Fessenden, R.W., 1977. Rate constants and mechanism of reaction of sulfate radical anion with aromatic compounds. Journal of the American Chemical Society 99, 163–164.

Nikolaou, A., Meric, S., Fatta, D., 2007. Occurrence patterns of pharmaceuticals in water and wastewater environments. Analytical and bioanalytical chemistry 387, 1225–1234.

Norman, R.O.C., Storey, P.M., West, P.R., 1970. Electron spin resonance studies. Part XXV. Reactions of the sulphate radical anion with organic compounds. Journal of the Chemical Society B: Physical Organic 1087–1095.

Oh, W.-D., Chang, V.W., Lim, T.-T., 2017. A comprehensive performance evaluation of heterogeneous $Bi_2Fe_4O_9$/peroxymonosulfate system for sulfamethoxazole degradation. Environmental Science and Pollution Research 1–10.

Oh, W.-D., Dong, Z., Lim, T.-T., 2016. Generation of sulfate radical through heterogeneous catalysis for organic contaminants removal: Current development, challenges and prospects. Applied Catalysis B: Environmental 194, 169–201.

Oh, W.-D., Lua, S.-K., Dong, Z., Lim, T.-T., 2014. High surface area DPA-hematite for efficient detoxification of bisphenol A via peroxymonosulfate activation. Journal of Materials Chemistry A 2, 15836–15845.

Olmez-Hanci, T., Arslan-Alaton, I., 2013. Comparison of sulfate and hydroxyl radical based advanced oxidation of phenol. Chemical Engineering Journal 224, 10–16.

Organization, W.H., Supply, W.J.W., Programme, S.M., 2015. Progress on sanitation and drinking water: 2015 update and MDG assessment. World Health Organization.

O'Shea, K.E., Dionysiou, D.D., 2012. Advanced oxidation processes for water treatment. ACS Publications.

Petitto, S.C., Marsh, E.M., Carson, G.A., Langell, M.A., 2008. Cobalt oxide surface chemistry: The interaction of CoO(100), Co_3O_4(110) and Co_3O_4(111) with oxygen and water. Journal of Molecular Catalysis A: Chemical 281, 49–58.

Petran, A., Radu, T., Culic, B., Turcu, R., 2016. Tailoring the properties of magnetite nanoparticles clusters by coating with double inorganic layers. Applied Surface Science 390, 1–6.

Qi, F., Chu, W., Xu, B., 2013. Catalytic degradation of caffeine in aqueous solutions by cobalt-MCM41 activation of peroxymonosulfate. Applied Catalysis B: Environmental 134, 324–332.

Raja, P., Bensimon, M., Klehm, U., Albers, P., Laub, D., Kiwi-Minsker, L., Renken, A., Kiwi, J., 2007. Highly dispersed PTFE/Co_3O_4 flexible films as photocatalyst showing fast kinetic performance for the discoloration of azo-dyes under solar irradiation. Journal of Photochemistry and Photobiology A: Chemistry 187, 332–338.

Rani, S.K., Easwaramoorthy, D., Bilal, I.M., Palanichamy, M., 2009. Studies on Mn (II)-catalyzed oxidation of α-amino acids by peroxomonosulphate in alkaline medium-deamination and decarboxylation: A kinetic approach. Applied Catalysis A: General 369, 1–7.

Ren, Y., Lin, L., Ma, J., Yang, J., Feng, J., Fan, Z., 2015. Sulfate radicals induced from peroxymonosulfate by magnetic ferrospinel MFe_2O_4 (M=Co, Cu, Mn, and Zn) as

heterogeneous catalysts in the water. Applied Catalysis B: Environmental 165, 572–578.

Richardson, J.T., 2013. Principles of catalyst development. Springer.

Rizzo, L., Manaia, C., Merlin, C., Schwartz, T., Dagot, C., Ploy, M.C., Michael, I., Fatta-Kassinos, D., 2013. Urban wastewater treatment plants as hotspots for antibiotic resistant bacteria and genes spread into the environment: a review. Science of the total environment 447, 345–360.

Rodriguez-Narvaez, O.M., Peralta-Hernandez, J.M., Goonetilleke, A., Bandala, E.R., 2017. Treatment technologies for emerging contaminants in water: A review. Chemical Engineering Journal 323, 361–380.

Romanos, G., Athanasekou, C., Likodimos, V., Aloupogiannis, P., Falaras, P., 2013. Hybrid ultrafiltration/photocatalytic membranes for efficient water treatment. Industrial & Engineering Chemistry Research 52, 13938–13947.

Romanos, G.E., Athanasekou, C.P., Katsaros, F.K., Kanellopoulos, N.K., Dionysiou, D.D., Likodimos, V., Falaras, P., 2012. Double-side active TiO_2-modified nanofiltration membranes in continuous flow photocatalytic reactors for effective water purification. Journal of Hazardous materials 211, 304–316.

Ryan, C.C., Tan, D.T., Arnold, W.A., 2011. Direct and indirect photolysis of sulfamethoxazole and trimethoprim in wastewater treatment plant effluent. Water research 45, 1280–1286.

Sadri, F., Ramazani, A., Massoudi, A., Khoobi, M., Azizkhani, V., Tarasi, R., Dolatyari, L., Min, B.-K., 2014. Magnetic $CoFe_2O_4$ nanoparticles as an efficient catalyst for the oxidation of alcohols to carbonyl compounds in the presence of oxone as an oxidant. Bull. Korean Chem. Soc 35, 2029.

Salunkhe, R.R., Tang, J., Kamachi, Y., Nakato, T., Kim, J.H., Yamauchi, Y., 2015. Asymmetric supercapacitors using 3D nanoporous carbon and cobalt oxide electrodes synthesized from a single metal–organic framework. ACS nano 9, 6288–6296.

Saputra, E., Muhammad, S., Sun, H., Ang, H.M., Tadé, M.O., Wang, S., 2012. Red mud and fly ash supported Co catalysts for phenol oxidation. Catalysis Today 190, 68–72.

Segura, P.A., François, M., Gagnon, C., Sauvé, S., 2009. Review of the occurrence of anti-infectives in contaminated wastewaters and natural and drinking waters. Environmental health perspectives 117, 675.

Sehested, K., Rasmussen, O.L., Fricke, H., 1968. Rate constants of OH with HO_2, O_2-, and H_2O_2+ from hydrogen peroxide formation in pulse-irradiated oxygenated water. The Journal of Physical Chemistry 72, 626–631.

Senapati, K.K., Borgohain, C., Phukan, P., 2011. Synthesis of highly stable $CoFe_2O_4$ nanoparticles and their use as magnetically separable catalyst for Knoevenagel reaction in aqueous medium. Journal of Molecular Catalysis A: Chemical 339, 24–31.

Shah, N.S., He, X., Khan, H.M., Khan, J.A., O'Shea, K.E., Boccelli, D.L., Dionysiou, D.D., 2013. Efficient removal of endosulfan from aqueous solution by UV-C/peroxides: a comparative study. Journal of hazardous materials 263, 584–592.

Shao, J., Wan, Z., Liu, H., Zheng, Huiyuan, Gao, T., Shen, M., Qu, Q., Zheng, Honghe, 2014. Metal organic frameworks-derived Co_3O_4 hollow dodecahedrons with controllable interiors as outstanding anodes for Li storage. Journal of Materials Chemistry A 2, 12194–12200.

Sharma, V., Kumar, R.V., Pakshirajan, K., Pugazhenthi, G., 2017. Integrated adsorption-membrane filtration process for antibiotic removal from aqueous solution. Powder technology 321, 259–269.

Shi, P., Dai, X., Zheng, H., Li, D., Yao, W., Hu, C., 2014. Synergistic catalysis of Co_3O_4 and graphene oxide on Co_3O_4/GO catalysts for degradation of Orange II in water by advanced oxidation technology based on sulfate radicals. Chemical Engineering Journal 240, 264–270.

Shi, P., Su, R., Wan, F., Zhu, M., Li, D., Xu, S., 2012a. Co_3O_4 nanocrystals on graphene oxide as a synergistic catalyst for degradation of Orange II in water by advanced oxidation technology based on sulfate radicals. Applied Catalysis B: Environmental 123, 265–272.

Shi, P., Su, R., Zhu, S., Zhu, M., Li, D., Xu, S., 2012b. Supported cobalt oxide on graphene oxide: Highly efficient catalysts for the removal of Orange II from water. Journal of hazardous materials 229, 331–339.

Shukla, P., Sun, H., Wang, S., Ang, H.M., Tadé, M.O., 2011a. Co-SBA-15 for heterogeneous oxidation of phenol with sulfate radical for wastewater treatment. Catalysis Today 175, 380–385.

Shukla, P., Sun, H., Wang, S., Ang, H.M., Tadé, M.O., 2011b. Nanosized Co_3O_4/SiO_2 for heterogeneous oxidation of phenolic contaminants in waste water. Separation and Purification Technology 77, 230–236.

Shukla, P., Wang, S., Singh, K., Ang, H.M., Tadé, M.O., 2010. Cobalt exchanged zeolites for heterogeneous catalytic oxidation of phenol in the presence of peroxymonosulphate. Applied Catalysis B: Environmental 99, 163–169.

Shukla, P.R., Wang, S., Sun, H., Ang, H.M., Tadé, M., 2010. Activated carbon supported cobalt catalysts for advanced oxidation of organic contaminants in aqueous solution. Applied Catalysis B: Environmental 100, 529–534.

Sichel, C., Garcia, C., Andre, K., 2011. Feasibility studies: UV/chlorine advanced oxidation treatment for the removal of emerging contaminants. Water research 45, 6371–6380.

Stefan, M.I., 2017. Advanced oxidation processes for water treatment: fundamentals and applications. IWA publishing.

Su, S., Guo, W., Leng, Y., Yi, C., Ma, Z., 2013. Heterogeneous activation of Oxone by $Co_xFe_{3-x}O_4$ nanocatalysts for degradation of rhodamine B. Journal of hazardous materials 244, 736–742.

Sun, H., Tian, H., Hardjono, Y., Buckley, C.E., Wang, S., 2012. Preparation of cobalt/carbon-xerogel for heterogeneous oxidation of phenol. Catalysis today 186, 63–68.

Sun, H., Wang, Y., Liu, S., Ge, L., Wang, L., Zhu, Z., Wang, S., 2013. Facile synthesis of nitrogen doped reduced graphene oxide as a superior metal-free catalyst for oxidation. Chemical Communications 49, 9914–9916.

Sun, J., Li, X., Feng, J., Tian, X., 2009. Oxone/Co^{2+} oxidation as an advanced oxidation process: comparison with traditional Fenton oxidation for treatment of landfill leachate. Water research 43, 4363–4369.

Syafei, A.D., Lin, C.-F., Wu, C.-H., 2008. Removal of natural organic matter by ultrafiltration with TiO_2-coated membrane under UV irradiation. Journal of colloid and interface science 323, 112–119.

Tan, C., Gao, N., Deng, Y., Zhang, Y., Sui, M., Deng, J., Zhou, S., 2013. Degradation of antipyrine by UV, UV/H_2O_2 and UV/PS. Journal of hazardous materials 260, 1008–1016.

Torad, N.L., Hu, M., Ishihara, S., Sukegawa, H., Belik, A.A., Imura, M., Ariga, K., Sakka, Y., Yamauchi, Y., 2014. Direct Synthesis of MOF-Derived Nanoporous Carbon with Magnetic Co Nanoparticles toward Efficient Water Treatment. Small 10, 2096–2107.

Trovó, A.G., Nogueira, R.F., Agüera, A., Fernandez-Alba, A.R., Sirtori, C., Malato, S., 2009. Degradation of sulfamethoxazole in water by solar photo-Fenton. Chemical and toxicological evaluation. Water research 43, 3922–3931.

Tsitonaki, A., Petri, B., Crimi, M., Mosba ek, H., Siegrist, R.L., Bjerg, P.L., 2010. In situ chemical oxidation of contaminated soil and groundwater using persulfate: a review. Critical Reviews in Environmental Science and Technology 40, 55–91.

Venkatachalapathy, B., Ramamurthy, P., 1996. Reactions of nitrate radical with amino acids in acidic aqueous medium: a flash photolysis investigation. Journal of Photochemistry and Photobiology A: Chemistry 93, 1–5.

Wang, C., Wang, H., Luo, R., Liu, C., Li, J., Sun, X., Shen, J., Han, W., Wang, L., 2017. Metal-organic framework one-dimensional fibers as efficient catalysts for activating peroxymonosulfate. Chemical Engineering Journal 330, 262–271.

Wang, S., Tian, J., Wang, Q., Zhao, Z., Cui, F., Li, G., 2019. Low-temperature sintered high-strength CuO doped ceramic hollow fiber membrane: Preparation, characterization and catalytic activity. Journal of Membrane Science 570, 333–342.

Wang, X., Shi, F., Huang, W., Fan, C., 2012. Synthesis of high quality TiO_2 membranes on alumina supports and their photocatalytic activity. Thin Solid Films 520, 2488–2492.

Wang, Y., Ao, Z., Sun, H., Duan, X., Wang, S., 2016. Activation of peroxymonosulfate by carbonaceous oxygen groups: experimental and density functional theory calculations. Applied Catalysis B: Environmental 198, 295–302.

Wang, Yu, Cheng, J., Huang, M., Liu, M., Li, M., Xu, C., 2017. Effects of surface modification with Co 3 O 4 nanoparticles on the oxygen permeability of $Ba_{0.5}Sr_{0.5}Co_{0.8}Fe_{0.2}O_{3-\delta}$ membranes. Applied Surface Science 416, 574–580.

Wang, Y., Sun, H., Ang, H.M., Tadé, M.O., Wang, S., 2014. Magnetic Fe_3O_4/carbon sphere/cobalt composites for catalytic oxidation of phenol solutions with sulfate radicals. Chemical Engineering Journal 245, 1–9.

Wang, Y., Zhao, S., Fan, W., Tian, Y., Zhao, X., 2018. The synthesis of novel Co-Al_2O_3 nanofibrous membranes with efficient activation of peroxymonosulfate for bisphenol A degradation. Environmental Science: Nano.

Wang, Yanbin, Zhao, X., Cao, D., Wang, Yan, Zhu, Y., 2017. Peroxymonosulfate enhanced visible light photocatalytic degradation bisphenol A by single-atom dispersed Ag mesoporous gC_3N_4 hybrid. Applied Catalysis B: Environmental 211, 79–88.

Westerhoff, P., Aiken, G., Amy, G., Debroux, J., 1999. Relationships between the structure of natural organic matter and its reactivity towards molecular ozone and hydroxyl radicals. Water research 33, 2265–2276.

WP, W., Yang, H., Xian, T., JL, J., 2012. XPS and magnetic properties of $CoFe_2O_4$ nanoparticles synthesized by a polyacrylamide gel route. Materials Transactions 53, 1586–1589.

Wu, R., Qian, X., Rui, X., Liu, H., Yadian, B., Zhou, K., Wei, J., Yan, Q., Feng, X.-Q., Long, Y., 2014. Zeolitic Imidazolate Framework 67-Derived High Symmetric Porous Co_3O_4

Hollow Dodecahedra with Highly Enhanced Lithium Storage Capability. Small 10, 1932–1938.

Xia, H., Zhu, D., Luo, Z., Yu, Y., Shi, X., Yuan, G., Xie, J., 2013. Hierarchically structured Co_3O_4@ Pt@MnO_2 nanowire arrays for high-performance supercapacitors. Scientific reports 3.

Xu, L., Wang, J., 2011. A heterogeneous Fenton-like system with nanoparticulate zero-valent iron for removal of 4-chloro-3-methyl phenol. Journal of hazardous materials 186, 256–264.

Xu, L.J., Chu, W., Gan, L., 2015. Environmental application of graphene-based $CoFe_2O_4$ as an activator of peroxymonosulfate for the degradation of a plasticizer. Chemical engineering journal 263, 435–443.

Xu, R., Zeng, H.C., 2004. Self-generation of tiered surfactant superstructures for one-pot synthesis of Co_3O_4 nanocubes and their close-and non-close-packed organizations. Langmuir 20, 9780–9790.

Yang, Q., Choi, H., Al-Abed, S.R., Dionysiou, D.D., 2009. Iron–cobalt mixed oxide nanocatalysts: heterogeneous peroxymonosulfate activation, cobalt leaching, and ferromagnetic properties for environmental applications. Applied Catalysis B: Environmental 88, 462–469.

Yang, Q., Choi, H., Chen, Y., Dionysiou, D.D., 2008. Heterogeneous activation of peroxymonosulfate by supported cobalt catalysts for the degradation of 2, 4-dichlorophenol in water: the effect of support, cobalt precursor, and UV radiation. Applied Catalysis B: Environmental 77, 300–307.

Yang, Q., Choi, H., Dionysiou, D.D., 2007. Nanocrystalline cobalt oxide immobilized on titanium dioxide nanoparticles for the heterogeneous activation of peroxymonosulfate. Applied Catalysis B: Environmental 74, 170–178.

Yang, Y., Lu, X., Jiang, J., Ma, J., Liu, G., Cao, Y., Liu, W., Li, J., Pang, S., Kong, X., 2017. Degradation of sulfamethoxazole by UV, UV/H_2O_2 and UV/persulfate (PDS): formation of oxidation products and effect of bicarbonate. Water research 118, 196–207.

Yao, Y., Cai, Y., Wu, G., Wei, F., Li, X., Chen, H., Wang, S., 2015. Sulfate radicals induced from peroxymonosulfate by cobalt manganese oxides ($Co_xMn_{3-x}O_4$) for Fenton-like reaction in water. Journal of hazardous materials 296, 128–137.

Yao, Y., Lian, C., Hu, Y., Zhang, J., Gao, M., Zhang, Y., Wang, S., 2017. Heteroatoms doped metal iron–polyvinylidene fluoride (PVDF) membrane for enhancing oxidation of organic contaminants. Journal of hazardous materials 338, 265–275.

Yao, Y., Yang, Z., Zhang, D., Peng, W., Sun, H., Wang, S., 2012. Magnetic $CoFe_2O_4$–graphene hybrids: facile synthesis, characterization, and catalytic properties. Industrial & Engineering Chemistry Research 51, 6044–6051.

Yin, R., Guo, W., Du, J., Zhou, X., Zheng, H., Wu, Q., Chang, J., Ren, N., 2017. Heteroatoms doped graphene for catalytic ozonation of sulfamethoxazole by metal-free catalysis: Performances and mechanisms. Chemical Engineering Journal 317, 632–639.

Yin, R., Guo, W., Wang, H., Du, J., Zhou, X., Wu, Q., Zheng, H., Chang, J., Ren, N., 2018. Selective degradation of sulfonamide antibiotics by peroxymonosulfate alone: Direct oxidation and nonradical mechanisms. Chemical Engineering Journal 334, 2539–2546.

Yun, E.-T., Lee, J.H., Kim, J., Park, H.-D., Lee, J., 2018. Identifying the Nonradical Mechanism in the Peroxymonosulfate Activation Process: Singlet Oxygenation Versus Mediated Electron Transfer. Environmental science & technology.

Zalibera, M., Rapta, P., Staško, A., Brindzová, L., Brezová, V., 2009. Thermal generation of stable spin trap adducts with super-hyperfine structure in their EPR spectra: An alternative EPR spin trapping assay for radical scavenging capacity determination in dimethylsulphoxide. Free Radical Research 43, 457–469.

Zhang, B.-T., Lin, J.-M., 2010. Chemiluminescence and energy transfer mechanism of lanthanide ions in different media based on peroxomonosulfate system. Luminescence 25, 322–327.

Zhang, B.-T., Zhang, Y., Teng, Y., Fan, M., 2015. Sulfate radical and its application in decontamination technologies. Critical Reviews in Environmental Science and Technology 45, 1756–1800.

Zhang, L., Zhao, X., Ma, W., Wu, M., Qian, N., Lu, W., 2013. Novel three-dimensional Co_3O_4 dendritic superstructures: hydrothermal synthesis, formation mechanism and magnetic properties. CrystEngComm 15, 1389–1396.

Zhang, T., Chen, Y., Wang, Y., Le Roux, J., Yang, Y., Croué, J.-P., 2014. Efficient peroxydisulfate activation process not relying on sulfate radical generation for water pollutant degradation. Environmental science & technology 48, 5868–5875.

Zhang, T., Zhu, H., Croué, J.-P., 2013. Production of sulfate radical from peroxymonosulfate induced by a magnetically separable $CuFe_2O_4$ spinel in water: efficiency, stability, and mechanism. Environmental science & technology 47, 2784–2791.

Zhang, W., Tay, H.L., Lim, S.S., Wang, Y., Zhong, Z., Xu, R., 2010. Supported cobalt oxide on MgO: highly efficient catalysts for degradation of organic dyes in dilute solutions. Applied Catalysis B: Environmental 95, 93–99.

Zhou, Y., Jiang, J., Gao, Y., Ma, J., Pang, S.-Y., Li, J., Lu, X.-T., Yuan, L.-P., 2015. Activation of peroxymonosulfate by benzoquinone: a novel nonradical oxidation process. Environmental science & technology 49, 12941–12950.

Zhou, Z., Zhang, Y., Wang, Z., Wei, W., Tang, W., Shi, J., Xiong, R., 2008. Electronic structure studies of the spinel $CoFe_2O_4$ by X-ray photoelectron spectroscopy. Applied Surface Science 254, 6972–6975.

Zhu, K., Jin, C., Klencsár, Z., Ganeshraja, A.S., Wang, J., 2017. Cobalt-iron Oxide, Alloy and Nitride: Synthesis, Characterization and Application in Catalytic Peroxymonosulfate Activation for Orange II Degradation. Catalysts 7, 138.

Zhu, Z.-S., Qu, J., Hao, S.-M., Han, S., Jia, K.-L., Yu, Z.-Z., 2018. α-Fe_2O_3 Nanodisk/Bacterial Cellulose Hybrid Membranes as High-Performance Sulfate-Radical-Based Visible Light Photocatalysts under Stirring/Flowing States. ACS applied materials & interfaces 10, 30670–30679.

Zhuang, Y., Lin, Q., Zhang, L., Luo, L., Yao, Y., Lu, W., Chen, W., 2016. Mesoporous carbon-supported cobalt catalyst for selective oxidation of toluene and degradation of water contaminants. Particuology 24, 216–222.